

Spiral Galaxies with Thick Box/Peanut Bulges

Dissertation

zur
Erlangung des Doktorgrades (Dr. rer. nat.)
der
Mathematisch-Naturwissenschaftlichen Fakultät
der
Rheinischen Friedrich-Wilhelms-Universität
Bonn

vorgelegt von

Daniela Vergani

aus

Mailand (Italien)

Bonn, Juni 2003

Angefertigt mit Genehmigung
der Mathematisch-Naturwissenschaftlichen Fakultät
der Rheinischen Friedrich-Wilhelms-Universität Bonn

1. Referent: Professor Dr. U. Klein
2. Referent: Professor Dr. R.-J. Dettmar

Tag der Promotion:
18. Juni 2003

Contents

Abstract	1
1 Introduction	3
1.1 Bulge Working Definitions	3
1.2 Bulge Formation Mechanisms	4
Old-Bulge Formation or Hierarchical Merging Scenarios	4
Early-Bulge Formation or Secular Evolution Scenarios	5
1.3 Thesis Outline	5
2 H I observations and data analysis	9
2.1 Introduction	9
2.1.1 BPS bulges	9
2.1.2 BPS bulges and bars	10
2.1.3 Mergers as possible formation scenario	10
2.1.4 Bar formation models	11
2.1.5 The purpose of this project	11
2.2 The Sample	12
2.3 The observations	12
2.3.1 HI observations and data reduction	12
Global Profile and HI masses	15
Determination of the center and the systemic velocity	15
2.4 Morphology and kinematics of the individual galaxies	15
Atlas of the observations	16
2.4.1 ESO 383-05	19
2.4.2 IC 4745	20
2.4.3 NGC 1055	23
2.4.4 UGC 9759	25
2.4.5 NGC 7183	28
2.4.6 NGC 5719	28
2.4.7 IC 4757	30
2.4.8 UGC 10205	33
2.5 Discussion	37
2.6 Conclusion	40

3	Optical and near-infrared observations, data reduction, and analysis	45
3.1	Introduction	45
3.2	The Data	47
3.2.1	The Sample	47
3.2.2	Optical observation and data reduction	47
3.2.3	Near-infrared observations and data reduction	55
3.3	The isophotal images and the observed surface brightness profiles	56
3.4	Parameters of Thick Boxy Bulges	61
3.5	Summary	67
4	Stellar and gaseous kinematics in four galaxies with thick box/peanut bulges	71
4.1	Introduction	71
4.2	Spectroscopic Observations and Data Reductions	72
4.3	Observational results	73
4.3.1	The stellar and ionized gas kinematics	73
	NGC 5719	73
	IC 4745	79
	IC 4757	79
	NGC 7183	80
4.3.2	The HI gas morphology and kinematics in NGC 5719	81
	HI moment map	81
	Velocity field	81
	Position-velocity diagram	82
	Channel maps	83
4.4	Discussion	83
4.5	Conclusion	86
5	Rotation Curves in Edge-On Systems	89
5.1	Rotation velocity measurements and observational problems	89
5.2	Warping effects on the rotation curve	92
5.3	A new approach: Warped Modified Envelope Tracing	96
5.3.1	Outline of the method	96
5.3.2	Testing rotation curves by modeling	97
5.4	Summary	100
6	Deviations from symmetry	103
6.1	Introduction	103
6.1.1	The purpose	104
6.1.2	Sample	104
6.2	Quantifying asymmetries	104
6.2.1	Deviations in the near-infrared surface distribution	104
6.2.2	Deviations in the HI surface density distribution	105
6.2.3	Deviation of the kinematic axis.	105
6.2.4	Deviations in the rotation curve	106
6.2.5	Deviations in the HI line profiles	106
6.2.6	Deviations in the masses contained in the approaching and receding sides	107
6.2.7	Warp classification	107

6.2.8	Table descriptions	107
6.3	Discussion	109
6.3.1	Fraction and statistics of warps	109
6.3.2	Asymmetrical indices	111
6.3.3	Mechanisms triggering lopsidedness	120
6.4	Conclusion	121
7	A particular case: NGC 1055 and infalling gas from the surrounding intergalactic medium	125
7.1	Introduction	125
7.2	NGC 1055	126
7.3	Data acquisition and observational results	127
7.3.1	Observations	127
7.3.2	Morphological and kinematics HI asymmetries	128
7.4	Modeling	129
7.5	Discussion	133
7.6	Conclusion	135
8	Summary and Future Research	139
8.1	HI observational results	139
8.2	Optical and near-infrared analysis	139
8.3	Stellar and gaseous kinematics in the central regions	139
8.4	Rotation curves in edge-on spirals	140
8.5	Asymmetries in the stellar and gaseous components	140
8.6	Future work	140
	Acknowledgments	143

Abstract

In this thesis, observations and data analysis are reported for a sample of edge-on disk galaxies with thick box/peanut bulges. A consistent fraction of bulges deviate from the classical spheroidal shape and display excess light at z -height, which resemble a box or a peanut when viewed in the edge-on orientation.

The close connection of bars and box/peanut-shaped bulges is observationally and theoretically supported by several authors. Interactions can provide a very efficient mechanism to trigger instabilities in the disks, and initiate or speed up the bar formation. Once a bar is formed, it is free to evolve in a box/peanut structure due to buckling and thickening.

The main goal of this project is the measurement of the kinematics and the morphology of spiral galaxies with a particular class of bulges in order to find out relicts of interactions. I have studied the kinematics of the innermost region (by optical long-slit spectroscopy) and at larger scale (via HI 21-cm line) of these galaxies. Investigations of asymmetries in near-infrared images and kinematic indices on the HI observations were also performed. A new technique to derive the rotation curve from the HI observation is presented.

All these new results suggest a scenario where interactions have triggered instabilities in the disk by buckling the box/peanut structure. The thicker box/peanut bulge galaxies are likely to have experienced a mass infall.

1

Introduction

One of the most striking characteristics when looking at the objects in large optical surveys is the variety of the building-blocks of the Universe, the galaxies. An early task, taken up chiefly by Edwin Hubble at the Mount Wilson Observatory in the Twenties of last century was to see if the great variety of objects could be placed in some kind of orderly sequence.

Hubble arranged galaxies in a sequence determined by different criteria. Galaxies are divided into three classes of objects defined by their structures: elliptical, normal and barred spiral galaxies (Fig. 1.1). The elliptical galaxies vary in appearance from those which appear circular to those which are quite elliptical. Hubble designed these galaxies with the letter E (standing for ellipticals) followed by a number specifying the degree of ellipticity. This number ranged from 0 for galaxies which appeared circular to 7 for the most elliptical ones. At the termination of the elliptical series the sequence divides into two parallel sequence: normal spiral (designed by S) and barred spiral (designed by SB) galaxies.

There is no preferred orientation for the galaxies in space. However, due to the criteria adopted for the classification the spiral galaxies are plotted in their face-on appearance.

If we displayed the sequence in an edge-on view we would find out that the barred galaxies appear very differently: Superimposed on the galaxy a vertical component with an X-shaped (or box/peanut) structure appear superposed to the bulge.

1.1 Bulge Working Definitions

The relative importance of the bulge component is immediately realized, as the principal criterion for the morphological classification of galaxies adopted in the famous “tuning fork” sequence by Hubble (1926) is the “relative size of the unresolved nuclear region”. Hubble used the term of *nucleus* of a galaxy instead of bulge, while nowadays, this word is commonly referred to the very central, innermost (<30 pc) part of a galaxy. The degree of resolution in the arms and the extent to which the spiral arms are unwound are the other two criteria which determine the position of a galaxy along the diagram.

Historically, a bulge is defined as smooth light distribution that stretches out of the central part of the disk in highly-inclined galaxies. According to this definition bulges of spiral galaxies are generally related to small elliptical galaxies in the center of a large spiral, and any non-disk light is allocated to the bulge component (Wyse, Gilmore & Franx 1997)

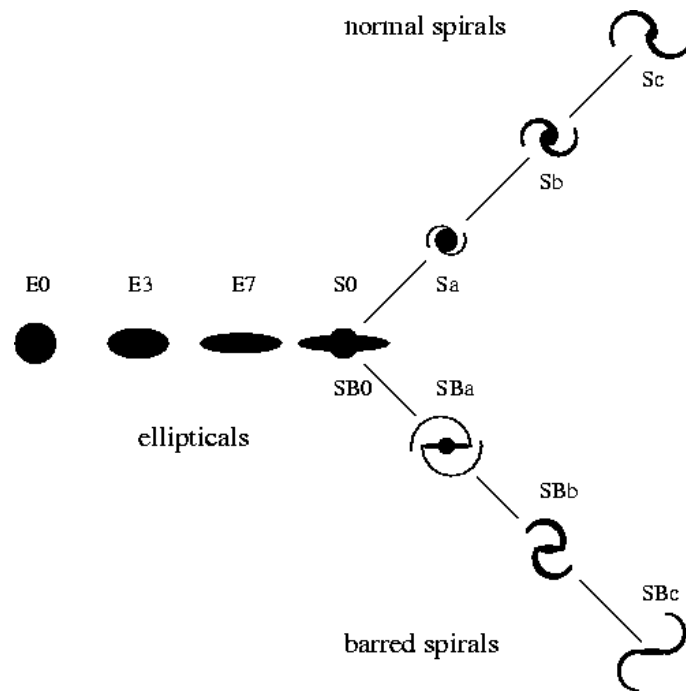


Figure 1.1 Hubble's classification scheme (1926). On the left are the various elliptical galaxies which are classified by the shape of their elliptical outline. On the right are the normal and barred spiral galaxies and the sub-types (Sa, Sb, Sc) in each class.

Instead, a conventional definition of a bulge, adopted for the STScI bulge meeting (Carollo, Ferguson, & Wyse 1999) is the central mass concentration in excess of the inward extrapolation of the outer exponential profile. With this definition, a bulge should be defined also in late-type dwarf galaxies as long as the surface brightness shows a central excess with respect to an exponential contribution.

No mention is given to the age, metallicities and kinematics due to the unclear and debated question of the formation mechanism of a bulge which are introduced in the next section.

1.2 Bulge Formation Mechanisms

Old-Bulge Formation or Hierarchical Merging Scenarios

The old-bulge scenario was proposed by Eggen, Lynden-Bell & Sandage in 1962. They suggested a rapid monolithic dissipational collapse of an over-density region. A gaseous component possessing low angular momentum falls into the central region of a galaxy and initiates the bulge formation. The higher-angular-momentum gas forms the disk later on. Bulges form also by accretion of protogalactic fragments (Searle & Zinn 1978) or by mergers (Toomre 1977, Kauffmann et al. 1993). Following these schemes, a bulge is the oldest component of a galaxy.

Early-Bulge Formation or Secular Evolution Scenarios

Secular evolution scenarios describes the bulge as the result of the vertical thickening of the disk under the influence of the bar structure (Combes & Sanders 1981; Hasan, Pfenniger & Norman 1993). The result of this mechanism is a small-size bulge, which however could be inflated by later accretion events.

In particular, the secular evolution mechanism is well suited for explaining the formation of box/peanut structures. The stellar kinematics in these components support the association with bars (Kuijken & Merrifield 1995, Bureau 1998) as well as N-body simulations (i.e. Athanassoula 2002). Bulges do not appear as a separated component with respect to disks in the broadband color distributions (Peletier & Balcells 1996). Stars formed in the inner disk end up in the bulge due to bar buckling. Thus stellar orbits are bent and brought outside the equatorial plane. This view provides a natural explanation for the continuity observed in the properties of the stellar populations in disks and in bulges (Wyse et al. 1997). However, it was also proposed that tidal interaction and accretion events could originate box/peanut structures. A more exhaustive description of the formation mechanisms will be given in Ch. 2.

Throughout this thesis the conciser term *box/peanut-shaped bulge* is used instead of the more appropriate *box/peanut structure projected into the center*.

1.3 Thesis Outline

In this thesis we analyze the large-scale morphological and dynamical properties of thick box/peanut-shaped bulge galaxies. We search for relations between structural and physical parameters and between small- and large-scale kinematics. These are addressed in the following chapters.

Chapter 2 introduces the basic topics with an historical note on the bulges and their formation mechanisms. It describes observations and data analysis in the HI 21-cm line obtained with the VLA and the ATCA telescopes during the period between July 1997 and May 2000.

Optical and near-infrared observations taken in different runs at several telescopes (Calar Alto 1.23-m telescope, Danish 1.54-m telescope, ESO/La Silla New Technology Telescope) and the interpretation of the individual galaxies are presented in Ch. 3. Surface brightness profiles, radial and vertical isophotes are shown, along with the parameters of the bulge component (effective surface brightness, effective radius and structural parameter n) as derived from modeling the Sérsic functional form on the vertical light distribution in the near-infrared frames.

Chapter 4 describes optical long-slit spectroscopic observations for a subsample taken at the NTT/La Silla ESO telescope in July 2002. The kinematics of the stellar and gaseous components in the innermost region are presented and compared with the large-scale kinematics.

Chapter 5 addresses a new approach to extract the rotation curves in warped galaxies. The development of the warped method, a tool to study rotation curves in moderately resolved, edge-on galaxies, is a crucial step for this research. Using the modeling procedure, the large-scale kinematics of three galaxies was determined using as input the rotation curves extracted with the newly developed method.

In Ch. 6 the morphological and dynamical deviations from symmetry are quantified. The method of asymmetric indices is used, which intends to parameterize asymmetries in galaxies and correlates them with the structural properties of spiral galaxies.

Chapter 7 deals with a case studied in more detail: NGC 1055 which reveals deviations from symmetry in the density distribution and in the kinematics. In order to investigate the HI kinematics a three-dimensional modeling of the target galaxy was developed. Finally, Ch. 8 summarizes this thesis work and gives an outlook on future perspectives.

References

- Athanassoula E., 2002, *ApJ* 569, L83
- Bureau M., 1998, Ph.D. thesis, Australian National University, Australia
- Carollo C.M., Ferguson H.C., Wyse R.F.G., 1999, "The formation of galactic bulges" eds. C.M. Carollo, H.C. Ferguson, R.F.G. Wyse. Cambridge, U.K.; Cambridge University Press
- Combes F., Sanders R.H., 1981, *A&A* 96, 164
- Eggen O.J., Lynden-Bell D., Sandage A.R., 1962, *ApJ* 136, 748
- Hasan H., Pfenniger D., Norman C., 1993, *ApJ* 409, 91
- Hubble E.P., 1926, *ApJ* 64, 321
- Kauffmann G., White S.D.M., Guiderdoni B., 1993, *MNRAS* 264, 201
- Kuijken K., Merrifield M. R., 1995, *ApJ* 443, L13
- Peletier R.F., Balcells M., 1996, *AJ* 111, 2238
- Searle L., Zinn R., 1978, *ApJ* 225, 357
- Toomre A., 1977, *ARA&A* 15, 437
- Wyse R.F.G., Gilmore G., Franx M., 1997, *ARA&A* 35, 637

2

H I observations and data analysis

In this chapter HI observations are reported for a sample of edge-on disk galaxies with thick box/peanut bulges. These bulge-dominated systems are characterized by complex morphologies and kinematics. All galaxies presented in the following show asymmetries and prominent irregularities in the HI.

The proposed mechanisms for the formation of box/peanut-shaped (BPS) bulges are reviewed, in particular stressing the role of interaction events as an element for triggering bars (tidally induced bar), which might account for the large fraction of peculiarities (warps, anomalous emission and asymmetries) in the distribution and the kinematics of HI in the objects of this sample.

Concerning the question whether interactions contribute significantly to the formation of the BPS structure, we can confirm the theoretical predictions. In fact, galaxy interaction might be the likely formation mechanism to reshape the bulge in thick BPS bulge galaxies. The peculiarities analyzed in the context of possible accretion events with a comparison of the interaction events in other systems are discussed. Finally a discussion is presented whether and how these results on prominent BPS bulges can be extended to the class of BPS bulge galaxies.

2.1 Introduction

Bulges are one of the dominant components in spiral galaxies. They play an important role in the formation and evolution of galaxies. Although a clear picture of the mechanism responsible for the bulge formation is still not defined, the hypothesis of internal evolution (Combes et al. 1990) seems to describe well the development of a particular sample of bulges: the box/peanut-shaped (BPS) bulges.

2.1.1 BPS bulges

A consistent fraction of bulges deviate from the classical spheroidal shape and display excess light above the plane at galactocentric radii which appear box or peanut shaped when viewed edge-on. The existence of BPS bulges has been recognized for many years (Burbidge & Burbidge 1969). The fraction of spiral galaxies with a BPS bulge reported by different authors ranges between very small values (1.2%, Jarvis 1986; 13%, de Souza & dos Anjos 1987) to approximately 50% in the more recent statistics (45%, Dettmar & Barteldrees 1988; Lütticke et al. 2000), up to the majority (two thirds) of all spiral galax-

ies according to de Vaucouleurs (1963). This discrepancy between the results of different authors can be explained by the lack of objective criteria to estimate the boxiness of the bulges. Moreover, some studies suffered from the limited number of small diameter systems in their samples (Shaw 1987), or only include the more prominent cases. Therefore, it is not surprising that the fraction of BPS bulges varies with different authors. Nevertheless, despite the different criteria to identify and detect the BPS bulges they represent a non-negligible class of spiral galaxies.

2.1.2 BPS bulges and bars

There is a general agreement that a bar is related to the box/peanut shape of the light distribution. The close connection of bars and BPS bulges is observationally supported by work on stellar kinematics (Bureau & Freeman 1999, Merrifield & Kuijken 1999), on statistical studies (Lütticke et al. 2000) and on few direct cases (e.g. Bettoni & Galletta 1994 on NGC 4442, Quillen et al. 1996 on NGC 7582) as well as by recent N-body simulations (Athanasoula 2002). Typically after 1 Gyr from a bar formation, the inner parts (up to few kpc) inflate and form a peanut structure when the bar is viewed side-on or a boxy structure when viewed end-on (Combes et al. 1990). The instabilities responsible for this phenomenon are called in literature with different terms: bending, box-peanut, buckling, or fire-hose instabilities. The nature of these instabilities is still under debate, and they could be vertical resonances (Pfenniger 1984, 1985; Combes et al. 1990) or fire-hose type instabilities (Fridman & Poliachenki 1984).

2.1.3 Mergers as possible formation scenario

However, it was also proposed that accretion events would *directly* reproduce the axisymmetric cylindrically rotating BPS bulges without passing through the events of the bar formation. The merger of two disks of galaxies of similar sizes could create a BPS distribution of the light (Rowley 1988). However, the constraints on the orientation of the spin and orbital angular momenta of the two galaxies are too restrictive to justify the large fraction of BPS bulges (Binney & Petrou 1985).

Although major mergers between spirals of comparable mass have received most attention because of their spectacular features, the minor mergers were claimed to play an active role in a wide range of linked phenomena, one of those is the triggering of box/peanut bulges.

In the wide range of interaction events able to produce BPS bulges, a scenario was proposed in which the interaction of a spiral involves *one or more companions* of mass less than 10% of the main galaxy (minor merger event). BPS bulges can form directly through minor mergers of *a moderate-sized companion* into the progenitor spiral galaxies under certain condition of the velocity dispersion and decay time-scales of the companion (Binney & Petrou 1985, Rowley 1986). Hernquist & Quinn (1989), and Mihos et al. (1995) successfully showed with N-body simulations that the BPS structure is a long-lived structure in this accretion scenario. In their work, they also argued that the aspect of the BPS bulge galaxies and polar-ring galaxies can share the same origin. Both arise through the cannibalism of a small galaxy by a large. In the first case the impact occurs with angles smaller than 45° , while the polar-ring galaxies result from accreted material at an oblique angle.

Repetitive infalls of companions were proposed as mechanism to reshape the bulges into box/peanut bulges (Binney & Petrou 1985). However, the limits imposed on the range of the orbital energies and angular momenta discourage this scenario. Moreover, usually the

relicts of these satellites are not seen in the surroundings of the BPS bulge galaxies, and Shaw (1987) did not reveal more satellites around BPS bulge galaxies than around those with spheroidal bulges. Controversial results are found in the literature on the role of the environment (Bureau 1998; van den Bergh 2002).

2.1.4 Bar formation models

In the previous section the processes (bars or mergers) were discussed which are considered to be responsible for the BPS structure. However, how does a bar form? At present, two scenarios are widely assumed for the bar formation. The *spontaneous bar model* predicts bar formation through the spontaneous instabilities in relatively cool and rotationally supported disks, while in the *tidally induced bar model* the bar is triggered by interactions (e.g. Miwa & Noguchi 1998, Noguchi 1987, Gerin, Combes & Athanassoula 1990). Mihos et al. (1995) in their numerical simulations and Lütticke et al. (2000) in statistical studies on the environment supported the tidally induced bar scenario.

In this scenario, the interactions excite the development of a bar in a disk and induce the formation of a strong bar. After the development of the bar in the disk as a response to the perturbation of the companion, the distribution reshapes into a box/peanut structure due to buckling and thickening (Noguchi 1987; Gerin, Combes & Athanassoula 1990; Mihos 1995, Bureau & Freeman 1999). As the tidally induced bar model invokes the bar formation as well as it requires an interaction event, this scenario is also called the *hybrid scenario* (Bureau & Freeman 1999).

2.1.5 The purpose of this project

Based on the fact that interaction events produce a highly asymmetric distribution and complex kinematics of the gaseous component, large deviations from symmetry in the morphology and kinematics will indicate a galaxy which is interacting with nearby companions. In order to discern different bar formation scenarios (spontaneous instabilities or bars triggered by interactions) one of the diagnostics is the frequency of peculiarities of the thick BPS bulge galaxies. Whether tidally induced bars, spontaneous bars or other mechanisms are the reasons for the origin and the evolution of our sample of prominent BPS bulge galaxies, they all may leave different traces which should be observed.

For this investigation a sample of eight thick BPS bulge galaxies was selected. An investigation of the HI distribution and kinematics of these galaxies is presented, and the global parameters are derived in order to compare with previous cases in the literature. Finally, the present investigation is used to discuss the likely formation mechanism of this class of objects.

The chapter is organized as follows: in Sect. 2.2 a description of the sample selection is presented, in Sect. 2.3 the observations and the data reduction are described. Results on individual cases are shown in Sect. 2.4. Our study on the statistics of warps, their shapes as well as the fraction of peculiarities are reported in Sect. 2.5. We also discuss the connection between HI and the bulge shape, and possible formation scenarios for these galaxies with an overview of the minor merger events in other systems.

Throughout this chapter we use a Hubble constant of $H_0 = 75 \text{ km s}^{-1} \text{ Mpc}^{-1}$.

2.2 The Sample

The galaxies of this sample were selected from the Third Reference Catalog of Bright Galaxies (de Vaucouleurs et al. 1991; henceforth RC3) on the basis of their orientation. Only galaxies with edge-on orientations and diameters above $2'$ at the B_{25} isophote in the Digital Sky Survey (DSS) were chosen. The selected objects have a ratio of the bulge length (B_{length}) to the diameter at the 25th B magnitude (D_{25}) larger than the typical value for classical bulges. The bulge length is defined as the length marked by increasing light distribution compared to the exponential disk in a radial surface brightness profile well above a possible bar. The typical ratio of B_{length} / D_{25} is ranging from 0.10 to 0.42 for S0–Scd Hubble types, while for this sample it is larger than 0.5 (Lütticke et al. 2000).

The sample does not include systems with major interaction, strongly disturbed ones, or those with a nearly disrupted morphology as these can hardly be morphologically classified.

The objects of this investigation are BPS bulge galaxies, which however show remarkable differences compared with the classical BPS bulge galaxies in the prominence and thickness of their BPS structures. Because of these morphological features, they were called thick box/peanut bulge galaxies (Lütticke et al. 2000).

These galaxies exist in all morphological types, which ensures that these objects form a homogeneous sample and do not represent only the earlier types of the BPS bulge galaxies. They represent 2% of all disk galaxies (S0–Sd), and 4% of all galaxies possessing BPS bulges.

2.3 The observations

2.3.1 HI observations and data reduction

Three galaxies (ESO 383-005, IC 4745, and IC 4757) were observed with the 1.5A-km array of the Australia Telescope Compact Array (ATCA) in May 2000. The more compact EW350-m configuration (October 2001) was used to improve the uv-coverage and the sensitivity in one target source (IC 4745). A 1.5-MHz band with 256 velocity channels was used, which results after Hanning smoothing in a radial velocity resolution of ~ 6.59 km s $^{-1}$. The bandpass was centered on the optical systemic velocity of each galaxy. The second IF observed at the frequency 1984 MHz with a bandwidth of 128 MHz and 33 channels. Each galaxy was observed for 12 hours, and a nearby phase calibrator every hour for 20 minutes after each target scan. The flux density was rescaled by observing PKS 1934-638 for ~ 10 minutes during each observing run, based on the continuum flux density scale of Baars et al. (1977).

The data reduction of the ATCA observations was done using the MIRIAD package (Sault et al. 1995). An interference spike generated by the ATCA acquisition system was present at 1408 MHz and removed from the data.

In the case of the observations of IC 4745 with more configurations, a separate data cube was made for each of the configurations to inspect the data. The data were combined after calibration and continuum subtraction.

Another 5 galaxies (NGC 1055, UGC 9759, NGC 7183, NGC 5719, UGC 10205) were observed with the Very Large Telescope (VLA) in different runs. The HI observations were performed in July 1997, April 2000, and May 2000 with the VLA in the C-array. Using the 4ABCD spectral line mode, the field was simultaneously observed in two partially overlapping spectral bands (IF1 and IF2). The calibration and the continuum subtraction were

	NGC 1055	ESO 383-005	IC 4745	UGC 9759
Field Center (J2000)	02 ^h 41 ^m 44 ^s .7 +00°26'31".00	13 ^h 29 ^m 23 ^s .69 −34°16'22".99	18 ^h 42 ^m 35 ^s .67 −64°56'35".29	15 ^h 10 ^m 41 ^s .10 +55°20'57".00
Array, Configuration	VLA, C	ATCA, 1.5A	ATCA, 1.5A+EW352	VLA, C
Date, Integration time	Jun 26, 96, 6hr	May 20, 00, 12hr	May 21, 00, 12hr Oct 23, 01, 12hr	Apr 25, 00, 8hr
Observed Freq. (MHz)				
IF1	1415.13	1403.01	1398.01	1403.74
IF2	1416.50	1984.0	1984.0	1404.91
Flux and Bandp. Cal.	0137+331	1934-638	1934-638	1331+305
Phase and Gain Cal.	0242-215	1320-446	1814-637	1438+621
Synth. beam	15".28 × 13".71	36".18 × 20".25	32".67 × 27".64	12".00 × 11".57
Chan. sep. (km s ^{−1})	5.19	6.59	6.42 ¹	5.15
Bandwidth (kHz)	1562.50	1562.50	1562.50	1562.50
	NGC 7183	NGC 5719	IC 4757	UGC 10205
Field Center (J2000)	22 ^h 02 ^m 21 ^s .6 −18°54'58".00	14 ^h 40 ^m 56 ^s .4 −00°19'07".00	18 ^h 43 ^m 55 ^s .72 −57°09'58".19	02 ^h 41 ^m 44 ^s .7 +00°26'31".00
Array, Configuration	VLA, C	VLA, C	ATCA, 1.5A	VLA, C
Date, Integration time	Apr 23, 00, 8hr	Apr 17, 00, 8hr	May 23, 00, 12hr	May 17, 00, 8hr
Observed Freq. (MHz)				
IF1	1407.39	1411.67	1404.01	1389.34
IF2	1408.56	1412.84	1984.0	1390.51
Flux and Bandp. Cal.	1331+305, 0137+331	1331+305	1934-638	1331+305
Phase and Gain Cal.	2206-185	1419+064	1814-637	1609+266
Synth. beam	20".15 × 12".10	15".51 × 14".09	26".42 × 16".91	11".55 × 11".00
Chan. sep. (km s ^{−1})	5.15	5.15	6.59	5.15
Bandwidth (kHz)	1562.50	1562.50	1562.50	1562.50

Table 2.1 HI Observations and Instrumental Parameters

done using the Astronomical Image Processing System (AIPS)¹. The visibilities were examined with the program TVFLG, with which the *UV* data of poor quality were flagged. The primary flux density calibrators also served as bandpass calibrators. The phases and gains were calibrated with observations of the secondary calibrators in the neighborhood of the target objects before and after each target scan. The list of calibrators is given in Tab. 1. The task UVLSF was used for the continuum subtraction by fitting a linear baseline to a selected group of channels. The emission-free channels taken at the edges of the band were selected by visual inspection. The *UV* data were then transformed to the *XY* plane and cleaned using the program IMAGR.

The cleaned cubes were spatially smoothed to a resolution about twice as low as the original, and used as masks for the original cube: pixels with signal below 3σ in the smoothed cube were set to zero in the original cube. Further data processing was car-

¹AIPS is distributed by the National Radio Astronomy Observatory.

Object	Morphology	Scale Ratio	R_{HI}/R_{25}	v_{sys}	$M_{\text{tot,HI}}$	M_{HI}/L_B	$\langle \Sigma \rangle$	
(1)	Type	T	kpc/1'	km s^{-1}	$10^9 M_{\odot}$	L_{\odot}/M_{\odot}	$M_{\odot} \text{ pc}^{-2}$	
(1)	(2)	(3)	(4)	(5)	(6)	(7)	(8)	(9)
NGC 1055	SBb	3.2	3.84	1.54	991.65 ± 9.76	4.24	0.38	3.41
ESO 383-05	Sbc	3.8	13.83	1.56	3567.04 ± 6.60	9.58	0.45	2.40
IC 4745	Sab	1.9	18.02	2.24	4646.93 ± 6.42	18.26	0.43	3.27
UGC 9759	Sbc	3.8	13.13	6.28	3386.44 ± 9.10	4.64	0.47	3.73
NGC 7183	S0-a	-0.7	10.05	1.19	2592.43 ± 7.05	5.20	0.43	3.23
NGC 5719	SBab	2.4	6.69	2.04	1724.99 ± 7.50	7.09	0.98	5.11
IC 4757	S0-a	-0.2	13.50	0.88	3480.87 ± 6.20	1.56	0.19	6.90
UGC 10205	Sa	1.0	25.00	0.48	6446.52 ± 6.10	1.21	0.04	5.16

Table 2.2 (1): Galaxy Name; (2), (3): Morphological Type from LEDA; (4): Linear/Angular Scale Ratio; (5) Optical to HI radius ratio; (6) The systemic velocity; (7) The total HI mass; (8) The total HI mass to the B-band luminosity. (9) Mean surface density $\langle \Sigma \rangle$

ried out with the Groningen Image Processing System (GIPSY, van der Hulst et al. 1992), taking advantage also from the Karma visualization package (Gooch 1995). The image cubes were made with both natural and uniform (or robust-Briggs') weighting. The final maps shown in this paper were extracted from the best compromise between the resolution and sensitivity which were obtained using an intermediate weight between natural and uniform, corresponding to a robust weight of 0.5. Tab. 1 lists the sizes of the restoring beams.

Maps of the HI distribution were obtained by taking the zeroth and first moment of the spectrum. Velocity field maps were derived by fitting half a Gaussian to the extreme edges of the velocities in the spectra, e.g. to the lowest radial velocities on the approaching side and to the highest ones on the receding. The details of this method are described in Ch. 5. The adopted fitted Gaussian dispersion was of the same order as the velocity resolution of the observation.

Due to the procedure to isolate the HI emission region in order not to add noise in the final map and to improve the S/N, the noise in the integrated map varies from pixel to pixel. The sigma level in each pixel of the integrated map depends on the number of non-blank pixels (at the same position in the individual channel maps) that were added to produce the integrated map itself. For that reason, the procedure suggested by Verheijen & Sancisi (2001) to compute the noise in the zeroth moment map was followed.

The HI properties derived for the target objects are summarized in Tab. 2.2.

The continuum data were also reduced in MIRIAD. The continuum maps were made from the average of line-free channels near the ends of the bandpass, and subtracted from all the frequency channels using the UVLIN algorithm. The continuum-subtracted maps were then cleaned to remove side-lobes due to the continuum emission and corrected for the primary beam attenuation. The peak of the continuum-subtracted maps is used as first guess for the center determination, as is explained in the next sections.

Global Profile and HI masses

The HI mass from our radio observations is calculated from the flux density integral and the distances derived from these observations. The integrated flux density is derived from the beam-corrected masked cube. Applying the same mask as the one used in the CLEANing process enables us to obtain a better S/N ratio in the integration by setting the region outside the mask to zero.

The HI mass, M_{HI} , is given by:

$$M_{\text{HI}} = 2.36 \cdot 10^5 D^2 \int S dV \quad (2.1)$$

where M_{HI} is the total mass in M_{\odot} , D the distance to the galaxy in Mpc and S the flux density in Jy. The integral is taken over all the velocities in km s^{-1} .

Determination of the center and the systemic velocity

The center of the galaxies and their systemic velocity were fixed very carefully. For an investigation of the lopsidedness phenomenon the inaccuracy of these two parameters could severely affect the analysis.

When the continuum emission is detected, the peak of the continuum source could mark the center as the first guess. Most of the time it is weak, but the detected continuum emission turned out to be sufficient in all objects. As the continuum maps are taken from the HI line-free channels of the same observations the subtraction procedure does not introduce any additional positional error.

Another method to define the center is the ellipse-fitting technique, which unfortunately failed in the case of both the optical image and the total HI map. In fact, the strong dust lane projected toward the center regions yields large errors in the optical regime. Moreover, asymmetries and the non-uniform distribution of the HI all over the disk are clear indications that a pure surface method might easily create artifacts in the results.

Finally, the center of the HI layer has been fixed by using the following method: The HI emission in the innermost region (approximately $< R_{25}$) – which is very often symmetrically distributed – is used. Channels with equal rotation velocities with respect to the systemic velocity are displayed in the same panel, as shown in panel C of the atlas figures. Regions without emission were blanked before. Using the innermost emission, the internal major axis is traced as line which intersects the column density peaks of both approaching and receding sides. The dynamical center will be the position which lies along the major axis of the galaxy, and – simultaneously – minimizes the asymmetries of the position-velocity diagram.

The systemic velocity is calculated by visually inspecting the channel maps in a first approach, then the position-velocity diagram along the major axis is used. The systemic velocity is the velocity which minimizes the asymmetries in the position-velocity diagram, taking into the account any peculiarity of the galaxies.

2.4 Morphology and kinematics of the individual galaxies

In the following subsections the results from the HI observations in the individual galaxies are reported. HI was detected in all the observed galaxies. However, the amount of the neutral hydrogen is particularly low in IC 4757 and UGC 10205.

Atlas of the observations

In the following pages, a seven-panel figure for each galaxy is displayed. The notation is as follows:

Panel a): Total HI column density distribution superimposed on a optical (DSS) image.

Panel b): Velocity field as derived with the method outlined in Ch. 5. The spatial resolution is plotted in the lower left corner.

Panel c): Channel maps with equal rotation velocities as given in each panel (upper right). The size of the synthesized beam is indicated by the ellipse in the lower right-hand corner of the last map. The cross represents the dynamical center. The straight line represents the internal plane of the HI distribution.

Panel d): Position-velocity diagram obtained from the data cube, and taken along the HI major axis. The x -axis indicates arcminutes from the dynamical center, and the horizontal line identifies the systemic velocity.

Panel e): HI radial surface density distribution from a strip integral of the brightness distribution. The profiles of the approaching and the receding side are superimposed. The solid line represents the mean profile.

Panel f): Synthesized HI line profile. The arrow represents the mid-point velocity at 50% of the flux density (W_{50}).

Panel g): Rotation velocities as a function of the radius in arc seconds, obtained from the Warped Modified Envelope Tracing method (Ch. 5). The approaching and the receding sides are superimposed.

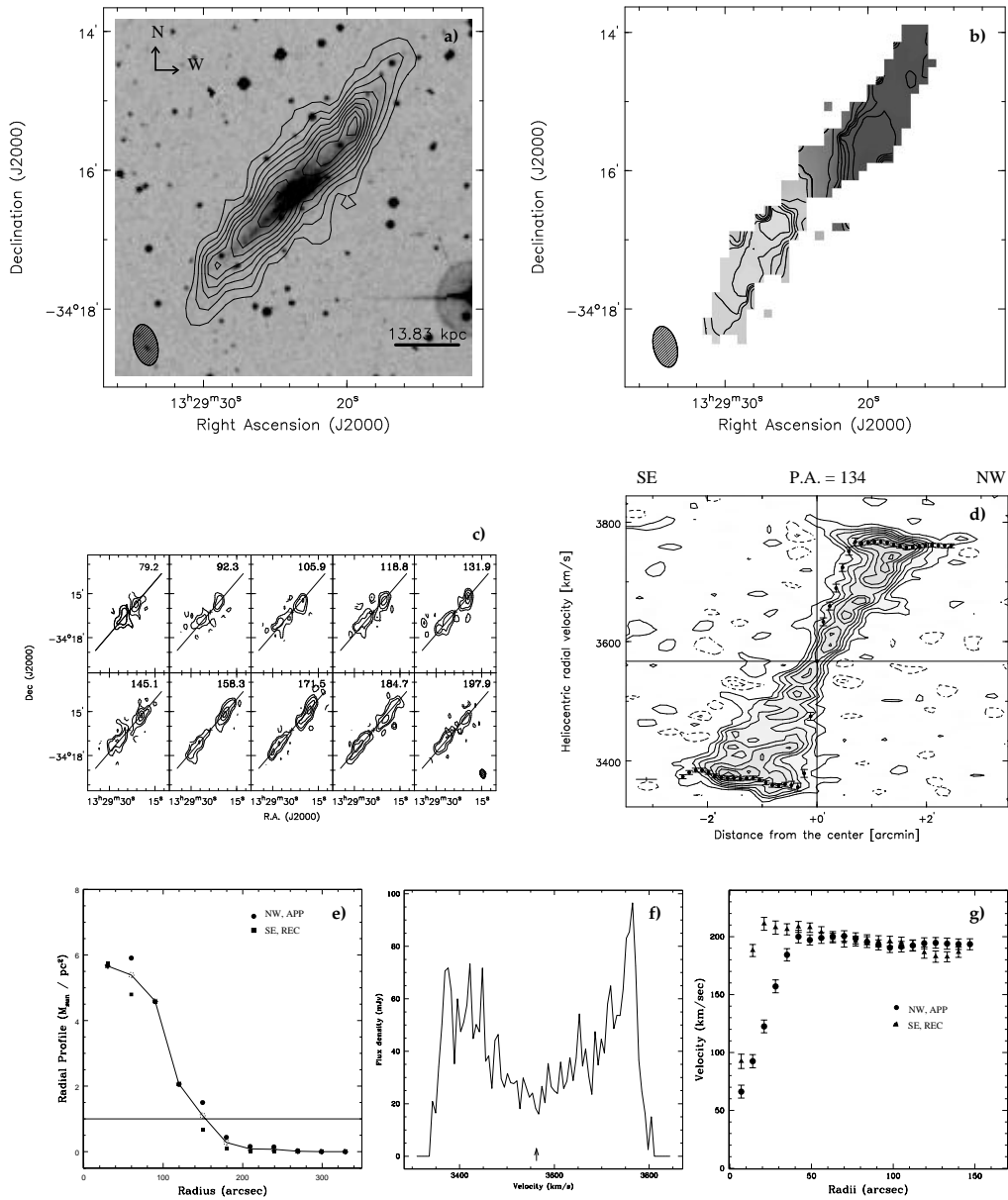


Figure 2.1 Atlas for ESO 383-005. **a)** Contour representation of the total HI column density distribution superimposed on an optical (DSS) image. The contour levels are $3.5 (4.6\sigma)$ to $28.7 \times 10^{20} \text{ atoms cm}^{-2}$ in steps of $2.8 \times 10^{20} \text{ atoms cm}^{-2}$. The spatial resolution is $36''18 \times 20''25$. $1'$ is $\sim 13.83 \text{ kpc}$. **b)** Velocity field with contours and gray scales from 3375 km s^{-1} (east; light shading) to 3800 km s^{-1} (west; dark shading) in increments of 10 km s^{-1} in the outer regions, and 50 km s^{-1} in the innermost area. **c)** Channel maps with equal rotation velocities have contours at -5.2 (dashed), -2.6 , $2.6 (2.1 \sigma)$, 5.2 , 8.7 , 12.2 , 15.7 , $19.2 \text{ mJy beam}^{-1}$. **d)** Position-velocity diagram has contour levels at -4 (dashed), -2 , and from $2 (1.6 \sigma)$ to 17 mJy beam^{-1} in steps of $2.5 \text{ mJy beam}^{-1}$. The grey-scale ranges from 1.0 to $19.0 \text{ mJy beam}^{-1}$ in steps of $0.5 \text{ mJy beam}^{-1}$. **e)** HI radial surface density distribution from a strip integral of the brightness distribution. **f)** Synthesized HI line profile obtained by integrating the data cube along both spatial axes. **g)** Rotation velocities as a function of the radius in arcseconds.

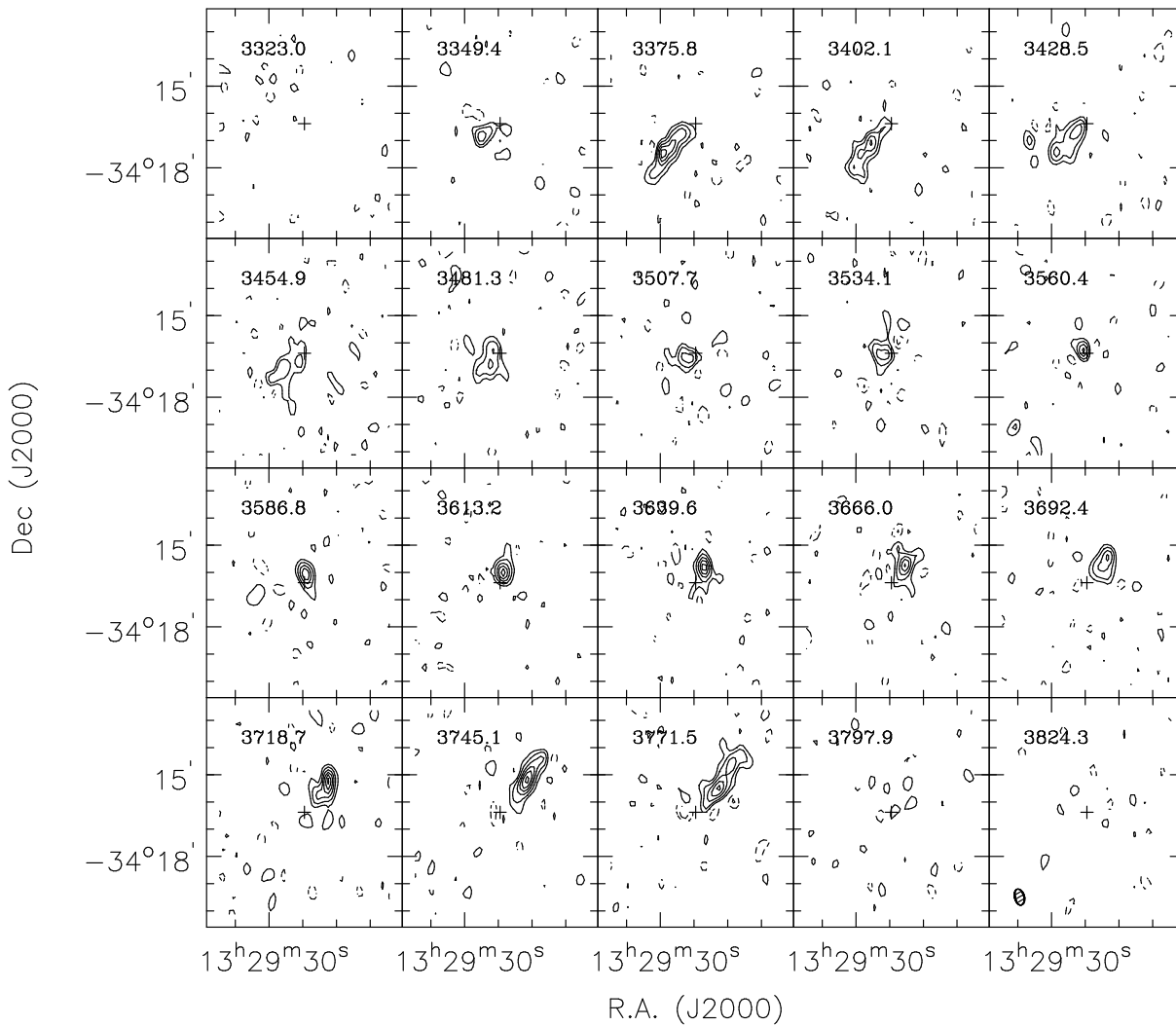


Figure 2.2 The channel maps of ESO 383-005 show every fifth channel. Contours are at -5.2 (dashed), -2.6 , 2.6 (2.1σ), 5.2 , 8.7 , 12.2 , 15.7 , 19.2 mJy beam^{-1} . The channel velocity is given in each panel. The size of the synthesized beam is indicated by the ellipse in the lower left-hand corner of the last map. The cross represents the dynamical center.

2.4.1 ESO 383-05

ESO 383-05 is an edge-on Sbc galaxy with a prominent dust-lane. The upper part of the galaxy is particularly contaminated by the strong dust lane (Fig. 2.1a). A region of dust absorption is observed above the major axis on the north-western side. In the north-west, the stellar disk appears to be tilted starting from $70''$ (16.1 kpc) from the center with respect to the major axis (134°) of the galaxy. On the south-eastern side, the disk is mildly warped in the same direction assuming an U-shaped optical warp.

Kemp & Meaburn (1993) reported on traces of fainter material to the north of the north-western part of the disk and parallel to the disk. A faint tilted arc seems to depart from this diffuse structure connecting to the disk at the outer part.

With other 12 galaxies, ESO 383-05 is a member of the LGG 353 group in which IC 4296 is the brightest one (Garcia 1993). The projected distance of the nearest companion NGC 5140 located at north-west with respect to ESO 383-05 is approximately $45''$ (≈ 10.3 kpc, assuming a distance of 47.5 Mpc). Other 9 members of this group are located within a radius of 1.5 Mpc, while the remaining four galaxies stay at larger distances.

Fig. 2.1a shows the total HI column density distribution of this source superimposed to the optical image. The HI disk extends to about $1.5 R_{25}$ ($R_{25} = 1'65$). The HI distribution coincides with the major axis of the optical galaxy (134°). At the edges of the distribution, the HI contours are pulled out and up to the North and out and down to the South, resembling the typical *integral-sign* of a warp. The HI disk starts to deviate with an offset of some degrees with respect to the kinematic axis exactly at the same position where the optical light tilts ($70''$, $0.7 R_{25}$). The resulting HI warp is very regularly distributed in amplitude and with the same elongation in both directions.

This map reveals also – especially above the major axis – HI emission observed up to $z \sim 20''$ (4.6 kpc) extending northward, and projected toward the center (Fig. 2.1c). The resulting disk is a very thick structure. This behavior could be due to projection effects from the warped distribution observed at the edges of the HI emission. The emission extending above the plane shows a close correspondence with the extra-feature previously observed in the stellar luminosity by Kemp & Meaburn (1993).

The north-western side of the galaxy has a HI peak column density of an order of magnitude denser than the other half at the same distance from the center. In fact, the north-western HI emission is very bright reaching column densities of $\sim 3.7 \times 10^{21}$ atoms cm^{-2} . This lopsided distribution toward receding velocities is also clearly visible in the HI flux density profile.

The integrated HI flux density has a value of $17.93 \text{ Jy km s}^{-1}$, which agrees with the single-dish measurement (Theureau et al. 1998) and implies a total HI mass of $9.58 \times 10^9 M_\odot$ assuming a distance of 47.57 Mpc. The gas-to-luminosity ratio, M_{HI}/L_B , is $0.45 M_\odot/L_\odot$.

The velocity field of this system reveals strong deviations from regular, solid-body rotation. It shows chaotic motions in the region previously described as extra-features with the optical counter-part.

Fig. 2.1b displays contours of the HI velocity versus position along the major axis of the HI emission (P.A. 134°). Along the major axis the HI kinematics is relatively undisturbed on large-scale, and the projected rotation curve is reasonably symmetric with respect to the center. Firstly, the rotation curve rises out to $30''$ (6.9 kpc) reaching a velocity of about 205 km s^{-1} . It flattens off immediately beyond the peak out to the last measured point ($145''$, 33.4 kpc). In the innermost region ($< 30''$), the approaching velocities increase

faster than the receding velocities. However, asymmetries in the velocity pattern are never larger than 12 to 14 km s^{-1} . An inclination of 90° was adopted. The rotation curve shown in Fig. 2.1g was obtained by applying the method described in Ch. 5. The error bars of the rotation curve reflect the formal errors on the velocities and those caused by the fitting procedure.

The heliocentric systemic velocity is found at $(3567 \pm 6.6) \text{ km s}^{-1}$ from the radio observations. This value is consistent with the mid-point of the global HI profile. The value of the heliocentric systemic velocity is in reasonable agreement with previously reported values which range between 3604 km s^{-1} (Theureau et al. 1998) and 3637 km s^{-1} (da Costa et al. 1986).

2.4.2 IC 4745

The prototypical thick boxy bulge galaxy IC 4745 has been classified as a spiral of type Sab (Fig. 2.3a). In the optical, the edge-on galaxy IC 4745 looks quite regular, with a dust lane extended along its major axis (179°).

IC 4745 belongs to the rich LGG 422 group (30 members). The closest galaxy ESO 103-049 is at a projected distance of $10'$ (180.2 kpc). The other two closer morphologically unclassified galaxies (PGC 62142 and 62152) are at distances larger than $25'$ (450.5 kpc, assuming the angular scale $1' = 18.02 \text{ kpc}$), the other members are much further away.

The neutral hydrogen emission is symmetrically distributed within the optical radius ($R_{25} = 1'.05$, Fig. 2.3a). Further out it starts to strongly deviate with respect to the optical major axis (179°), as it is clearly observed in the channel maps (Fig. 2.4). In total, the HI emission exceeds about two times the optical radius. This is shown in Fig. 2.3a where the total HI flux density distribution is superimposed to an optical (B band) DSS image.

The most striking feature revealed by the total intensity map is the southern tail-like structure extending far from the center ($4'.5$, 81.1 kpc) with a significant degree of misalignment with respect to the main HI body (up to 25°).

Similarly to the previous case, ESO 383-005, the presence of gas at high- z (i.e. above the galactic plane) projected toward the central region is observed in Fig. 2.3a at the position $\alpha_{2000} = 18^{\text{h}} 42^{\text{m}} 39^{\text{s}}.2$, $\delta_{2000} = -64^\circ 42' 39''$ level of $\approx 2 \times 10^{21} \text{ atoms cm}^{-2}$ in the East and $\alpha_{2000} = 18^{\text{h}} 42^{\text{m}} 32^{\text{s}}.1$, $\delta_{2000} = -64^\circ 56' 20''$ in the West. This projected high- z HI emission is produced by the tilted emission of the inner region. It could be observed in the velocity range between 4582 km s^{-1} and 4679 km s^{-1} on the south-eastern and between 4679 km s^{-1} and 4736 km s^{-1} on the north-western side in the channel maps (Fig. 2.4) and within the inner 150 km s^{-1} of the rotation velocity from the systemic velocity (Fig. 2.3d).

Within the main optical body, the HI emission shows a quite regular kinematics, as shown by the velocity field. Both approaching and receding sides of the rotation curve reach the peak-velocity ($\approx 260 \text{ km s}^{-1}$) at $50''$. Beyond the peak, asymmetries between the two halves of the rotation curve are relatively small ($< 10 \text{ km s}^{-1}$).

The position-velocity diagram taken along the major axis of the HI distribution shows how the neutral hydrogen emission is distributed in a rotating disk associated with the dust lane (Fig. 2.3d). The HI density distribution is strongly asymmetric with respect to the two halves of the galaxy in the position-velocity diagram. In fact, there is a condensation of HI around the *bumps* in the receding side, in the range around 4679 km s^{-1} .

HI emission was detected over a wide velocity range (from $\sim 4382 \text{ km s}^{-1}$ to $\sim 4923 \text{ km s}^{-1}$), with an integrated HI flux density of $20.15 \text{ Jy km s}^{-1}$ at the assumed distance of 61.95 Mpc. The total HI mass of $1.82 \times 10^{10} M_\odot$ is finally estimated from the global profile. The integrated HI flux profile shows the double-peaked characteristics of

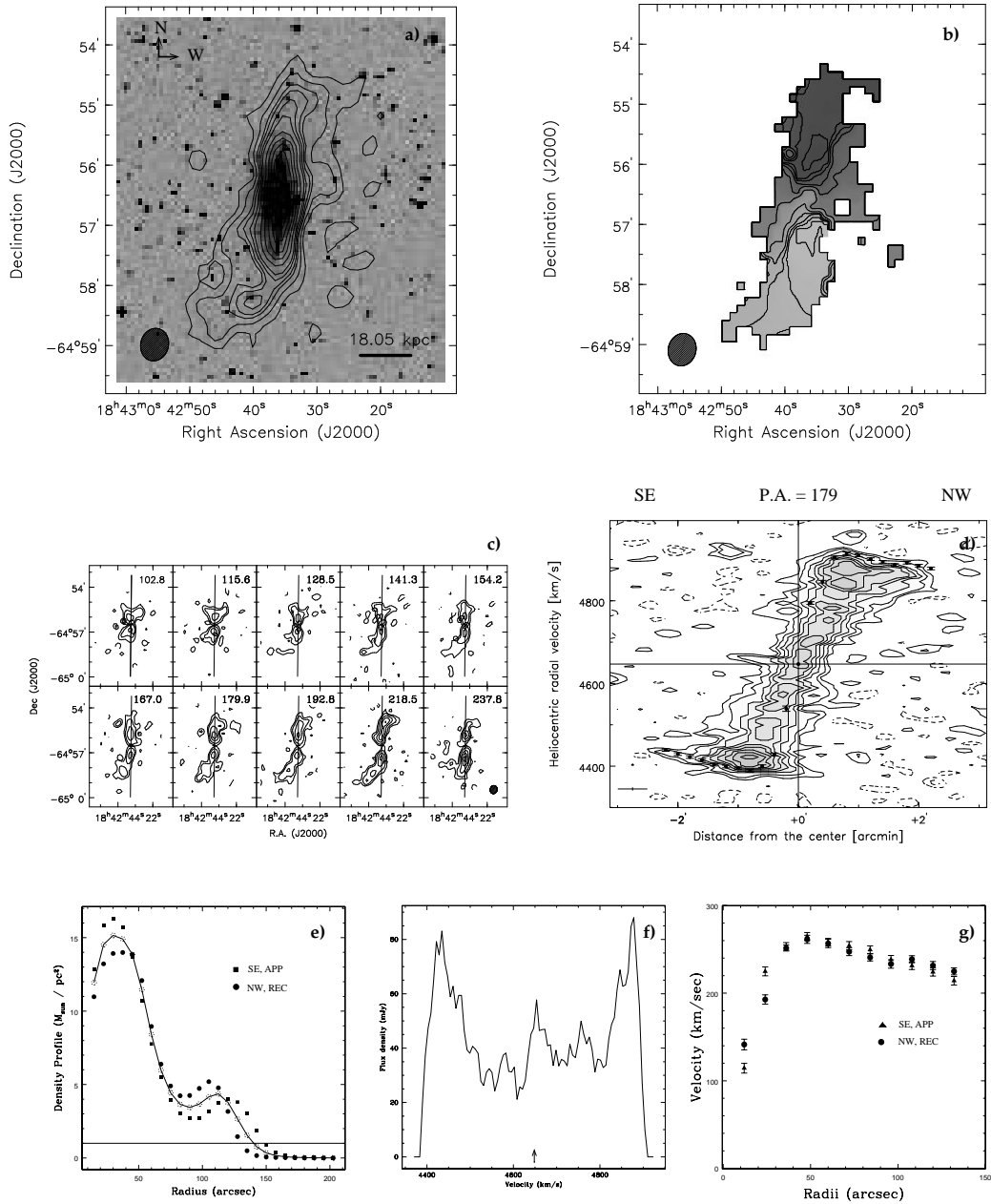


Figure 2.3 Atlas for IC 4745. **a)** Contour representation of the total HI column density distribution superimposed on an optical (DSS) image. The contour levels are 0.5 (2.1σ), 1, 1.5, 1.8, 2.2, 2.6 to 13.8×10^{20} atoms cm^{-2} in steps of 0.8×10^{20} atoms cm^{-2} , and from 20 to 44 in steps of 6×10^{20} atoms cm^{-2} . The spatial resolution is $32''.67 \times 27''.64$. $1'$ is ~ 13.83 kpc. **b)** Velocity field with contours and gray scales from 3362 km s^{-1} (east; light shading) to 3762 km s^{-1} (west; dark shading) in increments of 10 km s^{-1} in the outer regions, and 50 km s^{-1} in the innermost area. **c)** Channel maps with equal rotation velocities have contours at -5.2 (dashed), -2.6 , 2.6 (2.1σ), 5.2 , 8.7 , 12.2 , 15.7 , 19.2 mJy beam^{-1} . **d)** Position-velocity diagram has contour levels at -4 (dashed), -2 , and from 2 (1.6σ) to 17 mJy beam^{-1} in steps of 2.5 mJy beam^{-1} . The grey-scale ranges from 1.0 to 19.0 mJy beam^{-1} in steps of 0.5 mJy beam^{-1} . **e)** HI radial surface density distribution from a strip integral of the brightness distribution **f)** Synthesized HI line profile obtained by integrating the data cube along both spatial axes. **g)** Rotation velocities as a function of the radius in arcseconds.

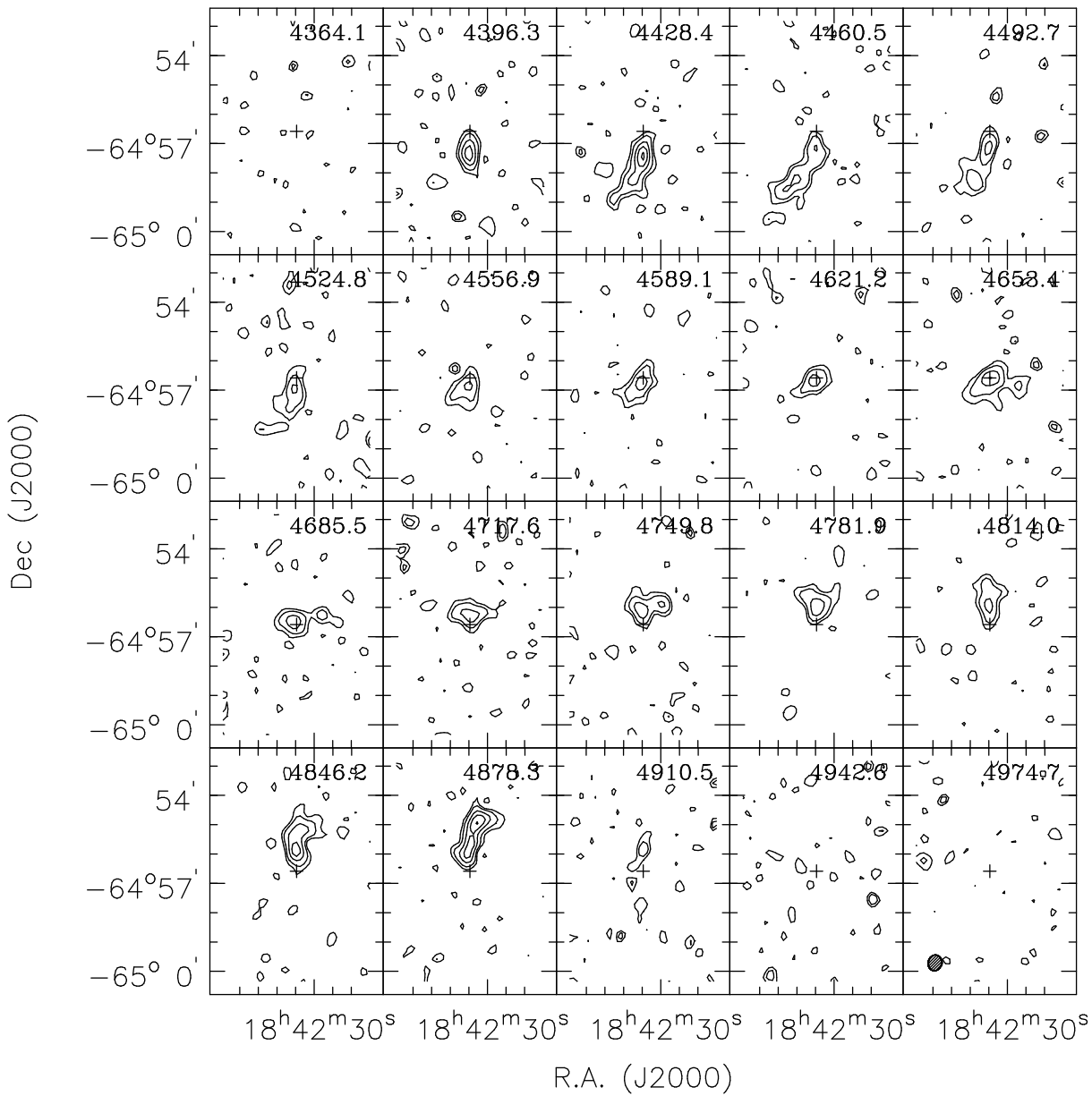


Figure 2.4 The channel maps of IC 4745 show every fifth channel. Contours are at -5.2 (dashed), -2.6 , 2.6 (2.1σ), 5.2 , 8.7 , 12.2 , 15.7 , 19.2 mJy beam^{-1} . The channel velocity is given in each panel. The size of the synthesized beam is indicated by the ellipse in the lower left-hand corner of the last map. The cross represents the dynamical center.

spirals, with separate peaks and condensation of gas near to the systemic velocity in the receding part. This feature in the HI flux profile is recognized in the channels between 4658 and 4617 km s⁻¹ on the western part of the main HI distribution.

The heliocentric systemic velocity of (4646.93 ± 6.42) km s⁻¹ is in reasonable agreement with previously estimated values, which range from 4570 km s⁻¹ (Dressler 1991) to 4730 km s⁻¹ (Fairall 1988)

2.4.3 NGC 1055

NGC 1055 is cataloged in RC3 as a spiral barred SBb galaxy with a prominent dust lane along its major axis (105°, Fig. 2.5a). It shows a thick box/peanut bulge and its diameter, with a value of $D_{25} = 7'.6$, makes this galaxy the 106th largest galaxy on the sky (RC3).

Together with other six members, NGC 1055 is part of a small group (LGG 73, Garcia 1993). The galaxy NGC 1068 is located at the projected distance of only 30' to the south-east (115.2 kpc, assuming a distance of 13.22 Mpc). However, also UGC 2162 and NGC 1073 are within $\approx 65'$ (250 kpc) from NGC 1055, while the other three members are at larger distances.

The HI distribution is more extended than the optical emission ($R_{\text{HI}}/R_{25} = 1.54$, Fig. 2.5a). The HI emission extends beyond 5'.5 south-west from the center, and 6' on the north-western side. The main internal plane of the HI distribution is elongated along the optical position angle (105°). The total intensity map reveals a regular gas disk inside the optical body. However, on the north-western side the HI distribution appears asymmetric starting from 3'.5 from the center at the level of emission of 1.8×10^{21} atoms cm⁻². The redshifted gas south-west of the center is receding. The peak of the diffuse material in the north-west – which seems quite unsettled – is weak, and lacks any obvious optical counterpart. On the approaching side, the emission responsible for the out-spread, warped HI distribution is seen in the channel maps at the north-western edge with velocities around 850 km s⁻¹. There is evidence in these channels (from 822 to 884 km s⁻¹) as well as in the total intensity map (north-western side) for a peculiar emission. This peculiar HI emission does not appear as separate distribution, but shows clearly the same velocity of the main disk, as it is shown by the rotation curve in which there is not any trace of discontinuity. In the south a smooth trend of bending pulls the contours out and up. The south-eastern, receding HI emission deviates toward a higher position angle (few degrees). This feature is observed at a velocity around 1151 km s⁻¹ (at 15 kpc from the center) in the channel maps (Fig. 2.6), and it is responsible for the soft bending at the south-eastern edge in the total intensity map. Finally, the outer HI disk does not bend away from the central plane as it is usual for warped galaxies (i.e. forming a point-symmetric *integral sign*), but rather bends in the same direction (i.e. forming a mirror symmetry with respect to the minor axis).

Overall, the distribution of the velocity field is quite symmetric. However, disturbed contours are visible on both outer halves of the velocity field at the extreme velocities, especially on the north-western side, where also a stronger change in the position angle is observed.

In the position-velocity diagram – taken along a position angle of 105° – HI is detected up to 5' from the center, and even further on the south-eastern side. The position-velocity diagram appears to have an asymmetric shape, with a higher density and a bump at lower velocities. The rotation velocities projected onto the position-velocity diagram shows a very fast increase of the velocity within the inner 30'' up to ≈ 190 km s⁻¹ on both sides. At approaching velocities, a bump in the rotation is observed around 160''. Asymmetries

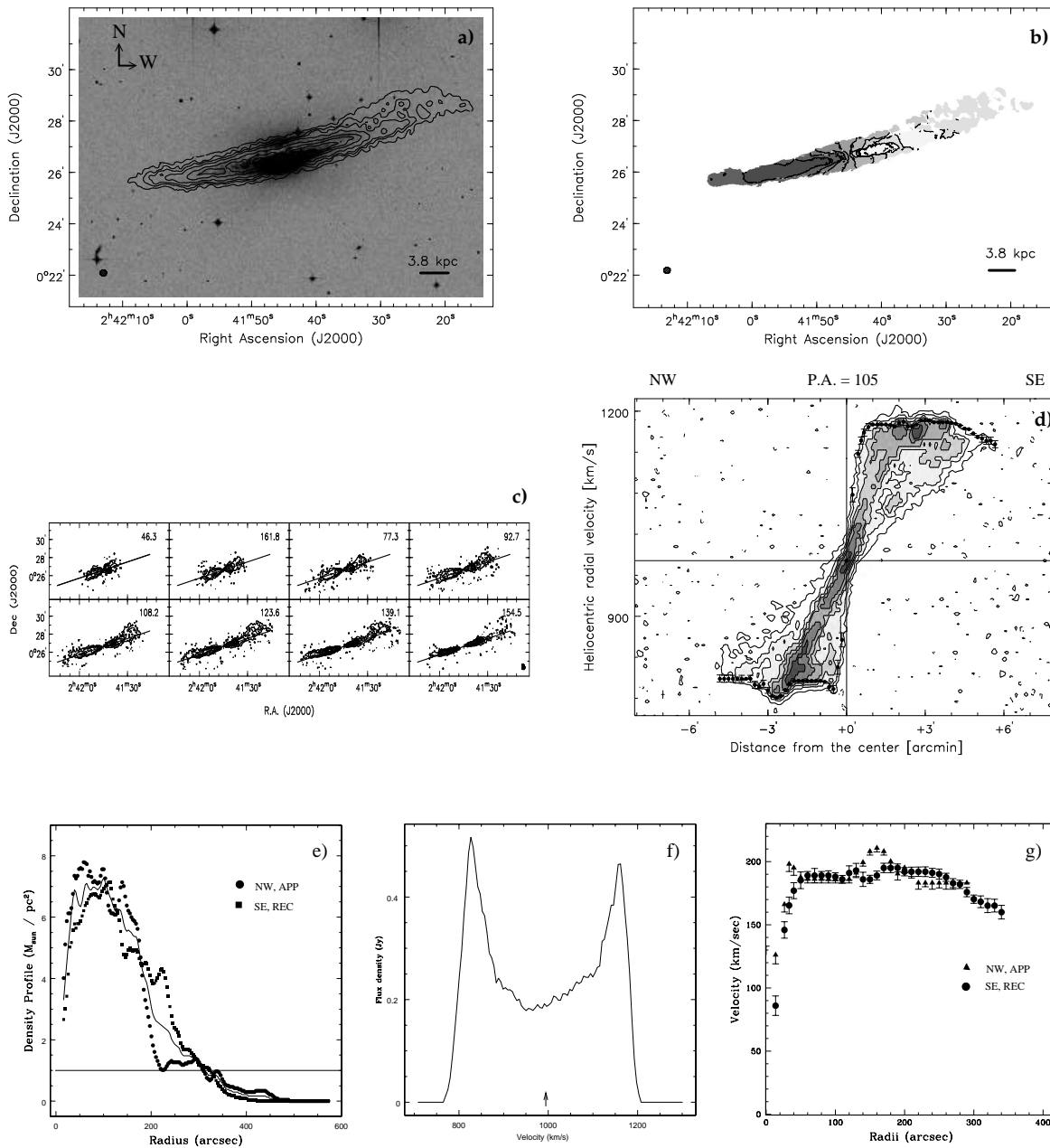


Figure 2.5 Atlas for NGC 1055. **a)** Contour representation of the total HI column density distribution superimposed on an optical (DSS) image. The contour levels are at $2 (4\sigma)$, 6 , 10×10^{20} atoms cm^{-2} , and from 18 to 88 atoms cm^{-2} in steps of 20×10^{20} atoms cm^{-2} . The spatial resolution is $15''.28 \times 13''.71$. $1'$ is ~ 3.8 kpc. **b)** Velocity field with contours and gray scales from 761 km s^{-1} (east; light shading) to 1182 km s^{-1} (west; dark shading) in increments of 50 km s^{-1} . **c)** Channel maps with equal rotation velocities have contours at -4 (dashed), -1.5 , $1.5 (2\sigma)$, ..., $29.5 \text{ mJy beam}^{-1}$ in steps of 4 mJy beam^{-1} . **d)** Position-velocity diagram has contour levels at -2 (dashed), -2 , $2 (2.7\sigma)$, 5 , 8 , 11 , 15 , 20 , 25 , 30 mJy beam^{-1} . The grey-scale ranges from 5 to 30 mJy beam^{-1} in steps of 3 mJy beam^{-1} . **e)** HI radial surface density distribution from a strip integral of the brightness distribution **f)** Synthesized HI line profile obtained by integrating the data cube along both spatial axes. **g)** Rotation velocities as a function of the radius in arcseconds.

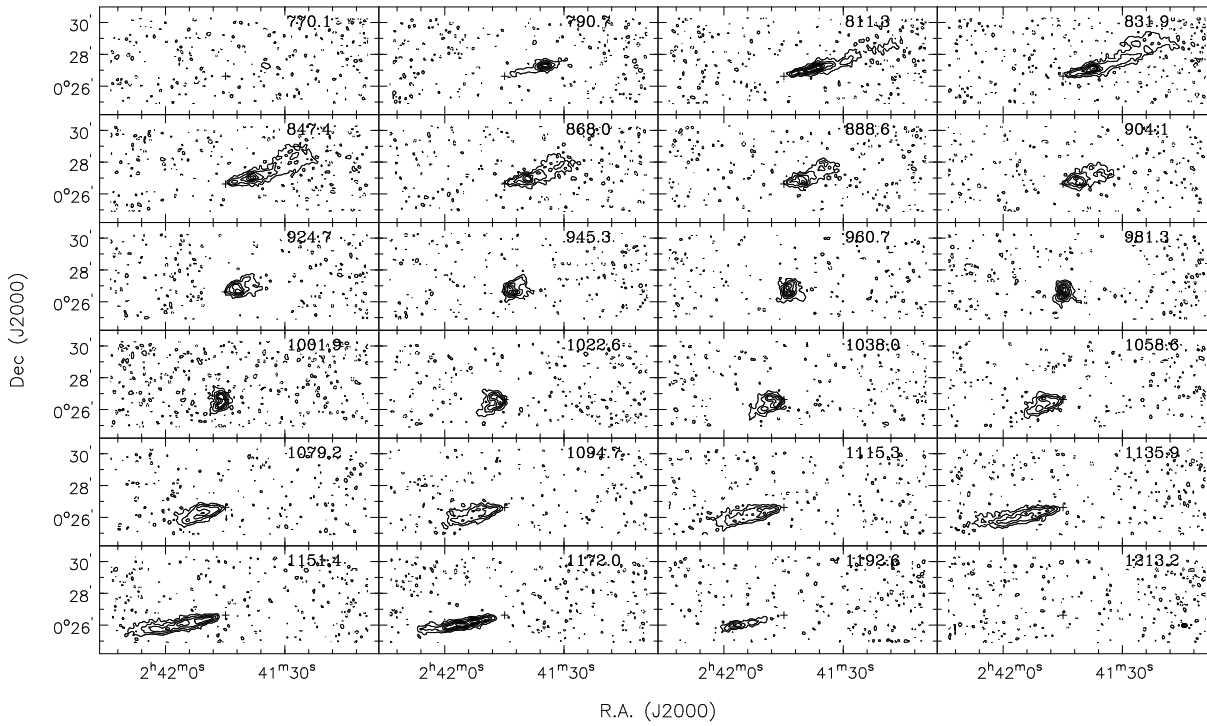


Figure 2.6 The channel maps of NGC 1055 show every fourth channel. Contours are at -4 (dashed), -1.5 , 1.5 (2σ), ..., 29.5 mJy beam^{-1} in steps of 4 mJy beam^{-1} . The channel velocity is given in each panel. The size of the synthesized beam is indicated by the ellipse in the lower left-hand corner of the last map. The cross represents the dynamical center.

between the two halves of the rotation curve are visible especially at larger radii, and are in the order of 10 to 20 km s^{-1} .

The integrated HI flux density (102.76 Jy km s^{-1}) profile shows the double-peaked characteristics of spirals, without any strong trend of lopsidedness. It implies a total HI mass of $4.9 \times 10^9 M_{\odot}$ using a distance of 13.22 Mpc, which is in good agreement with previous measurements (Huchtmeier & Richter 1989, Martin 1993).

Inspecting the channel maps, and by folding the position-velocity diagram a value of (991.65 ± 9.76) km s^{-1} is found for the heliocentric systemic velocity. The other values found for the heliocentric systemic velocity agree well with our findings (ranging between 790 km s^{-1} (de Vaucouleurs & de Vaucouleurs 1976) and 1077 km s^{-1} (Fricke & Kollatschny 1989))

2.4.4 UGC 9759

UGC 9759 is classified as Sc in the Uppsala General Catalogue of Galaxies (Nilson 1973). The optical morphology is illustrated in Fig. 2.7a. The extent of the optical emission, R_{25} , is $50''$ (10.9 kpc) measured from the center to the B_{25} isophote magnitude. Despite the fact that the optical images are strongly contaminated by a dust lane which crosses the front of the galaxy aligned parallel to the major axis (52°), the box/peanut bulge is clearly recognizable. A change in the line-of-node with respect to the inner major axis starts at $20''$ (4.4 kpc) from the center. Starting from the very inner region, the stellar light appears lopsided giving a general aspect of asymmetric structure.

Garcia (1993) associated UGC 9759 to the small LGG 395 group (7 members). The closest

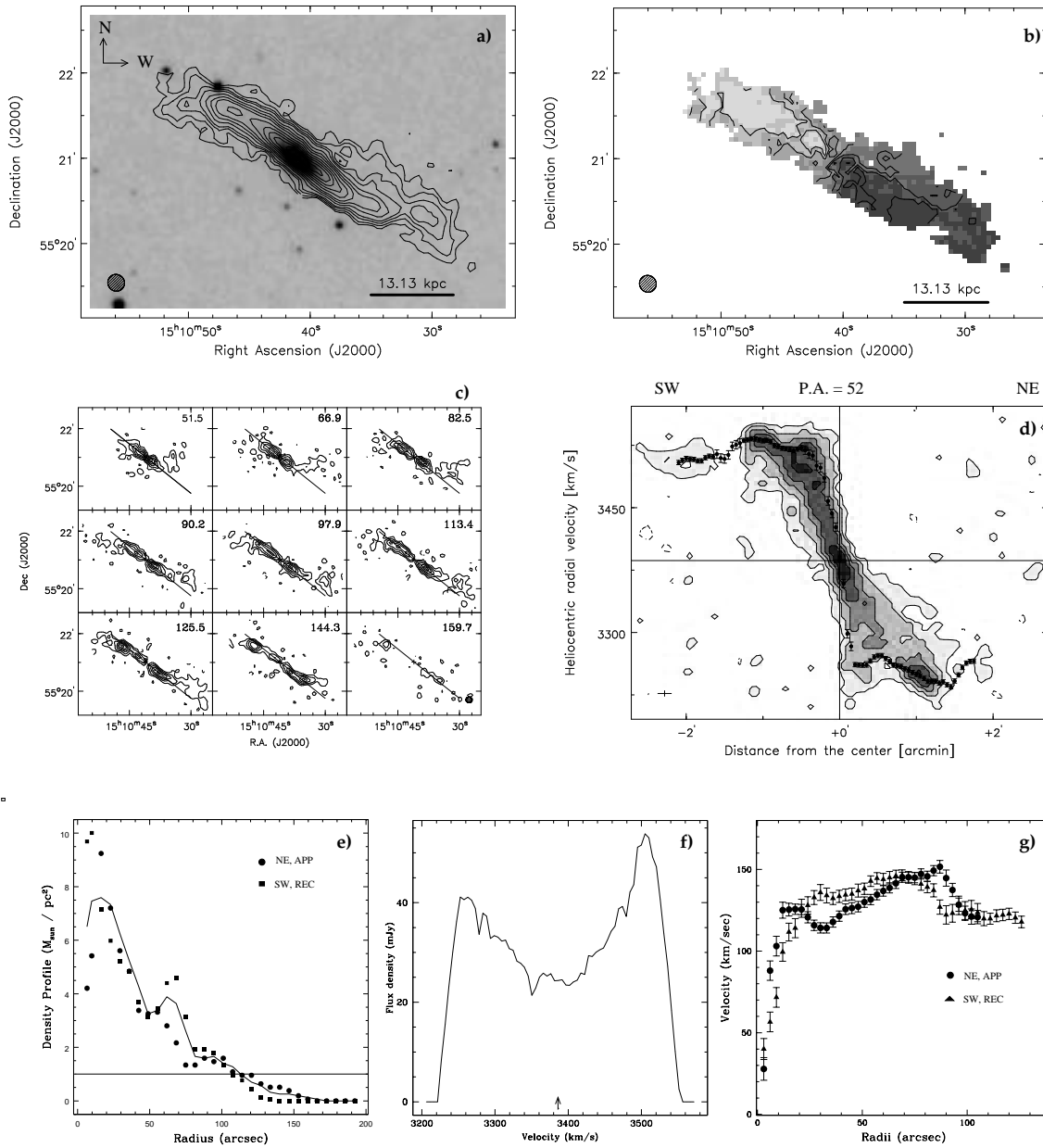


Figure 2.7 Atlas for UGC 9759. **a)** Contour representation of the total HI column density distribution superimposed on an optical (DSS) image. The contour levels are 2.5 (5.9σ), 4, 6, 8, 12, 16 $\times 10^{20}$ atoms cm^{-2} , and from 20 to 55 $\times 10^{20}$ atoms cm^{-2} in steps of 6×10^{20} atoms cm^{-2} . The spatial resolution is $11''.00 \times 11''.57$. $1'$ is ~ 13.13 kpc. **b)** Velocity field with contours and gray scales from 3220 km s^{-1} (east; light shading) to 3560 km s^{-1} (west; dark shading) in increments of 50 km s^{-1} . **c)** Channel maps with equal rotation velocities have contours at -2 (dashed), -0.9 , 0.9 (2σ), and from 1.8 to 6.8 mJy beam^{-1} in steps of 1.2 mJy beam^{-1} . **d)** Position-velocity diagram has contours at -2 (dashed), -0.9 , 0.9 (2σ), and from 1.8 to 6.8 mJy beam^{-1} in steps of 1.2 mJy beam^{-1} . The grey-scale ranges from 0.9 to 6.8 mJy beam^{-1} in steps of 1.2 mJy beam^{-1} . **e)** HI radial surface density distribution from a strip integral of the brightness distribution **f)** Synthesized HI line profile obtained by integrating the data cube along both spatial axes. **g)** Rotation velocities as a function of the radius in arcseconds.

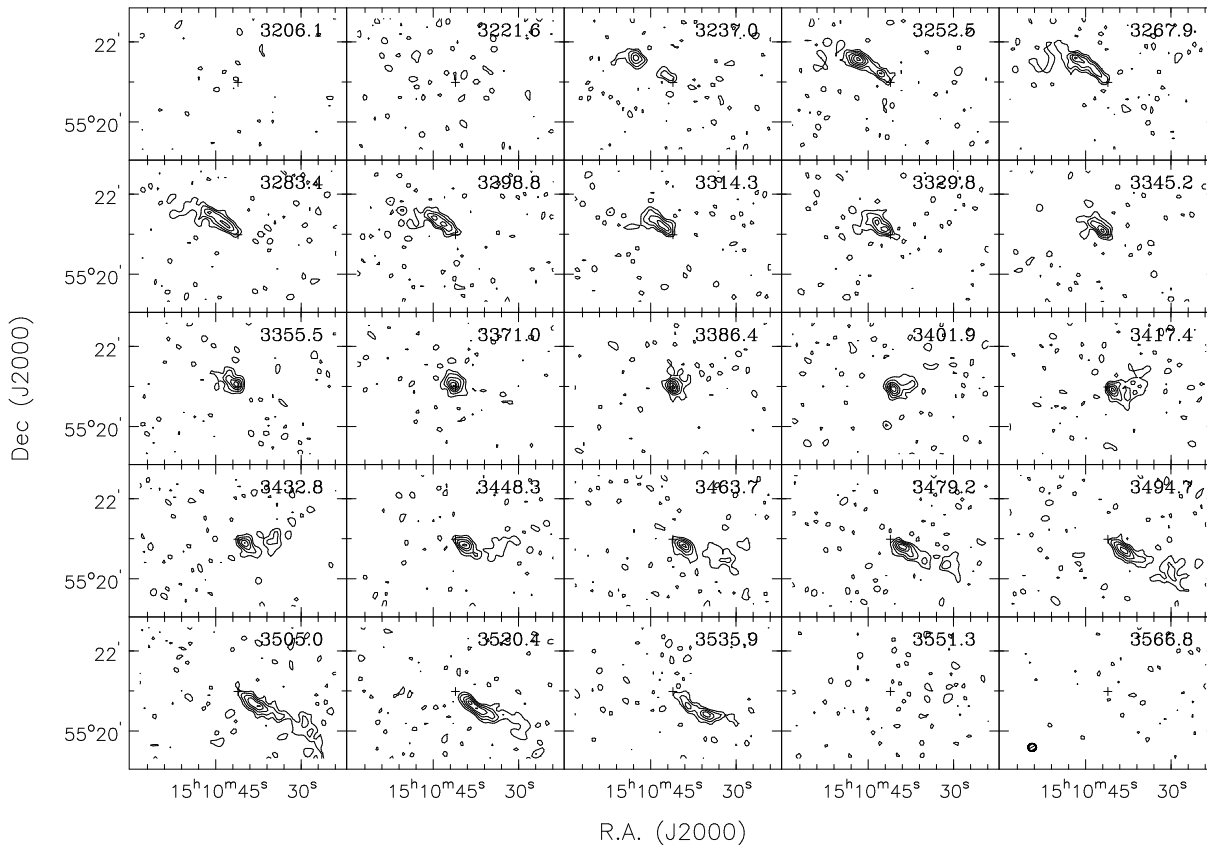


Figure 2.8 The channel maps of UGC 9759 show every third channel. Contours are at -2 (dashed), -0.9 , 0.9 (2σ), and from 1.8 to 6.8mJy beam^{-1} in steps of 1.2mJy beam^{-1} . The channel velocity is given in each panel. The size of the synthesized beam is indicated by the ellipse in the lower left-hand corner of the last map. The cross represents the dynamical center.

galaxy, NGC 5905, is at a projected distance of $30'$ (393 kpc). Within a radius of $50'$ there are 3 other galaxies (NGC 5874 at $42'$ or 551 kpc, NGC 5876, and NGC 5908 both at $\approx 50'$ or 656 kpc).

At the adopted distance (45.15 Mpc), the full extent of the HI emission covers 1.5 (19.7 kpc) from the center at the level of emission of 4×10^{20} atoms cm^{-2} (Fig. 2.7a). The HI disk is significantly larger in extent than the stellar component ($R_{\text{HI}}/R_{25} = 6.28$). Neutral hydrogen in UGC 9759 is distributed in an *integral-sign* shaped, warped disk bending by $\approx 10^\circ$ over the major axis (52°). An *additional HI emission* of low surface brightness extends to the north-west outward from the main, warped disk, and is correlated with a luminous structure visible in the optical image. This HI emission is observed in the channel maps between 3401.9 km s^{-1} and 3448.3 km s^{-1} (Fig. 2.8). It has an offset from the major plane of $\approx 12^\circ$ (Fig. 2.7c).

The velocity field shows the change of the line-of-nodes in the outer regions. Above the major plane, at the north-western, receding velocities the contours are distorted, probably due to the superposition of the rotation from the *additional HI emission*. The receding, south-western side of the position-velocity diagram is more extended (up to 2.5) than the less luminous approaching side, resulting in an overall lopsided shape. The opposite sides

of the rotation curve rise with an approximately equal, and steep, slope in the innermost region, however the behavior changes beyond $20''$. As a result, the rotation curve and the line profile are lopsided between receding and approaching sides.

The HI flux density integral of $9.64 \text{ Jy km s}^{-1}$ is in good agreement with single-dish determinations (Haynes & Giovanelli 1991; Theureau et al. 1998). This measurement implies a total HI mass of $4.64 \times 10^9 M_{\odot}$.

A heliocentric systemic velocity of $(3386.44 \pm 9.10) \text{ km s}^{-1}$ has been assumed for UGC 9759. The other measurements for the heliocentric systemic velocity for UGC 9759 range between 3420 km s^{-1} (Theureau et al. 1998) and 3454 km s^{-1} (Falco et al. 1999).

2.4.5 NGC 7183

NGC 7183 is optically classified as S0a exhibiting an overall symmetric shape at lower surface brightness (Fig. 2.9a). In the south-west, diffuse stellar material is observed outside the main body of the galaxy. The inner region is dominated by a dust lane aligned parallel to the major axis (79°).

Despite no information is available on group memberships for this system in Garcia's (1993) investigation, Lauberts (1982) reported on several small companions for NGC 7183.

The HI distribution is slightly more extended compared with the optically detected dimension and reaches $2'$ (20.1 kpc) from the center ($R_{\text{HI}}/R_{25} = 1.2$). The south-western, approaching side of the HI disk tilts up to 9° with respect to the HI disk at 79° . This tilted HI emission is recognizable at the extreme edge of the velocity range (around 2411 to 2462 km s^{-1}). No significant changes are observed in the HI axis on the north-eastern side. Hence, the galaxy assumes an asymmetric, L-shaped warped system.

The radial velocity field shows symmetric isocontours with respect to the center within $2'$. Beyond this radius, the isovelocity contours appear crowded and chaotic.

In the warped region, the HI content is smaller than on the opposite side. The position-velocity diagram shows clearly a higher column density at receding velocities, and the HI line profile has a lopsided shape. Despite the lopsided morphology, the HI kinematics appears very regular, and no asymmetries between receding and approaching sides are recognized in the rotation curve (Fig. 2.9g).

The integrated HI flux density of $17.09 \text{ Jy km s}^{-1}$ agrees well with the single-dish measurement by Huchtmeier & Richter (1989). The flux density integral corresponds to a total HI mass of $5.20 \times 10^9 M_{\odot}$ for the assumed distance of 35.9 Mpc . The gas-to-luminosity ratio is $0.43 M_{\odot}/L_{\odot}$.

The heliocentric systemic velocity is found at $(2592.43 \pm 7.05) \text{ km s}^{-1}$ from the present radio observations. This value is in reasonable agreement with previously estimated values for the heliocentric systemic velocity which are ranging between 2535 (Colless et al. 2001) and 2636 km s^{-1} (Da Costa et al. 1998).

2.4.6 NGC 5719

NGC 5719 and NGC 5713 form a binary system consisting of a Sab galaxy and a Sbc galaxy that belong to the group LGC 386 (Garcia 1993) together with other 20 galaxies.

The total HI distribution is well extended compared to the stellar disk ($R_{\text{HI}}/R_{25} = 2.04$), as it is shown in Fig. 2.11a. The kinematics of the interacting galaxies is quite complex, as well as the innermost kinematics of the internal disk of NGC 5719. The position-velocity diagram along the optical major axis reveals several structures, with peculiar kinematics (Fig. 2.11d). The channel maps are shown in Fig. 2.12.

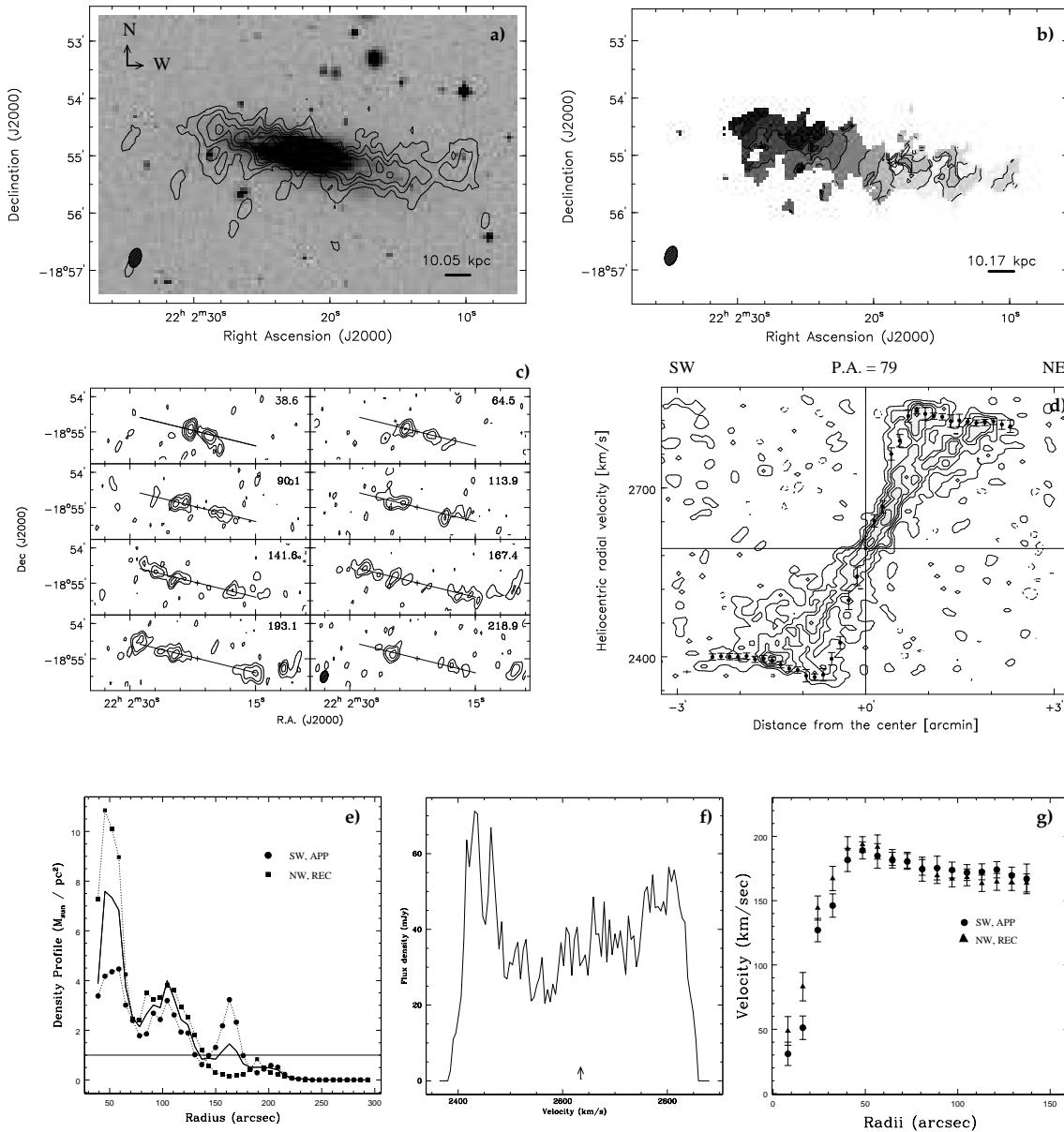


Figure 2.9 Atlas for NGC 7183. **a)** Contour representation of the total HI column density distribution superimposed on an optical (DSS) image. The contour levels are from 3.5 (5.7σ) to 18.5×10^{20} atoms cm^{-2} in steps of 5×10^{20} atoms cm^{-2} , and at 30 , and 40×10^{20} atoms cm^{-2} . The spatial resolution is $20''.15 \times 12''.10$. $1'$ is ~ 10.17 kpc. **b)** Velocity field with contours and gray scales from 2400 km s^{-1} (west; light shading) to 3850 km s^{-1} (east; dark shading) in increments of 50 km s^{-1} . **c)** Channel maps with equal rotation velocities have contours at -1.5 (dashed), 1.5 (1.6σ), 3 , 4 , 5 , 6 , 8 , 10 , 12 mJy beam^{-1} . **d)** Position-velocity diagram has contour levels at -3 (dashed), -1.5 , 1.5 (1.6σ), 3 , 4 , 5 , 6 , 8 , 10 , 12 mJy beam^{-1} . The grey-scale ranges from 1.5 to 9.5 mJy beam^{-1} in steps of 2 mJy beam^{-1} . **e)** HI radial surface density distribution from a strip integral of the brightness distribution **f)** Synthesized HI line profile obtained by integrating the data cube along both spatial axes. **g)** Rotation velocities as a function of the radius in arcseconds.

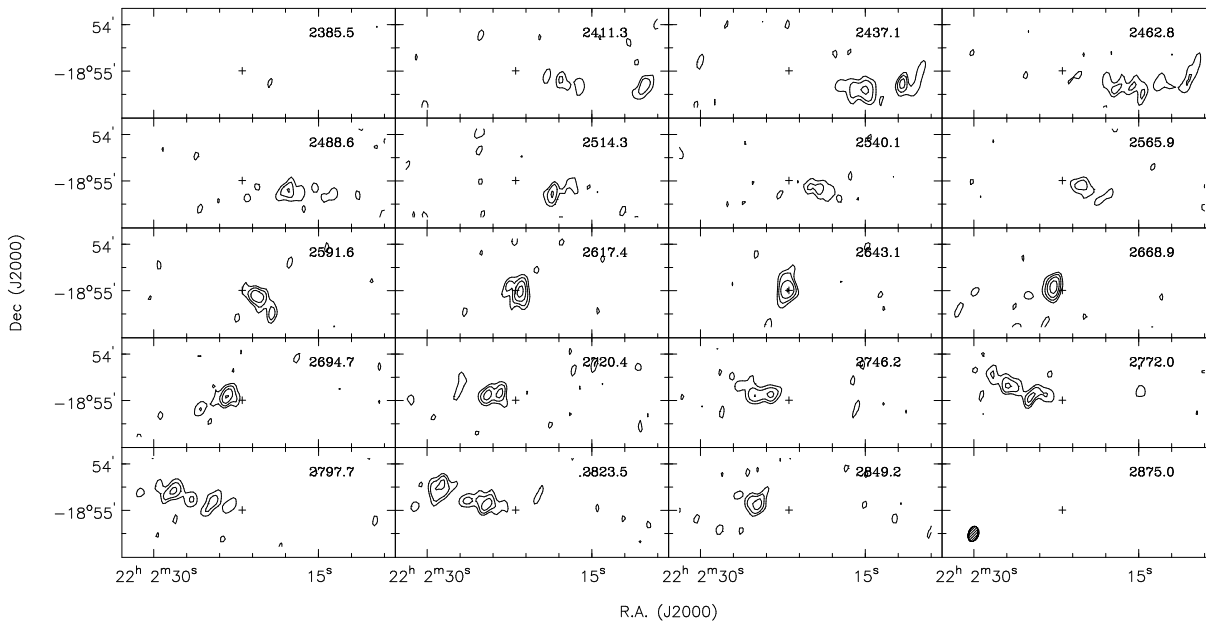


Figure 2.10 The channel maps of NGC 7183 show every fifth channel. Contours are at -1.5 (dashed), 1.5 (1.6σ), 3 , 4 , 5 , 6 , 8 , 10 , 12 mJy beam^{-1} . The channel velocity is given in each panel. The size of the synthesized beam is indicated by the ellipse in the lower left-hand corner of the last map. The cross represents the dynamical center.

The detailed description of this system is reported in Sect. 4.

2.4.7 IC 4757

IC 4757 is classified as S0a, and possesses a large bulge component and a strong dust lane along its major axis (157° , Fig. 2.13a). The bulge shows box-shaped isophotes down to the lower surface brightness levels. No evidence of a disk component is observed in IC 4757, neither obvious optical peculiarities. However, Lütticke (1999) reported on the detection of a small color gradient along the radial distance and faint substructures interpreted as merger remnants, especially on the north-eastern side. The galaxy is fainter than the completeness limit ($B_0 < 14^m$) in the sample of Garcia (1993) and no information is reported about a group membership of this object.

The HI emission in this galaxy is quite weak and concentrated in the optical body up to $\sim 45''$ (10.12 kpc) from the center. The main distribution is extended along the major axis of the galaxy (157°). The total HI integrated map shows a tail of the distribution at its south-western side, which is elongated at a position angle increased of $\approx 10^\circ$ with respect to the main plane. The south-western HI tail reaches a distance further out, 2.5 (33.75 kpc) from the center. The amount of mass involved in this diffuse tail is however quite small, and represents only a small fraction ($2.3 \times 10^7 M_\odot$) of the total mass.

The velocity field shows a regularly rotating disk, and the tail structure is rotating toward receding velocities. The position-velocity diagram shows a fast rotating structure within the inner $40''$, which represents the centrally peaked HI distribution. A second structure is observed at the receding velocities extended up to $3'$. This emission represents the warped tail at the south-western edge of the system observed in the total integrated HI map. The emission belonging to the tail appears in the channel maps starting

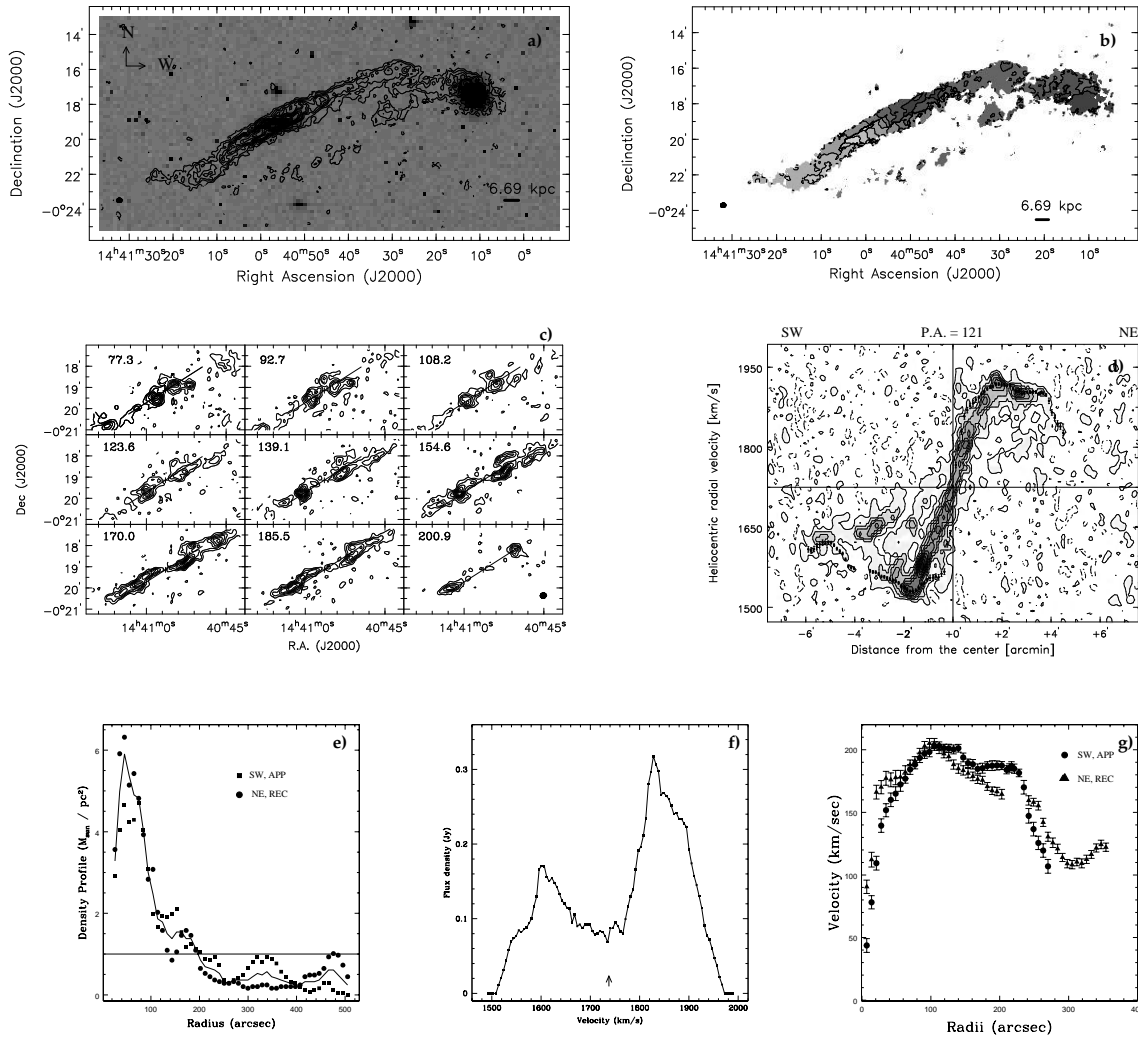


Figure 2.11 Atlas for NGC 5719. **a)** Contour representation of the total HI column density distribution superimposed on an optical (DSS) image. The contour levels are from 1 (3σ) to 15×10^{20} atoms cm^{-2} in steps of 3×10^{20} atoms cm^{-2} , and at 21, 30, 35 $\times 10^{20}$ atoms cm^{-2} . The spatial resolution is $15''.51 \times 14''.09$. $1'$ is ~ 6.69 kpc. **b)** Velocity field with contours and gray scales from 1400 km s^{-1} (east; light shading) to 2000 km s^{-1} (west; dark shading) in increments of 50 km s^{-1} . **c)** Channel maps with equal rotation velocities have contour levels at -1.2 (dashed), -2, and from 1.2 (2.3σ) to $13.0 \text{ mJy beam}^{-1}$ in steps of $1.2 \text{ mJy beam}^{-1}$. **d)** Position-velocity diagram has contours at -1.85 (dashed), -0.75, 0.75 (1.4σ), ..., $13.0 \text{ mJy beam}^{-1}$ in steps of $1.1 \text{ mJy beam}^{-1}$. The grey-scale ranges from 1.1 to $13.0 \text{ mJy beam}^{-1}$ in steps of $1.1 \text{ mJy beam}^{-1}$. **e)** HI radial surface density distribution from a strip integral of the brightness distribution **f)** Synthesized HI line profile obtained by integrating the data cube along both spatial axes. **g)** Rotation velocities as a function of the radius in arc seconds.

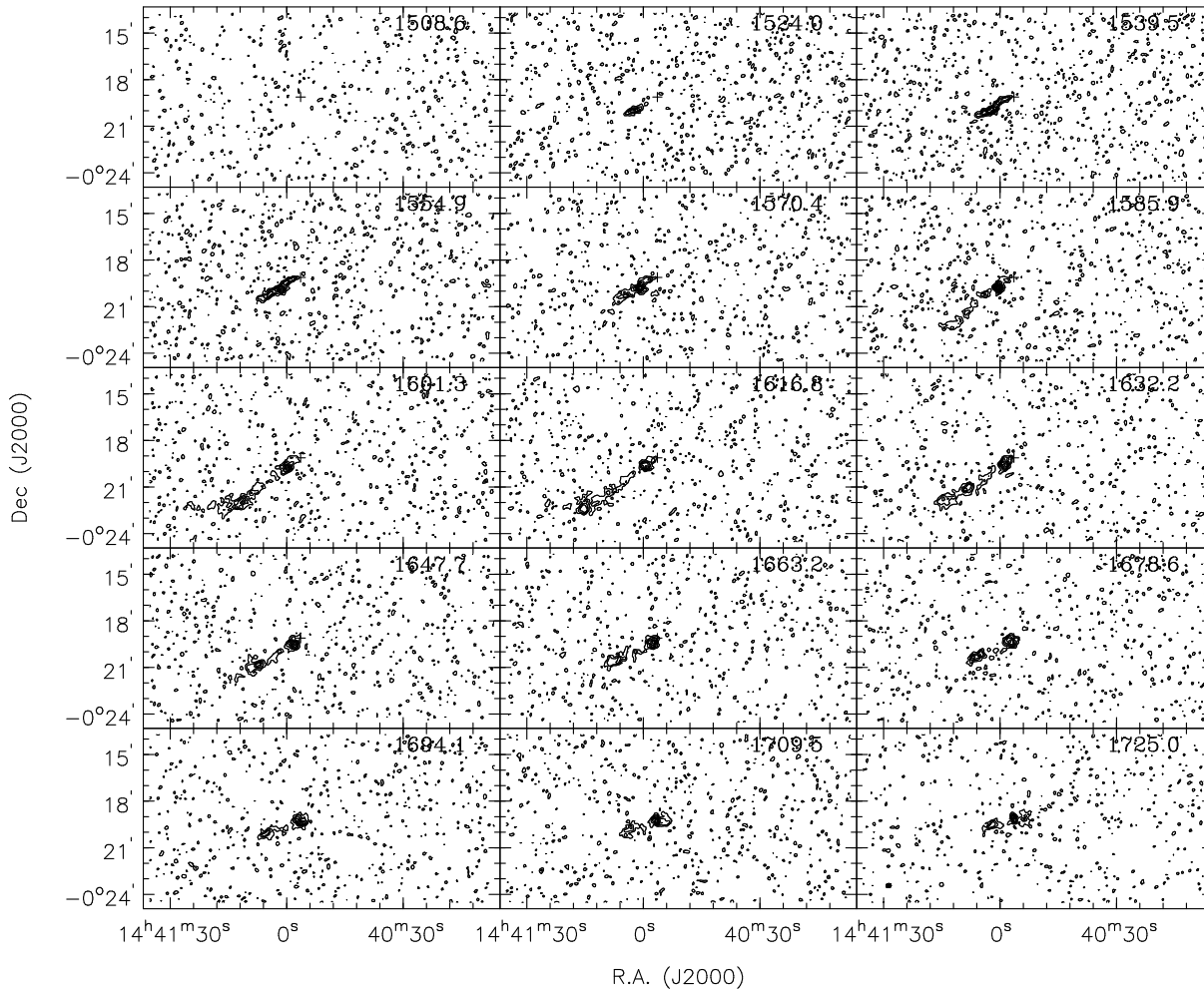


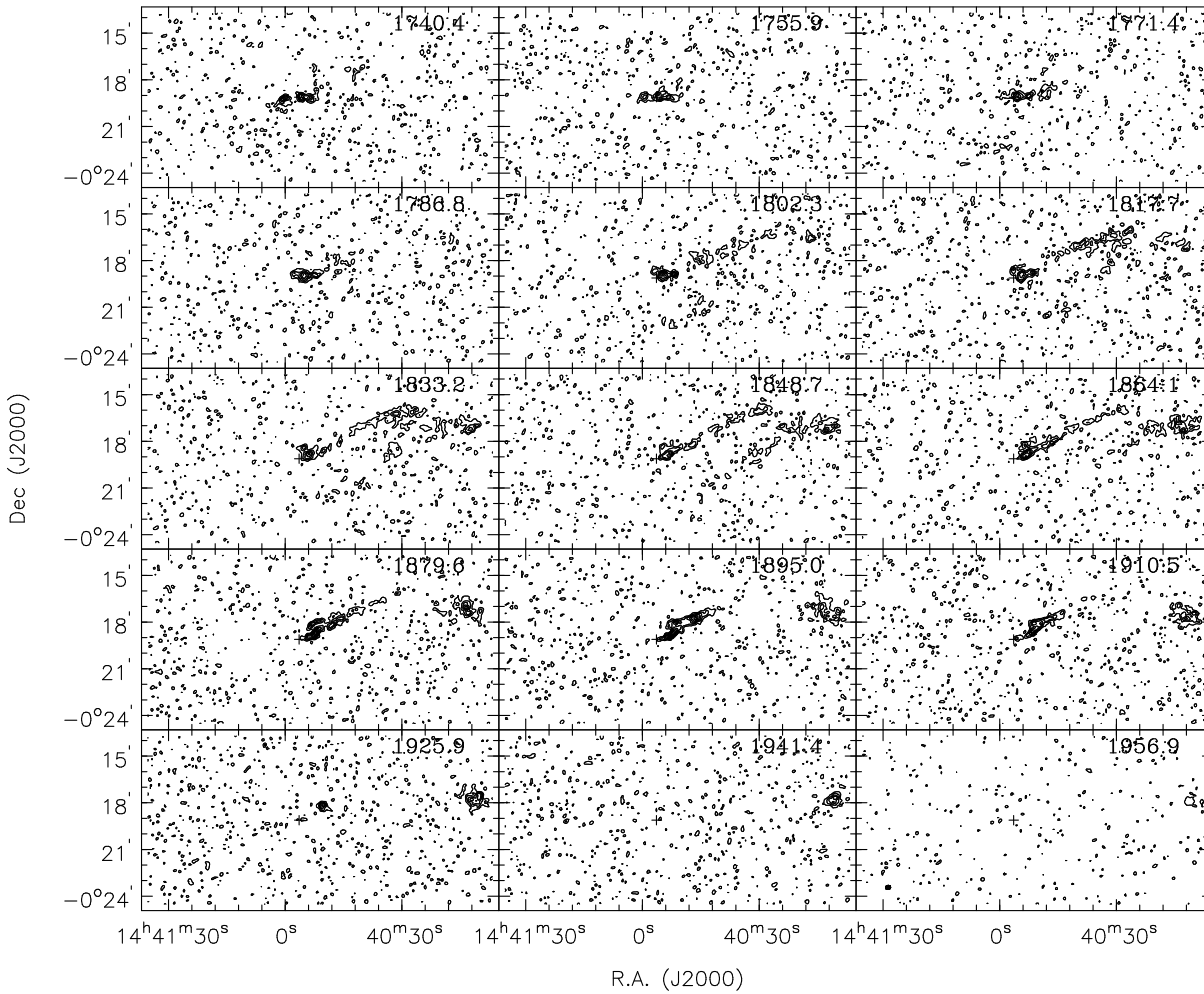
Figure 2.12 The channel maps of NGC 5719 show every fourth channel. The contour levels are -1.2 (dashed), -2 , and from 1.2 (2.3σ) to 13 mJy beam^{-1} in steps of $1.2 \text{ mJy beam}^{-1}$. The channel velocity is given in each panel. The size of the synthesized beam is indicated by the ellipse in the lower left-hand corner of the last map. The cross represents the dynamical center.

from 3540 km s^{-1} consecutively for $\approx 100 \text{ km s}^{-1}$.

Both, the approaching and the receding side of the rotation curve are rising with the same slope up to a velocity of $\approx 170 \text{ km s}^{-1}$ at $20''$ (4.5 kpc). Beyond the peak, the decline of the receding velocities is stronger than that on the approaching side. However, it can be explained by the depression in the HI distribution. In fact, the approaching side shows a more regular behavior. The receding rotation is traced out to $4'$ from the center, while the approaching side of the rotation curve ceases at $2'$.

The HI flux density profile derived from the present HI observations is quite asymmetric. The integrated HI flux density has a value of $3.07 \text{ Jy km s}^{-1}$, and the total HI mass computed from the global profile is $1.56 \times 10^9 M_{\odot}$, assuming a distance of 46.4 Mpc .

The systemic velocity is found at the velocity of $(3480 \pm 6.20) \text{ km s}^{-1}$ estimated from a visual inspection of the channel maps and by folding the position-velocity diagram. However, the lopsided column density distribution and the relatively non-homogeneous

Figure 2.12 *Continued*

HI emission have been reflected in the systemic velocity determination. These features make it difficult to correctly identify the systemic velocity, which might be shifted to lower velocities if the HI-blob at $4'$ from the center at the approaching velocities (around 3200 km s^{-1}) is real. This suspicion is supported by the different measurement ($3413 \pm 39 \text{ km s}^{-1}$) found by Fisher et al. (1995).

2.4.8 UGC 10205

UGC 10205 was classified as Sa spiral by Nilson (1973) and by de Vaucouleurs et al. (1991). This galaxy has been included in a list of polar-ring galaxies by Bettoni et al. (2001). It has a prominent dust lane extending across the major axis (Fig. 2.15a). Vega-Beltran et al. (1997) detected the presence of three kinematically distinct gaseous components, two of which give a *figure-of-eight* appearance to its stellar velocity curve. Studying the ionized gas velocity curves of a sample of Sa spirals, also Rubin et al. (1985) noticed along the south-eastern side of UGC 10205 “a curious three-velocity system” within $15''$ ($\approx 6.3 \text{ kpc}$ at the assumed distance of 85.9 Mpc) of the center. Vega-Beltran et al. (1997) observed a faint ring-like structure around the galaxy (around $B \approx 25^m$), especially pronounced on the eastern side. Reshetnikov & Evstigneeva (1999) proposed as origin of the peculiari-

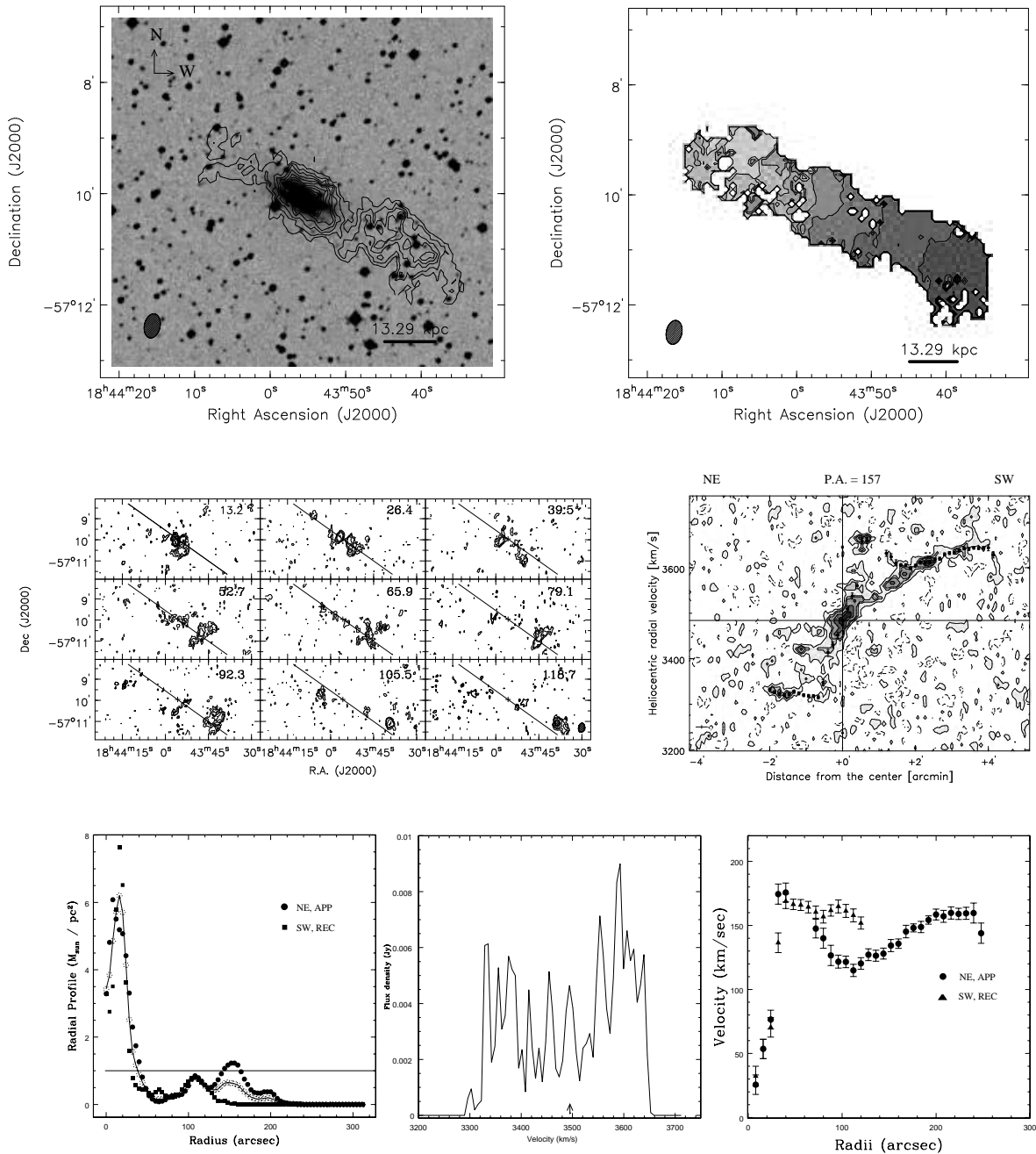


Figure 2.13 Atlas for IC 4757. **a)**: Contour representation of the total HI column density distribution superimposed on an optical (DSS) image. The contour levels are from $1.5 (2.8\sigma)$ to 11.5×10^{20} atoms cm^{-2} in steps of 1.0×10^{20} atoms cm^{-2} . The spatial resolution is $26''.42 \times 16''.91$. $1'$ is ~ 13.29 kpc. **b)**: Velocity field with contours and gray scales from 3280 km s^{-1} (east; light shading) to 3680 km s^{-1} (west; dark shading) in increments of 50 km s^{-1} . **c)**: Channel maps with equal rotation velocities have contours at -2.9 (dashed), $2.9 (2.5 \sigma)$, ..., $9.9 \text{ mJy beam}^{-1}$ in steps of 1 mJy beam^{-1} . **d)**: Position-velocity diagram has contours at -3 (dashed), $-1.5, 1.5 (1.3 \sigma), 3, 4, 6, 8, 10 \text{ mJy beam}^{-1}$. The grey-scale ranges from 1.5 to 9 mJy beam^{-1} in steps of $1.5 \text{ mJy beam}^{-1}$. **e)**: HI radial surface density distribution from a strip integral of the brightness distribution **f)**: Synthesized HI line profile obtained by integrating the data cube along both spatial axes. **g)**: Rotation velocities as a function of the radius in arcseconds.

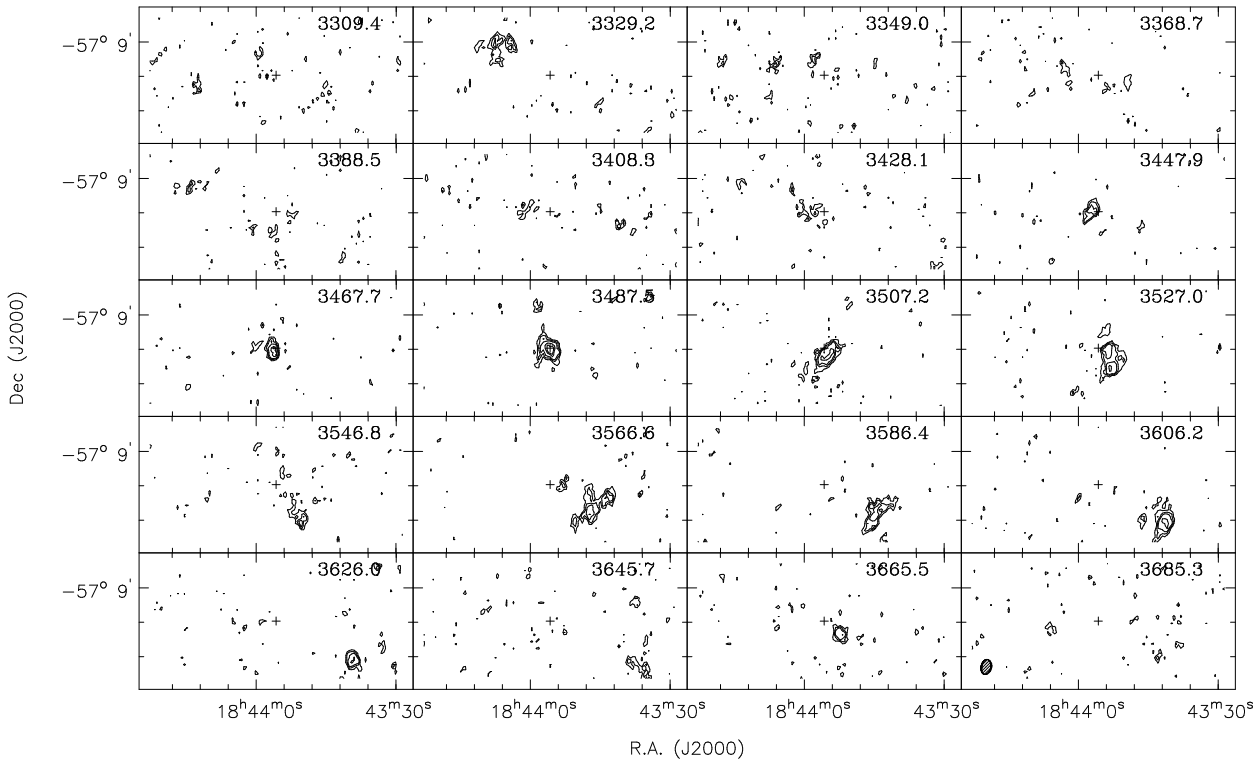


Figure 2.14 The channel maps of IC 4757 show every third channel. Contours are at -2.9 (dashed), 2.9 (2.5σ), ..., 9.9 mJy beam^{-1} in steps of 1 mJy beam^{-1} . The channel velocity is given in each panel. The size of the synthesized beam is indicated by the ellipse in the lower left-hand corner of the last map. The cross represents the dynamical center.

ties of UGC 10205 a capture and tidal disruption of a small type E/S0 companion by the massive central galaxy.

The HI emission up to the level of 1.2×10^{20} atoms cm^{-2} is well distributed in a fast-rotating disk with a position angle of 132° . Beyond this level, at lower column densities the emission is dishomogeneous, and forms an envelope around the optical body.

In Fig. 2.17, a deep optical image (B-band contours, CAHA 1.23-m telescope, 50 minutes) is overlaid to the HI column density. The HI tail-like structure extends outside a radius of about $1'$ (complex A in Fig. 2.17), superimposed to a region of higher optical surface brightness which mimics an arc. This tail is observed between 0.7 mJy beam^{-1} (1.6σ) and 1.7 mJy beam^{-1} (4σ) in the position-velocity diagram at a position angle of 149° (Fig. 2.18). Beyond the radius at $1'$, a HI complex (B in Fig. 2.17) is detected to the south at a very low level (3.1×10^{20} $\text{atoms cm}^{-2} \approx 1\sigma$). This southern complex B is elongated neither along the major axis of the stellar disk nor that of the HI disk but instead along a position angle of 186° . Both, complex B and complex C (northern counterpart of complex B) are detected at a 4σ -level (Fig. 2.18).

The HI emission covers a large range of velocities, and is lopsided in morphology because the receding, north-western emission has a larger extent. The kinematics is lopsided as well, the receding velocities rise less steeply than the approaching ones.

A value of 0.69 Jy km s^{-1} is found for the integrated HI flux density which is about 60% less than in single-dish measurements (Theureau et al. 1998, van Driel et al. 2000). The present observations do not cover the entire velocity range of UGC 10205 ($W_{20} = 556$

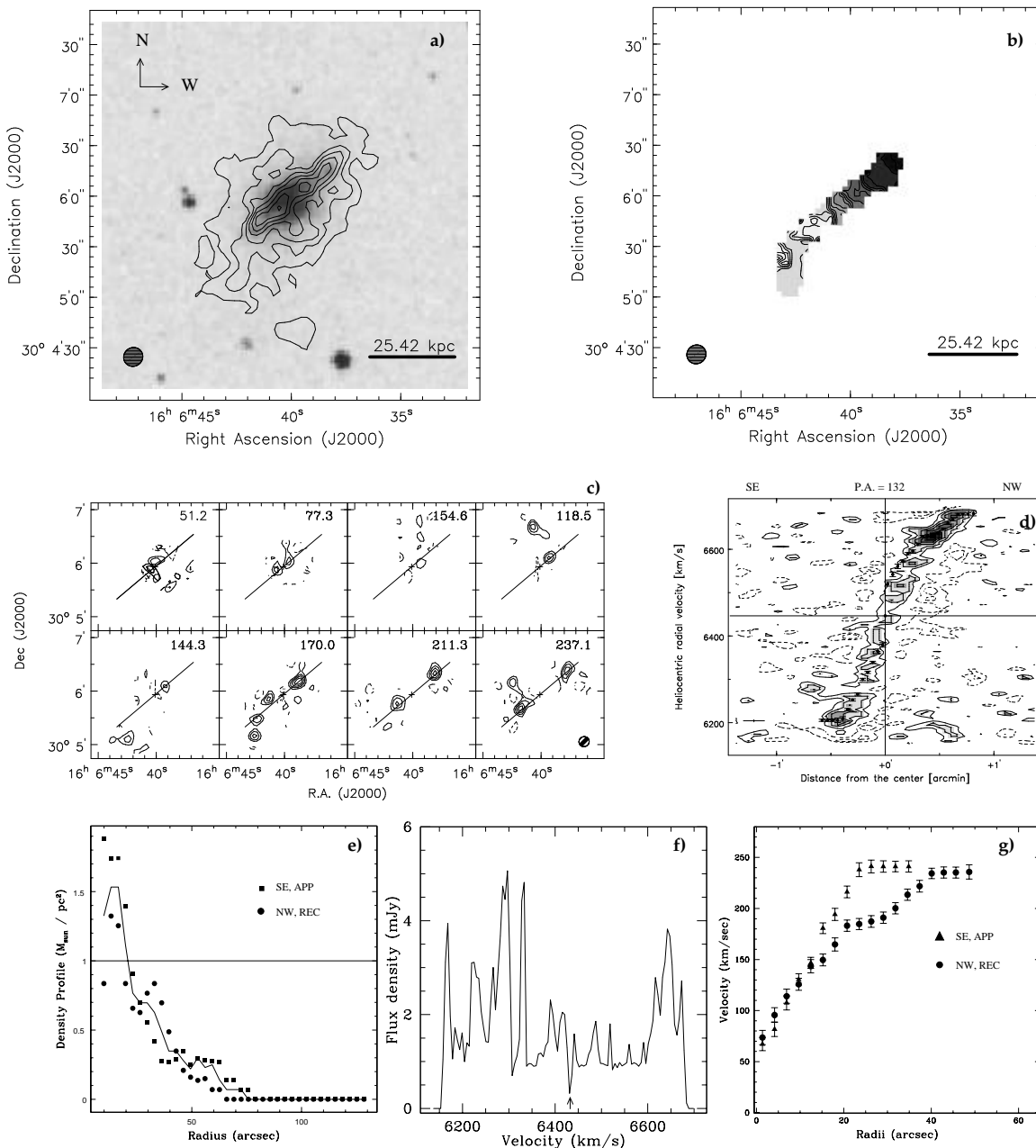


Figure 2.15 Atlas for UGC 10205. **a)**: Contour representation of the total HI column density distribution superimposed on an optical (DSS) image. The contour levels are $3.5 (1\sigma)$ to 35×10^{19} atoms cm^{-2} in steps of 5×10^{19} atoms cm^{-2} . The spatial resolution is $11''55 \times 11''00$. $1'$ is ~ 25.42 kpc. **b)**: Velocity field with contours and gray scales from 6150 km s^{-1} (east; light shading) to 6700 km s^{-1} (west; dark shading) in increments of 25 km s^{-1} . **c)**: Channel maps with equal rotation velocities have contours at -0.7 (dashed), $0.7 (1.6 \sigma)$, ..., $3.2 \text{ mJy beam}^{-1}$ in steps of $0.5 \text{ mJy beam}^{-1}$. **d)**: Position-velocity diagram has contour levels at -1.2 (dashed), $-0.6, 0.6 (1.4 \sigma)$ to 3 mJy beam^{-1} in steps of $0.6 \text{ mJy beam}^{-1}$. The grey-scale ranges from 0.9 to $12.7 \text{ mJy beam}^{-1}$ in steps of $0.6 \text{ mJy beam}^{-1}$. **e)**: HI radial surface density distribution from a strip integral of the brightness distribution **f)**: Synthesized HI line profile obtained by integrating the data cube along both spatial axes. **g)**: Rotation velocities as a function of the radius in arcseconds.

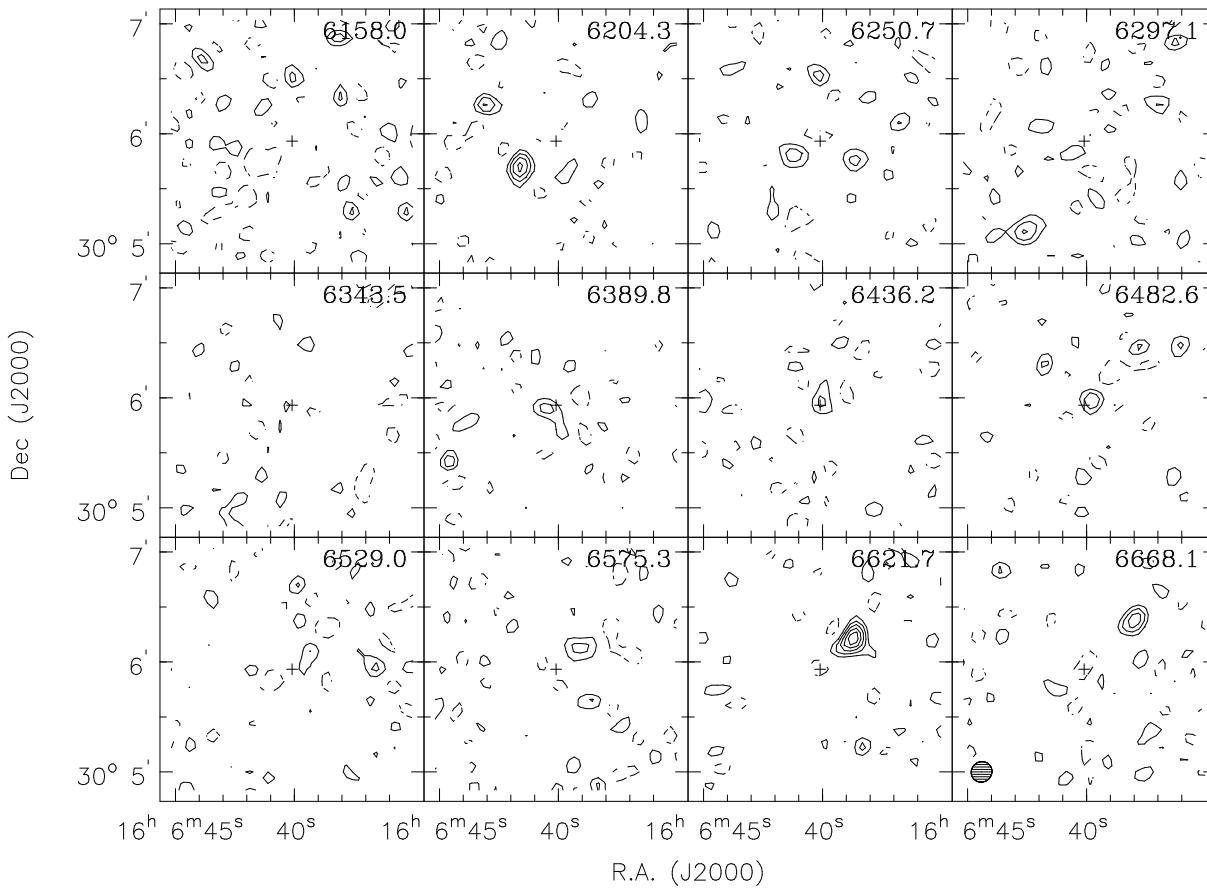


Figure 2.16 The channel maps of UGC 10205 show every ninth channel. Contours are at -0.7 (dashed), 0.7 (1.6σ), ..., $3.2 \text{ mJy beam}^{-1}$ in steps of $0.5 \text{ mJy beam}^{-1}$. The channel velocity is given in each panel. The size of the synthesized beam is indicated by the ellipse in the lower left-hand corner of the last map. The cross represents the dynamical center.

km s^{-1}), and some HI emission certainly remained undetected. Also the quality of the continuum subtraction was limited by the large velocity range of UGC 10205.

The integrated HI flux density found in these observations implies a total HI mass of $1.21 \times 10^9 M_{\odot}$, assuming a distance of 85.9 Mpc.

The systemic velocity determined adopting the center of HI symmetry of $(6446.52 \pm 6.10) \text{ km s}^{-1}$ disagrees with the previously estimated velocities of $(6583 \pm 5) \text{ km s}^{-1}$ and $(6581 \pm 15) \text{ km s}^{-1}$ by Vega-Beltran et al. (1997) and Rubin et al. (1985), respectively. The reason for this discrepancy could be due to the adopted center of symmetry of stellar velocities in the innermost, peculiar region (within $13''$). Using as center of symmetry the HI kinematics the HI heliocentric systemic velocity is lower than 130 km s^{-1} compared with the results from stellar kinematics.

2.5 Discussion

In this chapter a detailed study of the HI emission in edge-on galaxies using the Australia Telescope Compact Array and the Very Large Array is presented. The most unexpected result from the analysis of the presented sample is the presence of large deviations from the normal distribution of the neutral hydrogen.

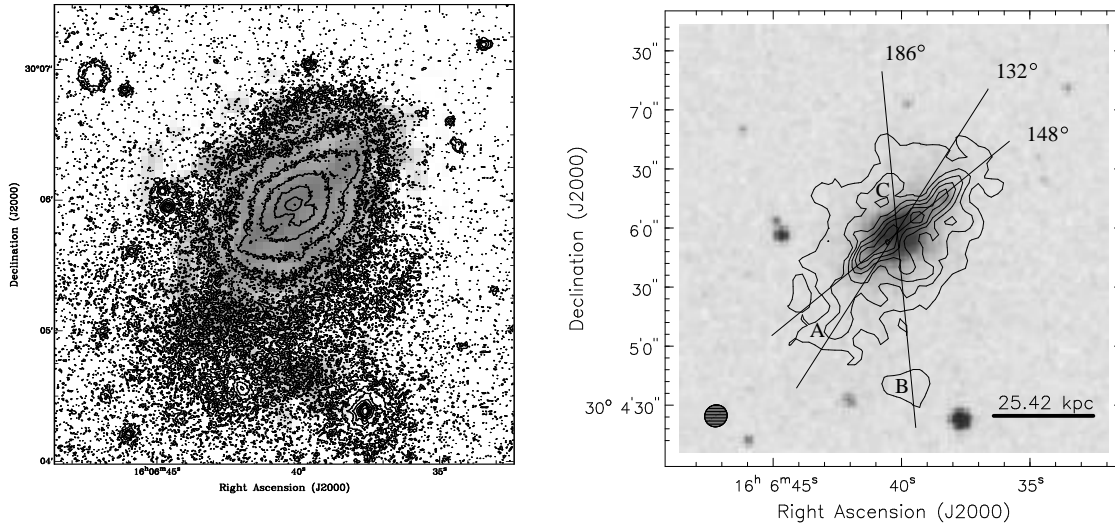


Figure 2.17 **Left** The isophote images of the R-band surface brightness (CAHA-1.23m, 40 minutes) The contours of the isophotal images are plotted starting from the brighter contour (16) down to the limiting surface brightness (25.9 R magn, 3σ level = 25.95 R magn). In grey-scale the total HI column density distribution ranges between 3.5 to 35×10^{19} atoms cm^{-2} in steps of 5×10^{19} atoms cm^{-2} . **Right** The total HI column density distribution with the peculiar HI emission (complex A, B, and C), and the kinematic axis of the position-velocity diagram reported in Fig. 2.18.

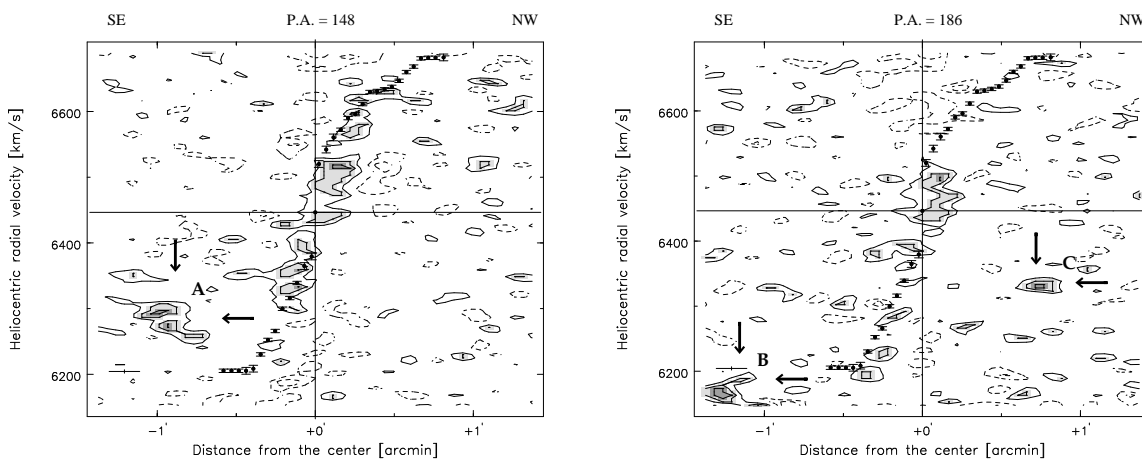


Figure 2.18 Position-velocity diagrams along different kinematic axis.

A large massive and prominent bulge constitutes the primary selection criterion of this sample. The observed galaxies possess a prominent and box/peanut-shaped bulge; therefore, they are classified as thick box/peanut bulge galaxies.

They present peculiarities in the morphological distribution of the neutral hydrogen. Sometimes, tails or bridges are detected as in the major interaction of NGC 5719 with the companion, NGC 5713, and in IC 4745 where an extended southern tail is identified. In other cases, the majority of the HI galactic disks are found to be surrounded by extra HI emission with different location in the galactic plane. This is the case for the southwestern, receding region in the disk of UGC 9759, and NGC 7183 presents the same peculiarity on the southwestern, approaching side too. Diffuse emission is identified in the north-western, approaching region in NGC 1055 as well.

In all the galaxies the orientation of the HI distribution is parallel to the major axis of the optical body, beyond the optical emission a warp is observed in all the galaxies of the sample. Cases of symmetric warped HI distribution are observed, as well as cases in which the HI emission does not appear mirror-symmetric with respect to the center of the galaxy, like in the case of NGC 1055, NGC 7183, and IC 4757.

In half of the sample, the neutral hydrogen is distributed in extended disks or rings (ESO 383-05, IC 4745, NGC 1055, and UGC 9759), while in IC 4757, UGC 10205, NGC 5719, and NGC 7813 it has a non-regular and patchy distribution, especially at the outer edges of the HI emission.

The 21-cm line analysis shows that the peculiarities seen in the distribution and kinematics of the neutral hydrogen are probably related to the existence of tidal interaction and accretion events. The overall kinematics suggests that these systems are not dynamically settled. Due to the relatively small projected distances to the other members of the group, it seems likely that the presented galaxies have undergone minor interactions with their companions. However, it is worth to notice that no sign of HI emission has been detected from companions in the observed velocity range. The anomalies and peculiar emissions belong all the time to the HI disk of the target object.

In the soft merger scenario, the presence of prominent bulges might be physically related to BPS structures. Depending on the characteristics of the interaction and on the parameters of the impact, the accreted material from external companions could contribute to the outer disk (Simard et al. 1999) or to the growth of the bulge (Aguerri et al. 2001). In both cases, however, the interaction produces perturbations in the disk which might trigger the BPS structures.

With the assumption that the classification of a galaxy as barred with face-on orientation leads to the BPS isophotes if seen in edge-on orientation, the fraction of barred galaxies possessing a minor merging history is searched in literature. BPS/barred structures have been sought in a sample of best known cases of minor merger galaxies compiled by Sancisi (1999). In most of the cases the explored galaxies are nearly face-on. Considering spiral galaxies, five cases of non-barred galaxies (NGC 262, NGC 628, NGC 4254, NGC 4826, NGC 5635) and eleven cases of barred galaxies are minor merging systems. In particular, in four cases strong bars (SB; NGC 1023, NGC 3359, NGC 4027, NGC 4694), and in seven cases weak bars or oval distortions (SAB; NGC 1961, NGC 2146, NGC 2782, NGC 3067, NGC 3310, NGC 4654, NGC 5457) plus one case of direct classification of a BPS bulge galaxies (NGC 4565, Lütticke 1999) are detected.

However, these values of the fraction of barred galaxies represent only a lower limit. Because a bar is a short-lived structure, especially in a case of interaction events where it can be easily destroyed by mass accretion (but also newly triggered by interactions).

As mentioned above, only in galaxies with edge-on orientations the BPS structures are visible, and bars in galaxies are easily destroyed by the influence of interactions. Because of these effects, the question whether all accreted systems possess BPS structures remains unanswered.

García-Ruiz (2001) analyzed a sample of 26 edge-on galaxies from the WHISP (Westerbork HI Survey of Spiral and Irregular Galaxies) catalogue. He reported lopsidedness indices for both HI morphology and kinematics. The averaged values for the kinematic and density lopsidedness indices for un-barred galaxies (S) are 3.49 and 3.94, while for barred galaxies (SB) these values increase to 5.37 and 4.68, respectively.

Major mergers hamper the formation of bar-like instabilities, the disk is dynamically too hot to start the bar formation. Major mergers are seen relatively rarely at redshift < 1 , while the rate of this event increases dramatically with increasing redshift (van den Berg 2002). Moreover, only few percent of the mass of the disk funneling into the center could dissolve a hypothetically formed bar. Based on these considerations, the fraction of barred galaxies is expected to decrease with increasing redshift. On the other hand, minor mergers become a common event in the local universe predominating the major events. Therefore, the combination of these two (minor and major merger) events with different amounts of involved accreted material might work in the direction to increase the fraction of the barred system in the local universe.

Controversial results are found in the literature on the role of the environment (Bureau 1998; van den Bergh 2002). Lütticke (1999) found an increasing value of projected satellites around the galaxies with thick box/peanut bulges compared to spheroidal bulge galaxies.

The absence of the symmetry in the HI morphology and kinematics has been taken as evidence for the merger evolution. The lack of companions may represent different (more advanced) stages of accretion processes with the accreted galaxy no longer visible. This could be the case of the spiral galaxies with peculiar HI morphologies and kinematics similar to those found in this investigation.

2.6 Conclusion

A study of a sample of galaxies with box/peanut bulges has been performed by means of the HI 21-cm line. The main result of this analysis is the high frequency of peculiarities identified in all the target objects. Lopsided HI distributions, peculiarities in the emission and kinematics of the neutral hydrogen component as well as symmetric and asymmetric warps are detected with different strength and amplitudes in the sample.

The theoretical prediction is confirmed that interaction is the formation mechanism of the BPS structure in thick box/peanut bulge galaxies, with the assumption that the detected peculiarities are relicts of past or on-going interactions.

At present, it cannot be discerned whether these BPS structures result from bars produced through global instabilities induced by interactions (hybrid scenario) or directly from material accreted during infalling satellites (accretion scenario).

Unfortunately, with our limited number of objects we are not able to extend this conclusion to the wider class of BPS spiral galaxies. However, as could be verified from a comparison with literature data, the trend of increasing peculiarities from spheroidal towards box/peanut bulges is real. Further analysis will be performed.

The origin of the BPS structure in spiral galaxies has still to be settled. It is not even clear whether prominent BPS bulge galaxies form a separate category of galaxies with definite properties or whether they simply represent the extreme tail of the distribution towards

the box/peanut bulge galaxies. In any case, they present interesting questions concerning the formation and the evolution of bars and BPS components given the unusually large fraction of asymmetries.

Summarizing it can be stated that based on the presently available observations the merger scenario is favored as origin of this class of galaxies. In any case it enhances their formation processes.

References

- Aguerri J.A.L., Balcells M., Peletier R.F., 2001, *A&A* 367, 428
- Athanassoula E. 2002, *ApJ* 569, L83
- Begeman K.G., 1987, Ph.D. thesis, Univ, Groningen, The Netherlands
- Bettoni D., Galletta G., 1994, *A&A* 281, 1
- Bettoni D., Galletta G., García-Burillo S., Rodríguez-Franco A., 2001, *A&A* 374, 421
- Binney J., 1992, *ARA&A* 30, 51
- Binney J., Petrou M., 1985, *MNRAS* 214, 449
- Bosma A., 1991, in S. Casertano, P. Sackett and F. Briggs (eds.), Cambridge University Press, p.181
- Briggs F.H., 1990, *ApJ* 352, 15
- Burbidge G. R., Burbidge E. M., 1969, *Nature* 222, 735
- Bureau M., 1998, Ph.D. thesis, Australian National University, Australia
- Bureau M., Freeman K.C., 1999, *AJ* 118, 126
- Colless M., Dalton G., Maddox S., Sutherland W., Norberg P. et al., 2001, *MNRAS* 328, 1039
- Combes F., Debbasch F., Friedli D., Pfenniger D., 1990, *A&A* 233, 82C
- da Costa L. Nicolaci Willmer C.N.A., Pellegrini P.S., Chaves O.L., Rit e C. et al., 1998, *AJ* 116, 1
- Dettmar R.-J., Barteldress A., 1988, *BAAS* 20, 1085
- Dettmar R.-J., L utticke R., 1999, *ASP Conf. Ser.* 165 (Gibson B.K., Axelrod T.S., Putman M.E., eds.) p. 95
- de Souza R.E., Dos Anjos S., 1987, *A&AS* 70, 465
- de Vaucouleurs G., 1963, *ApJS* 8, 31
- de Vaucouleurs G., de Vaucouleurs A., 1976, *AJ* 81, 595
- de Vaucouleurs G., de Vaucouleurs A., Corwin J.R., Buta R.J., Paturel G., Fouque P., 1991
- Dressler A., 1991, *ApJS* 75, 241
- Fairall A.P., 1988, *MNRAS* 230, 69
- Falco E.E., Kurtz M.J., Geller M.J., Huchra J.P., Peters J. et al., 1999, *PASP* 111, 438
- Fisher K.B., Huchra J.P., Strauss M.A., Davis M., Yahil A., Schlegel D., 1995, *ApJS* 100, 69

- Fricke K., Kollatschny W., 1989, *A&AS* 77, 75
- Fridman, A. M., Poliachenki, V. L'vovich 1984, 'Physics of gravitating systems - Vol.1: Equilibrium and stability, Vol.2: Nonlinear collective processes: Nonlinear waves, solitons, collisionless shocks, turbulence. Astrophysical applications', New York, Springer
- Garcia A.M, 1993, *A&AS* 100, 47
- García-Ruiz I., 2001, Ph.D. thesis, Univ. Groningen, The Netherlands
- Gentile G., Vergani D., Salucci P., Kalberla P., Klein U., 2002, in *ALMA extragalactic and Cosmology Science Workshop on Dark Matter*, Bordeaux
- Gerin M., Combes F., Athanassoula L., 1990, *A&A* 230, 37
- Gooch R.E., 1995, 'Space and the Spaceball', in *Astronomical Data Analysis Software and Systems IV*, ASP Conf. Ser. 77, ed. R.A. Shaw, H.E. Payne, & J.J.E. Hayes, ASP, San Francisco, p. 144
- Haynes M.P., Giovanelli R., 1991, *ApJS* 77, 331
- Hernquist L., Mihos J.C., 1995 *ApJ* 448, 41
- Hernquist L., Quinn P.J., 1989, *ApJ* 342, 1
- Huchtmeier W. K., Richter O.-G., 1989, 'A General Catalog of HI Observations of Galaxies. The Reference Catalog', Springer, Berlin
- Jaffe W., Ford H., Ferrarese L., van den Bosch F., O'Connell R.W., 1996, *ApJ* 460, 214
- Jarvis B.J., 1986, *AJ* 91, 65
- Kemp S.N., Meaburn, J., 1993, *A&A*, 274, 19
- Lauberts A., 1982, *ESO/Uppsala survey of the ESO(B) atlas*, Garching: European Southern Observatory (ESO),
- Lütticke R., 1999, Ph.D. Thesis, Ruhr-Universität Bochum, Germany
- Lütticke R., Dettmar R.-J., Pohlen M., 2000, *A&AS* 145, 405
- Merrifield M.R., Kuijken K., 1999, *A&A* 345, 47
- Mihos J.C., 1995, *ApJ* 428, L75
- Mihos J.C., Walker I.R., Hernquist L., Mendes de Oliveira C., Bolte M., 1995, *ApJ* 447, 87
- Miwa T., Noguchi M., 1998, *ApJ* 499, 149
- Nilson P., 1973, 'Uppsala general catalogue of galaxies', *Acta Universitatis Upsalien-sis. Nova Acta Regiae Societatis Scientiarum Upsaliensis - Uppsala Astronomiska Observatoriums Annaler*, Uppsala: Astronomiska Observatorium
- Noguchi M., 1987, *MNRAS* 228, 635

- Pfenniger D., 1984, *A&A* 134, 373
- Pfenniger D., 1985, *A&A* 150, 112
- Quillen A.C., Ramirez S.V., Frogel J.A., 1996, *ApJ* 470, 790
- Reshetnikov V.P., Evstigneeva E.A., 1999, *ARep* 43, 367
- Rowley G. 1988, *ApJ* 331, 124
- Rowley G. 1986, Ph.D. thesis, The Australian Natl. Univ., Australia
- Rubin V.C., Burstein D., Ford W.K., Thonnard N., 1985, *ApJ* 289, 81
- Sancisi R., 1999, *Ap&SS* 269, 59
- Sancisi R., Allen R.J., 1979, *A&A* 74, 73
- Sellwood J.A., 2000, *ASP Conf. Ser.*, 197, 3
- Schweizer F., 2000, *RSPTA* 358, 2063
- Shaw M.A., 1987, *MNRAS* 229, 691
- Simard L., Pritchett C.J., 1999, *PASP* 111, 453
- Theureau G., Bottinelli L., Coudreau-Durand N., Gouguenheim L., Hallet N. et al., 1998, *A&AS* 130, 333
- van den Bergh S. 2002, *AJ* 124, 782
- van Driel W., Arnaboldi M., Combes F., Sparke L.S., 2000, *A&AS* 141, 385
- van der Hulst J.M., Terlouw J.P., Begeman K.G., Zwitter W., Roelfsema P.R., 1992, *ASP Conf.Ser.* 25, Worrall D.M., Biemesderfer C., & Barnes J., eds., p. 131
- Vega-Beltran J.C., Corsini E.M., Pizzella A., Bertola F., 1997, *A&A* 324, 485
- Verheijen M.A.W., Sancisi R., 2001, *A&A* 370, 765
- Walker I.R., Mihos J.C., Hernquist L., 1996, *ApJ* 460, 121

3

Optical and near-infrared observations, data reduction, and analysis

In this chapter we present optical and near-infrared observations of 14 edge-on disk galaxies with box/peanut shaped bulges. These bulge-dominated systems are characterized by complex stellar morphologies. All selected galaxies have shown asymmetries and prominent irregularities in their light distributions. In the following we concentrate in particular on vertical near-infrared profiles. 1-D fitting studies which have been performed using the Sérsic law are presented. Correlations between bulge parameters and their morphological classes in thick box/peanut bulges are investigated, and results are compared with classical box/peanut and spheroidal bulges.

3.1 Introduction

Spiral galaxy bulges show remarkable diversities in the shapes of the surface brightness profiles. They are generally described by the $r^{1/n}$ Sérsic formula, where n is the shape parameter of the bulge. This formula reduces to the de Vaucouleurs law ($r^{1/4}$) for n equal to 4 and to the exponential law for n equals 1.

The bulge parameter n might be related to several structural and evolutionary properties of galaxies. Andredakis, Peletier, & Balcells (1995) reported a correlation between n and morphological type and between n and the bulge-to-disk luminosity ratio. Following this study, the value of n drops with morphological type T from 4 to 1. The earlier types are described by the de Vaucouleurs law ($n = 4$), despite the large scatter due to misclassification of the S0s and presence of several subclasses. The profiles become steeper toward the later types, which are well fitted by the exponential law. Caon et al. (1993) reported a correlation of n with luminosity as well as effective radius.

Modeling this observed tendency assuming bulges as $r^{1/4}$ spheroids, Andredakis, Peletier, & Balcells (1995) found that the disk formed later than the bulge in all types of galaxies. The decrease of n is the imprint of the disk formation. However, because the $r^{1/4}$ spheroid could not account for large changes of n , the bulges in the range $2 < n < 4$ remain unexplained, at least without considering secular evolution mechanisms.

Despite the general tendency to consider merging as an efficient way to generate $r^{1/4}$

TABLE 3.1. Log of the observations

Galaxy (1)	Coordinate J2000		Telescope (4)	Date (5)	Band (6)	Exp. Time (7)	Faintest isophote (8)
	R.A. (2)	Dec. (3)					
NGC 1030	02 ^h 39 ^m 50 ^s .8	+18° 01' 27" "	1.23m/CAHA	20-21 Sep 2000	B	40	26.45
			1.23m/CAHA	20-21 Sep 2000	R	60	26.27
			1.23m/CAHA	13 Sep 2000	H	114	22.70
NGC 1055	02 ^h 41 ^m 45 ^s .4	+00° 26' 35" "	1.23m/CAHA	22-23 Sep 2000	B	20	27.55
			1.23m/CAHA	22-23 Sep 2000	R	46	26.61
			1.23m/CAHA	15 Sep 2000	H	85	22.68
NGC 1589	04 ^h 30 ^m 45 ^s .50	+00° 51' 51" "	Dan 1.5m	1998 ^a	B	40	25.40
			Dan 1.5m	1998 ^a	R	10	25.30
			1.23m/CAHA	13 Sep 2000	H	206	22.72
ESO 494-022	08 ^h 05 ^m 32 ^s .37	−24° 48' 50" "	Dan 1.5m	24 Mar 2001	B	90	27.00
			Dan 1.5m	24 Mar 2001	R	38	25.89
			NTT/ESO	28 Mar 2001	K _s	52	21.99
NGC 3573	11 ^h 11 ^m 18 ^s .98	−36° 52' 24".8	Dan 1.5m	22 Mar 2001	B	65	26.62
			Dan 1.5m	22 Mar 2001	R	92	26.27
			NTT/ESO	28 Mar 2001	K _s	52	22.34
ESO 506-003	12 ^h 21 ^m 49 ^s .53	−25° 04' 38".4	Dan 1.5m	22 Mar 2001	B	95	27.28
			Dan 1.5m	22 Mar 2001	R	80	26.39
			NTT/ESO	28 Mar 2001	K _s	52	22.42
ESO 322-100	12 ^h 49 ^m 26 ^s .69	−41° 27' 47".8	Dan 1.5m	24 Mar 2001	B	102	27.23
			Dan 1.5m	24 Mar 2001	R	38	25.74
			NTT/ESO	28 Mar 2001	K _s	52	22.09
ESO 383-005	13 ^h 29 ^m 23 ^s .73	−34° 16' 23".5	Dan 1.5m	23 Mar 2001	B	85	26.10
			Dan 1.5m	23 Mar 2001	R	75	26.44
			NTT/ESO	28 Mar 2001	K _s	52	21.62
ESO 021-004	13 ^h 32 ^m 39 ^s .64	−77° 50' 31".7	NTT/ESO	28 Mar 2001	K _s	52	22.38
NGC 5719	14 ^h 40 ^m 56 ^s .43	−00° 19' 07".5	Dan 1.5m	23 Mar 2001	B	95	27.08
			Dan 1.5m	23 Mar 2001	R	89	26.23
			NTT/ESO	28 Mar 2001	K _s	52	22.03
UGC 09759	15 ^h 10 ^m 41 ^s .10	+55° 21' 00" "	1.23m/CAHA	20 Sep 2000	B	90	26.86
			1.23m/CAHA	20 Sep 2000	R	80	26.21
			1.23m/CAHA	15 Sep 2000	H	90	21.76
ESO 514-005	15 ^h 19 ^m 03 ^s .07	−23° 49' 16".4	Dan 1.5m	24 Mar 2001	B	65	26.38
			Dan 1.5m	24 Mar 2001	R	45	26.31
			NTT/ESO	28 Mar 2001	K _s	52	22.13
UGC 10205	16 ^h 06 ^m 40 ^s .29	+30° 05' 54".7	1.23m/CAHA	21-22 Sep 2000	B	50	25.95,
			1.23m/CAHA	21-22 Sep 2000	R	90	26.70
			1.23m/CAHA	14 Sep 2000	H	32	21.00
NGC 7183	22 ^h 02 ^m 21 ^s .64	−18° 54' 58".5	1.23m/CAHA	23 Sep 2000	B	90	26.81
			1.23m/CAHA	23 Sep 2000	R	140	25.71
			1.23m/CAHA	14 Sep 2000	H	137	22.31

Table 3.1 (1) Name of the galaxy; (2), and (3) Coordinates (J2000); (4) Telescope used for the target objects; (5) Date of the observations; (6) Observed band; (7) Exposure time; (8) One σ limiting surface brightness expressed in mag arcsec^{−2}.

surface brightness profiles (Gerhard 1981, Barnes 1988), Haynes et al. (2000) reported on five Sa galaxies with kinematic evidence of past minor mergers without disturbed morphology, where $n = 2$ yields the best fit to four of them.

In a statistical study to determine the frequency of the box/peanut bulges a small fraction of edge-on galaxies was found to possess disturbed and prominent box-shaped bulges called Thick Boxy Bulges (TBBs, Lütticke et al. 2000). N-body and hydrodynamical simulations for stars in barred potentials and gas kinematic studies have demonstrated that resonances induced by bars are able to reproduce the box/peanut structure and the observed complex gas kinematics in galactic centers. In the galaxies investigated here, however, the bulge extent is much too large to be explained by resonant orbits in a bar potential (Lütticke et al. 2000). The alternative mechanism of infalling material through accretion events has been proposed to generate the prominent box/peanut bulges.

In order to study the photometric properties of these thick box/peanut bulges, multi-wavelength imaging data (B, R and H or K_s) were obtained. Near-infrared minor-axis surface-brightness profiles of 14 TBB galaxies are considered here, and are fitted using the Sérsic formula. Properties of the bulges (such as the effective radius, r_{eff} , the bulge parameter n and the effective surface brightness, μ_e) are derived and compared with spheroidal bulges, as well as with classical box/peanut bulges. The results are discussed in the context of the hypothesis that minor mergers of companions could have a strong influence on the creation of bulges in thick box/peanut bulge galaxies.

This chapter is organized as follows: in Sect. 3.2 the data sets are described. Section 3.3 contains the description of the surface brightness profiles. The decomposition procedures used to obtain the parameters of thick box/peanut bulge galaxies and the inter-relations of these parameters are discussed in Sect. 3.4. Section 3.5 contains the results of this study and our conclusions.

3.2 The Data

3.2.1 The Sample

We have studied a sample of 14 galaxies with prominent bulges selected from a complete magnitude and diameter-limited survey of highly inclined galaxies. The galaxies were selected from the Third Reference Catalogue of Bright Galaxies (de Vaucouleurs et al. 1991; henceforth RC3) on the basis of their orientation (nearly edge-on) and their diameters. The details of the thick box/peanut bulge sample are reported in Sect. 2.2.

In the near-infrared regime, two different types of edge-on galaxies were used as a comparison sample in the same morphological range ($-2 < T < 3$) and with equal optical sizes. The galaxies in the first sample taken for comparison possess classical box/peanut bulges and those of the second sample hold spheroidal bulges selected according the bulge classification explained by Lütticke et al. (2000). All together, we have a control sample of 12 classical box/peanut bulge and 12 spheroidal bulge galaxies. The data were collected from different observations in related projects.

3.2.2 Optical observation and data reduction

The optical observations were obtained at the European Southern Observatory (ESO) on La Silla (Chile), and Centro Astronómico Hispano Alemán (CAHA), Calar Alto (Spain). In both runs we used the standard Johnson B and R filters. The southern hemisphere galaxies were observed with the Danish 1.54-m telescope which was equipped with the

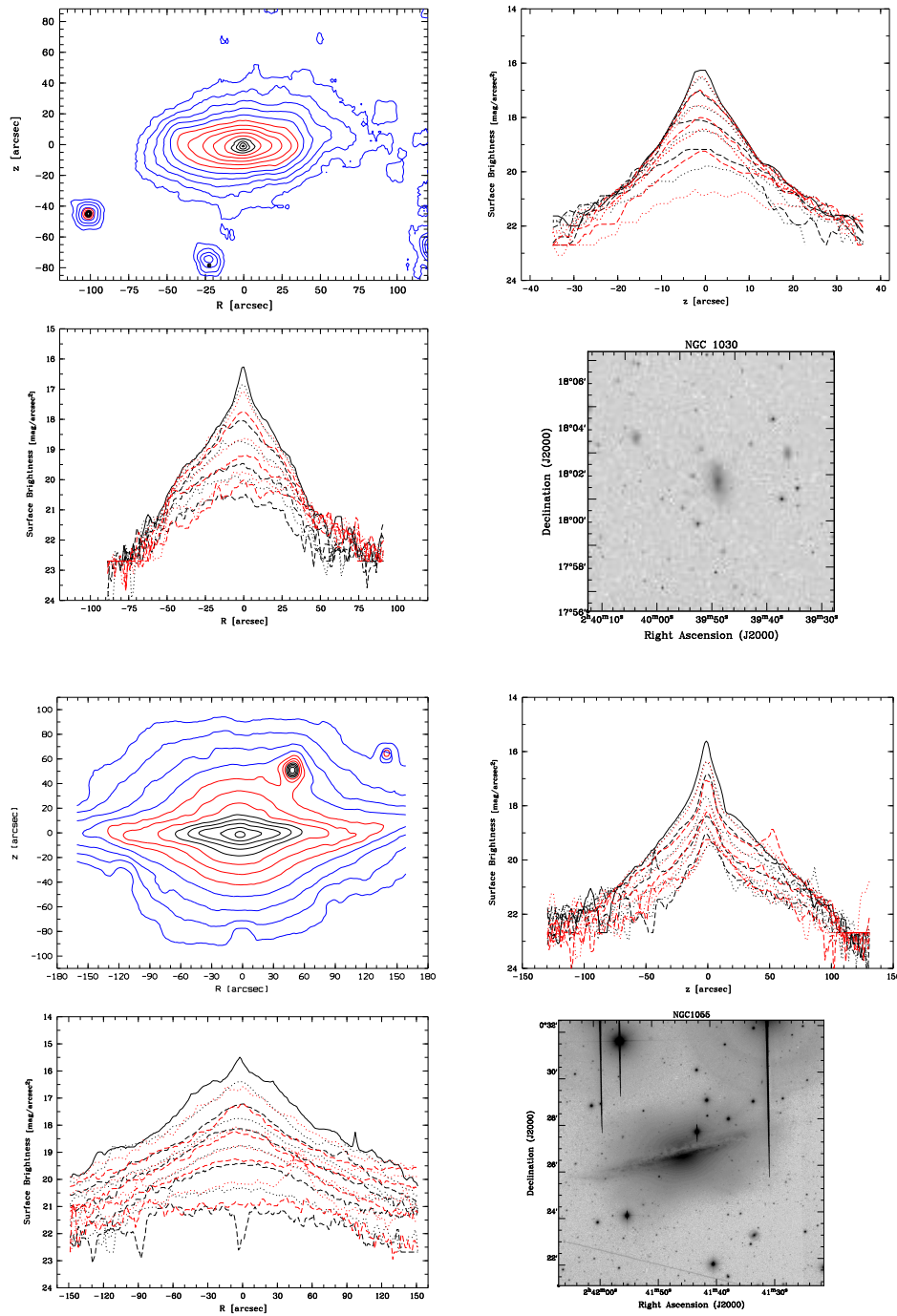


Figure 3.1 In every four panels it is represented for each galaxy: (*Top, Left*) The isophote images of the surface brightness rotated to the major axis. The contours of the isophotal images are plotted starting from the brighter contour down to the limiting surface brightness (3σ). (*Top, Right*) Observed surface brightness profiles along the minor axis (solid line) and perpendicular to the galactic (dotted and dashed line consecutively) up to the radius corresponding to the 3σ surface brightness. (*Bottom, Left*) Observed surface brightness profiles along (solid line) and parallel (dotted and dashed line consecutively) to the major axis plotted with intervals of $1 \text{ mag arcsec}^{-2}$ in the inner region, and of $0.5 \text{ mag arcsec}^{-2}$ further on. (*Bottom, Right*) Gray scale representation of an optical image (R-band) in real coordinate and orientation. *Top*: NGC 1030; *Bottom*: NGC 1055

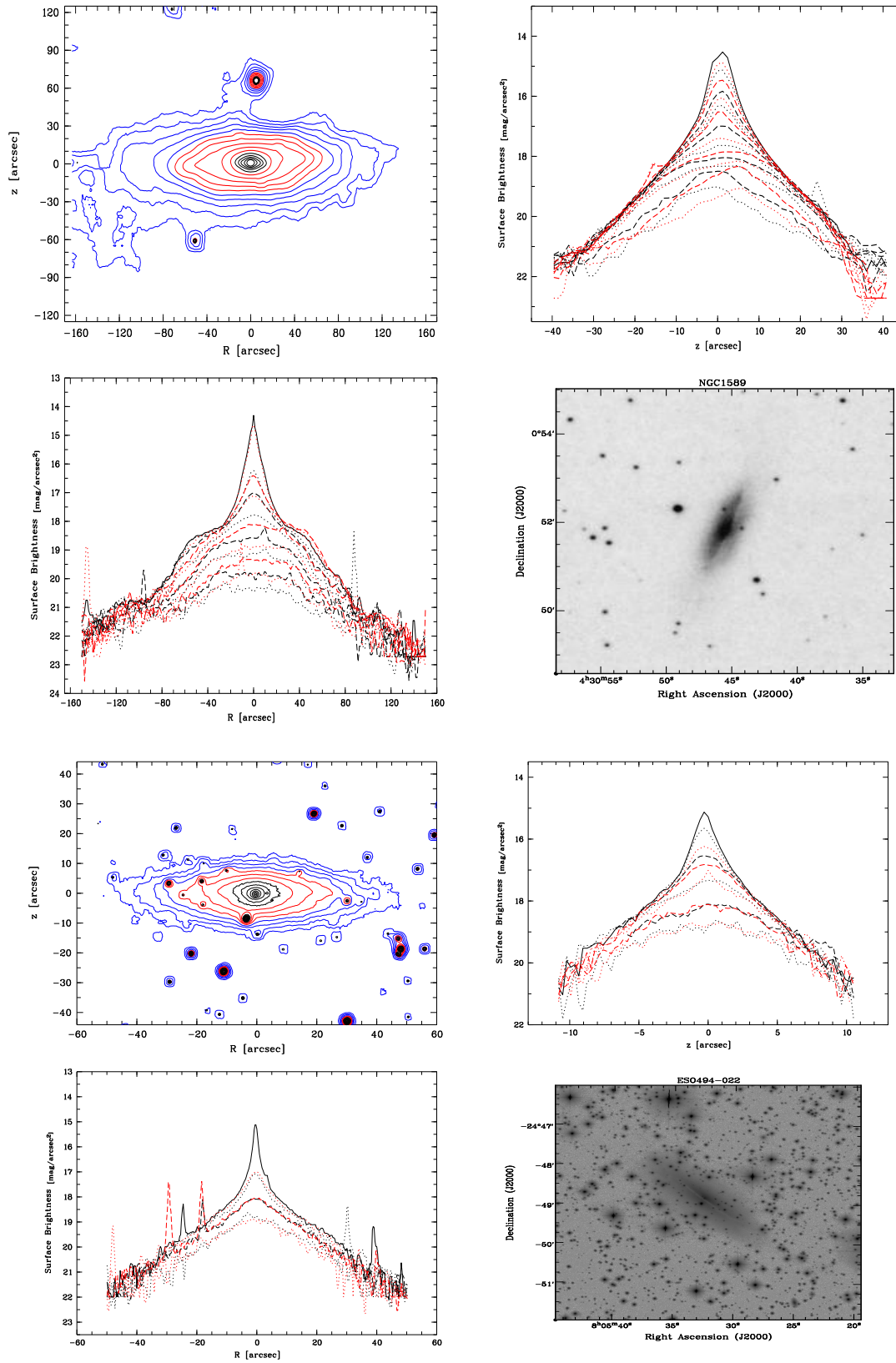


Figure 3.1 Continued. Top: NGC 1589; Bottom: ESO 494-022.

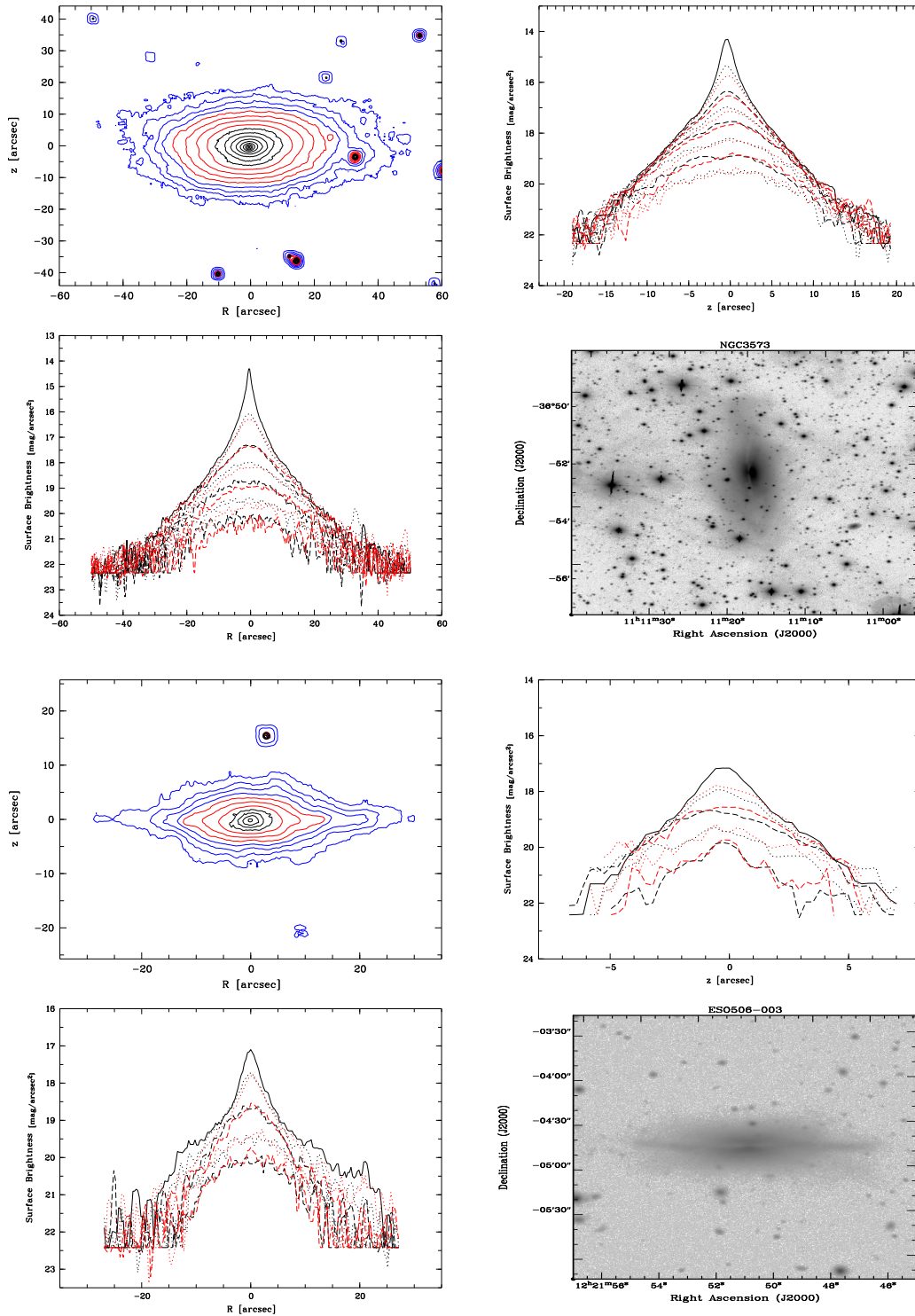


Figure 3.1 Continued. Top: NGC 3573; Bottom: ESO 506-003.

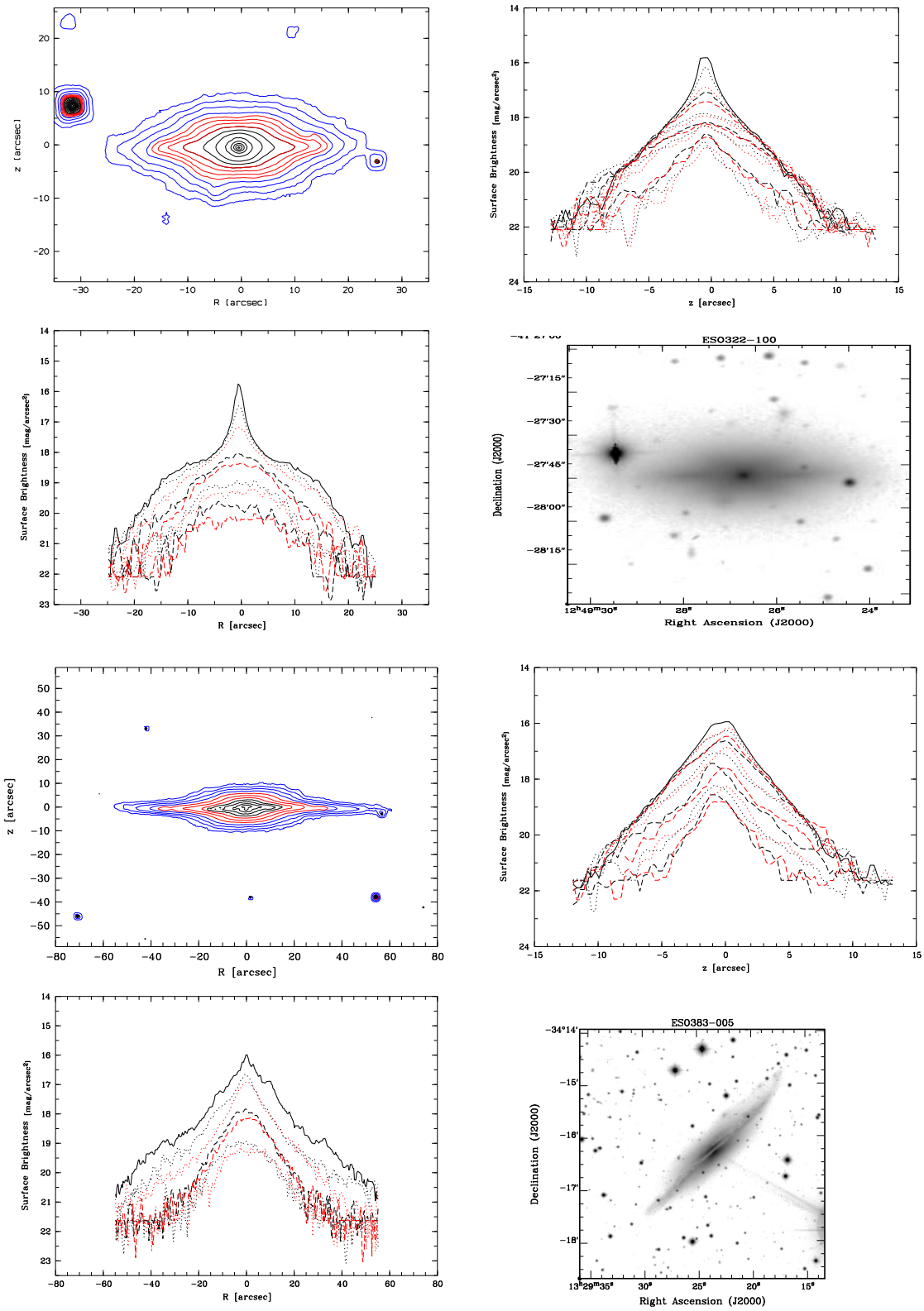


Figure 3.1 Continued. Top: ESO 322-100; Bottom: ESO 383-005.

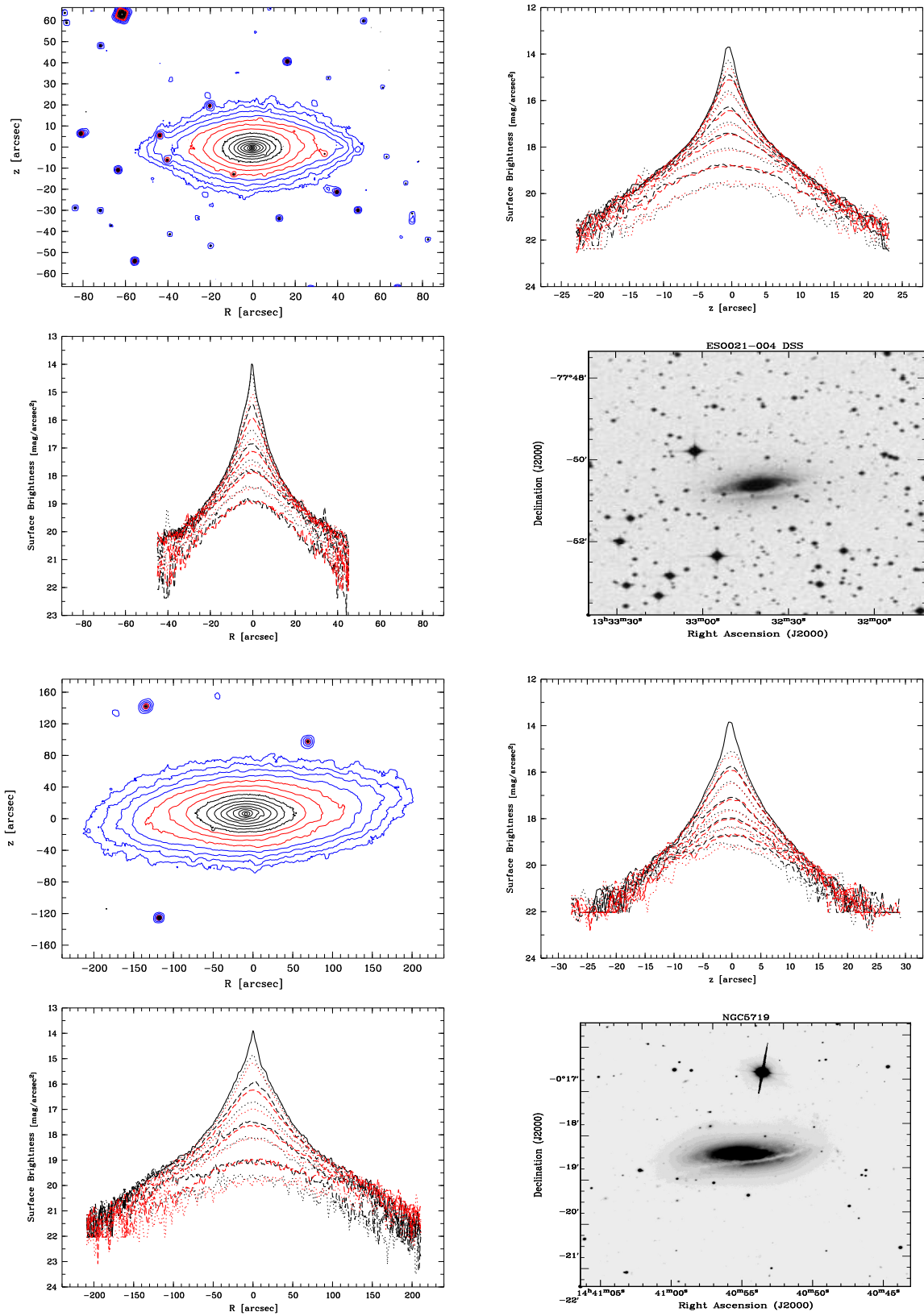


Figure 3.1 Continued. Top: ESO 021-004; Bottom: NGC 5719.

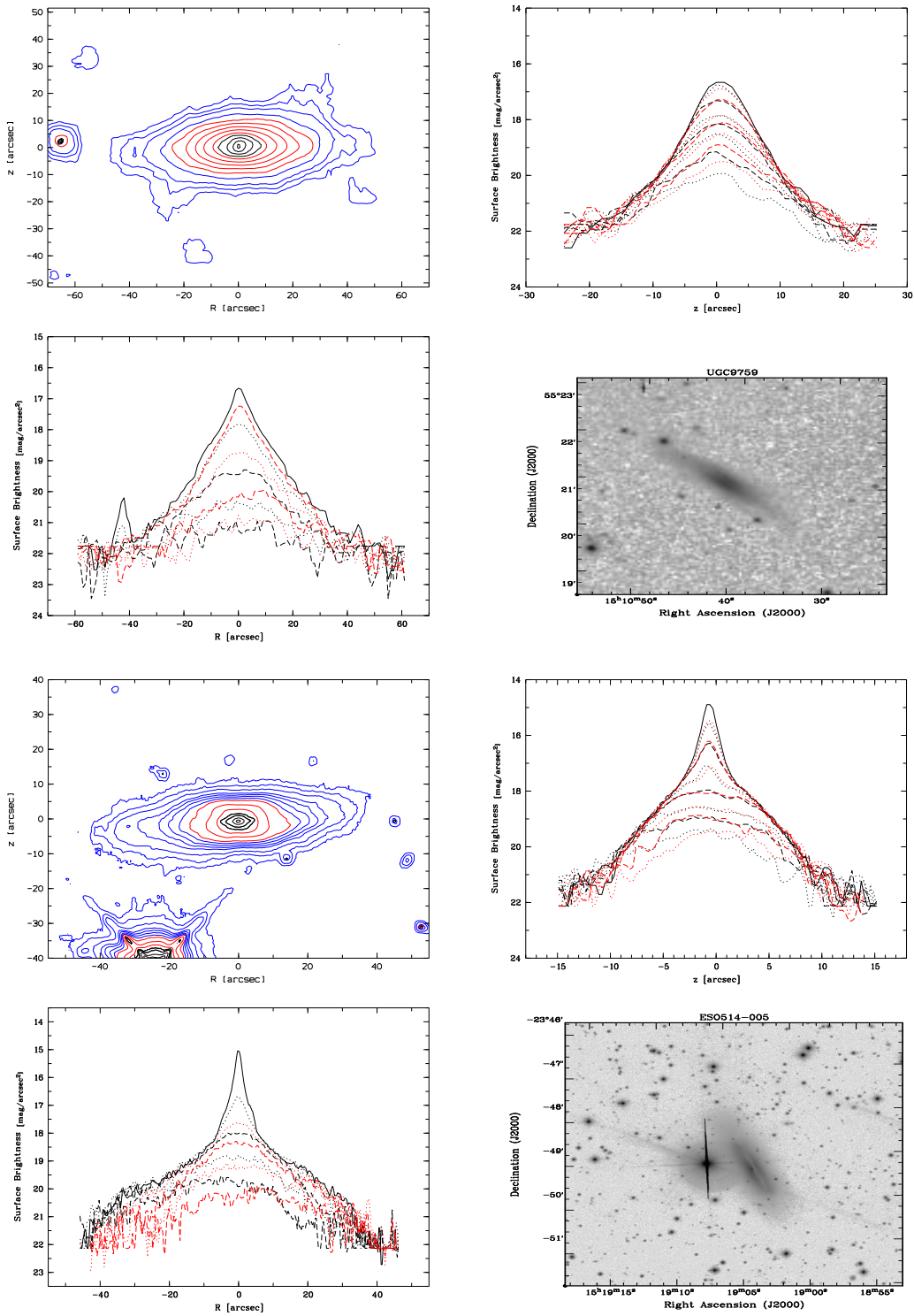


Figure 3.1 Continued. Top: UGC 09759; Bottom: ESO 514-005.

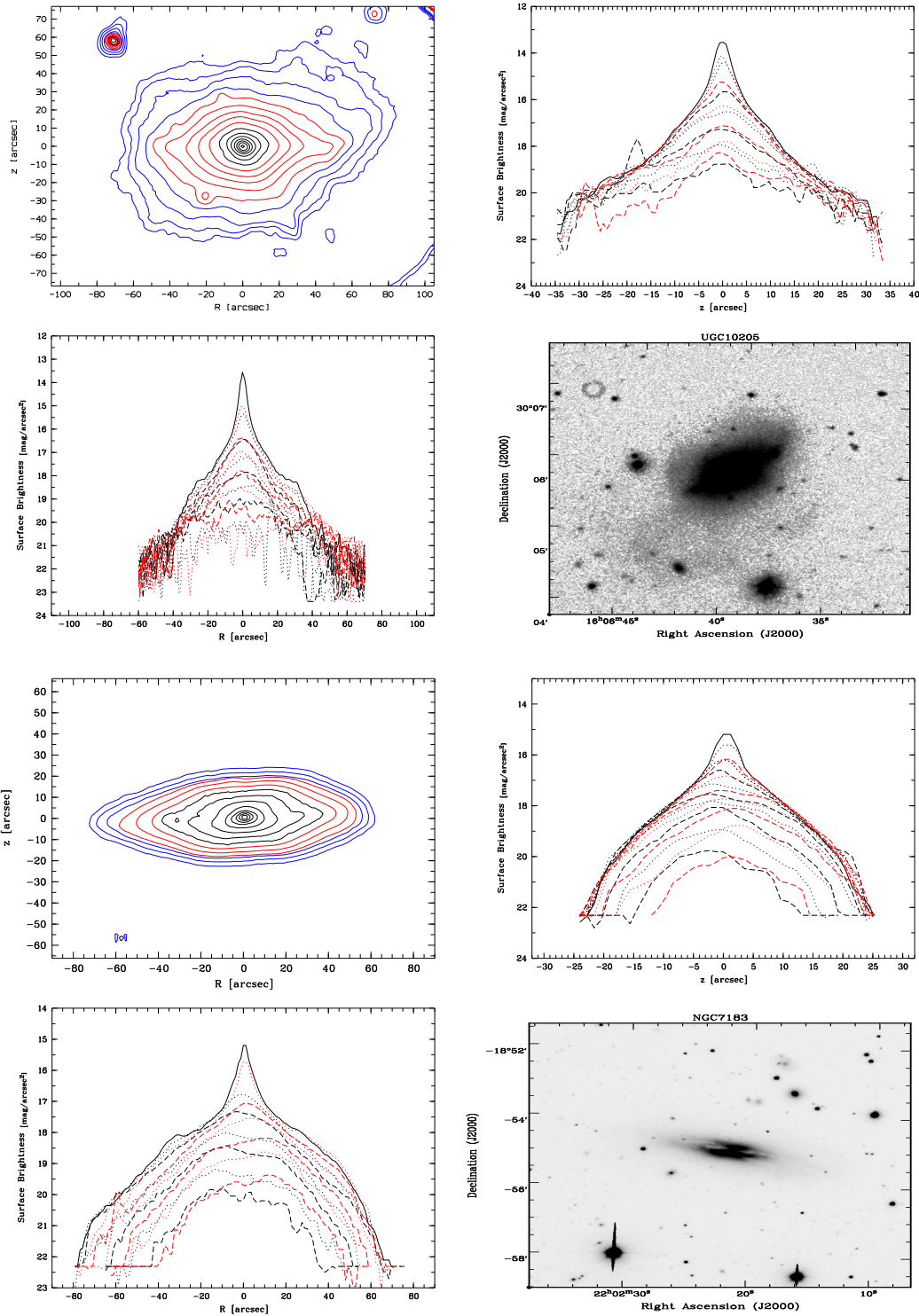


Figure 3.1 Continued. Top: UGC 10205; Bottom: NGC 7183.

2052 × 2052 pixel² LORAL/LESSER CCD with a 13''7 × 13''7 field of view (0''39/pixel). The northern galaxies were observed at the 1.23-m Calar Alto telescope equipped with the 2052 × 2052 pixel² SITe#2b CCD and a 90'' × 90'' field of view giving an image scale of 0''49/pixel.

The weather was photometric during most of the nights, the typical seeing was 1''0 to 1''5 (median FWHM = 1''2)

The data were reduced using the IRAF¹ software package with the standard reduction procedures. For all runs, the bias frame was constructed using frames with an integration time of 0 sec, taken with closed CCD-shutter. After the bias subtraction, master flat fields in each band were obtained by using all exposures taken with the same filter. From the flat fielded frames, the bad columns were removed by the standard fitting routine.

The exposure times of the individual frames were 70 min in B and 50 min in R. The details of the observations are summarized in Tab. 3.1.

Photometric standard stars from the E-regions (Graham 1982) and from Landolt (1992) fields were observed several times during the nights in order to set the zero point magnitudes, the extinction and color corrections. A total of 5 stars in at least 4 different fields were obtained for the photometric calibrations. The following transformations were calculated:

$$b_{instr} = B - 22.37(\pm 0.08) + 0.31(\pm 0.06) \times X + (B - R) \times 0.13 \quad (3.1)$$

$$r_{instr} = R - 22.39(\pm 0.04) + 0.25(\pm 0.03) \times X + (B - R) \times 0.58 \quad (3.2)$$

where B and R are the standard magnitudes, b_{instr} and r_{instr} the instrumental magnitudes, X the mean airmass of the observations.

3.2.3 Near-infrared observations and data reduction

The near-infrared observations were done at two different telescopes, the nine southern galaxies with the SOFI infrared spectrograph and imaging camera at the 3.5-m New Technology Telescope (NTT) of the European Southern Observatory (ESO) at La Silla (Chile), and five northern objects with the MAGIC camera at the 1.23-m CAHA telescope at Calar Alto (Spain). The SOFI imager/spectrometer was equipped with a 1024 × 1024 pixel Rockwell Hawaii array with a pixel size of 0''292 and a field of view of 4'94 × 4'94. The MAGIC camera with a 256 × 256 NICMOS3 array was used in the high-resolution mode (1''2/pixel), the only one available for that telescope. The field of view is 5' × 5'. We observed in September 2000 (CAHA) with the Johnson H-band filter, instead of K-band to avoid the large thermal emission of the latter, and in March 2001 (ESO) using the K_s (central wavelength, $\lambda_c = 2.162 \mu\text{m}$, $\delta\lambda = 0.297 \mu\text{m}$) filter because of the lower sky background.

During both observations, the on-source position was dithered by a few arcseconds between subsequent exposures in order to remove the bad pixels. The entire procedure was controlled by a macro program. We recorded object and sky frames alternately with a spatial separation of $\approx 5'$.

The effective exposure time for each individual galaxy was 30 min in K_s, resulting from an average of 6 exposures of 10 s each. The typical on-source exposure times were 40 to

¹IRAF is distributed by NOAO, which is operated by AURA Inc., under contract with the National Science Foundation

90 min with the H filter. Due to the highly variable background, the observations were split into integrations of 8×10 s each.

Standard stars taken from the Infrared NICMOS Standard Stars list (provided by Persson) and from the list of Faint Standard Stars (Elias et al. 1982) were observed every hour to provide photometric calibration.

The data were reduced using IRAF and plotted using MIDAS². Two different types of flat fields were compared. Firstly, we obtained differential dome flat fields by subtracting lamp-on and lamp-off images of the illuminated dome and secondly flats by combining all the frames of the observed field in different ways. Because of the smaller pixel-to-pixel variations estimated by the mean of the sky levels, the frames were flat-fielded with the master sky frames, which were constructed by median filtering right before and after on-source frames normalized to their mean value. Finally, the sky-subtracted and flat-fielded images were aligned using the common field stars and co-added to produce the final image.

After eliminating frames from non-photometric parts of the nights, we obtained the coefficients of the calibration transformations. The zero point offset and the extinction coefficients are $c_{0,H} = 21.219 \pm 0.29$, $c_{2,H} = 0.13 \pm 0.06$ for the H-band and $c_{0,K_s} = 20.756 \pm 0.13$, $c_{2,K_s} = 0.06 \pm 0.01$ for the K_s -band.

The galaxies were then rotated to their major axis. The position of the galaxy centers and the rotation angles were determined from the near-infrared data. As a first guess, the centers were estimated from the central intensity peaks.

Then the galaxy was folded in the vertical and horizontal direction to fix the center and extract the position angle. Almost all galaxies present deviation from asymmetry at the lower intensity levels. Therefore, we restricted the folding procedure to the inner, brighter regions which are typically more symmetric.

3.3 The isophotal images and the observed surface brightness profiles

Isophotal final maps of all observed objects in the near infrared, the radial and vertical surface brightness profiles, as well as R-band optical images are presented in Fig. 3.1. For each object we have indicated the name at the top of the isophotal image. The contours of the surface brightness are plotted starting from the brighter contour down to the limiting surface brightness (3σ , as tabulated in Tab. 3.1). The interval between successive contours is 1 mag arcsec⁻² in the inner region, further out the contours of the isophotal images are plotted equally spaced with 0.5 mag arcsec⁻². In order to improve the signal-to-noise ratio the data are spatially smoothed in the radial and in the vertical direction.

Radial (vertical) profiles were extracted at several positions (on average 6 to 7 cuts depending on the size of the galaxy) parallel (perpendicular) to the major axis, and plotted at increasing and decreasing z (r) up to the 3σ contours. The profiles are superimposed in order to acquire information on the asymmetries in the light contents.

The superimposed profiles reveal the presence of a bar and its characteristics. A plateau in the radial profile indicates the presence of a bar embedded in the bulge (de Carvalho & da Costa 1987). However, the detection of a bar is often problematic in edge-on galaxies. Asymmetries in the stellar content could be often confused with the bar signature, and end-on bars do not leave any conspicuous trace of their presence in

²MIDAS is developed and maintained by the European Southern Observatory

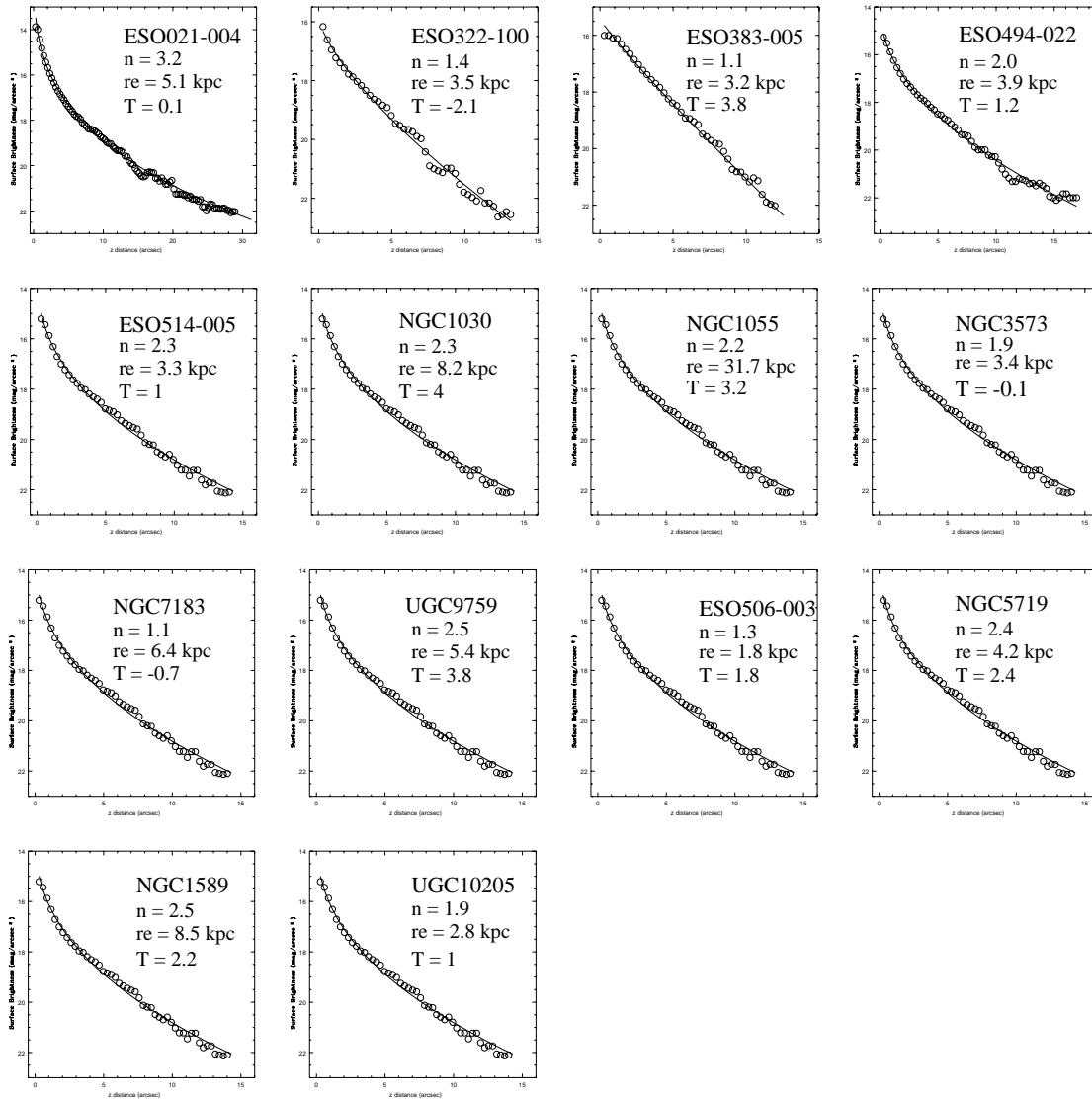


Figure 3.2 We have investigated the surface brightness vertical profiles of the thick box/peanut bulges, which result from near-infrared data using the $r^{1/n}$ Sérsic formula. The bulge profile is given by the open circle, the $r^{1/n}$ fit by the solid line. For every galaxy the exponent n of the Sérsic formula is given, along with the effective radii (re), and the Hubble stage (T).

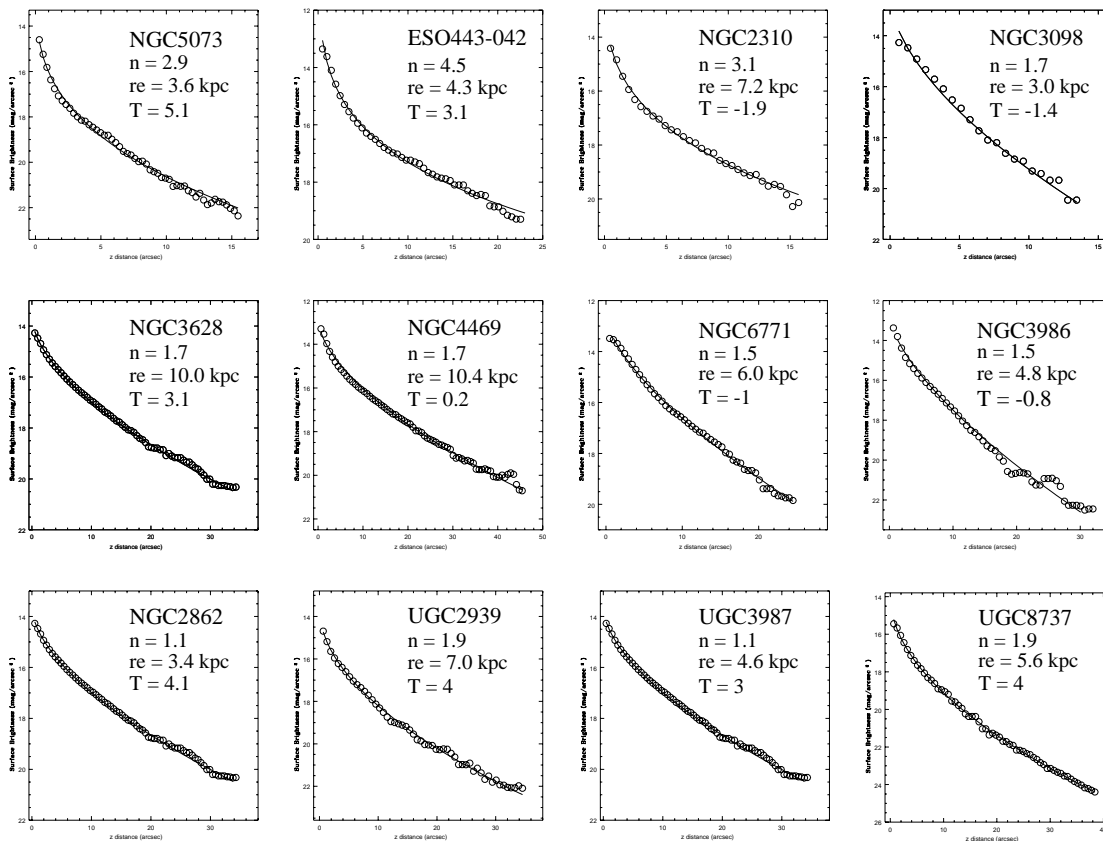


Figure 3.3 We have investigated the surface brightness vertical profiles of the classical box/peanut bulges, which result from near-infrared data using the $r^{1/n}$ Sérsic formula. The bulge profile is given by the open circle, the $r^{1/n}$ fit by the solid line. For every galaxy the exponent n of the Sérsic formula is given, along with the effective radii (re), and the Hubble stage (T).

the light distribution, thus in the radial profile.

Notes on individual objects:

- NGC 1030: Intermediate-type Sbc galaxy, almost edge-on oriented. The contours are distorted and a region of spread emission is observed on the right-hand side, while at the opposite edge the contour lines are pulled out and up at low contour levels. At optical wavelengths these peculiarities dominate also the upper side of the galaxy, they do not resemble emission knots, but rather bright tidal features which are visible out to $40''$ above the dust-lane (Fig. 3.1). In the profile along the major axis no sign of a bar is seen. It shows however excess light on the left-side (North-East) that causes the bump in the contours (at $R=50''$, $z=10''$) of the isophotal map (Fig. 3.1). Seven other classified galaxies physically belong to the group of NGC 1030, within a range of 580 km s^{-1} . Several satellites – without distance information – are also detected in the surroundings of NGC 1030.
- NGC 1055: early-type galaxy, classified as barred in LEDA catalog, although no signs of bar structure is observed in spectroscopic observations (Shaw 1993). The contours

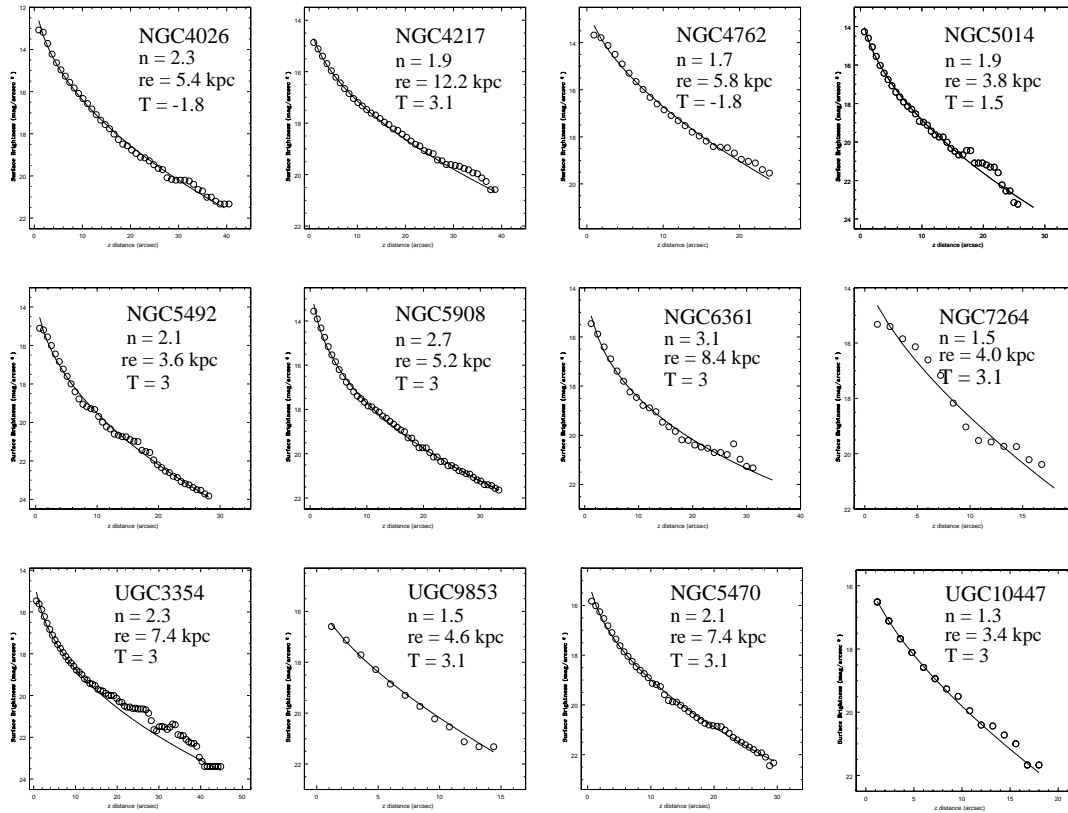


Figure 3.4 We have investigated the surface brightness vertical profiles of the spheroidal bulges, which result from near-infrared data using the $r^{1/n}$ Sérsic formula. The bulge profile is given by the open circle, the $r^{1/n}$ fit by the solid line. For every galaxy the exponent n of the Sérsic formula is given, along with the effective radii (re), and the Hubble stage (T).

reveal a strong bulge component of almost quadratic shape. No significant deviations are detected in the covered spatial range, but on the right-hand side the contours of the disk are bending away from the central plane which is probably caused by extinction from the prominent dust-lane. A thin disk component is visible and dominates the central part. A bump on the right-hand side (around $30''$) reveals an excess of light in this region. This might be the indication for a weak bar or a relict-like structure. Also in the near-infrared regime the prominent dust lane causes the right-hand depression in the vertical surface brightness profile. In the optical images, plumes and knots depart from the main disk and extend far from the center.

- NGC 1589: member of a triple system with NGC 1587 and NGC 1588 at $12'$ (RC2). The central region is obscured by a dust lane. Excess light emission in the optical as well as in the near-infrared is observed at the outskirts of the disk. It resembles a ring-like component or spiral arm tilted by some degrees with respect to the major axis of the galaxy. A strong plateau is detected along the radial profile which indicates a bar structure at position $z = +7''$ above the galactic plane.
- ESO 494-022: Sa, edge-on galaxy possibly paired with ESO 494-023 (Lauberts 1982). Several stars are superimposed to the galaxy and in the surroundings. The isophotes

appear quite symmetric and box/peanut shaped in the outer regions. No signs of bars are detected along the radial profile. Several absorption lanes are observed in the optical images, which cause the asymmetric shape of the vertical profile.

- NGC 3573: A regular shape is revealed in the near-infrared surface brightness contours of this S0a galaxy. The box/peanut shape is detected at the last contours. At optical wavelengths NGC 3573 reveals lopsided arms. No plateau is seen in the light profile. The profiles along and parallel to the minor axis show the typical depression of extinction due to a dust lane.
- ESO 506-003: disk galaxy with Sab morphological classification, with perfect edge-on orientation. The near-infrared surface brightness appears quite regularly distributed, with the right-hand side more extended than the opposite side. In the optical images, a strong X-shaped structure is superimposed to the galaxy. The left-hand disk is starting to deviate from the symmetric distribution, and a L-shaped warp is observed in ESO 506-003. In the radial profile no bar is revealed in this galaxy.
- ESO 322-100: lenticular (S0) galaxy paired with ESO 322-100 at a projected distance of $1/6$, and physically related (550 km s^{-1} of velocity separation). The bulge appears flattened, and a thin disk is observed in the near-infrared surface brightness. At optical wavelengths, a X-shaped is superimposed to the bulge. The radial profile detects the embedded disk, and a weak sign of bump in the light is detected in the outer region, likely a bar-structure ($z = \pm 10''$).
- ESO 383-005: Sbc spiral galaxy with flattened bulge and extended, straight disk. The contours in the near-infrared show a regularly distributed surface brightness, without peculiar features but in the optical an out-of-plane spiral arm affects the right-hand, upper side. The dust-lane appears inclined with respect to the major axis of the galaxy. No signs of irregularities in the vertical profile are detected nor a bump in the radial one
- ESO 021-004: Bulge dominated system (S0a) with high degree of symmetry as observed in the radial and vertical profiles. No sign of bar is revealed in ESO 021-004. No optical observations were performed on this galaxy.
- NGC 5719: Complex morphology and large deviation from symmetry in the outer parts of NGC 5719 are observed due to the interacting companion NGC 5713. The dust-lane crosses the main body largely skewed. Faint optical structures follow the inclined dust-lane, and bright knots are detected in connection with the location of the dust-lane. No plateau in the light profile is observed.
- UGC 09759: intermediate type galaxy (Sbc) with strong bulge and without disk component. Asymmetries in the near-infrared are detected at low surface brightnesses, where the contours in the right, upper part and mirrored in the lower-left one show similar irregularities. The small angular size of UGC 09759 does not allow a detailed study of peculiarities but at optical wavelengths a disk structure is detected with faint substructures at the outer edges. No sign of bar is revealed from the light profile.
- ESO 514-005: early-type (Sa) galaxy with strong box/peanut shaped bulge, and warped disk. Near ESO 514-005 a bright star is superimposed. In the optical, diffuse and elongated structures are embedded in the main body. No sign of a bar is detected in the radial profile. Very bright peak from the bulge luminosity is observed.

- UGC 10205: S0a-Sa type galaxy with complex morphology in the near-infrared surface brightness. UGC 10205 presents distorted contours, and diffuse debris dominates on the right-hand, upper side of the galaxy. Optically, several peculiarities are observed (e.g. debris, ring) and possibly represent relicts of past interactions. A weak plateau of light is detected along the radial profile likely indicating a bar ($z = 30-35''$) or a peculiar structure.
- NGC 7183: early-type galaxy with lopsided shape detected in the near-infrared isophotal image. Irregularities in the light contents are particularly observed with respect to the center to the left-hand side which has an elongated profile, but also on the lower side (as observed in the vertical profile). In the optical image, NGC 7183 presents several planes of extinction. No sign of a bar is revealed from the light profile.

3.4 Parameters of Thick Boxy Bulges

In order to disclose some of the properties of the selected thick bulges, a 1-D fitting procedure was performed on the near-infrared vertical surface brightness profiles. Using the near-infrared data is easier and more effective than the optical bands because of the relative lack of absorption-related features at these wavelengths, especially for our sample in which all members are dusty galaxies. In order to avoid the contribution from the disk component the fitting procedure is applied to the vertical instead of the radial surface brightness profiles.

Because of the high inclination of the galaxies we can assume that the vertical surface brightness of the galaxies in the sample consists mainly of the bulge light. For systems having an inclination i larger than 86° , the results obtained from the profiles should not be affected by the orientation (van der Kruit & Searle 1981, de Grijs et al. 1997). Since the galaxies are nearly edge-on, the results presented here are not corrected for inclination effects.

We consider the vertical light distribution as described by the Sérsic functional form. The $r^{1/n}$ formula was introduced by Sérsic (1968) as follows:

$$I_{bulge}(r) = I_e 10^{-b_n((r/r_e)^{1/n} - 1)} \quad (3.3)$$

where I_{bulge} is the surface brightness of the bulge in flux density at a distance r from the center, I_e is the intensity at the effective radius, r_e , which encloses half of the light, n is the shape parameter which measures the steepness of the luminosity profile of the bulge. The factor b_n in the approximated form is given by $b_n = 1.9992n - 0.3271$ for $1 < n < 10$ (Capaccioli 1987).

The Sérsic formula written in surface magnitude units has the form:

$$\mu_{bulge}(r) = \mu_e + c_n((r/r_e)^{1/n} - 1) \quad (3.4)$$

where c_n is simply $2.5 b_n$.

In order to avoid the seeing-dominated region, and not to include the contamination from dust-lanes, the fitted region is restricted a priori. The atmosphere of the Earth and the scattering within the telescope can alter the results on the intensity and shape parameters in the inner regions. We have applied an inner cutoff radius to the surface brightness

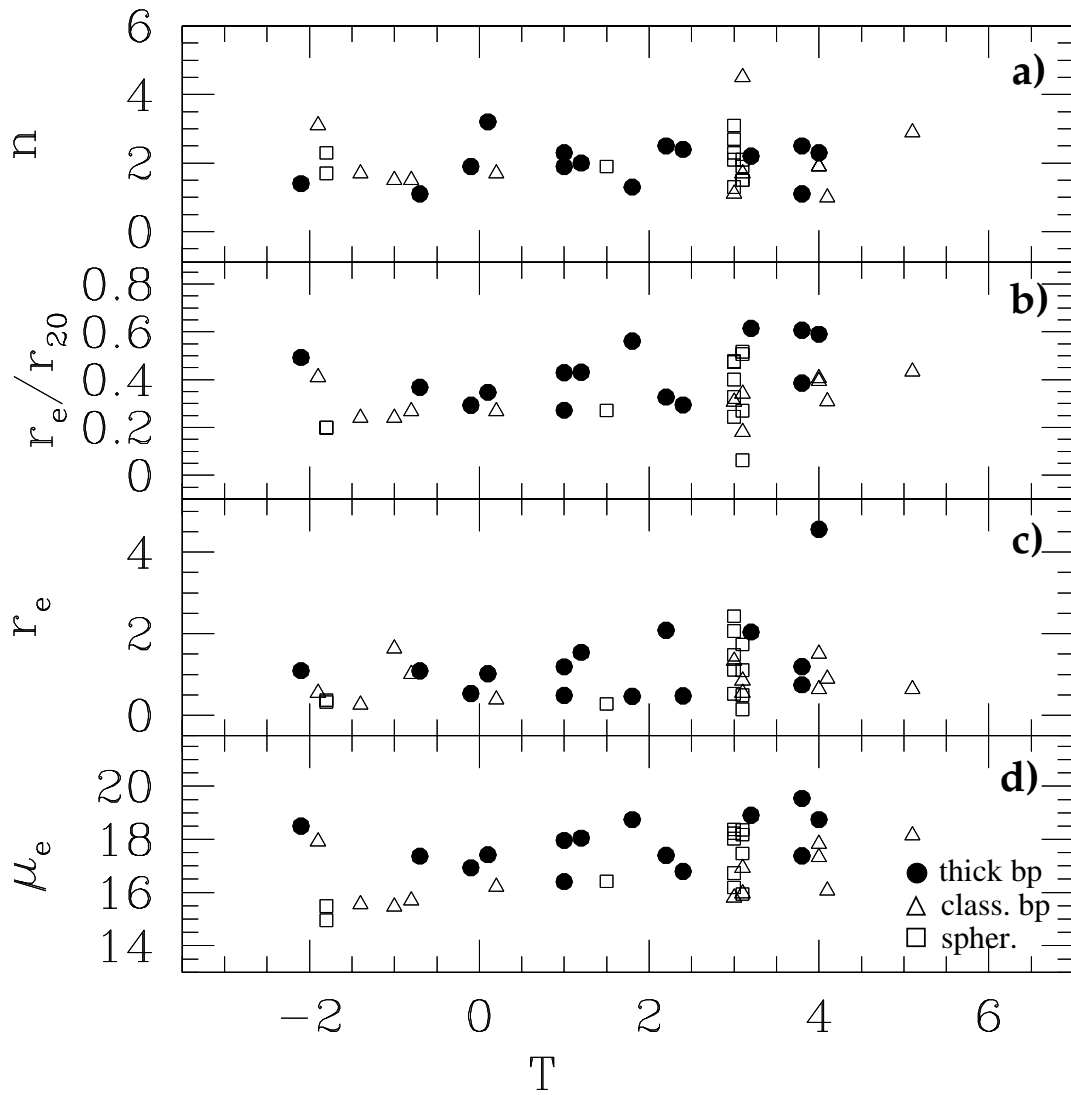


Figure 3.5 The best-fitting bulge parameters are plotted versus the morphological classification. The errors are not reported in order do not create confusion in the symbols, they are tabulated in Tab. 3.2.

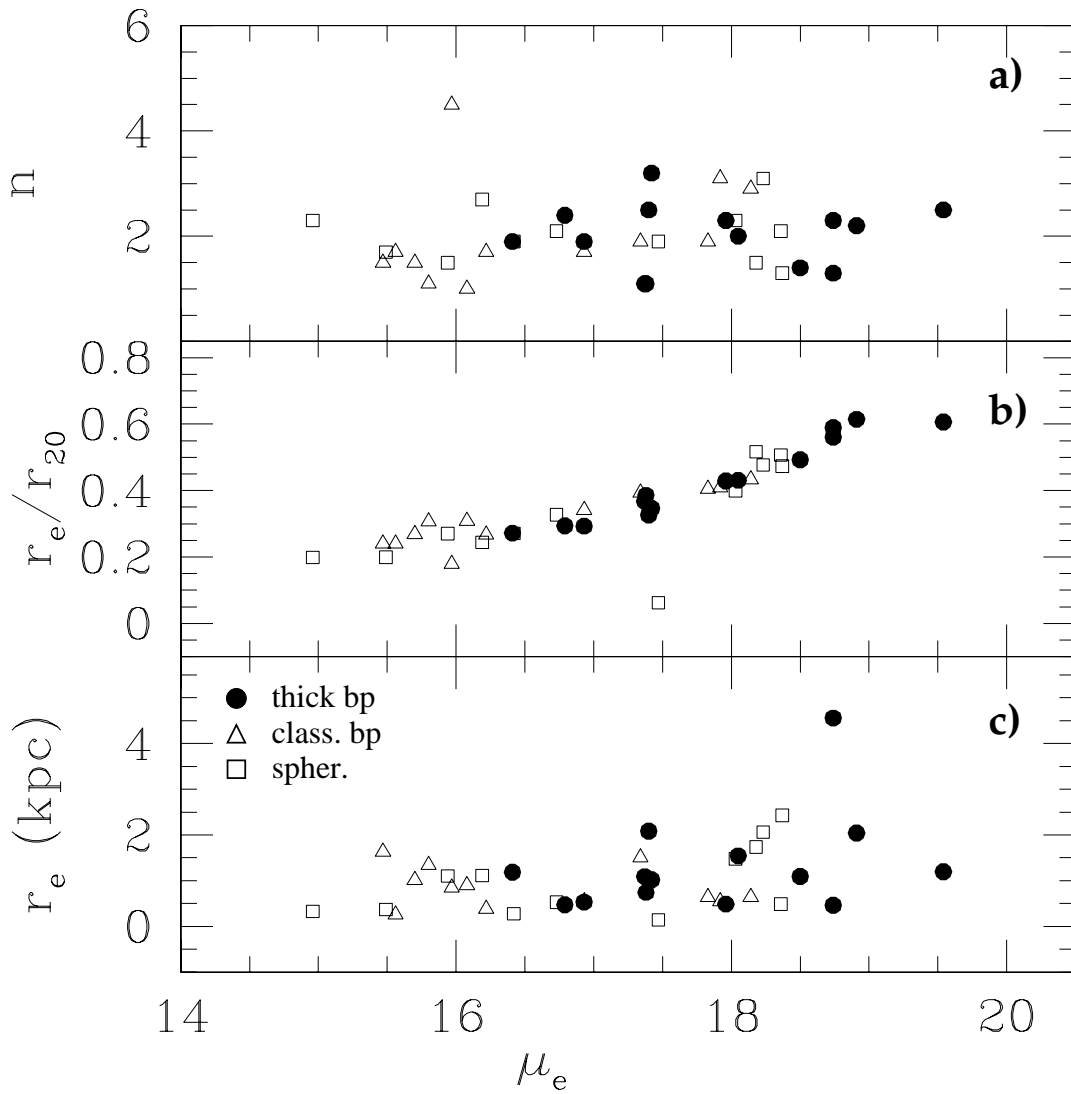


Figure 3.6 The best-fitting μ_e is plotted versus the other bulge parameters. The errors are not reported in order do not create confusion in the symbols, they are tabulated in Tab. 3.2.

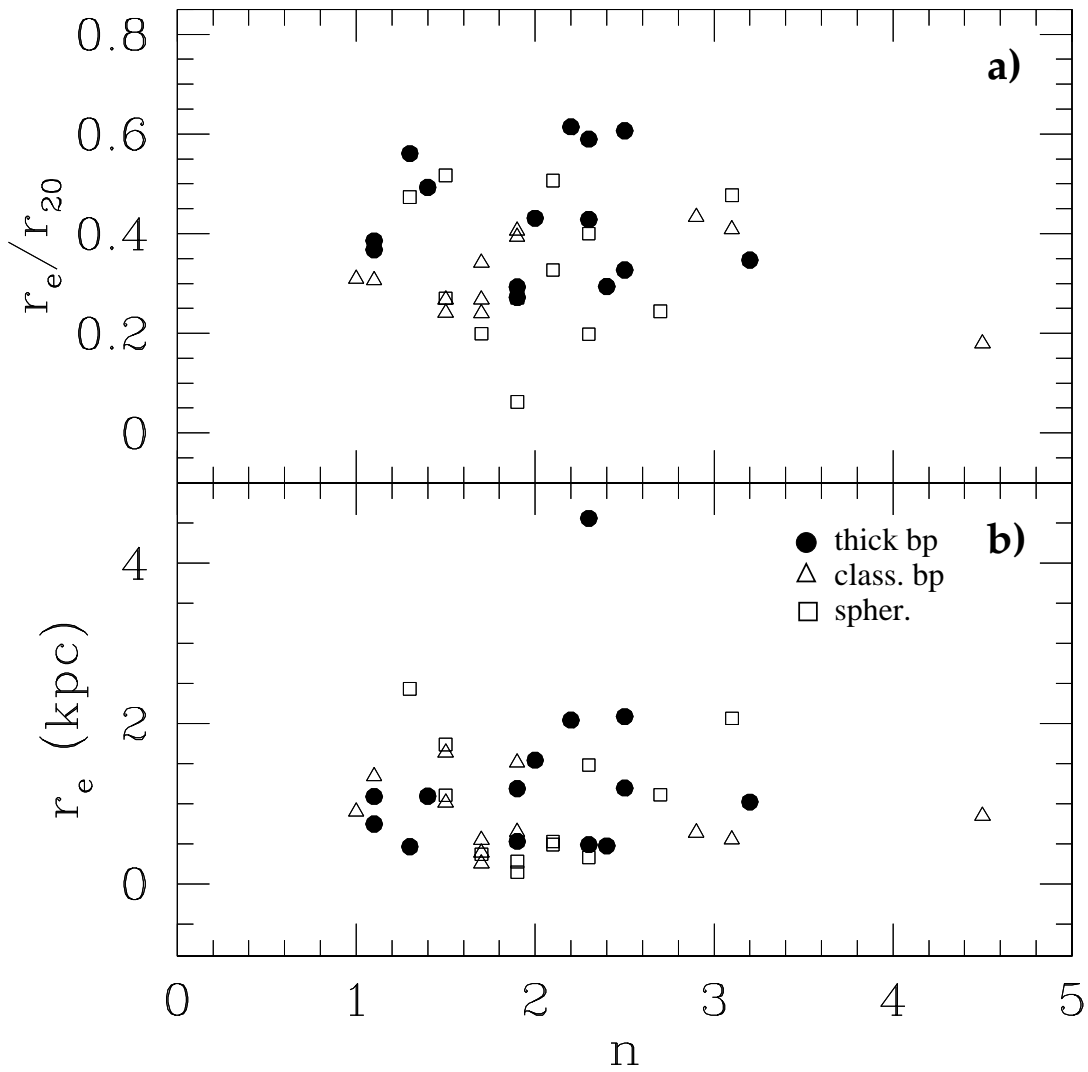


Figure 3.7 The best-fitting effective radius is plotted versus the n bulge parameter. The errors are not reported in order do not create confusion in the symbols, they are tabulated in Tab. 3.2.

TABLE 3.2. Parameters of the bulge fitting procedure

Galaxy	Morphology		Bulge	
	Type	μ_e	r_e	n
(1)	(2)	(3)	(4)	(5)
NGC 1030	+4.0±2	18.74±0.4	8.2±0.3	2.3±0.2
NGC 1055	+3.2±1	18.91±0.2	31.7±1.6	2.2±0.2
NGC 1589	+2.2±1	17.40±0.3	8.5±0.2	2.5±0.2
ESO 494-022	+1.2±1	18.05±0.4	3.9±0.1	2.0±0.2
NGC 3573	-0.1±1	16.93±0.3	3.4±0.2	1.9±0.2
ESO 506-003	+1.8±1	18.74±0.3	1.8±0.1	1.3±0.2
ESO 322-100	-2.1±1	18.50±0.2	3.5±0.1	1.4±0.3
ESO 383-005	+3.8±1	17.38±0.2	3.2±0.2	1.1±0.3
ESO 021-004	+0.1±1	17.42±0.3	5.1±0.2	3.2±0.2
NGC 5719	+2.4±1	16.79±0.2	4.2±0.1	2.4±0.2
UGC 09759	+3.8±3	19.54±0.6	5.4±0.3	2.5±0.3
ESO 514-005	+1.0±0	17.96±0.3	3.3±0.2	2.3±0.2
UGC 10205	+1.0±0	16.41±0.2	2.8±0.1	1.9±0.4
NGC 7183	-0.7±1	17.37±0.8	6.4±0.3	1.1±1.0
NGC 2310	-1.9±1	17.92±0.1	7.2±0.2	3.1±0.2
NGC 2862	+4.1±1	16.08±0.1	3.4±0.1	1.0±0.2
NGC 2939	+4.0±0	17.34±0.2	7.0±0.2	1.9±0.2
NGC 3098	-1.4±1	15.56±0.1	3.0±0.1	1.7±0.4
NGC 3628	+3.1±0	16.93±0.2	10.0±0.2	1.7±0.3
NGC 3986	-0.8±2	15.70±0.2	4.8±0.3	1.5±0.2
NGC 3987	+3.0±0	15.80±0.2	4.6±0.1	1.1±0.3
NGC 4469	+0.2±1	16.22±0.1	10.4±0.2	1.7±0.2
ESO 443-042	+3.1±1	15.97±0.1	4.5±0.1	4.5±0.3
NGC 5073	+5.1±1	18.14±0.1	3.6±0.2	2.9±0.2
UGC 8737	+4.0±0	17.83±0.3	5.6±0.1	1.9±0.3
NGC 6771	-1.0±0	15.47±0.2	6.0±0.2	1.5±0.2
NGC 4026	-1.8±1	14.96±0.2	5.4±0.1	2.3±0.2
NGC 4217	+3.1±1	17.47±0.2	12.2±0.1	1.9±0.3
NGC 4762	-1.8±1	15.49±0.3	5.8±0.2	1.7±0.3
NGC 5014	+1.5±2	16.42±0.2	3.8±0.2	1.9±0.4
NGC 5492	+3.0±0	16.73±0.3	3.6±0.2	2.1±0.2
NGC 5908	+3.0±0	16.19±0.2	5.2±0.1	2.7±0.2
NGC 6361	+3.0±0	18.23±0.3	8.4±0.3	3.1±0.3
NGC 7264	+3.1±0	15.94±0.4	4.0±0.2	1.5±0.2
UGC 3354	+3.0±0	18.03±0.3	7.4±0.2	2.3±0.7
UGC 9853	+3.1±0	18.18±0.2	4.6±0.2	1.5±0.2
NGC 5470	+3.1±0	18.36±0.2	7.4±0.1	2.1±0.3
UGC 10447	+3.0±0	18.37±0.3	5.4±0.3	1.3±0.3

Table 3.2 (1) Name of the galaxy; (2) Morphological type according to LEDA Catalogue; (3) Effective surface brightness (mag arcsec^{-2}); (4) Effective radius (arcsec); (5) Best-fitting n for the bulge component.

profiles, which is taken to be equal to the seeing point-spread function. The full width at half maximum for each object is measured on several un-saturated stars of each image.

Sky level variations, background noise, and magnitude calibration uncertainties are sources of error on the final parameters. The quoted errors of the parameters represent the corresponding uncertainties in the sky level subtraction for each image, which is the main source of error in the image. The estimated difference in deriving the value for these parameters represents the error in the fitting procedure. The final change of the parameters are in the order of 6% to 8%. The estimated errors are tabulated in Tab. 3.2. A Hubble constant of $H_0 = 75 \text{ km s}^{-1} \text{ Mpc}^{-1}$ is assumed to convert the parameter r_e into physical values.

Since the bulge parameters strongly depend on the fitting procedure, we performed the same analysis in a consistent way for two different comparison samples: classical box/peanut bulges and spheroidal bulges.

In Fig. 3.2 we present the vertical profiles taken from the near-infrared data along the minor axis of the thick box/peanut bulges. Each diagram shows the observed surface-brightness profile as filled square, the fit model as solid line. For every galaxy, the exponent n of the Sérsic formula is given along with the Hubble stage (T). The same profiles are presented also for the galaxies of the comparison sample in Fig. 3.3 for classical box/peanut bulges, and Fig. 3.4 for spheroidal bulges. The extracted parameters for the galaxies are listed in Tab. 3.2.

The fits provide good accuracy in reproducing the light distribution of all galaxies in the three samples. On average the profiles are well fitted until the surface brightness reaches the background level. Further on, the profile is the sum of the very low surface brightness and noise; this point is reached in general at $22 K_s \text{ mag arcsec}^{-2}$.

NGC 7183 is the only galaxy that presents large deviations from the fitted distribution in its central region possibly due to a disk component which affects the profile. The contours of NGC 7183 are strongly boxy at all z and asymmetries between the two sides of the galaxy are observed in the isophotal plot (Fig. 3.1). In this case, the fit is not very reliable.

We have compared the parameters which characterize the light distribution in the thick box/peanut bulges with those obtained for the comparison samples. The analogous dependences are superimposed for the different samples in order to compare possibly different trends.

The relations of the bulge parameters μ_e , r_e , r_e/r_{20} , and n with the morphological type T (taken from the LEDA catalogue), are presented in Fig 3.5. The correlations are shown for the parameter r_e/r_{20} , which represents a sort of normalization of the light profile in order to avoid the effect of intrinsically different galaxy sizes.

Bulge parameters do not correlate with the morphological type in the target galaxies. In particular, the result of Andredakis, Peletier, & Balcells (1995) and Graham (2001) that the bulge index, n , reaches higher values in early-type galaxies cannot be reproduced in any of the bulge classes, mainly because of the small number statistics. Despite the fact that the target galaxies are spanning a morphological-type range between -2.1 and 5.1 , the large majority of the morphological types is between -2 and $+4$ and a clustering of points at $T = 3$ is observed for spheroidal, and classical box/peanut bulges.

Both bulge parameters are combined in the $\mu_e - r_e$, $\mu_e - r_e/r_{20}$, $\mu_e - n$ relations (Fig. 3.6). In Fig. 3.3, we plotted the radius versus the n parameter ($r_e - n$, and $r_e/r_{20} - n$). Thick box/peanut bulges have a mean value for μ_e equals to $17.87 \text{ mag arcsec}^{-2}$ (stand. dev. 0.91), classical box/peanut and spheroidal bulges have $\mu_e = 16.58 \text{ mag arcsec}^{-2}$ (stand. dev. 0.99) and $17.03 \text{ mag arcsec}^{-2}$ (stand. dev. 1.22), respectively. Thus, there is a

slight indication that the surface brightness at the half-light radius, μ_e , is fainter for thick box/peanut bulges compared with that of the classical box/peanut and spheroidal bulges (Fig. 3.6). Consequently, because fainter surface brightnesses tend to be combined with larger effective radii in thick box/peanut bulges – as expected from the narrower total luminosity range – the classical box/peanut and spheroidal bulges present a narrower distribution in effective radii (0.30-1.63 kpc) with respect to thick box/peanut bulges (0.47-4.55 kpc, Fig. 3.6c).

Mean values for effective radii, r_e , in the three classes of bulges are $r_e = 1.32$ kpc (stand. dev. 1.07, thick box/peanut bulges), 0.86 kpc (stand. dev. 0.42, classical box/peanut bulges), and 1.00 kpc (stand. dev. 0.67, spheroidal bulges). A trend in the box/peanut bulges between the r_e/r_{20} ratio is observed as a function of the effective surface brightness (Fig. 3.6b).

In the morphological range between -2 and $+5.1$, the mean value and the standard deviation of n are 2.01 (stand. dev. 0.37), 2.04 (stand. dev. 0.99), 2.03 (stand. dev. 0.62) for thick, classical box/peanut and spheroidal bulges, respectively.

Based on the definition of μ_e and r_e , the box/peanut bulges are structurally different. The cause of this diversity can be the different mechanism of formation of this class. Components like an X-shape makes the concentration of the light along the minor axis direction shallower, as the light is concentrated above and below the major plane but at further distance from the minor axis. Thus, the isophotes of box/peanut bulges are depressed along the minor axis. Based on the μ_e and r_e trend we confirm the earlier prediction by Binney & Petrou (1985) that the vertical structures in box/peanut bulges are different from those of the more spheroidal bulges, while the n parameters in box/peanut bulges do not show significant differences to the other classes of bulges.

Examining the residuals and the errors, we conclude that the bulge profile for thick box/peanut bulges is well described by the Sérsic law with bulge parameter $n = 2$, and it has to be preferred to both the de Vaucouleurs law and the exponential law (Tab. 3.2).

With respect to the r_e parameter (Fig. 3.3), the values for n tend to be randomly distributed in spheroidal bulges, in box/peanut bulges they are slightly correlated with increasing effective radii, but with a large scatter. In general, we do not find the trend which implies larger n with increasing r_e for elliptical and lenticulars (Caon et al. 1993) and for spiral galaxies (Andredakis 1997). This is certainly because of our analysis along the vertical profile instead of the radial one which would give a flatter light distribution. The radial analysis has not been performed because of the influence of the disk component which is hard to separate from the contribution of a bulge-dominated system.

3.5 Summary

In this chapter, we have presented near-infrared and optical observations of our sample of thick boxy bulge galaxies. Peculiarities in the light distribution, and dust lanes sometimes on several planes are often observed. These asymmetries are interpreted as possible relics of recent accretion events.

A few galaxies possess disk components, the large part of them presents strong box/peanut isophotes starting from the inner surface brightness.

Bars can be detected using the plateau of the light in the radial profiles, but only one strong bar and other three possibly weak bars were found among the fourteen galaxies. This represents a lower limit due to the problem related with the orientation of a bar.

The light distribution in the bulge is defined by three parameters, the half-light radius

r_e , the surface brightness at the r_e radius, and the bulge shape index n . By applying a 1D fit of the light distribution of galaxies with thick bulges using the Sérsic law, we obtained the following results:

- Bulge parameters do not correlate with the morphological type in the target galaxies. In particular, the n versus morphological type relation is not observed.
- Fainter effective surface brightnesses, and larger effective radii are detected in thick box/peanut bulges with respect to the classical box/peanut and spheroidal bulges. Based on this result, we can infer that vertical surface brightnesses in box/peanut bulges are structurally different from those of the more spheroidal bulges.
- Box/peanut (thick and classical) bulge classes show a correlation between the effective radii normalized to the K_s 20-mag level versus the effective surface brightness.
- Box/peanut bulges are well described with the bulge parameter $n = 2$ in the fits of the Sérsic law.
- Investigations on the vertical profiles do not show the larger n - increasing r_e correlation.

Finally, as far as the shape parameters (larger r_e , fainter μ_e) are concerned, there is an indication for differences between thick box/peanut bulges and classical box/peanut bulges. This might indicate a different formation mechanism of thick box/peanut bulges. Interaction events could have a larger imprint on growing bulges as a result of a larger amount of fresh gas. This gas can, in turn, fuel nuclear starbursts and active galactic nuclei. Most intense nuclear activity is commonly found in collisional systems. The larger rate of stellar content could further inflate the box/peanut shaped orbits.

References

- Andredakis Y.C., Peletier R.F., Balcells M., 1995, MNRAS 275, 874
- Barnes J.E., 1988, ApJ 331, 699
- Caon N., Capaccioli M., D'Onofrio M., 1993, MNRAS 265, 1013
- Capaccioli M., 1987, IAU Symposium 127, Dordrecht D., Reidel Publishing Co. ed., p. 47-60.
- de Carvalho R.R., da Costa R.L., 1987, A&A 171, 66
- Elias J.H., Frogel J.A., Matthews K., Neugebauer G., 1982, AJ 87, 1029
- Gerhard O.E., 1981, MNRAS 197, 179
- Graham J. A., 1982, PASP 94, 244
- Graham A.W., 2001, AJ 121, 820
- Haynes M.P., Jore K.P., Barrett E.A., Broeils A.H., Murray B.M., 2000, AJ 120, 703
- Landolt A.U., 1992, AJ 104, 340
- Lauberts A., 1982, ESO/Uppsala survey of the ESO(B) atlas, Garching: European Southern Observatory (ESO),
- Lütticke R., Dettmar R.-J., Pohlen M., 2000, A&AS 145, 405
- Sérsic J.L., 1968, Atlas de Galaxias Australes (Córdoba: Observatorio Astronómico)
- Shaw M., 1993, A&A 280, 33

4

Stellar and gaseous kinematics in four galaxies with thick box/peanut bulges

New kinematic observations of the stellar and gaseous components in four galaxies with thick box/peanut bulges are presented. In one of the systems (NGC 5719), long-slit spectroscopic observations show a counter-rotating stellar system with the gaseous component. A second stellar component corotating with the gas extends within the inner 100 pc.

The kinematics and distribution of the neutral hydrogen in NGC 5719 is most peculiar as well. A long HI bridge extends from the south-eastern counter-tail of the edge-on galaxy NGC 5719 which points toward NGC 5713.

A preliminary analysis of the optical observations, and a comparison with the HI kinematics – in particular for NGC 5719 – is presented.

4.1 Introduction

Disk galaxies show a wealth of morphological and kinematic peculiarities. An increasing number of systems with lopsided kinematics in the rotation curves (Swaters et al. 1999, Schoenmakers 1999) and in their HI profiles (Richter & Sancisi 1994; Haynes et al. 1998) are reported in the literature.

A large fraction of disk galaxies possess large-scale asymmetries in the morphology, and warp phenomena are commonly observed in the stellar as well as in HI disks (e.g. Reshetnikov et al. 2002, García-Ruiz 2001). In these investigations, the frequency of galactic warps reaches up to about 50% or more. With about the same frequency, stellar bars (Miwa & Noguchi 1998) and X-shaped structures as observed in box/peanut bulges (Mihos et al. 1995) are found.

Somewhat less frequent (in roughly a quarter of disk galaxies, Barnes 2002) counter-rotating or otherwise decoupled central components have been observed and only few objects present kinematically decoupled stellar disks: the early-type galaxies NGC 3593 (Bertola et al. 1996), NGC 4138 (Jore, Broils & Haynes 1996), NGC 7217 (Merrifield & Kuijken 1994), and the lenticular (S0) NGC 4550 (Rubin, Graham, & Kenney 1992, Rix et al. 1992).

Different scenarios have been proposed to explain such phenomena, but all of them invoke merger events between galaxies.

Among encounters of two massive galaxies (Pfenniger 1993) or the interaction between

TABLE 1. Log of spectroscopic observations (galaxies).

Object	Coordinate (J2000)		P.A.	Date	U.T.	Exp. Time
NGC 5719	13 ^h 32 ^m 39 ^s .64	-77°50'31".7	96°	14 Jul 02	00 17	2700
NGC 5719			96°	15 Jul 02	00 31	3000
NGC 5719			121°	15 Jul 02	01 38	3000
NGC 5719			121°	15 Jul 02	02 29	3000
IC 4745	18 ^h 42 ^m 35 ^s .68	-64°56'35".3	179°	14 Jul 02	03 29	3000
IC 4745			179°	14 Jul 02	04 21	3000
IC 4745			179°	14 Jul 02	05 11	3000
IC 4757	18 ^h 43 ^m 55 ^s .73	-57°09'58".2	57°	15 Jul 02	04 48	3000
IC 4757			57°	15 Jul 02	05 39	3000
NGC 7183	22 ^h 02 ^m 21 ^s .64	-18°54'58".5	74°	14 Jul 02	07 54	3000
NGC 7183			74°	14 Jul 02	08 45	3000
NGC 7183			74°	14 Jul 02	09 36	1500

Table 4.1 (1) Galaxy Name of the sample; (2), (3) Coordinates; (4) Position angle of the slit; (5) Universal time of the starting acquisition; (6) Exposure time expressed in seconds.

a galaxy and a small-mass satellite (mass ratio usually less than 0.1), the minor merger event is the favorite mechanism for two reasons: Firstly, the slow encounters do not lead to disk destructions (Walker, Mihos, & Hernquist 1996). Secondly, minor mergers occur with much higher frequency than major ones (Lacey & Cole 1993).

This chapter presents observations and a preliminary analysis of the optical long-slit spectroscopy performed on a sample of four galaxies with thick box/peanut bulges. The optical observations include NGC 5719, NGC 7183, IC 4745 and IC 4757. For the interacting system NGC 5719/NGC 5713 the morphological and kinematic properties of the HI emission is reported. The HI observations and data reductions for the target galaxies are presented in Ch. 2.

This chapter is organized as follows: Sect. 4.2 describes the observations and the data reduction. In Sect. 4.3. we discuss the distribution and the kinematics of the target galaxies. In particular, the counter-rotating gas-stellar systems in NGC 5719 are analyzed. In the discussion (Sect. 4.4) special emphasis is put on the interaction events which have occurred in these systems.

4.2 Spectroscopic Observations and Data Reductions

Images and spectra of NGC 5719 were obtained on July 14-15 2002 at ESO's 3.5-m New Technology Telescope (NTT) at La Silla (Chile), using the ESO Multi-Mode Instrument (EMMI) in the REd Medium Dispersion (REMD) configuration. With the new generation MIT 2k × 4k chips, the spatial scale of the instrument was 0".1665 pixel⁻¹. After an on-line binning of 2 pixels along the spatial and dispersion directions, each pixel of the frame corresponds to 0.65 Å × 0".33. The grating no. 6¹ (instrumental dispersion 30km s⁻¹). was

¹EMMI manual. NTT Group ESO/La Silla.

used in combination with a $1''0 \times 300''$ slit.

We acquired long-slit spectra at the central wavelength of 521.7 nm, which yielded a wavelength coverage between 489.7 nm and 553.7 nm. The selected region includes the [OIII] line at $\lambda = 500.7$ nm emitted from the ionized gas, and the [Mg] triplet at $\lambda = 516.4, 517.3, 518.4$ nm used for the stellar kinematics.

The galaxy continuum was removed from the spectra by fitting a fourth to sixth order polynomial as in Bender et al. (1994). The complete journal of the observations is reported in Tab. 4.1 where the position axis of the slit, the date and the exposure time are compiled for each spectrum. Spectra of several giant stars (G5III to K7III) have been taken before every object exposure, and used as templates in measuring the stellar kinematics (Tab. 4.2).

We obtained the set of bias, flat-field images, and comparison spectra of HeAr for the wavelength calibration. The spectra were first cleaned to remove cosmic rays and bad columns and then corrected for bias and finally flat-fielded. The subsequent reduction was performed following the usual procedure outlined in the MIDAS (LONGSLIT) package. Measurements of the sky lines indicate that the wavelength calibration is uncertain at $\pm 10 \text{ km s}^{-1}$ at any position within the long-slit spectra.

Using the Fourier Correlation Quotient method (FCQ, Bender 1990) and following the prescriptions of Bender et al. (1994). We measured the stellar velocity and the velocity dispersion by fitting the LOSVD with a Gaussian, and the resulting stellar kinematics is reported in Fig.s 4.1, 4.2, 4.3, 4.4, and 4.5.

4.3 Observational results

4.3.1 The stellar and ionized gas kinematics

The velocity curves, the velocity dispersion profiles, and the corresponding $H\beta$ fluxes are reported for the stellar and gaseous components, along with the optical major axis of NGC 5719 (Fig. 4.1), IC 4745 (Fig. 4.3), IC 4757 (Fig. 4.4), and NGC 7183 (Fig. 4.5). In the case of NGC 5719, observations were performed also along the HI major axis (offset by 25° from the optical major axis).

NGC 5719

The gaseous components in NGC 5719 have a lopsided distribution with an extent beyond a radius at $35''$ (3.9 kpc) on the receding side, while they cease at $20''$ (2.23 kpc) on the approaching side. The velocity dispersion of the gas remains quite flat at a value of approximately 20 km s^{-1} .

The stellar content is in counter-rotation with the gas, and extends out to some $40''$ to $45''$. The rotation velocities have a peculiar shape in the intermediate region. They start with a steep increase, stay nearly constant around the systemic velocity (or even decrease) and assume a normal shape beyond $12''$ to $15''$. Also the velocity dispersion presents a curious behavior, corresponding to the central region a depression is observed at 140 km s^{-1} , further out the velocity dispersion increases up to 260 km s^{-1} , before decreasing again and assuming a typical value of 80 to 100 km s^{-1} in the external regions. The indication for the existence of a second stellar disk is inferred from the velocity dispersion trend. Around $\approx 7''$, one single point is fitted in the approaching region with a lower velocity dispersion ($\approx 20 \text{ km s}^{-1}$).

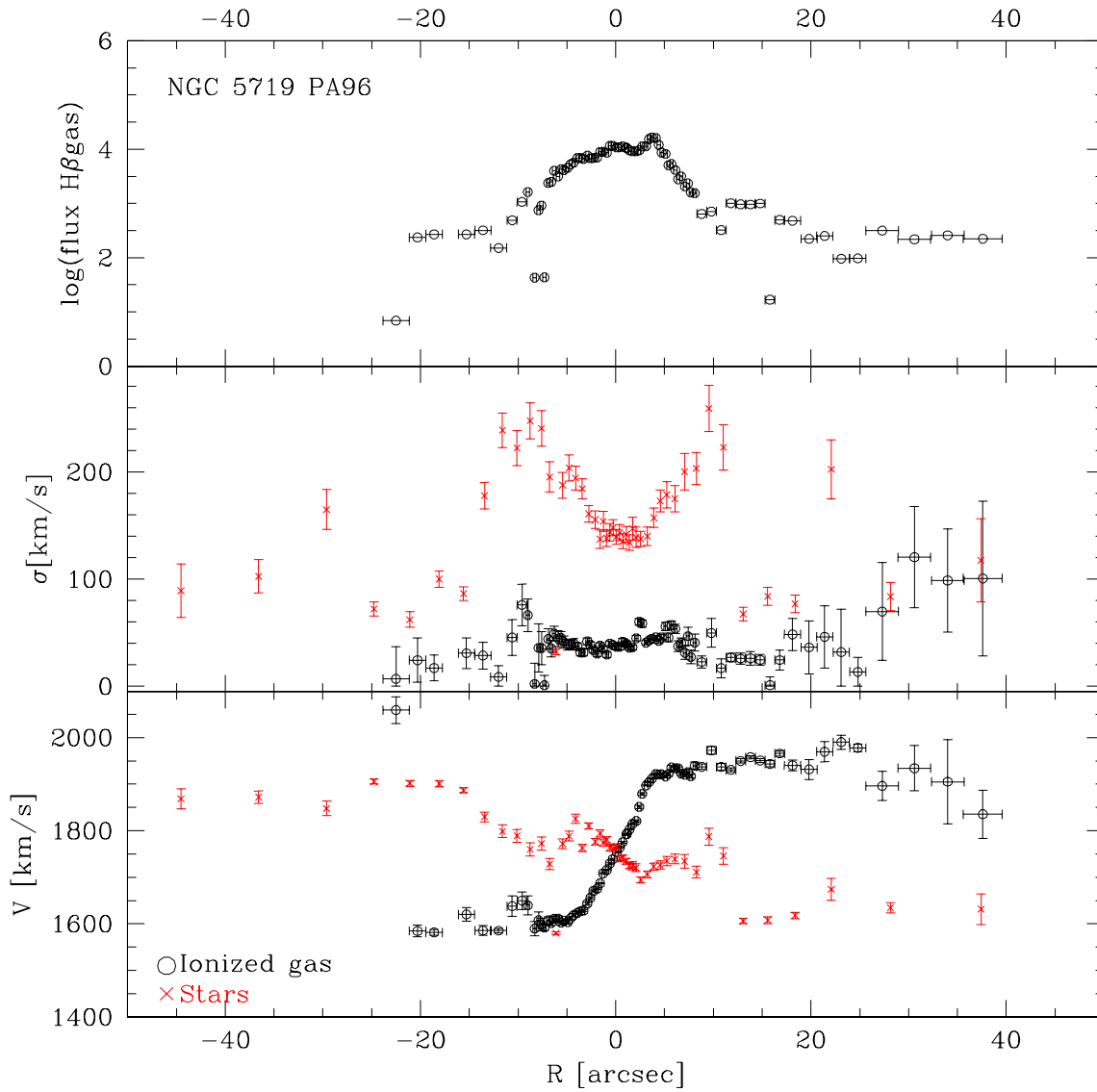


Figure 4.1 Stellar and ionized gas kinematics along the optical major axis ($\approx 96^\circ$) in NGC 5719. The stellar (cross symbols) and ionized gas (circle symbols) kinematics are plotted.

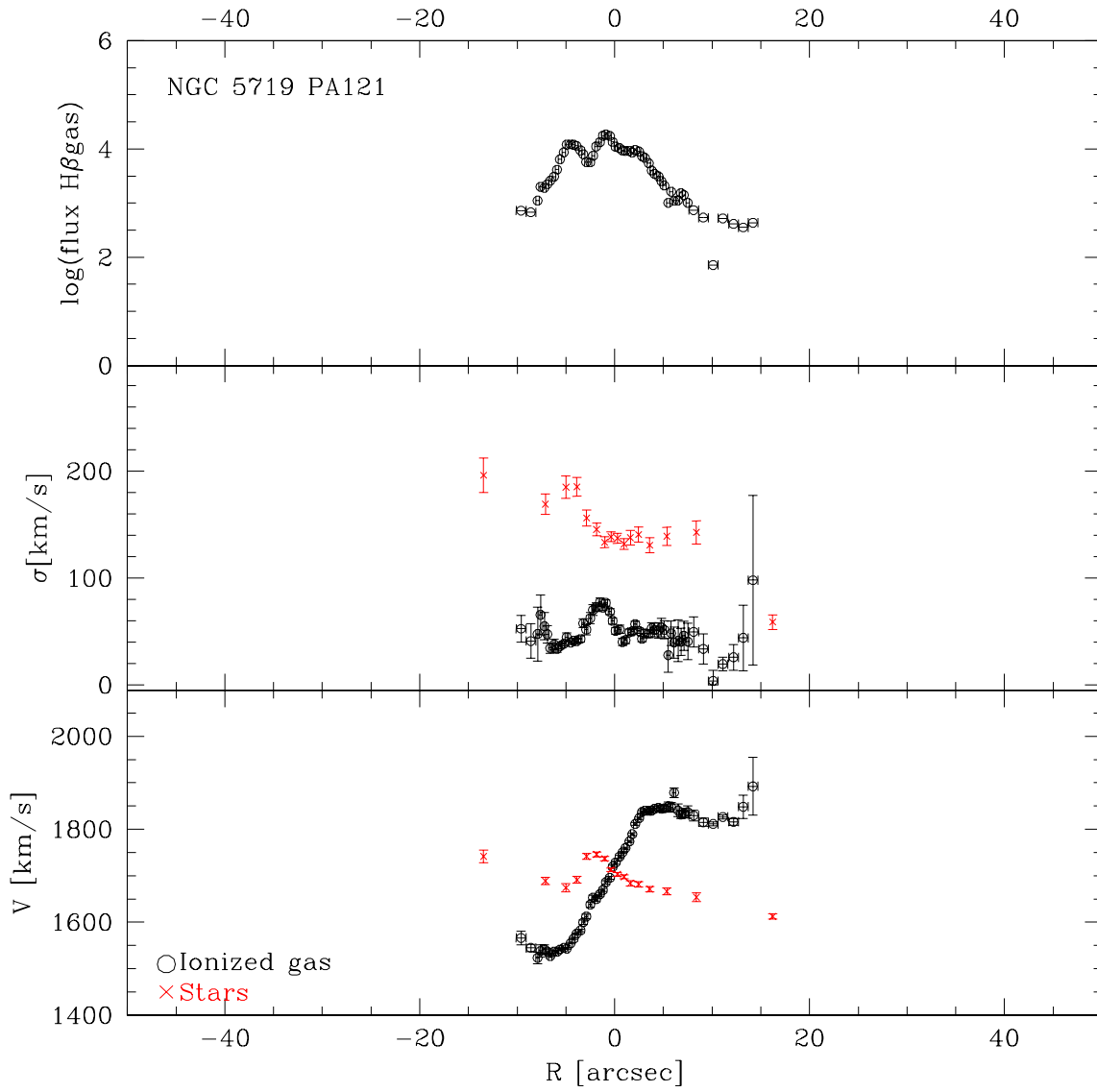


Figure 4.2 Stellar and ionized gas kinematics along the HI major plane ($\approx 121^\circ$) in NGC 5719. The stellar (cross symbols) and ionized gas (circle symbols) kinematics are plotted.

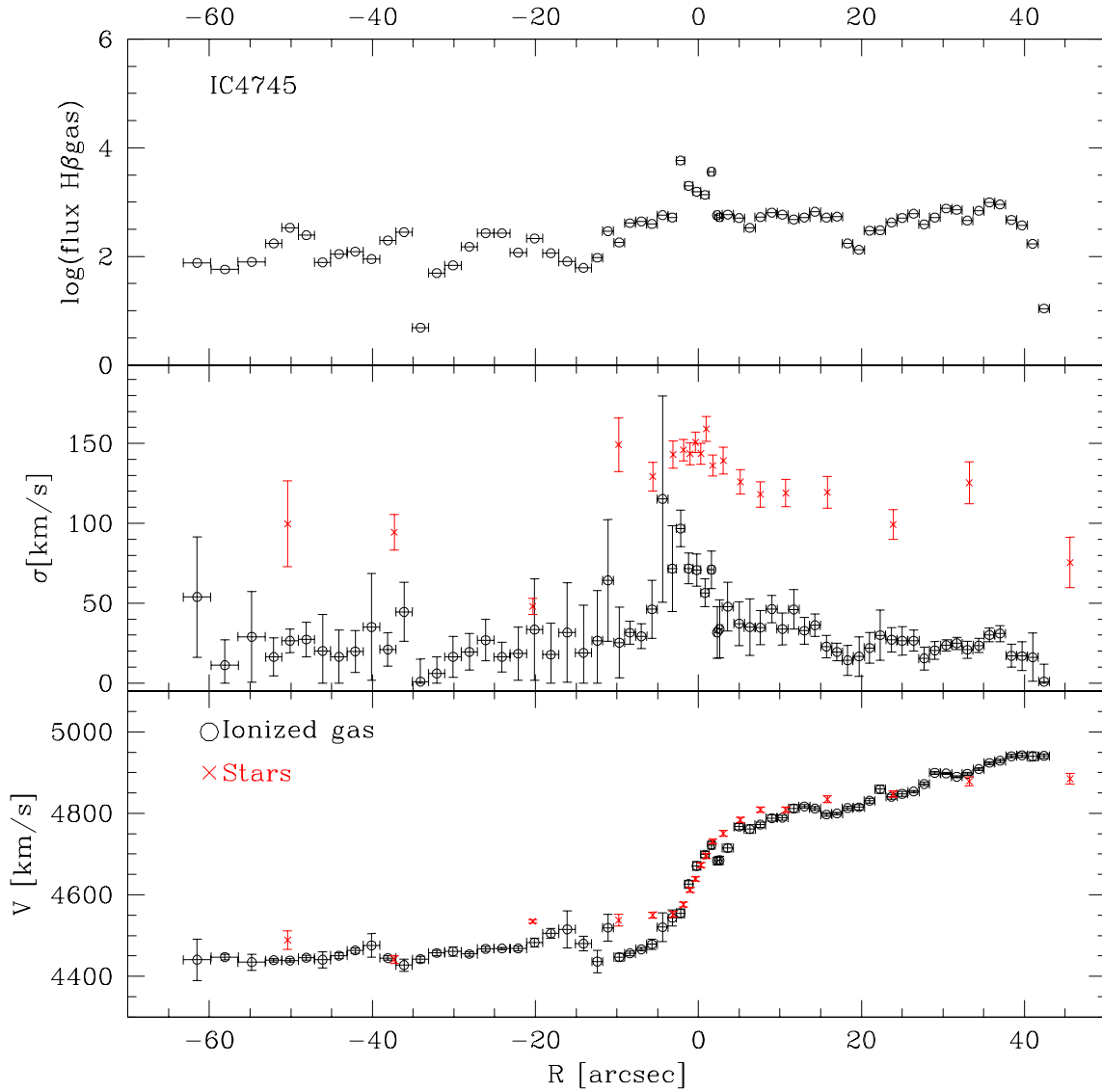


Figure 4.3 Stellar and ionized gas kinematics in IC 4745 along the optical major axis (179°). The stellar (cross symbols) and ionized gas (circle symbols) kinematics are plotted.

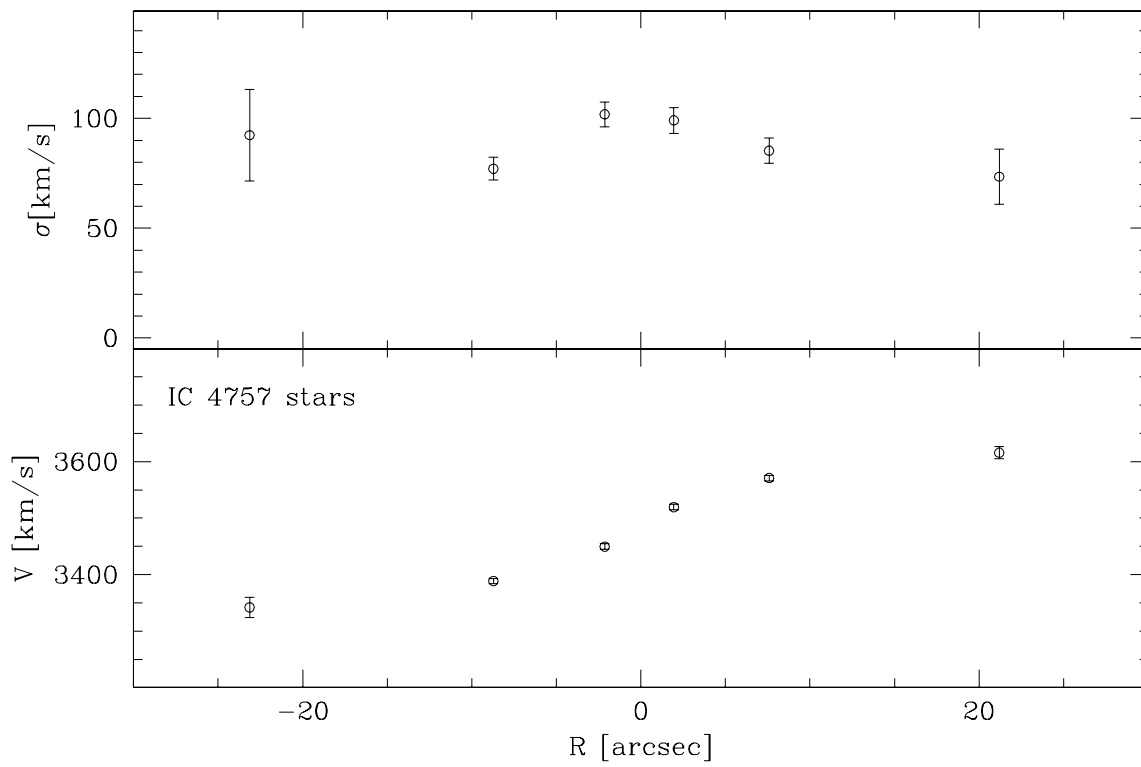


Figure 4.4 Stellar kinematics along the optical major axis (57°) in IC 4757. The stellar (circle symbols) kinematics is plotted.

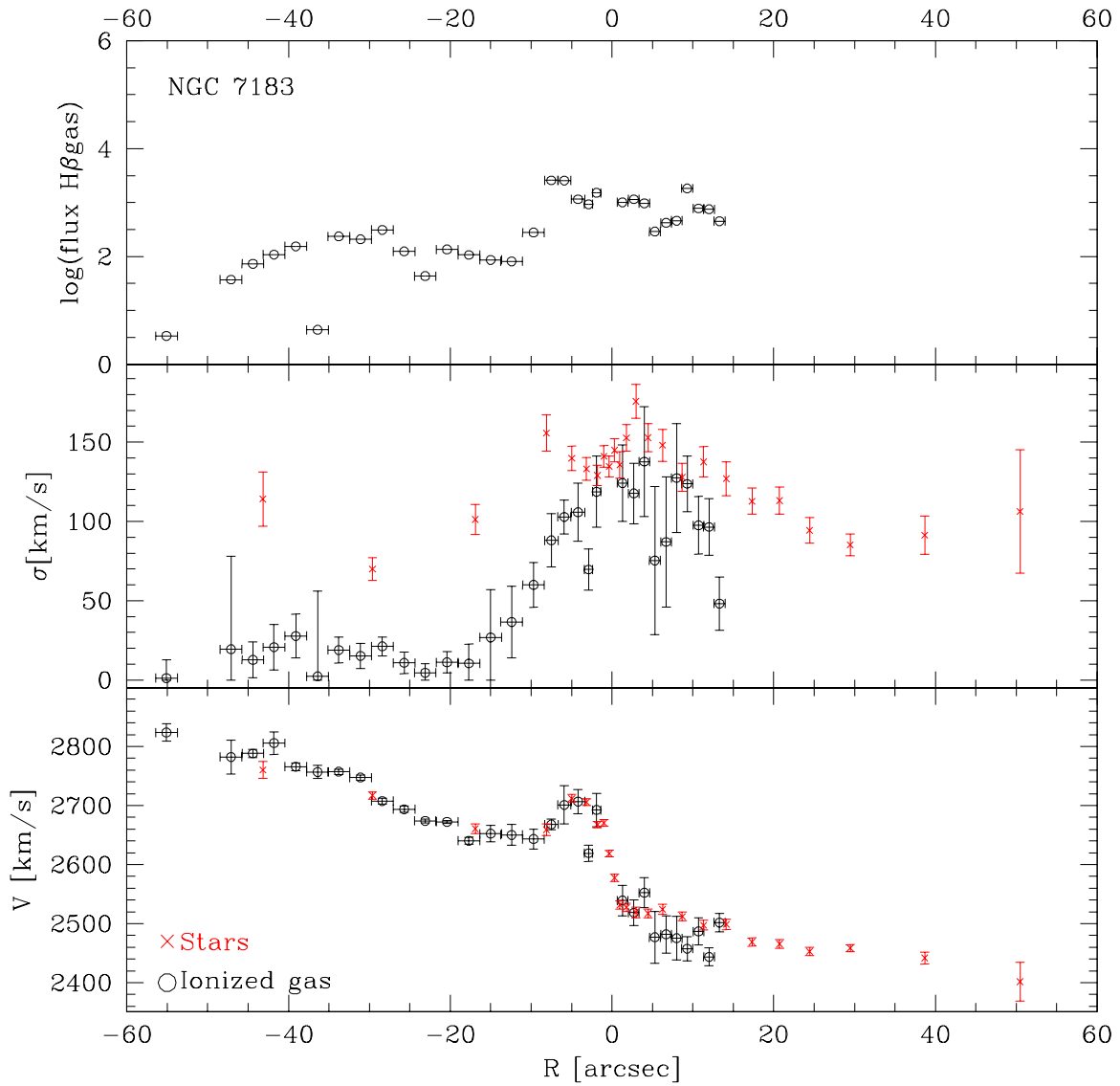


Figure 4.5 Stellar and ionized gas kinematics in NGC 7183 along the optical major axis ($\approx 74^\circ$). The stellar (cross symbols) and ionized gas (circle symbols) kinematics are plotted.

TABLE 2. Log of spectroscopic observations (template stars).

Object	Type	Date	U.T.	Exp. Time
HR 4699		14 Jul 02	23 10	50
HR 4932		14 Jul 02	23 24	40
HR 5196		14 Jul 02	23 32	600
HR 0188		14 Jul 02	10 20	2
HR 0188		14 Jul 02	10 21	1
HR 0188		15 Jul 02	10 26	50
HR 0188		15 Jul 02	10 28	30
HR 0334		14 Jul 02	10 23	2
HR 0334		14 Jul 02	10 24	1
HR 0334		14 Jul 02	10 26	20
HR 0334		14 Jul 02	10 28	30
HR 5370		15 Jul 02	23 51	3
HR 5370		15 Jul 02	23 53	40
HR 5370		15 Jul 02	23 57	160
HR 5315		15 Jul 02	00 01	4
HR 5315		15 Jul 02	00 03	250
HR 5315		15 Jul 02	00 08	110
HR 0489		15 Jul 02	10 20	55
HR 0194		15 Jul 02	10 30	70
HR 0294		15 Jul 02	10 33	85

IC 4745

The gaseous and stellar components extend beyond $40''$ (corresponding to 12 kpc) on the north-western side, on the opposite half the emission is traced further out ($60''$, 18.05 kpc). The velocity dispersion for the stellar component has a peak at around 150 km s^{-1} in the center, and falls back to an averaged value of 80 km s^{-1} on both sides at the last measured point. The velocity dispersion of the gas peaks at 100 km s^{-1} and decreases steeply to 25 km s^{-1} , already near the innermost region ($\approx 15''$).

The velocities on the receding side show a smooth increase up to the last observed point at $45''$ ($\approx 4950 \text{ km s}^{-1}$ or a difference of 300 km s^{-1} from the systemic velocity at 4647 km s^{-1}). On the south-east, approaching half, the velocities have a steeper increase, and stay nearly constant beyond $60''$. The stellar population is slowly rotating with respect to the gaseous component, particularly in the receding half where also the detection is weaker.

IC 4757

In IC 4757, only the stellar component is detected, and extends quite symmetrically on both sides, out to $20''$. The velocity dispersion ranges between 90 km s^{-1} (in the center)

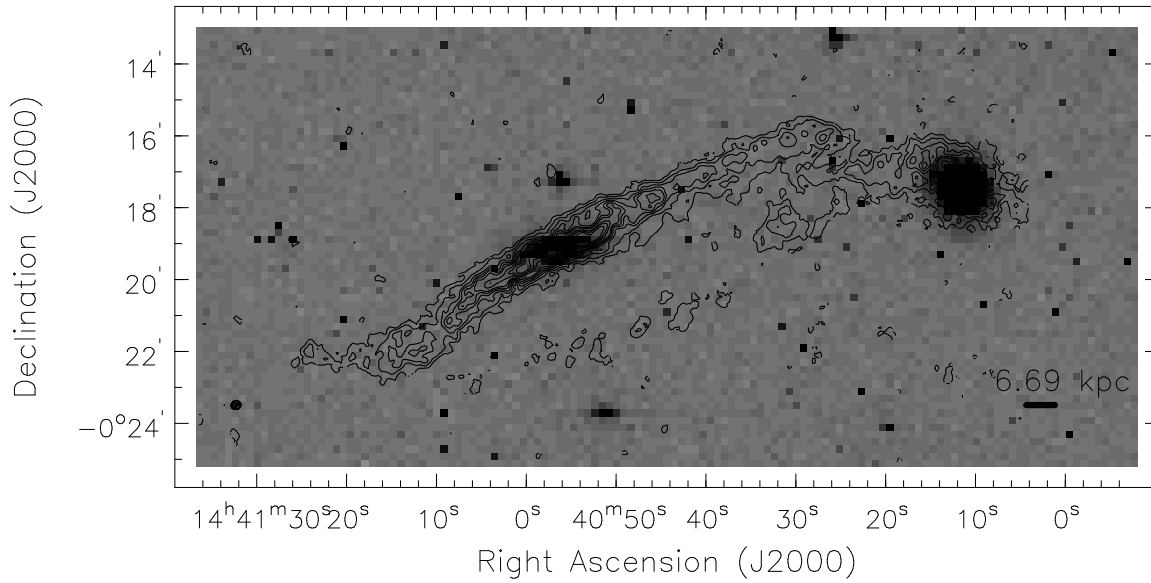


Figure 4.6 Contour representation of the total HI column density distribution of NGC 5719/5713 superimposed on an optical image (DSS). The contour levels are 1.3 (1σ , see text), 2.5, 10 to 20×10^{20} atoms cm^{-2} in steps of 3×10^{19} atoms cm^{-2} . The spatial resolution is $15''.51 \times 14''.09$. $1'$ is ~ 6.69 kpc assuming a distance of 23 Mpc. NGC 5719 belongs to the rich LGG 386 group (30 members). Together with NGC 5713 it forms a binary system as can be well observed in the HI emission.

and 75 km s^{-1} (at the outer radii).

NGC 7183

The kinematics of the stars and gaseous components shows a high degree of asymmetries, and a generally lopsided profile. The systemic velocity adopted for NGC 7183 by using the center of symmetry the gas velocities in the innermost region (within $10''$) is around 1590 km s^{-1} . With respect to this value, the velocities smoothly reach a value of 185 km s^{-1} in the outermost regions. In the inner region, the behavior of the two sides of the rotation curve is very different. Firstly, the emission from the gaseous component ceases at $13''$ on the approaching side, while the receding emission extends out to $60''$. On the same side, the rotation velocities of both stellar and gas contents have a bump at $5''$, beyond this radius the rotation curve is increasing until the last detected point, while on the approaching side, no kink in the emission is observed in the stellar kinematics. The center of rotation for the stellar component lies at higher velocities with respect to the systemic velocity extracted from the gaseous kinematics. The velocity dispersion for the stars peaks at 175 km s^{-1} and decreases to approximately 80 km s^{-1} in the outer regions. On the receding, north-eastern side the velocity dispersion has a range of 130 km s^{-1} in the center and decreases down to 10 km s^{-1} further out.

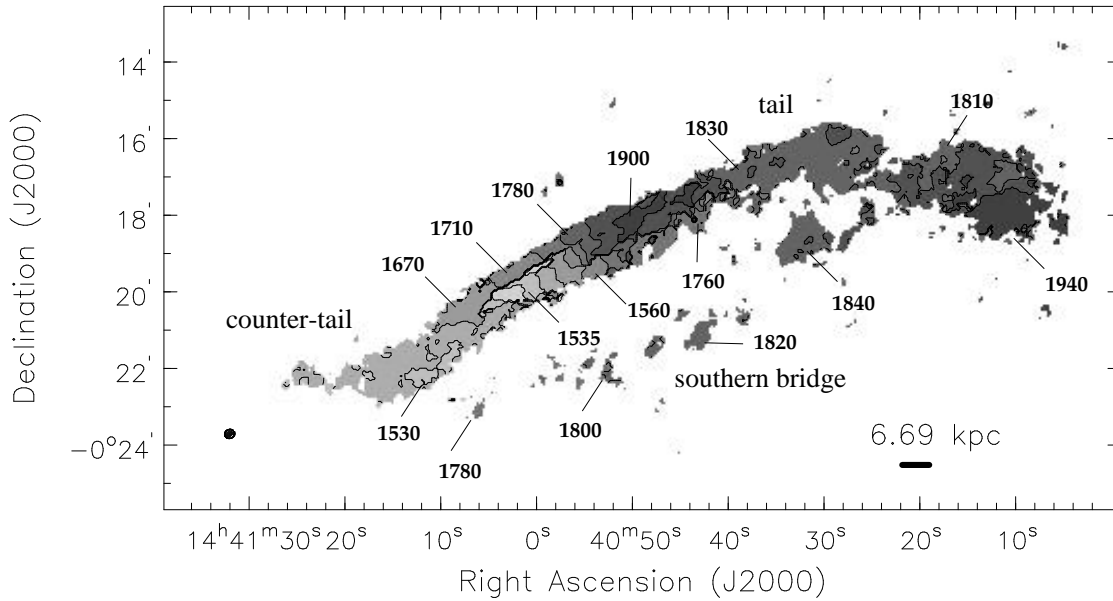


Figure 4.7 Velocity field with contours and gray scales from 1500 km s^{-1} (eastern, approaching side; light shading) to 2000 km s^{-1} (west, receding side; dark shading) in increments of 50 km s^{-1} . The systemic velocity derived from the HI observation has a values of $(1724.99 \pm 7.50) \text{ km s}^{-1}$.

4.3.2 The HI gas morphology and kinematics in NGC 5719

HI moment map

The neutral hydrogen emission is well extended compared to the stellar disk ($R_{\text{HI}}/R_{25} = 2.04$), as it is shown in Fig. 4.6 where the contours of the HI are superimposed on an optical image (DSS). The total HI distribution reaches out to a radius of $8'$ (53.5 kpc) on both sides of the dynamical center of NGC 5719. The orientation of the inner main plane of the HI disk (121°) appears skewed relative to the optical body (96°) and lies along the oblique dust lane tilted by $\approx 20^\circ$ with respect to the optical major axis of the galaxy. In the following we refer to the plane at 121° as the HI major axis.

Between the pair of interacting galaxies a copious tail is seen which connects the north-western edge of the disk in NGC 5719 with the surroundings of NGC 5713. A counter-tail is observed in the south-east of the disk in NGC 5719. At the location of its bending over nearly 180° begins a bridge of low column densities (southern bridge).

Velocity field

The velocity field of the system covers a range between 1550 and 1950 km s^{-1} , approximately (Fig. 4.7). The kinematics of the interacting galaxies is quite complex, and so is the innermost kinematics of the internal disk of NGC 5719.

In the very central disk of NGC 5719 the velocities have a linear increase. Different planes of the HI distribution (or a strong change of the line-of-nodes) projected along the line of sight are observed. This is evident in the copious emission which is rotating at higher velocities in the north-eastern side just above the major plane of the HI emission. This structure creates the *discontinuity* observed in the velocity field starting from

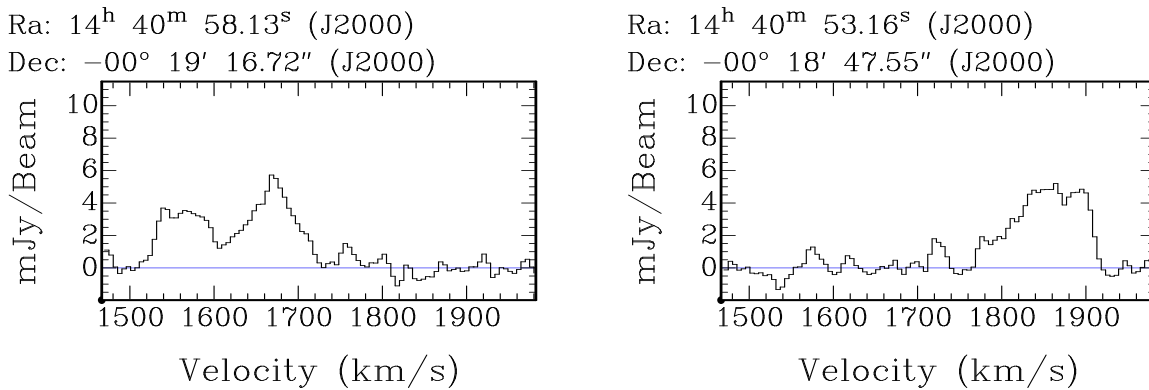


Figure 4.8 HI spectra for the major disk of NGC 5719, on the left the spectra on the eastern side, at $20''$ above the HI major axis. On the right, the spectra of the western region at $40''$ from the center.

the center up to $\approx 3'$ in the southern region. The *discontinuity* in the velocity field is particularly enhanced due to the adopted method which intends to trace the lowest radial velocities on the approaching side and the highest ones on the receding side (or envelope velocities), instead of an intensity weighted mean (1st moment). At the location of the *discontinuity*, the HI spectra show two distinct peaks, as shown in Fig. 4.8a, e.g. at the position RA(J2000) = $14^h 40^m 58^s 13$, DEC(J2000) = $-00^\circ 19' 16''$. At this location, the velocity field computed as envelope velocities assumes a value of $\approx 1550 \text{ km s}^{-1}$. On the opposite side, the spectra assume a complex structure (Fig. 4.8b), and singular peaks are not any more recognizable. Peaks on the south-eastern side have velocities with a larger discrepancy (up to 190 km s^{-1}) from the velocities of the main disk which creates the *discontinuity*. In the north-west, the velocity peaks move away from the velocities of the main disk of smaller values, and the velocity field is seen as a single structure. This behavior indicates a projected emission toward the center, the emission might physically represent a distinct rotating structure or emission at larger radii with tilted orientation.

The most blue-shifted gas content is detected in the base of the southern counter-tail. Starting from this location to the west, the velocities along the bridge increase up to the large HI clouds which connect the tail of NGC 5719 to the body of NGC 5713.

The total HI mass of the system has a value of $7.09 \times 10^9 M_\odot$. The emission from the bridge (including the large HI clouds between NGC 5719 and NGC 5713) has a mass of $7.71 \times 10^8 M_\odot$, but the separation between the main disk and the bridge is not clearly defined.

Position-velocity diagram

The position-velocity diagram along the optical major axis reveals several structures with complex kinematics (Fig. 4.9). The main HI distribution rotates on both sides up to $1' - 1.5'$. Peculiar emission is observed in the range between 1720 km s^{-1} and 1775 km s^{-1} at a radius around $1.5'$. This peculiar structure which appears in projection in the forbidden quadrant, points towards the emission from NGC 5713 at a much further distance ($12'$, 1925 km s^{-1}). This detected structure is rotating on a different plane in between the optical and HI main disk at an estimated position angle of $\approx 104^\circ$, and it is responsible of the *discontinuity* in the velocity field.

The position-velocity diagram along the major axis of the HI emission is shown in

Fig. 4.9. HI emission is detected up to $3'$, but emission is observed further out, rotating with slower line-of-sight velocities, like the weaker emission at approaching velocities (around 1650 km s^{-1}) between $2'$ and $6'$. The rotation curve is computed using the Warped Modified Envelope Tracing method (Sect. 5.3) toward the major plane of the neutral hydrogen and is superimposed to the diagram (Fig. 4.9). The HI dynamical center is assumed at $\text{RA}(J2000) = +14^{\text{h}} 40^{\text{m}} 56^{\text{s}}.40$, $\text{DEC}(J2000) = -00^{\circ} 19' 10''.2$. The line-of-nodes of the HI disk traced as peak intensity changes with radius, starting from the internal major axis (121°) up to 124° in the north and down to 119° in the south. The systemic velocity is found at $(1724.99 \pm 7.50) \text{ km s}^{-1}$.

Channel maps

The channel maps of the pair of galaxies are presented in two different forms due to the large angular separations. The innermost emission from the disk of NGC 5719 is presented separately in Fig. 4.10. In Fig. 2.12 the entire emission from NGC 5719 and NGC 5713 is plotted.

4.4 Discussion

We have presented optical long-slit observations of a sample of four galaxies with thick box/peanut bulges.

In one of the four systems we detected stellar and gas counter-rotation: In NGC 5719, the gaseous component is counter-rotating with respect to the primary stellar content. A secondary system of stars might be deduced from two considerations. Firstly, it can be inferred from the behavior of the rotation velocities. The rotation curve for the stars has a depression between $5''$ and $15''$, which indicates that the amplitude of the resulting profile is the sum of two different structures. The resulting sum is nearly zero, thus the velocities lie around the systemic one. Secondly, the velocity dispersion of the stars is extremely large in the regions between $5''$ to $15''$.

The primary population of stars which is counter-rotating with the gaseous component might originate from the newly acquired material. In this hypothesis, the gas funneled towards the center, finally settled into stable orbits and began to form stars (secondary stellar population). Otherwise, the primary population of stars belongs to a further accreted small system, already disrupted and no longer visible which has reached the innermost region of NGC 5719. The question whether the on-going merger observed in the HI emission is responsible for funneling the gas towards the nucleus or whether previous accretion events could account for the central counter-rotating stellar disk and finally for the newly secondary stellar population is still un-answered.

It is plausible to sketch a scenario in which the neutral hydrogen retains longer 'memories' of the orientation of an accretion event due to its larger extent. Thus it is most affected by interactions, and more dynamical time is requested to resettle the gas into stable orbits at larger radii. Several planes of rotating gaseous components are detected, thus the accretion starts at a time larger than at least two galactic rotation periods. The stars settled very fast in the center, and the rotation curve of the primary stellar component is well settled and regular in the outer regions. It has lost the 'memories' of previous interactions and the only clue is the decoupled orientation of the rotation. The oldest stellar component traced with the near-infrared reveals, however, a tilted surface distribution, which might suggest older disturbances.

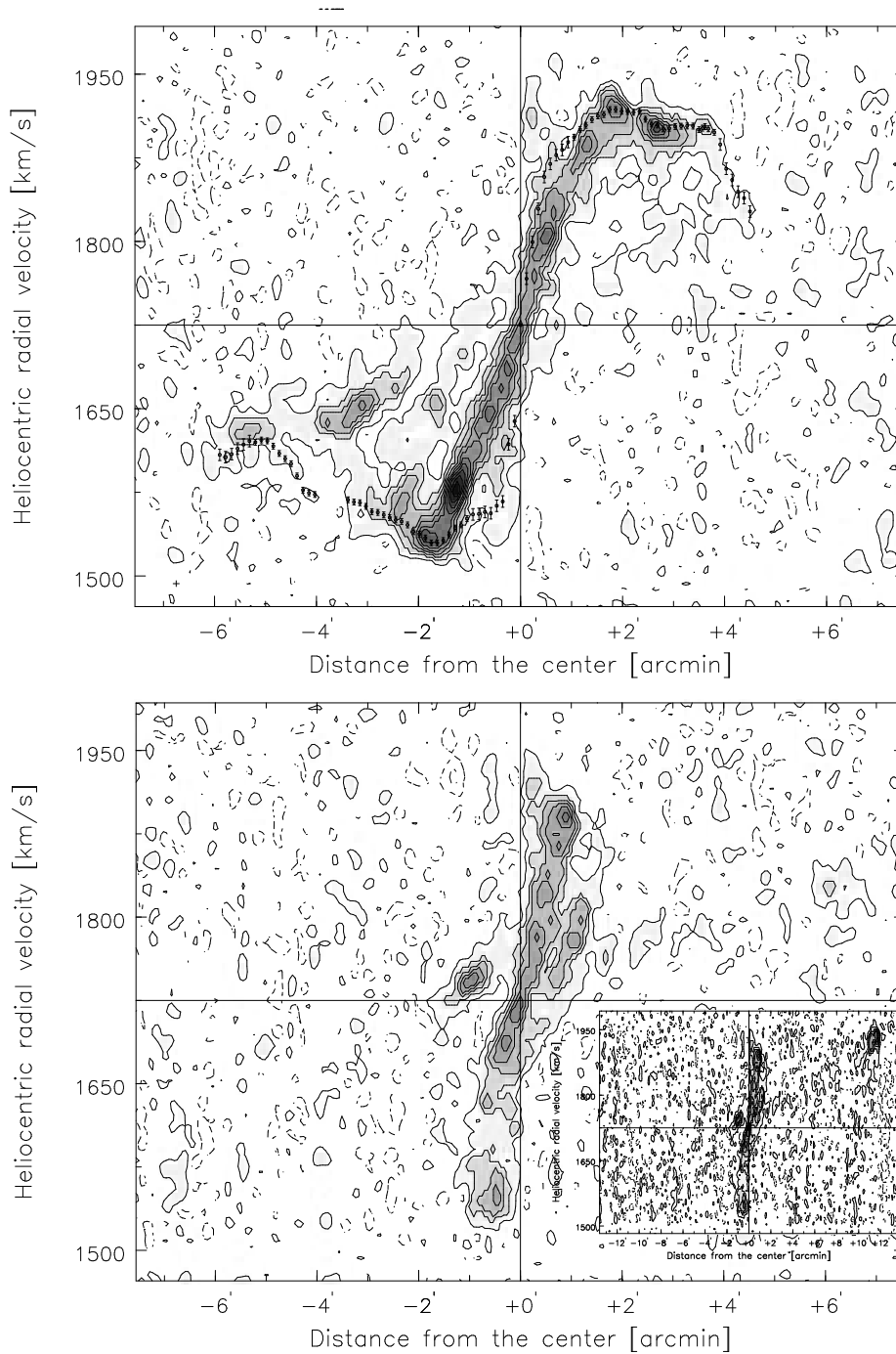


Figure 4.9 (*Top*) Position-velocity diagram obtained from the HI data cube taken along the HI major axis (121°) of NGC 5719. The dots represent the unaveraged rotation curve. The horizontal line indicates the systemic velocity (1724.99 ± 7.50). The contour levels are at -3, -1.5 (dashed) and from 1.5 ($\approx 1.34 \text{ mJy beam}^{-1}$) to 27σ in steps of 1.5σ . The angular and velocity resolutions are $15' \times 5.4 \text{ km s}^{-1}$ (as indicated at the bottom left of the panel). (*Bottom*) Position-velocity diagram along the optical major axis ($\approx 97^\circ$) of NGC 5719. In the bottom right, the equal diagram is plotted with larger angular resolution to enhanced the emission from NGC 5713 on the receding side at $12'$ from the center of NGC 5719.

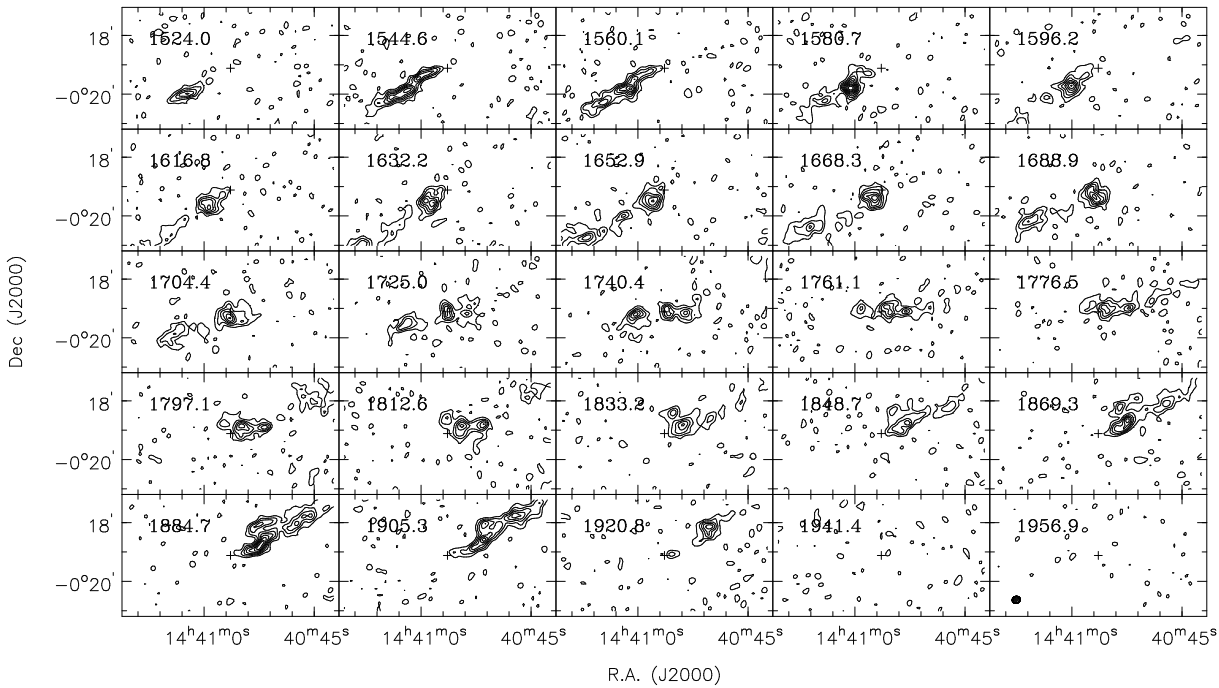


Figure 4.10 Channel maps of the observations in the innermost region of NGC 5719. The systemic velocity is at 991.65 km s^{-1} . The contour levels are at -3 , -1.5 (dashed) and from 1.5 ($\approx 1.34 \text{ mJy beam}^{-1}$) to 27σ in steps of 1.5σ . The angular and velocity resolutions are $\approx 15'' \times 15.5 \text{ km s}^{-1}$.

IC 4745, the kinematics of the stars agrees very well with the rotation of the neutral hydrogen at receding velocities. In the approaching side the stars have slower rotation with respect to the gas, and the shape of the rotation curve is fairly lopsided. The neutral hydrogen presents on the same side a long warped tail beyond a radius of $3'5$. It is likely that a source of disturbances could have influenced the internal kinematics as well as the large-scale kinematics traced by the neutral hydrogen.

IC 4757 is a quite gas-poor system. Ionized gas is not detected in the present observations, and the neutral gas shows as well a peculiar HI morphology and kinematics. In fact, clumps and a one-sided HI distribution characterize IC 4757. The HI rotation curve also presents peculiarities between the approaching and receding sides, while the stellar rotation curve is very symmetric. The origin of the gaseous components in IC 4757 is likely external.

In NGC 7183, one side of the optical position-velocity diagram shows a peaked distribution. At the same location, the kinematics of the stellar component reveals lopsided properties and a possible signature of bar structure. The HI properties resemble those of IC 4745, but with a shorter tail of the distribution on the south-western, approaching side.

Finally, the four galaxies show peculiar kinematics and a generally overall unsettled scenario. In one case, we detect stellar-stellar counter-rotation which increases the num-

ber of these known systems to five.

4.5 Conclusion

Long-slit spectroscopic observations are presented for four target galaxies with thick box/peanut bulges. Stellar and gas kinematics are compared with HI 21-cm observations. In particular, the case of the galaxy NGC 5719 in the interacting systems with NGC 5713 is discussed. This interacting pair is connected by a copious, gas bridge. There is no stellar counterpart in the tail and star formation might be ongoing. HI complexes are detected toward the central regions of NGC 5719 deriving likely from non coplanar rotation (warped distribution in the outer regions). In NGC 5719 counter-rotating stellar disks are detected in the innermost region. The fraction of peculiarities are quite high and interaction events could seriously affect the kinematics of these galaxies.

References

- Bender R., 1990, *A&A* 229, 441
- Bender R., Saglia R.P., Gerhard O.E., 1994, *MNRAS* 269, 785
- Bertola F., Cinzano P., Corsini E.M., 1996, *ApJ* 458, L67
- Jore K.P., Broeils A.H., Haynes M.P., 1996, *AJ* 112, 438
- Garcia A.M., 1993, *A&AS* 100, 47
- García-Ruiz I., 2001, Ph.D. thesis, Univ. Groningen, The Netherlands
- Haynes, M.P., van Zee L., Hogg D.E., Roberts M.S., Maddalena R.J., 1998, *AJ* 115, 62
- Lacey C., Cole S., 1993, *MNRAS* 262, 627L
- Merrifield M.R., Kuijken K., 1994, *ApJ* 432, 575
- Miwa T., Noguchi M., 1998, *ApJ* 499, 149
- Mihos J.C., Walker I.R., Hernquist L., Mendes de Oliveira C., Bolte M., 1995, *ApJ* 447, 87
- Pfenniger D., 1993, *IAU Symposium* 153, H. Dejonghe & H.J. Habing eds., Kluwer, Dordrecht, p. 387
- Reshetnikov V., Battaner E., Combes F., Jiménez-Vicente J., 2002, *A&A* 382, 513
- Richter O.-G., Sancisi R., 1994, *A&A* 290, 9
- Rix H., Franx M., Fisher D., & Illingworth G., 1992, *ApJ* 400, L5
- Rubin V.C., Graham J.A., & Kenney J.D.P., 1992, *ApJ* 394, L9
- Schoenmakers R.H.M., 1999, Ph.D. thesis, University of Groningen, The Netherlands
- Swaters R.A., Schoenmakers R.H.M., Sancisi R., van Albada T.S., 1999, *MNRAS* 304, 330
- Walker I.R., Mihos J.C., Hernquist L., 1996, *ApJ* 460, 121

5

Rotation Curves in Edge-On Systems

The main input to our study originates in rotation curves from which the mass and the kinematic differences between the two sides of a galaxy are derived. It is therefore essential to find the most reliable and accurate method to obtain the rotation curve from our HI data.

The procedure to derive the rotation curve from highly inclined galaxies is far from being simple. It gives rise to severe underestimates of the velocities if conducted with a classical approach. This is principally – in highly inclined galaxies – because of the integration along the line-of-sight of a large portion of the disk. Nevertheless, this investigation has to be performed in edge-on systems since our final goal is to investigate the box/peanut component, which is a vertical structure observable only in such inclined galaxies.

5.1 Rotation velocity measurements and observational problems

Rotation curves from spiral galaxies have been used as kinematic tracers and for inferring the role of the interaction events since the beginning of corresponding observational programs (e.g. Pease 1918, Babcock 1939, Mayall 1951, Oort 1940, Burbidge & Burbidge 1960). In particular, the HI 21-cm line is a favorite tool due to the large radial extent of atomic hydrogen, often exceeding the stellar component.

Rotation curves from 21-cm observations have been often derived using the tilted-ring method (Rogstad et al. 1974, Begeman 1987). This method assumes the galaxy to be composed of several concentric rings. Each ring is characterized by the following quantities: the circular velocity (v_c), the HI surface density (Σ_{HI}), the inclination (i), the position angle (ϕ), the center (x_0, y_0) and the systemic velocity (v_{sys}). The parameters are typically left free in the first iteration and subsequently fixed (usually starting with the center coordinates and the systemic velocity).

Note that the inclination and the circular velocities are closely coupled as the velocities are measured along the line-of-sight, v_{los} , from the velocity field¹.

The derived quantity is always the product of the two parameters: $v_{\text{los}} = v_c \times \sin(i)$. In nearly face-on galaxies ($i < 40^\circ$), this method provides accurate rotation curves disen-

¹The velocity field (spider diagram, butterfly diagram) of a spiral galaxy consists of velocity measurements of a rotating disk. In a planar, circular, rotating disk tilted by an angle i to the line-of-sight, the major axis of the projected ellipse is the line-of-nodes, and the isovelocity contours of v_{los} generate the velocity field.

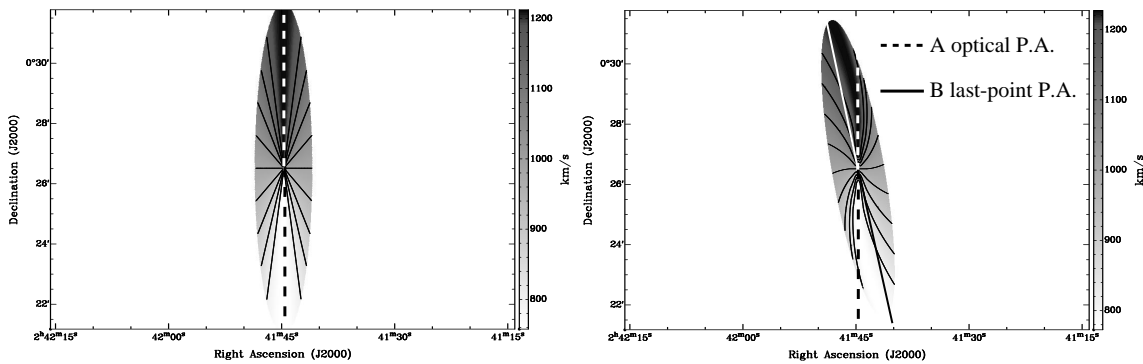


Figure 5.1 (*Left*) A velocity field of an unwarped disk galaxy. The dashed line represents the kinematic major axis which coincides with the optical major axis as derived from photometry. (*Right*) A velocity field of a warped ($r > 1R_{opt}$) disk galaxy. The dashed line (A) is aligned with the optical unwarped major axis ($r < 1R_{opt}$) and does no longer represent the kinematic major axis. The solid line (B) aligns with the position angle of the last observed point.

tangled from the inclination effects when high accuracies in the radial velocity field are provided (Begeman 1987). If this accuracy cannot be achieved, kinematic studies are preferentially performed on nearly edge-on galaxies where the $\sin(i)$ does not dramatically affect the results or even in cases of perfect edge-on orientations ($\sin(i) = 1$) when all the difficulties related to the de-projection can be avoided.

The advantage of the tilted-ring method is to determine several kinematic parameters from initially estimated values through an iterative fit to the velocity field. This method is most effective for galaxies mapped with sufficiently high spatial resolutions. Often, however, the combination of edge-on orientation ($75^\circ - 90^\circ$), intermediate angular resolution, and small angular size of a galaxy yields a poor sampling in every ring of the model, and results with low reliability are produced.

In edge-on galaxies we are faced with several difficulties. The fact that a finite beam intercepts a large portion of the disk (beam smearing), the effects of the inclination, and peculiarities of the galaxies are all inconveniences that produce a tail of the distribution in the velocity profiles at lower velocities toward the systemic velocity. Taking advantage of the improving sensitivities of telescopes, an increasing number of systems with extra-planar emission is now found in the literature (e.g. NGC 891, NGC 2403 and NGC 6946). In addition to the instrumental broadening and the projection effects of the inclination, also this extra-planar emission which slowly rotates with respect to the main disk contributes to the contamination of the velocity profiles. It produces a wing just in the direction of the lower velocities (with respect to the systemic velocity). As a result, the velocity field – on which the fitting of the tilted-ring method is performed – and the rotation curve have shallower gradients. Neither the velocity fields derived as intensity-weighted velocities (Warner et al. 1973) nor the ones determined from a fit of a single-peaked Gaussian to the velocity profiles provide good estimates for the kinematics, at least in highly inclined galaxies.

Instead of using the velocity field, the rotation curve can also be extracted as fit to the

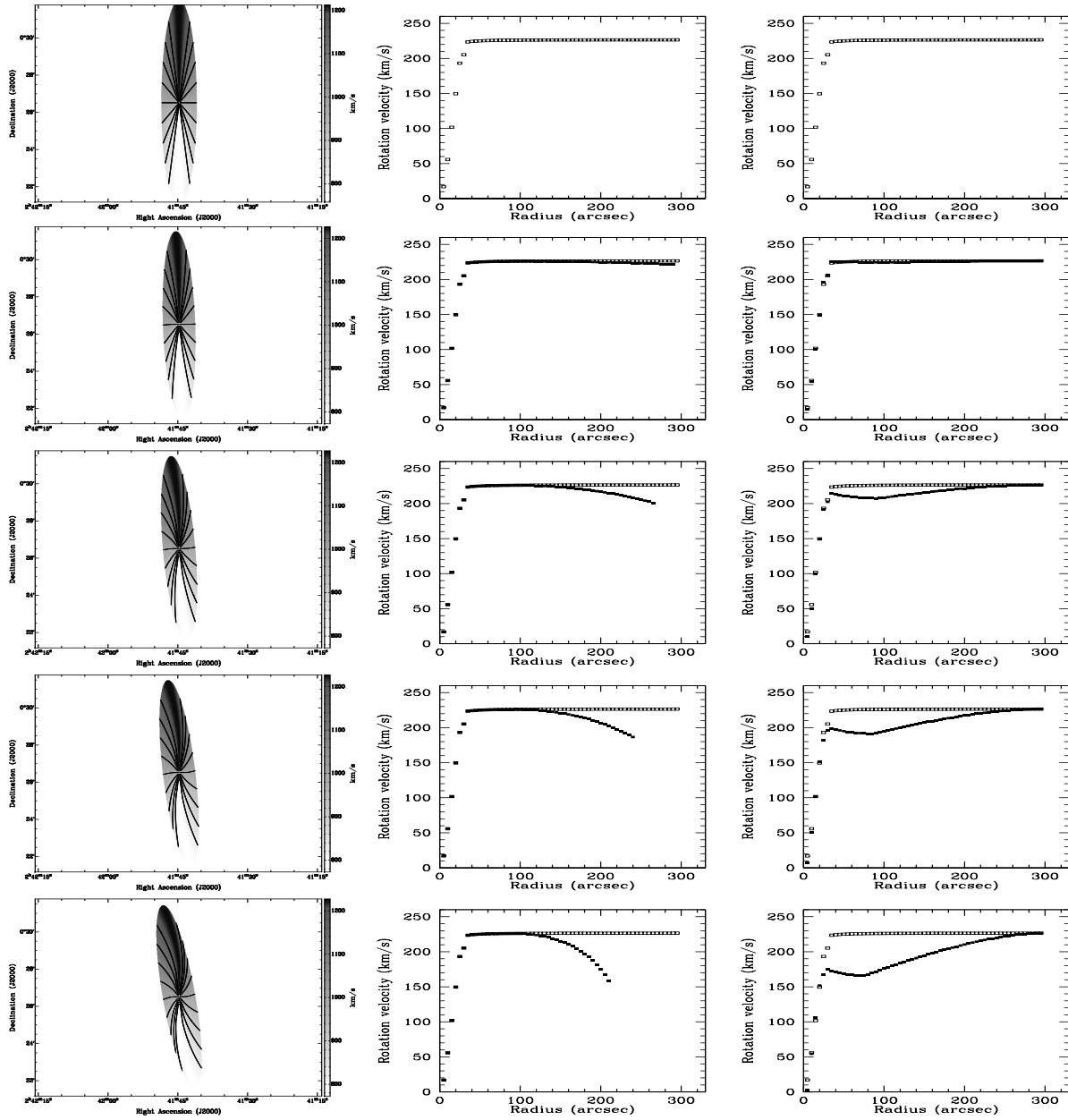


Figure 5.2 Models of unwarped, mildly warped (2°) up to strongly warped (5° , 7° , and 10°) velocity fields (left panels, from top to bottom), and the resulting rotation curves (filled squares) as extracted from two different angles of the position-velocity diagram: in the central panels derived along the optical major axis (line A in Fig. 5.1), and in the right panels taken from the position angle of the extreme edge of the warped emission (line B in Fig. 5.1). The open squares represent the true rotation curves traced along the ridge-line.

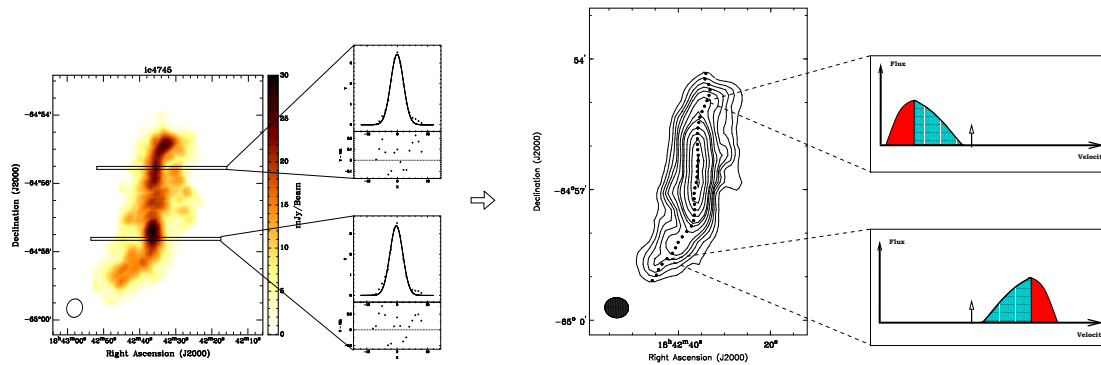


Figure 5.3 A new approach to extract the rotation curve could be used in warped and highly inclined galaxies which takes into account the variation of the line-of-nodes in these systems.

velocity profiles on the major axis of the galaxies (position-velocity diagram²).

The radial velocities are those values at which the surface brightness in the position-velocity diagram reaches a certain value of the maximum – defined and corrected in different ways depending on the adopted method (peak-intensity velocities by Mathewson et al. 1992, Mathewson & Ford 1996; envelope velocities by Sofue 1996, Olling 1996). Otherwise, as outlined in Sancisi & Allen (1979) rotational velocities are given by the lowest radial velocities on the approaching side and by the highest ones on the receding side, after having corrected for the instrumental broadening and random motions.

The disadvantages of using the position-velocity diagram for the extraction of rotation velocities become important when a warped system has to be investigated. Unfortunately, the position-velocity diagram contains kinematic information along a fixed position-angle, while in warped systems the line-of-nodes and hence the kinematic axis are changing with radius.

For a complete review on alternative methods to extract the rotation curves see Sofue & Rubin (2001) and references therein.

5.2 Warping effects on the rotation curve

The phenomenon of warping is quite common both in the HI distribution (Bosma 1991) and at optical wavelengths (Briggs 1990). According to general understanding, at least 50% of all spiral galaxies present warped systems. Taking into account geometrical factors (e.g. a warp is not detectable when the line-of-nodes lies close to the line-of-sight) several authors claim that even all galaxies possess warps.

²The position-velocity diagram is a two-dimensional slice drawn along an axis of a galaxy which represents the density of projected material as a function of the line-of-sight velocity, v_{los} , and projected position. A typical application of the position-velocity diagram is to take slices along the major axis of a rotating galaxy in order to obtain information on the kinematics in the galactic disk.

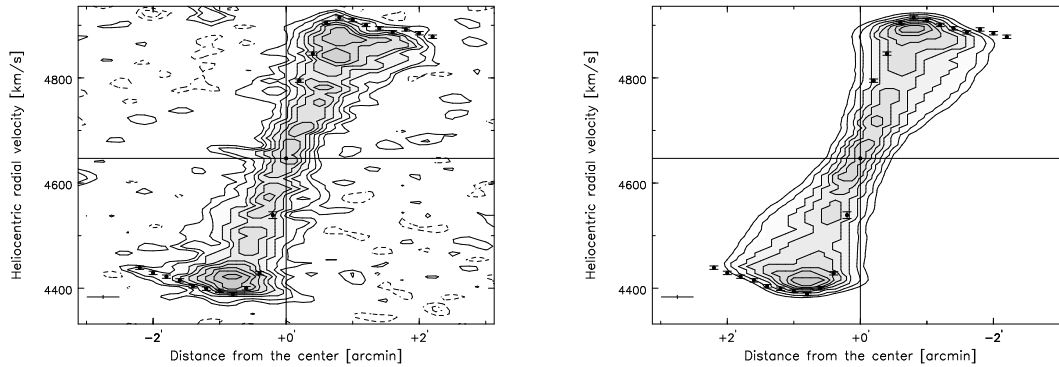


Figure 5.4 Position-velocity diagram taken along the major axis, for the observations (left) and for the synthetic data (right) of IC 4745. The contour levels are at -4 (dashed), -2 , and from 2 (1.6σ) to 17 mJy beam^{-1} in steps of $2.5 \text{ mJy beam}^{-1}$. The grey-scale ranges from 1.0 to $19.0 \text{ mJy beam}^{-1}$ in steps of $0.5 \text{ mJy beam}^{-1}$. The horizontal line indicates the systemic velocity. The x -axis indicates arcminutes from the dynamical center.

In order to investigate the effects of a variation of the line-of-nodes in the disk of a galaxy on the extraction of the rotation curve we have developed simple models of velocity fields. In these synthetic velocity fields the total extent of the emission reaches $3 R_{opt}$. Usually, the warping starts around the edge of the optical disk ($\approx 1 R_{opt}$, Briggs 1993). This situation has been reproduced by keeping constant the position angle in the innermost ($< 1 R_{opt}$) region. Moving from the inner region towards the outskirts, an increasing linear variation of the position angle ranging from $1 R_{opt}$ up to $3 R_{opt}$ was applied.

The input coordinates for building the synthetic velocity field were taken from the observations of NGC 1055. The systemic velocity is fixed to 1000 km s^{-1} for simplicity. The rotation curve is composed of averaged values taken from the sample presented in Ch. 2 with a steep increase toward a maximum and a constant value beyond. The assigned inner position angle is 0° . The rotation velocities were derived as envelope velocities from the position-velocity diagram.

Two extreme cases have been simulated:

- The rotation curve was extracted from the position-velocity diagram taken along the position angle determined from the optical photometric images, i.e. the optical major axis (line A in Fig. 5.1).
- The rotation curve was extracted from the position-velocity diagram taken along the position angle of the extreme edges of the warped emission (line B in Fig. 5.1).

In each of these two extremes the warp effect for four different situations was simulated: no warp and four different angles of the line-of-nodes in the velocity field of 2° (mild warp), 5° , 7° , and 10° (strong warp) starting from $1 R_{opt}$ up to $3 R_{opt}$. The resulting rotation curves are reported in Fig. 5.2.

Despite the naive model it is clearly noticeable that in a rotation curve extracted along a fixed (optical, A) axis of a warped galaxy the distance out to which the rotation curve can be traced is underestimated. This is because the emission at the outer radii starts to deviate from the major plane (Fig. 5.2, middle panels). Moreover, in both cases of the

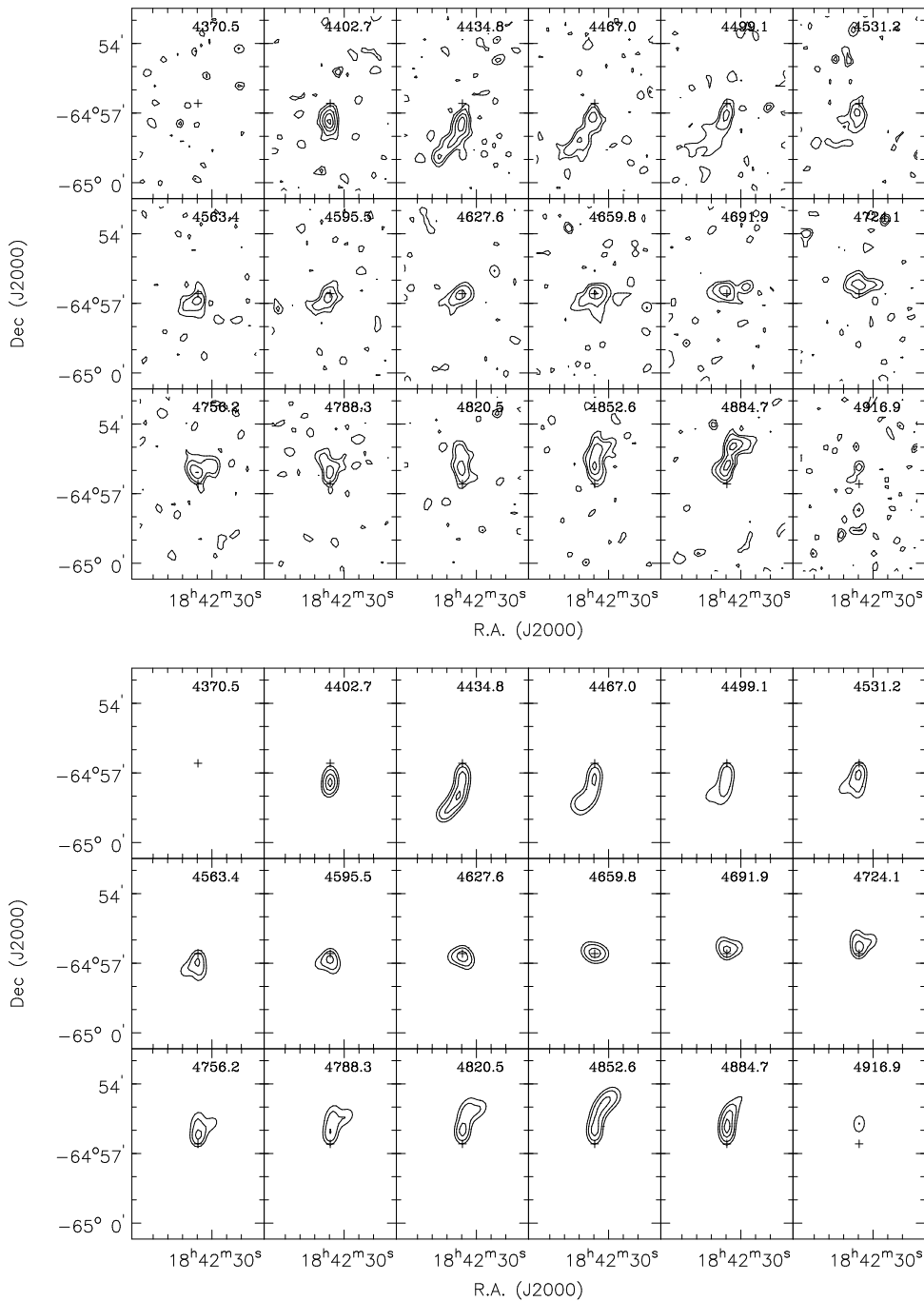


Figure 5.5 Channel maps for the observations (left), and for the synthetic data (right) of IC 4745. Contours are at -5.2 (dashed), -2.6 , 2.6 (2.1σ), 5.2 , 8.7 , 12.2 , 15.7 , 19.2 mJy beam^{-1} . The channel velocity is given in each panel. The size of the synthesized beam is indicated by the ellipse in the lower left-hand corner of the last map. The cross represents the dynamical center.

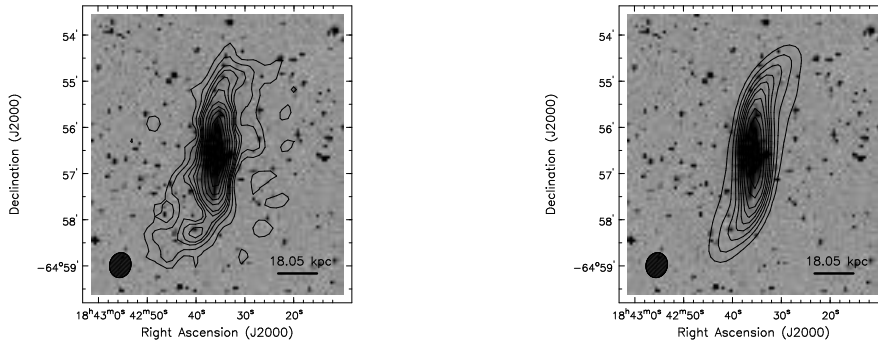


Figure 5.6 The total HI column density distribution superimposed on an optical image (DSS) for the observations (left), and for the synthetic data (right) of IC 4745. The contour levels are 0.5, 1, 1.5, 1.8, 2.2, 2.6 to 13.8×10^{20} atoms cm^{-2} in steps of 0.8×10^{20} atoms cm^{-2} , and from 20 to 44 in steps of 6×10^{20} atoms cm^{-2} . The spatial resolution is $32''/67 \times 27''/64$.

optical (A) major axis and extremely warped (B) major axis also the velocities are underestimated. In particular, this can be seen in the external region in the former case (Fig. 5.2, middle panels), and in the inner region in the latter case (Fig. 5.2, right panels). This is important as underestimated velocities in the external region can yield underestimated values of the dynamical mass included out to the last observed point. Also in the internal region a wrong mass distribution can be calculated assuming unrealistic velocities. As expected, the effects are more severe for larger warps (from top to bottom in Fig. 5.2). For larger warps the rotation velocities are underestimated up to $\approx 10\%$ of the maximum rotation velocity ($\approx 220 \text{ km s}^{-1}$), and the last observed point of $0.2 R_{opt}$. These values depend on the geometry of the galaxy.

Further problems are anticipated in the case of asymmetric warped distributions (i.e. U-shaped or L-shaped warped distribution). Asymmetric warps are quite common, it is estimated that they represent some 30% to 50% of all warped galaxies. Rotation curves estimated from an asymmetric warped distribution can have underestimated values only on the approaching or receding side of the galaxy (the side which is more affected by the morphological asymmetry). If so, by comparing the approaching and receding sides of such a rotation curve the kinematic lopsidedness – which reflects the differences between the two halves of the rotation curve – is overestimated. Cases of morphological disturbances in galaxies with regular kinematics are well-known, there are in fact indications that the morphological and kinematic lopsidedness are not coupled.

In warped systems the kinematic major axis is neither the main optical major axis nor the major axis of the last observable point, but rather a *flexible* axis. This is generally a limit in optical slit-spectroscopy in which the slit is often oriented a priori along the major axis determined from photometry. Nevertheless, this limit is not so severe, due to the fact that often the distribution of the stellar contents deviate only at the end of the optical body. However, in the case of HI, which extends far beyond the optical body where self-gravity is weaker and warping more pronounced, this represents a severe effect to be considered in the procedure when extracting rotation curves. The analysis could be limited to the region which is not affected by the warp, which would, however, lead to a considerable loss of information in a tracer like neutral hydrogen which is instrumental for the inves-

tigations on large scale. The 21-cm line has been used extensively as a kinematic tracer of the galactic potential of spiral galaxies. Indeed, its extent exceeding the stellar body is one of the main motivations for its use.

In order to overcome most of the disadvantages and to extract the maximum information out of the HI observations, a new approach to determine the rotation curve should be used in warped and highly inclined galaxies which takes into account the variation of the line-of-nodes in these systems.

5.3 A new approach: Warped Modified Envelope Tracing

In order to account for the effects of warped distributions we propose an improved tool to obtain the rotation velocities in edge-on, warped galaxies observed at moderate resolutions.

5.3.1 Outline of the method

We proceed as follows:

- 1) We determine the angle of the internal major axis from the central channels, which is very often aligned with the orientation of the largest extension in optical images. Channel maps with equal rotation velocities with respect to the systemic velocity are displayed in the same panel. The inner major axis coincides with the line which links the approaching with the receding peaks of the surface brightness in the channel maps. We rotate the galaxy to this axis around the assumed center as explained in Sect. 2.3.1.
- 2) We sample the HI integrated map in strips of half-a-beam along and parallel to the minor axis. Using a χ^2 -minimization we find in every strip the displacement with respect to the internal major axis of the peak intensity by fitting a Gaussian distribution. The ridge of the warp is determined by a fit to the density distribution down to 3σ in the HI total intensity distribution, as outlined by García-Ruiz (2001), and García-Ruiz et al. (2002). The ability to follow the ridge line (positions of maximum intensity) makes it possible to determine the amplitude of warping as a function of distance from the center (Bottema 1995).
- 3) With this spatial information we extract the velocity profiles along the ridge line where the velocities are likely tangential to the line-of-sight which represents the maximum rotation velocity at each radius. The velocity profiles are first corrected for instrumental broadening, then for the turbulence of the interstellar medium due to random motions which contributes to broaden the velocity profiles.

The systemic velocity, v_{sys} , is defined as the value which minimizes the asymmetries in the position-velocity diagram. With respect to this velocity, the approaching and the receding emission are mirror-symmetric.

Recent works have reported a range of typical values for turbulence of the interstellar medium between 10 and 13 km s^{-1} in the inner region which decreases to some 6 or 8 km s^{-1} at larger radii from the center (e.g. Kamphuis 1993). We use an average value ($\sigma_{\text{ISM}} = 10 \text{ km s}^{-1}$) of the velocity dispersion in the HI layer in spirals to correct for this effect.

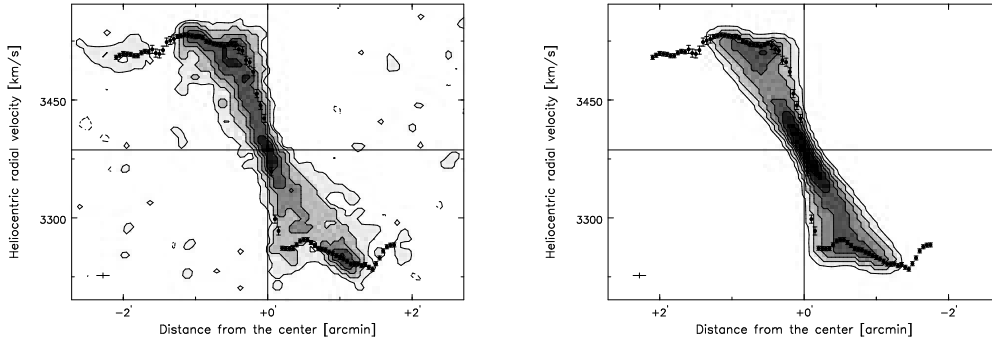


Figure 5.7 Position-velocity diagram taken along the major axis, for the observations (left) and for the synthetic data (right) of UGC 9759. The contour levels are at -2 (dashed), -0.9 , 0.9 (2σ), and from 1.8 to 6.8 mJy beam^{-1} in steps of 1.2 mJy beam^{-1} . The grey-scale ranges from 0.9 to 6.8 mJy beam^{-1} in steps of 1.2 mJy beam^{-1} . The horizontal line indicates the systemic velocity. The x -axis indicates arcminutes from the dynamical center.

The instrumental contribution to the profile broadening is assumed in the order of the channel separation of the observations (5 to 6 km s^{-1}).

Hence, the profiles are corrected following the recipe of Sofue (1996, Envelope Tracing Method):

$$v_{\text{rot}} = \frac{|v_t - v_{\text{sys}}|}{\sin(i)} - (\sigma_{\text{ISM}}^2 + \sigma_{\text{instr}}^2)^{1/2} \quad (5.1)$$

where v_t is the velocity at half maximum and v_{sys} is the systemic velocity. The inclination is i , σ_{instr} is the instrumental contribution to the profile broadening which is in the order of the channel separation of the observation, and the velocity dispersion is represented by the notation σ_{ISM} .

Thus, the corrected profiles are fitted by half a Gaussian to the extreme edges of the velocities. i.e. to the lowest radial velocities on the approaching side (dark shading in Fig. 5.3) and to the highest ones on the receding (light shading in Fig. 5.3).

According to Bosma (1978) who studied the effects of beam smearing on rotation curves in progressively smeared-out velocity fields, the velocity broadening and thus the rotation curve is scarcely affected by beam smearing if more than seven beam elements are present within the Holberg radius. In our cases, with some 4 to 5 beam elements within the Holberg radius, this threshold is not reached. Begeman (1987) proposed schemes to correct for beam smearing, which, however, are only effective in high signal-to-noise line profiles because the second derivative of the velocity field is required. Unfortunately, such significance levels are not reached for all galaxies in our sample. Thus the correction for the beam smearing is not applied, and the values for the rotation velocities represent an upper limit of the real values (Sancisi & Allen 1979).

5.3.2 Testing rotation curves by modeling

For three of the eight observed galaxies the modeling was performed in order to test the goodness of the derived rotation curves. IC 4745, UGC 9759, and NGC 1055 were selected for the modeling due to their extents and relatively symmetric distribution of the neutral hydrogen. In the following, we concentrate on the examples IC 4745 and UGC 9759, as

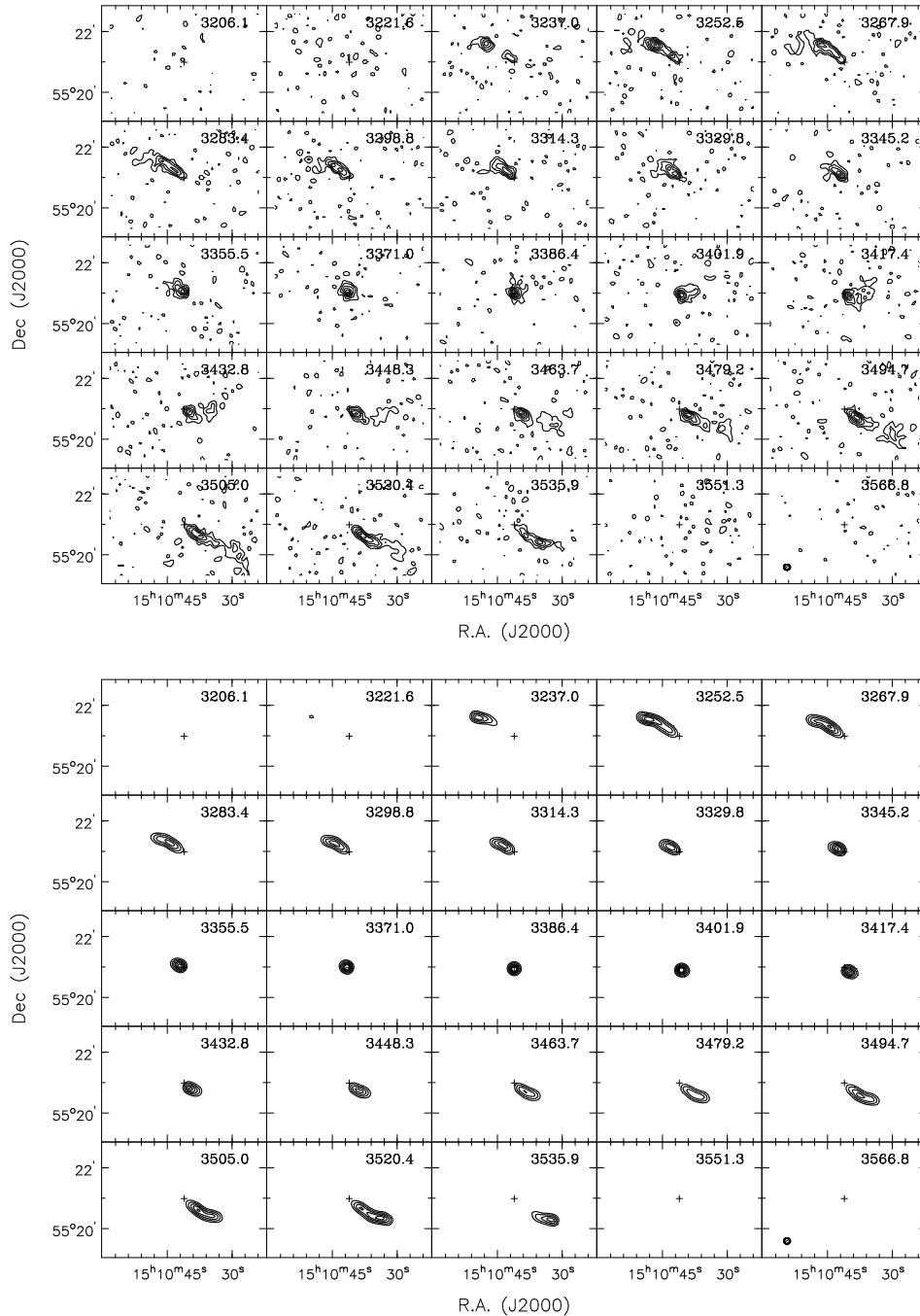


Figure 5.8 Channel maps for the observations (left), and for the synthetic data (right) of UGC 9759. Contours are at -2 (dashed), -0.9 , 0.9 (2σ), and from 1.8 to 6.8 mJy beam^{-1} in steps of 1.2 mJy beam^{-1} . The channel velocity is given in each panel. The size of the synthesized beam is indicated by the ellipse in the lower left-hand corner of the last map. The cross represents the dynamical center.

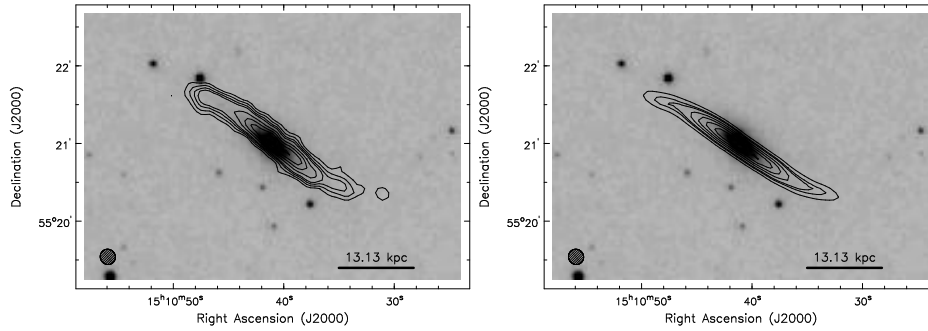


Figure 5.9 The total HI column density distribution superimposed on an optical images (DSS) for the observations (left), and for the synthetic data (right) of UGC 9759. The contour levels are at $8, 12, 16 \times 10^{20}$ atoms cm^{-2} , and from 20 to 55×10^{20} atoms cm^{-2} in steps of 6×10^{20} atoms cm^{-2} . The spatial resolution is $11''.00 \times 11''.57$.

the more extensive results on NGC 1055 are presented in Ch. 7.

The rotation curve and the position angle as derived from the Warped Modified Envelope Tracing method are applied in order to construct the synthetic data. A value of 10 km s^{-1} has been assumed for the velocity dispersion of the gas. The inclination is kept fixed at 90° . The other input parameters required for the modeling are taken directly from the observations. In particular, the values for the dynamical center are determined following the method explained in Sect. 2.3.1 and are reported in Tab. 6.2. The offsets between the stellar photometry and HI dynamical centers are of the order of few arcseconds ($\approx 4''$) in the case of IC 4745, while in UGC 9759 there is a difference of $20''$. The column densities at each radius are computed from a strip integral of the brightness distribution following the Lucy method (Warmels 1988). The systemic velocity is assumed as the velocity which minimizes the asymmetries of the rotation curve (Sect. 2.3.1). It is derived from a visual inspection of the channel maps and by folding the position-velocity diagram. The systemic velocities are in good agreement with other published measurements.

Once computed, the synthetic data were convolved to the resolution of the observations as reported in Tab. 2.1 to facilitate direct comparison with the observed data cube.

The results of the modeling are presented as follows:

- The position-velocity diagrams along the major axis for the observations and for the synthetic data for IC 4745 (Fig. 5.4) and UGC 9759 (Fig. 5.7).
- The channel maps of the data cube and synthetic cubes for IC 4745 (Fig. 5.5) and UGC 9759 (Fig. 5.8).
- The total HI integrated maps for IC 4745 (Fig. 5.6), and UGC 9759 (Fig. 5.9).

In the case of IC 4745, the position-velocity diagrams of the modeling and real data cubes match very nicely (Fig. 5.4). From the first contour up to the peak of the column densities the kinematics is reliably reproduced. The radial velocities at the last observed points in the approaching and receding sides agree precisely, as can be seen in the channel maps at the velocities 4402.7 km s^{-1} and 4916.9 km s^{-1} (Fig. 5.5). In Fig. 5.6, the ridge of the warp observed in the total HI map is well followed by the model. Possibly, the warping is not so smooth as shown by the model, and a change also of the inclination

should be added to the latter. However, this is beyond the goals of our present study and further results of these galaxies will be presented in the future.

The position-velocity diagram of UGC 9759 has a lopsided shape: the receding side has a higher, and peaked, column density compared with the deficit observed in the other approaching half (Fig. 5.7). In this case, the model fails to reproduce correctly the observations. The procedure to establish the model (GALMOD, GIPSY) characterizes the HI layer of the galaxy as rotating on circular orbits. Therefore, only regular structures can be described with the assumption of a symmetrically rotating disk. Because of this, the HI-blob which extends between $1'5$ and $2'5$ at velocities around 3500 km s^{-1} is not reproduced in the model (Fig. 5.7). The blob of emission is observed in the channel maps of the observations in a large number of channels (Fig. 5.8). It starts to be visible at the first contour level at velocity 3417.4 km s^{-1} , and disappears only at the edge of the emission (around 3520.4 km s^{-1}). This peculiar, asymmetric property of the disk in UGC 9759 is not reproduced in the synthetic channel maps. In the range between 3417.4 km s^{-1} and 3520.4 km s^{-1} only the main HI disk is modeled.

However, the shape of the warped distribution in the total integrated HI map up to $8 \times 10^{20} \text{ atoms cm}^{-2}$ is faithfully reproduced in the modeled map (Fig. 5.9). Down to this level, the column densities is peculiar and asymmetrically distributed, as can be seen in the deeper total HI-map in Fig 2.7.

5.4 Summary

Using the Warped Modified Enveloped Tracing method, the velocities are fitted by a Gaussian to the extreme edges of the velocity profiles at each position along the ridge line. It is not expected to have a single-peaked Gaussian in every velocity profile since the profiles are not symmetric around the peak. In this approach, only the most useful half (the external one) of the profile distribution is utilized. In this sense, this new procedure is an improvement of the already proposed Enveloped Tracing method (Sofue 1996, Olling 1996). In this new method, the fit over the broadened half owing to the lower velocities is avoided. Moreover, it can account for the change of the line-of-nodes and therefore the rotation velocities are traced along the kinematic axis, which allow the extraction of all the information in warped systems.

Successful modeling based on kinematic information (position angle and rotation velocities) was performed on three galaxies (IC 4745, UGC 9759, and NGC 1055) of the sample. Good agreements are found between synthetic data cubes and observations. The models are not able to account for strong peculiarities like strongly lopsided distributions or anomalous kinematics. However, the main characteristics of the HI emission are correctly traced. The fact that the original findings of the Warped Modified Envelope Tracing method are successfully reproducing those properties without altering the input values confirms the soundness of the method for deriving the rotation curves from edge-on galaxies observed at intermediate resolution. This is achieved without passing through the time-consuming, 3-D-modeling method.

References

- Babcock H.W., 1939, *LicOB* 498, 41
- Begeman K.G., 1987, Ph.D. thesis, University of Groningen, The Netherlands
- Bosma A., 1978, Ph.D. thesis, University of Groningen, The Netherlands
- Bosma A., 1991, in S. Casertano, P. Sackett and F. Briggs (eds.), Cambridge University Press, p.181
- Bottema R., 1995, *A&A* 295, 605
- Briggs F.H., 1990, *ApJ* 352, 15
- Briggs F.H., Rao S., 1993, *ApJ* 417, 494
- Burbidge E.M., Burbidge G.R., 1960, *ApJ* 132, 30
- García-Ruiz I., 2001, Ph.D. thesis, University of Groningen, The Netherlands
- García-Ruiz I., Sancisi R., Kuijken K., 2002, *MNRAS* 337, 459
- Kamphuis J.J., 1993, Ph.D. thesis, University of Groningen, The Netherlands
- Mathewson D.S., Ford V.L., Buchhorn M., 1992, *ApJ* 389, 5
- Mathewson D.S., Ford V.L., 1996, *ApJS* 107, 97
- Olling R.P., 1996, *AJ* 112, 457
- Oort J.H., 1940, *ApJ* 91, 273
- Pease F. G., 1918, *PASP* 30, 255
- Rogstad D.H., Lockart I.A., Wright M.C.H., 1974, *ApJ* 193, 309
- Rubin V.C., Burstein D., Ford W.K., Thonnard N., 1985, *ApJ* 289, 81
- Sancisi R., Allen R.J., 1979, *A&A* 74, 73
- Sofue Y., 1996, *ApJ* 458, 120
- Sofue Y., Rubin V., 2001, *ARA&A* 39, 137
- Warmels R.H., 1988, *A&AS* 72, 427
- Warner P.J., Wright M.C.H., Baldwin J.E., 1973, *MNRAS* 163, 163

6

Deviations from symmetry

6.1 Introduction

For a long time galaxies have been assumed to possess axisymmetric properties in their morphology and kinematics. Nowadays, as deviations from symmetry are in fact observed in a large fraction of galaxies, it is becoming established that asymmetries are the rule rather than the exception in visible and HI regimes.

Asymmetries have been studied at visual wavelengths by several authors who have found lopsided galaxies in some 30% of their samples (Rix & Zaritsky 1995; Kornreich et al. 1998). Richter & Sancisi (1994) quantified asymmetric global profiles to be present in 50% of their sample using single-dish 21-cm line surveys. Haynes et al. (1998) confirmed this estimate. By using HI aperture synthesis observations, large values for morphological and kinematic asymmetries are observed in several samples of face-on (Kornreich et al. 2000), nearly face-on (Kornreich et al. 2001), and inclined galaxies (García-Ruiz 2001).

Despite the evidence accumulated on departures from axi-symmetric properties (morphological, kinematic asymmetries, optical-HI offset centers), no clear relationship between morphological and kinematic asymmetries in the stellar and gaseous components and between these asymmetries and the general properties of galaxies are found (Kornreich et al. 1998, 2000, 2001; García-Ruiz 2000). This probably means that either these asymmetric characteristics do not represent different views of the same phenomenon or they are influenced by the same mechanisms but on different time-scales.

Two main mechanisms could account for asymmetries in galaxies. An asymmetric galaxy can be described by the response of a galactic disk to an imposed lopsided halo potential (Jog 1999). This model predicts a large percentage of rotationally asymmetric spiral galaxies. Differences of the order of 10% in the rotation curve – i.e. typically 20 to 30 km s⁻¹ between the two sides of the major axis – are expected in most spiral galaxies. Tidal interactions between galaxies (Beale & Davies 1969) or gas accretion from the surrounding intergalactic medium (Walker, Mihos & Hernquist 1996, Rix & Zaritsky 1995) have been suggested as a possible second cause for a globally lopsided disk.

The method of asymmetric indices – an approach which intends to parameterize asymmetries in galaxies – has turned out to be a powerful criterion to analyze the structural properties of spiral galaxies.

6.1.1 The purpose

Based on the fact that interaction events produce a highly asymmetric distribution and complex kinematics, large deviations from symmetry indicate a galaxy which is interacting with nearby companions.

One of the diagnostics to differentiate between the evolutionary history of a sample of galaxies – whether they have experienced a recent interaction or not – is the fraction of peculiarities disclosed in these objects compared to other classes of galaxies. In particular, in order to discern different bar formation scenarios (spontaneous instabilities or bars triggered by interactions) the frequency of deviations in the stellar population distribution of the target objects (galaxies with thick box/peanut bulges) compared to classical box/peanut and spheroidal-shaped bulge galaxies is important.

We study the statistics of warps, their shapes as well as lopsidedness by investigating and quantifying them with method of asymmetric indices. This approach allows us to investigate the likely formation mechanism of the thick box/peanut bulges.

6.1.2 Sample

We have studied a sample of 14 galaxies with prominent bulges selected from a complete magnitude and diameter-limited survey of highly inclined galaxies. The details of the sample selection are reported in Sect. 2.3.1.

A subsample of the thick box/peanut bulge galaxies (8 in total) was observed in HI 21-cm line emission performed with the VLA and ATCA. The observations and the data analysis are reported in Ch. 2.

6.2 Quantifying asymmetries

By relating the morphologies and kinematics of the galaxies in the sample we quantify their asymmetries. Possible deviations are studied also as a function of the global characteristics of the galaxies which might disclose possible correlations with their general properties.

Therefore, we define different quantities which parameterize the systematic deviations, These are the morphological asymmetries in the near-infrared band, the surface distribution of the HI, the deviations of the kinematic axis and asymmetries in the rotation curve, the HI line profile and in the mass contents of both sides of the galaxy.

6.2.1 Deviations in the near-infrared surface distribution

The deviations from morphological axisymmetry are quantified by rotating the image of the galaxy by 180° . The residuals, A_{nir} , of the rotated image (I_{180}) subtracted from the original one (I_0) is taken as the asymmetry measure (Conselice 1997).

$$A_{nir}^2 \equiv \frac{\sum \frac{1}{2}(I_0 - I_{180})^2}{\sum (I_0)^2} \quad (6.1)$$

The parameter A_{nir} is zero in a symmetric distribution and one in an asymmetric morphology.

This approach to consider the galaxy as a whole has the advantage of integrating a large number of points, which improves the results for small angular-sized, distant galaxies. However, it lacks any radial dependence compared with other methods, like those which

consider the galaxy as divided in a number of concentric rings (Zaritsky & Rix 1997) or in different sectors (Kornreich et al. 1998).

6.2.2 Deviations in the HI surface density distribution

The deviations from symmetry in the HI-distribution were calculated from the zeroth-moment map. The distribution of the surface density was determined using the Lucy-method (Warmels 1988) as implemented in the GIPSY¹ programs RADPROF and RADIAL. The galaxy is rotated along its internal major axis around the dynamic center. The choice of the center and the orientation of the HI disk are described in Sect. 2.3.1. The distribution is therefore calculated towards East ($-r$) and West ($+r$) with respect to the center.

We define the quantity D_{diff} as the difference between the radial surface density distribution integrated over a strip parallel to the minor axis of the brightness distribution (from west to east) of a galaxy. The integrated density in each $+nth$ (western) strip is compared with the corresponding $-nth$ (eastern) one. The density differences are then normalized to the mean of the density in these sectors.

$$D_{diff} \equiv \frac{|D_{+n} - D_{-n}|}{1/2(D_{+n} + D_{-n})} \quad (6.2)$$

The deviation from symmetry is quantified by the index, $A_{\Sigma_{HI}}$, defined as:

$$A_{\Sigma_{HI}} \equiv \frac{\sum_n (D_{diff}/\sigma_n^2)}{\sum_n 1/\sigma_n^2} \quad (6.3)$$

where σ accounts for the uncertainties of the measurements.

6.2.3 Deviation of the kinematic axis.

We have estimated the maximum deviation of the kinematic axis from the internal major axis considering each side of the galaxy separately.

As in the case of index $A_{\Sigma_{HI}}$ (Sect. 6.2.2) the galaxy has been rotated to the internal major axis around its dynamical center. For position angles of the major galactic plane smaller than 90° the galaxy is rotated anti-clockwise so that the major axis is the horizontal plane, for values larger than 90° a clock-wise rotation has been applied. For each part (eastern and western side) the maximum deviation of the position angle from the internal major axis has been calculated as deviation from the intensity peaks in the zeroth-moment map. Considering that the angles are calculated north-eastwards, a symmetric warped distribution will have $\alpha(+r) = -\alpha(-r)$, where α is defined as the angle between the outermost detected point and the internal major axis defined as described in Sect. 2.3.1.

The maximum deviations for each side were summed up and A_α has been adopted to quantify the symmetry of a warp:

$$A_\alpha = |\alpha(+r) + \alpha(-r)| \quad (6.4)$$

The medium between these angles $\alpha(+r)$, and $\alpha(-r)$ is taken as average angle $\langle\alpha\rangle$ of the warp. Following this notation, the more symmetric warped distribution will assume smaller values for $\langle\alpha\rangle$, otherwise larger values will be observed in asymmetric, one-sided, and U-shaped warps.

¹Groningen Image Processing System (van der Hulst et al., 1992)

6.2.4 Deviations in the rotation curve

Dynamic asymmetries are studied using the HI rotation curve of a galaxy. A ‘symmetric’ galaxy shows a fixed kinematic axis as function of the radius and a rotation curve which is identical both on the approaching and the receding side. Galaxies with kinematic large-scale asymmetries, however, show different slopes in both sides of the rotation curve. The measurement which reveals such kinematic asymmetries is given by the discrepancies between approaching and receding sides of the rotation curve. They are obtained by integrating the differences between both sides, normalized by the mean of the velocity width, according to the following formula:

$$v_{\text{diff}} \equiv \frac{\int |v_{\text{rot}}(+r) - v_{\text{rot}}(-r)| dr}{\int 0.5(v_{\text{rot}}(+r) + v_{\text{rot}}(-r)) dr} \quad (6.5)$$

Hence the symmetry parameter S_{kin} is:

$$S_{\text{kin}} = \frac{\sum_r v_{\text{diff}}(r)/\sigma_{\text{diff}}^2(r)}{\sum_r 1/\sigma_{\text{diff}}^2(r)} \quad (6.6)$$

where the $\sigma_{\text{diff}}(r)$ represents the uncertainties in the measurements.

6.2.5 Deviations in the HI line profiles

Deviations from the typical double-horned shape of the HI-line profiles have been frequently used in the study of the global symmetric properties of galaxies.

The symmetry index A_n is defined as the ratio between the flux density contained in the range of velocities higher, v_h , and lower, v_l , than the mid-point velocity between them. The velocities v_h and v_l are the extreme velocities with emission signal three times above the noise level in each channel. The analysis is therefore restricted to this portion of the spectrum. The mid-point velocity could be calculated using different strategies (see for completeness the techniques reported by Haynes et al. 1998). Here, the mid-point velocity is assumed as the mean value between the extreme velocities v_h and v_l .

The ratio between the flux densities in the intervals of velocities $v_l - v_{\text{med}}$ and $v_{\text{med}} - v_h$ is calculated using the following expression:

$$A_{l/h} \equiv \frac{\int_{v_l}^{v_{\text{med}}} S dv}{\int_{v_{\text{med}}}^{v_h} S dv} \quad (6.7)$$

Therefore, the symmetry index of the HI-line profiles is simply

$$A_n \equiv \begin{cases} A_{l/h}, & \text{if } A_{l/h} > 1 \\ 1/A_{l/h}, & \text{otherwise.} \end{cases} \quad (6.8)$$

The asymmetries in the global line profiles should be considered as a symptom of anomalous structures on a large kinematic scale and not just simple local events like bridges, tails or density enhancements (Richter & Sancisi 1994). This correspondence is not verified all the time. For NGC 4395, Wevers et al. (1986) show how anomalies in the kinematics do not produce a destruction of the asymmetric density distribution. This is one of the cases when the warp is oriented almost exactly along the line-of-sight. In this sense the fraction which was inferred from the global profiles can only be a lower limit. The normal case remains the one to find galaxies which only selected on the basis of the

symmetry of their HI distribution reveal high degrees of asymmetry in the kinematics of their disks.

However, the density distribution as well as the kinematics of the HI contribute to the shape of the global profile and the two observables conspire to influence both asymmetric morphological and kinematic indices. On average, the asymmetries in the global line profiles represent the large-scale deviations in the kinematics. It was observed that in a large number of cases, the kinematics rather than the distribution of the gas determines the asymmetry in the global profiles (Schoenmakers 1999).

6.2.6 Deviations in the masses contained in the approaching and receding sides

To quantify the lopsidedness in the HI distribution we have calculated the HI mass for each side of the galaxy (M_1 , M_2) with respect to the systemic velocity as defined in Sect. 2.1.1. Here, the lopsidedness index is defined as:

$$A_\rho = \frac{|M_1 - M_2|}{M_1 + M_2} \quad (6.9)$$

This parameter turns out to be very similar to the deviations from symmetry of the HI global profile, A_n . This should reflect the small differences in the mid-point velocity as derived from the global profile and the systemic velocity once the kinematic center has been accurately defined (see Sect. 2.1.2 for a detailed discussion). Due to this similarity between A_ρ and A_n the discussion on these parameters can be limited to the latter.

6.2.7 Warp classification

The different appearance of the warp for each individual galaxy is reported in Tab. 6.4. The warp is classified as S-, L-, or U-shape depending on the warp angle. A S-shaped warp is defined as the deviation which rises on one side, and symmetrically declines on the other. A galaxy possessing a one-sided warp is called L-shaped warped galaxy. This can happen when on the ‘unwarped’ side the HI emission ceases – or cannot be observed any more; another explanation could be that the unwarped side has the same extension as the opposite L-shaped warped part, but with its emission well settled in a flat disk. U-shaped warps are anti-symmetric deviations of the distribution whose orientations of both sides of the galaxy point in the same directions.

6.2.8 Table descriptions

Table 6.1 shows the final values for the asymmetric indices of the near-infrared surface density. The following information is compiled:

Column (1) – Object: Name of the galaxy;

Columns (2) and (3) – Morphology: The morphological Hubble type, T, and the number;

Column (4) – The total B magnitude;

Column (5) – A_{nir} : asymmetry measure of near-infrared surface brightness.

Table 6.2 lists the kinematic center of the target objects. The kinematic center is reported and the offset from the cataloged center is indicated.

In Tab. 6.3. values of the asymmetric parameters are tabulated. Coordinates of the galaxies can be found in Tab. 6.1. The following entries are listed:

Column (1) – Object: Name of the galaxy;

Column (2) – A_{kin} : asymmetry measure of the kinematics;

Object	Morphology		M_B	A_{nir}
(1)	Type	T	(4)	(5)
(1)	(2)	(3)	(4)	(5)
Thick BP Bs				
NGC 1030	Sbc	+4.0 ± 2	-22.14	0.2168
NGC 1055	SBb	+3.2 ± 1	-19.71	0.1157
NGC 1589	Sab	+2.3 ± 1	-21.79	0.0799
ESO 494-022	Sa	+1.2 ± 1	-21.44	0.7544
NGC 3573	S0a	-0.1 ± 1	-19.93	0.1805
ESO 506-003	Sab	+1.8 ± 1	-19.58	0.8710
ESO 322-100	S0	-2.1 ± 1	-19.89	0.6095
ESO 383-005	Sbc	+3.8 ± 1	-20.52	0.4118
ESO 021-004	S0a	+0.1 ± 1	-20.86	0.1710
NGC 5719	SBab	+2.4 ± 1	-19.48	0.1096
UGC 09759	Sbc	+3.8 ± 3	-19.65	0.6979
ESO 514-005	Sa	+1.0 ± 0	-19.42	0.3318
UGC 10205	S0a	+1.0 ± 0	-21.12	0.2940
NGC 7183	S0a	-0.7 ± 1	-19.84	0.1080
Class. BPs				
NGC 2310	S0	-1.9 ± 1	-18.55	0.8769
NGC 2862	SBbc	+4.1 ± 1	-21.54	0.0560
NGC 2939	Sbc	+4.0 ± 0	-21.11	0.3119
NGC 3098	S0a	-1.4 ± 1	-18.82	0.1265
NGC 3628	Sb	+3.1 ± 0	-21.24	0.8437
NGC 3986	S0a	-0.8 ± 2	-19.72	0.4222
NGC 3987	Sb	+3.0 ± 0	-21.33	0.2610
NGC 4469	SB0a	+0.2 ± 1	-17.78	0.5678
ESO 443-042	Sb	+3.1 ± 1	-20.61	0.6220
NGC 5073	SBc	+5.1 ± 1	-21.18	0.2706
UGC 8737	Sbc	+4.0 ± 0	-19.40	0.1976
NGC 6771	SB0a	-1.0 ± 1	-20.55	0.0420
Spher. Bs				
NGC 4026	S0	-1.8 ± 1	-19.56	0.0570
NGC 4217	Sb	+3.1 ± 1	-19.98	0.1616
NGC 4762	S0	-1.8 ± 1	-19.77	0.0625
NGC 5014	Sab	+1.5 ± 2	-18.42	0.2585
NGC 5492	Sb	+3.0 ± 0	-20.19	0.2535
NGC 5908	Sb	+3.0 ± 0	-21.34	0.0837
NGC 6361	Sb	+3.0 ± 0	-20.81	0.8687
NGC 7264	Sb	+3.1 ± 0	-21.00	0.2460
UGC 3354	Sab	+2.0 ± 0	-19.97	0.2658
UGC 9853	Sb	+3.1 ± 0	-21.06	0.2892
NGC 5470	Sb	+3.1 ± 0	-18.21	0.2124
UGC 10447	Sb	+3.0 ± 0	-20.85	0.2553

Table 6.1 (1) Galaxy Name of the sample Thick BPS Bulges; (2) and (3) Morphological Type from LEDA; (4) Total magnitude; (5) A_{nir} , symmetry number in NIR images.

Object	Kinematic center		Offset		Ref.
	α (J2000)	δ (J2000)	α (J2000)	δ (J2000)	
(1)	(2)	(3)	(4)	(5)	(6)
NGC 1055	+02 ^h 41 ^m 44 ^s .92	+00° 26' 37".5	0 ^s .3	2".0	A
ESO 383-05	+13 ^h 29 ^m 23 ^s .70	-34° 16' 15".5	0 ^s .1	4".5	A
NGC 5719	+14 ^h 40 ^m 56 ^s .40	-00° 19' 10".2	-	4".8	B
UGC 9759	+15 ^h 10 ^m 44 ^s .91	+00° 26' 37".5	3 ^s .9	21".9	A
UGC 10205	+16 ^h 06 ^m 40 ^s .10	+30° 05' 56".0	0 ^s .2	1".2	C
IC 4745	+18 ^h 42 ^m 35 ^s .68	-64° 56' 31".5	0 ^s .2	2".9	A
IC 4757	+18 ^h 43 ^m 55 ^s .73	-57° 09' 58".2	0 ^s .3	4".9	A
NGC 7183	+22 ^h 02 ^m 21 ^s .94	-18° 54' 39".6	0 ^s .3	19".7	A

Table 6.2 (1): Galaxy Name; (2) and (3): Kinematic Center; (4) and (5): Offset from the tabulated center given in the references; (6) A = Two micron all sky survey, B = Sloan digital sky survey, release as obtained 2001, C = Grogin & Geller 1999.

Column (3) – A_ρ : asymmetry measure of mass distribution with respect to the systemic velocity;

Column (4) – A_n : asymmetry measure of HI global profile with respect to the mid-point velocity;

Column (5) – $A_{\Sigma_{\text{HI}}}$: asymmetry measure of density distribution with respect to the morphological center;

The properties of the warp orientations are listed in Tab. 6.4 as follows:

Column (1) – Object: Name of the galaxy;

Column (2) – A_α : asymmetry measure of kinematic axis deviations.

Columns (3) and (4) – α_E and α_W : last-point deviation of the eastern and western HI distribution.

Column (5) – $\langle\alpha\rangle$: mean deviation of the kinematic axes.

Column (6) – Warp shape: The classification of the warp shape.

6.3 Discussion

6.3.1 Fraction and statistics of warps

One of the remarkable findings in this study of asymmetries in thick box/peanut bulge galaxies is the fraction of the warps observed in the neutral hydrogen emission. All galaxies in our sample possess warps of the gaseous component even if on different scales and in various shapes.

S-shaped warps are found in 5 (62%) of the observed galaxies. In one of them, NGC 5719, the classification has been referred to the innermost region. This is due to a very messy HI distribution on large scale because of the strong interaction with the nearby galaxy NGC 5713. However, in the innermost region the HI disk of NGC 5719 displays a quite symmetric S-shaped warp. Among these 5 S-shaped warped galaxies, ESO 383-005 presents a clearly regular, symmetric S-shaped warp. The other three S-

Object	A_{kin}	A_{ρ}	A_n	$A_{\Sigma_{HI}}$
(1)	(2)	(3)	(4)	(5)
NGC 1055	0.0460 ± 0.0031	0.1084 ± 0.0009	1.69 ± 0.0013	0.3596 ± 0.0912
ESO 383-05	0.1078 ± 0.0026	0.0229 ± 0.0006	1.04 ± 0.0011	0.2649 ± 0.0826
IC 4745	0.0452 ± 0.0031	0.0044 ± 0.0007	1.01 ± 0.0013	0.5323 ± 0.1043
UGC 9759	0.0964 ± 0.0029	0.0603 ± 0.0019	1.13 ± 0.0012	0.3183 ± 0.0348
NGC 7183	0.0629 ± 0.0032	0.0423 ± 0.0010	1.08 ± 0.0011	0.4626 ± 0.1082
NGC 5719	0.2149 ± 0.0024	0.0860 ± 0.0007	1.19 ± 0.0013	0.4417 ± 0.0855
IC4757	0.2048 ± 0.0036	0.6410 ± 0.0015	4.17 ± 0.0014	0.4276 ± 0.0867
UGC 10205	0.1778 ± 0.0021	0.4380 ± 0.0017	2.55 ± 0.0015	0.5851 ± 0.0118

Table 6.3 (1) Galaxy Name; (2) A_{kin} : asymmetry measure of the kinematics; (3) A_{ρ} : asymmetry measure of mass distribution with respect to the systemic velocity; (4) A_n : asymmetry measure of HI global profile with respect to the mid-point velocity; (5) $A_{\Sigma_{HI}}$: asymmetry measure of density distribution with respect to the morphological center.

shaped warped objects show HI emission with different extents on the two sides (IC 4745, UGC 9759, UGC 10205), and the general appearance is an asymmetric S-shaped warp.

L-shaped warps are found in two systems. Both, in IC 4757 and NGC 7183, one side of the disk well traces the position angle of the major axis while the opposite side bends by some degrees and creates the L-deviation. The north-eastern part of IC 4757 has a lower fraction of HI emission, and the L-shaped appearance might be caused by the absence of the neutral gas. In this part, however, no hint of the beginning of a warp is detected within the peculiar north-eastern distribution, although the detection is not strong enough to confirm it. In NGC 7183, a peculiar region of emission on the outer south-western side is tilted with respect to the orientation of the major HI disk. Apart from this HI complex which definitely belongs to the galaxy, the emission is fairly symmetric in the major disk.

The fraction of U-shaped warps versus the warped galaxies and the total sample (one over eight galaxies) is consistent with other statistics. A fraction of 2 U-shaped HI warped galaxies over 26 (8%) objects, and 10% of the warped galaxies are detected by García-Ruiz (2000). The two U-shaped warped galaxies in this investigation turn out to be strongly interacting with the nearby companions. Sanchez-Saavedra et al. (2003) find 5 galaxies with U-shaped warps in a sample of 266 objects, i.e. only 7% of the warped galaxies show U-shaped warps. In a sample of 108 galaxies, a larger number of U-shaped stellar warps (21, 19%) were observed by Schwarzkopf & Dettmar (2001) with a fraction of 29% of the entire warped galaxies.

The symmetric properties of the warps are also considered relevant. Symmetric warps are found in our investigation only in ESO 383-005, one out of eight (12.5%). Symmetric warps are found in 18.5% (26/71 warps), 10% (2/10 warps), and 88% (132/150 warps) by Schwarzkopf & Dettmar (2001), García-Ruiz (2000), and Sanchez-Saavedra et al. (2003), respectively. The fraction of symmetric warps is definitely larger in the stellar content rather than in the neutral hydrogen. The percentage of the asymmetric warps is very large compared with other measurements. If we assume that a warp is attributed to an interaction with a companion, the thick box/peanut bulges should live in a rich environment.

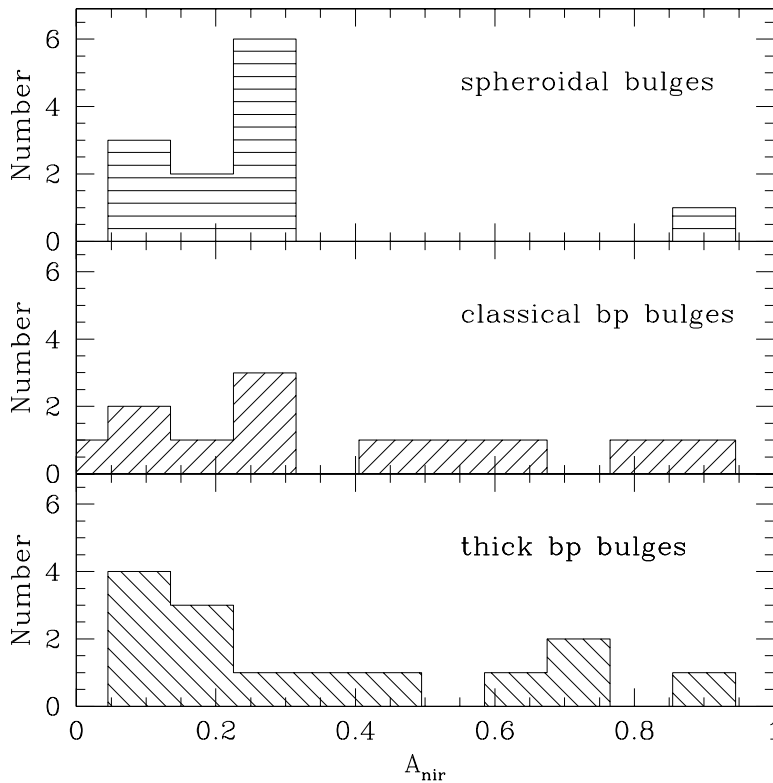


Figure 6.1 Comparison of the histograms of deviations in near-infrared images for the three classes of bulges. The histogram for the thick boxy/peanut bulges do not differ significantly from that of the classical box/peanut bulges, although the largest value for A is shown by a galaxy with a thick box/peanut bulge (ESO 506-003). There is a shift towards higher concentrations for smaller A_{nir} in spheroidal bulges which tells us the spheroidal bulge galaxies are the more symmetric galaxies in the older stellar population.

In conclusion, a large number of warps are found in the thick box/peanut bulge galaxies, they have a large variety of shapes (S, U-, and L-shape) and are mostly asymmetric.

6.3.2 Asymmetrical indices

Based on the present study, the indices of the near-infrared surface brightness in thick box/peanut bulges are found to be on average as asymmetric as those in the classical box/peanut bulges. In particular, 38 galaxies have values of the near-infrared deviations greater than 0.3 for about 40% of the galaxies with thick and classical box/peanut bulges, and only 8% with spheroidal bulges (or non-box/peanut bulges). In the sample of thick box/peanut bulges only one galaxy has $A_{nir} < 0.1$, and in the same sample four objects have A_{nir} measurements larger than 0.5. In the comparison sample, the latter values ($A_{nir} > 0.5$), are reached only in one spheroidal bulge galaxy and three classical box/peanut bulge galaxies. Two of the classical box/peanut and three galaxies of the spheroidal bulge sample possess A_{nir} smaller than 0.1 (Fig. 6.1).

Hence, thick box/peanut bulges do not have larger asymmetries in the older stellar component than classical box/peanut bulges, despite the fact that the sample of thick

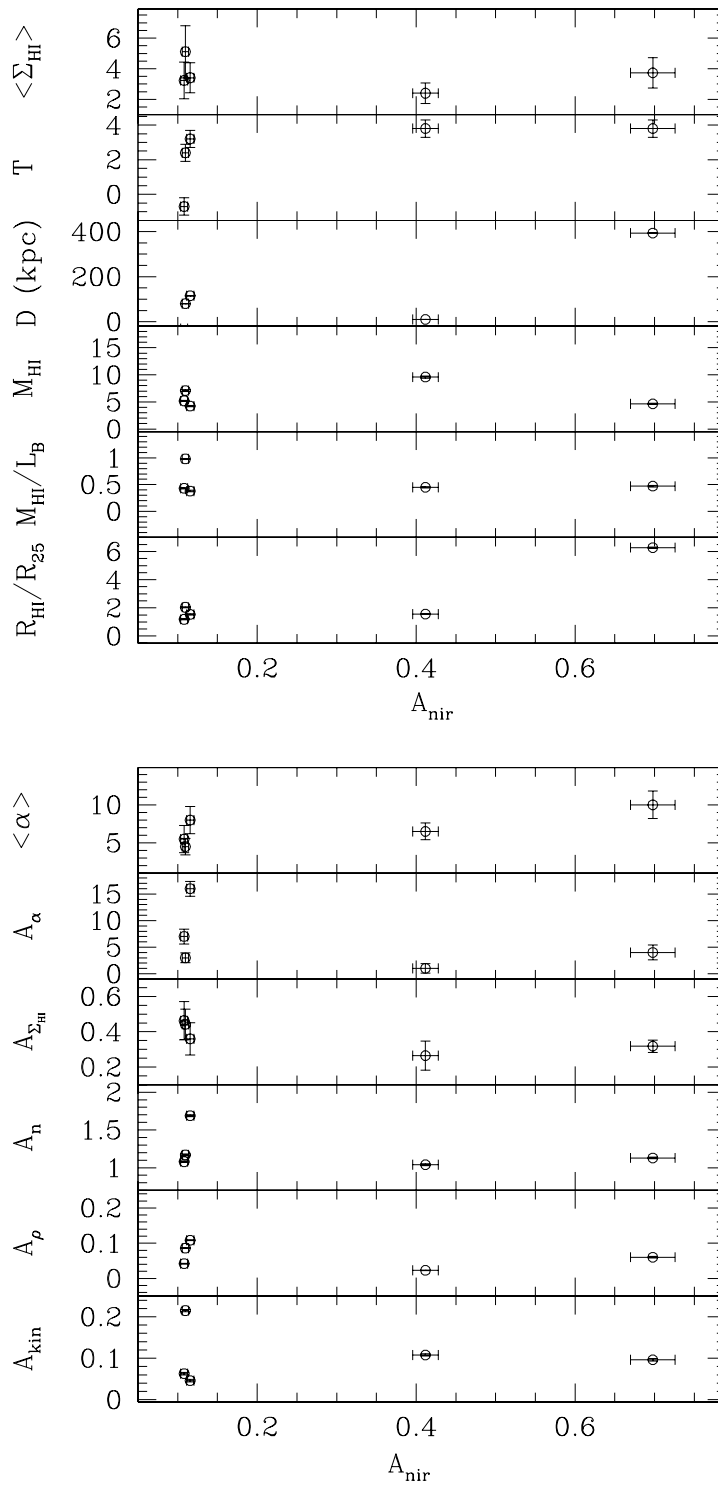


Figure 6.2 Near-infrared asymmetric index, A_{nir} , versus the global properties of the galaxies (*upper*), and the kinematic and morphological indices (*lower*).

Object	A_{α} ◦	α_E ◦	α_W ◦	$\langle\alpha\rangle$ ◦	Warp shape
(1)	(2)	(3)	(4)	(5)	(6)
NGC 1055	$+16 \pm 1.4$	$+6 \pm 0.7$	$+10 \pm 1.2$	$+8.0 \pm 1.8$	U
ESO 383-05	$+1 \pm 0.9$	-6 ± 0.7	$+7 \pm 0.7$	$+6.5 \pm 1.1$	S
IC 4745	$+15 \pm 1.3$	$+21 \pm 0.6$	-6 ± 1.2	$+13.5 \pm 1.7$	S
UGC 9759	$+4 \pm 1.4$	-8 ± 0.8	$+12 \pm 1.1$	$+10.0 \pm 1.8$	S
NGC 7183	$+7 \pm 1.4$	-2 ± 0.9	$+9 \pm 1.1$	$+5.5 \pm 1.8$	L
NGC 5719	$+3 \pm 0.9$	-6 ± 0.7	$+3 \pm 0.6$	$+4.5 \pm 1.1$	S ¹
IC4757	$+4 \pm 0.8$	-8 ± 0.3	$+12 \pm 0.7$	$+10.0 \pm 1.0$	L
UGC 10205	$+3 \pm 1.6$	-11 ± 1.3	$+8 \pm 0.9$	$+9.5 \pm 1.8$	S

Table 6.4 (1) Galaxy Name; (2) A_{α} : asymmetry measure of kinematic axis deviations; (3) and (4) α_E and α_W : last-point deviation of the eastern and western HI distribution; (5) $\langle\alpha\rangle$: mean deviation of the kinematic axes; (6) Classification of the shape of the warp. (S¹) Warp classification restricted to the inner 6' region.

box/peanut bulges shows the largest values for A_{nir} . Based on the near-infrared asymmetric indices, A_{nir} , calculated on the galaxy as a whole we cannot argue for a different formation mechanism in thick box/peanut bulges with respect to the classical box/peanut bulges. The mechanism responsible for bulge thickening either does not influence the older stellar content while affecting the younger, newly formed stellar component or it has no impact on the surface brightness distribution without implying deviations in the galaxy as a whole.

It is worth to note that the two samples of bulges with box/peanut shaped structures, thick $\langle A_{nir, tbp} \rangle = 0.3602$, and classical box/peanut bulges, $\langle A_{nir, cbp} \rangle = 0.3828$, on average possess larger deviations compared to the spheroidal bulges, $\langle A_{nir, s} \rangle = 0.2512$. The mechanism which triggers the thick and classical box/peanut structures in galaxies displaces the surface brightness from a homogeneous to non-asymmetric distribution of the older stellar component. In this scenario, interactions should play a more influential role in the evolution of the box/peanut galaxies, because as expected they show a larger fraction of asymmetries. A radial dependence analysis with an accurate S/N, within and beyond R_{25} could help in this study to investigate the evolution history of these galaxies in more detail.

In comparison with the global properties for the thick box/peanut bulges, the only slightly significant dependence should be the near-infrared deviations and the size of the HI disk at the level of $1 M_{\odot} \text{pc}^{-2}$ to the optical disk (A_{nir} versus R_{HI}/R_{25}). Larger deviations in the near-infrared surface brightness are shown by the galaxies which are more extended in HI, and vice-versa. There is a mild tendency for galaxies with asymmetric near-infrared distribution to show larger warp amplitudes but well-settled HI distribution as can be observed in the relations: $A_{nir} - \langle\alpha\rangle$, and $A_{nir} - A_{\Sigma_{\text{HI}}}$, (Fig. 6.2. lower panels). No further conclusive statistical results can be obtained due to the limited sample size.

Kinematic asymmetries are equally distributed in all ranges of HI to optical size (A_{kin} versus R_{HI}/R_{25}). Perhaps the more massive galaxies seem more stable against rotation

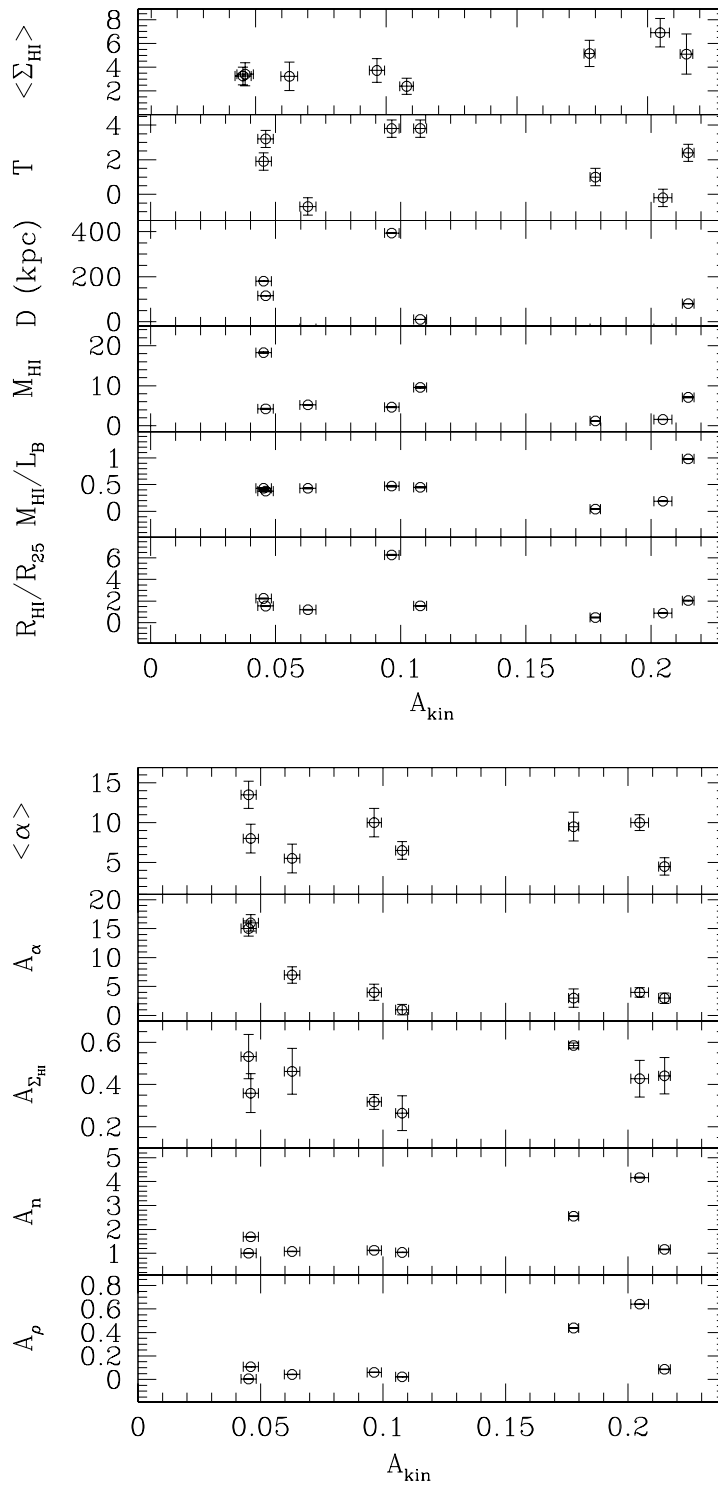


Figure 6.3 Kinematic asymmetric index, A_{kin} , versus the global properties of the galaxies (upper), and the kinematic and morphological indices (lower).

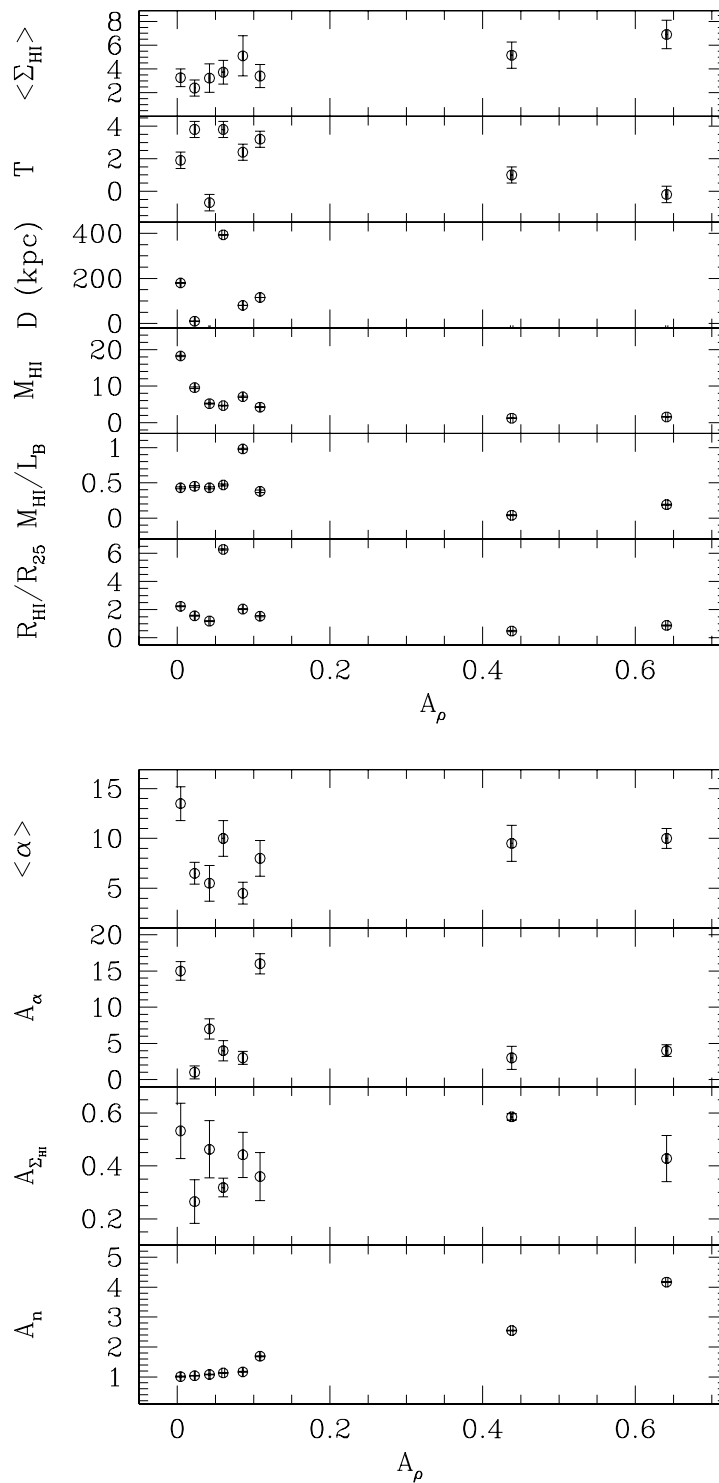


Figure 6.4 Deviations in the masses contained in the approaching and receding side of the galaxies, A_ρ , versus the global properties of the galaxies (*upper*), and the kinematic and morphological (*lower*).

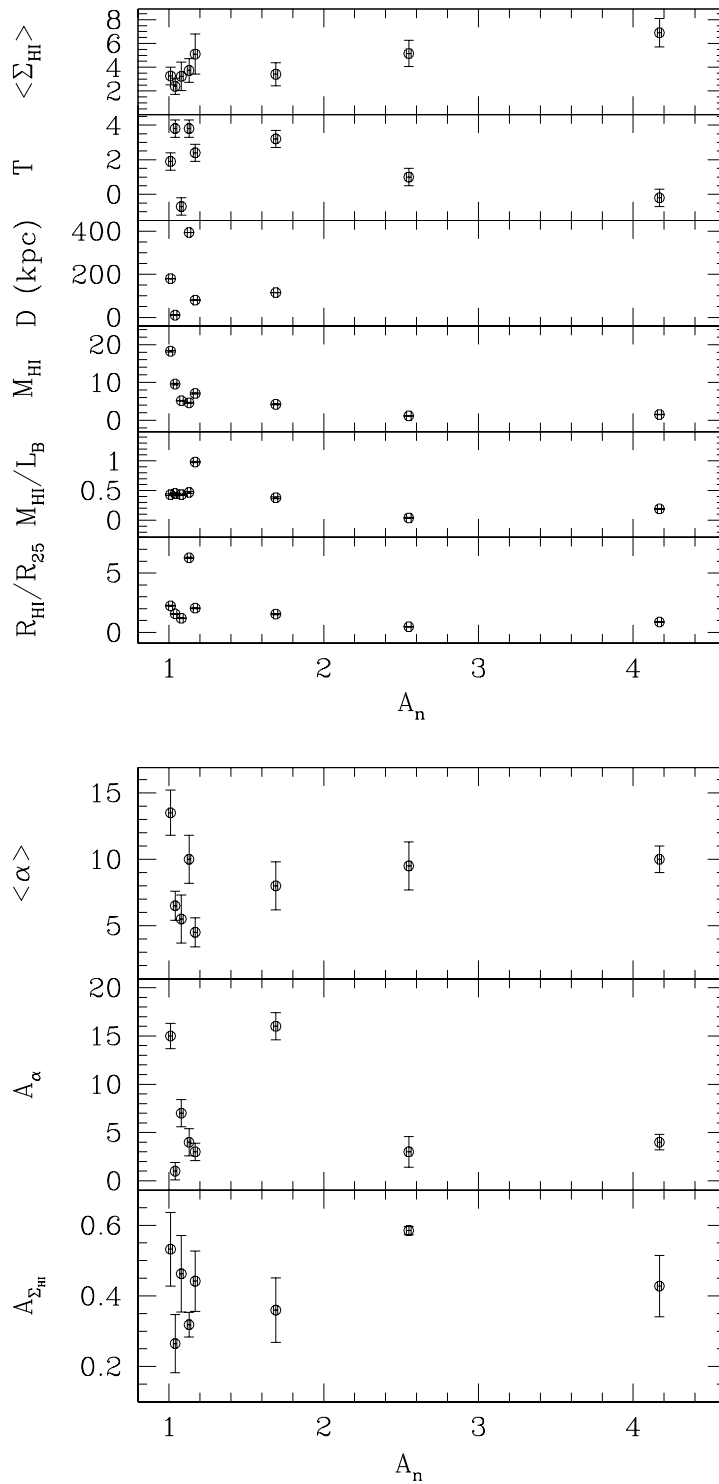


Figure 6.5 Deviations in the HI line profiles, A_n , versus the global properties of the galaxies (*upper*), and the kinematic and morphological indices (*lower*).

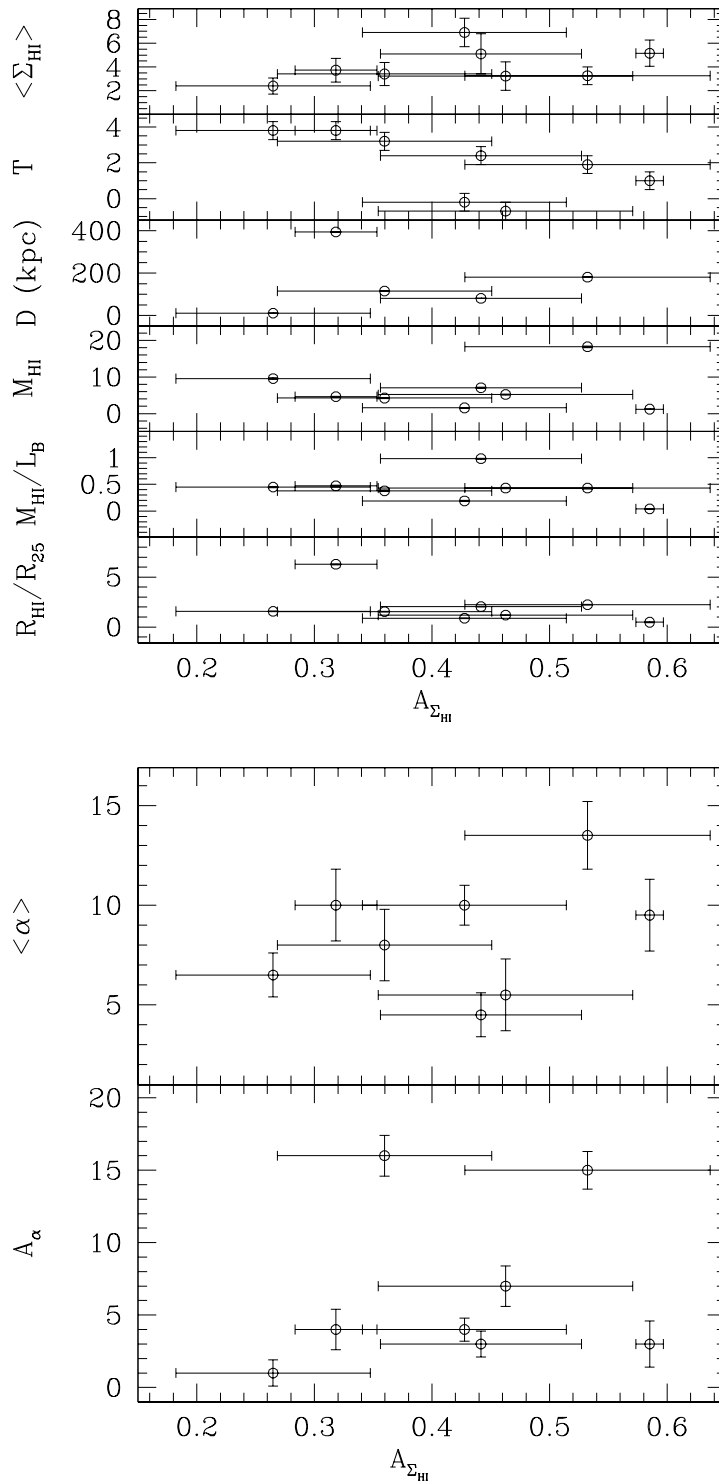


Figure 6.6 Deviations in the column densities between the western and eastern side of neutral hydrogen distribution, $A_{\Sigma_{HI}}$, versus the global properties of the galaxies (*upper*), and the morphological indices (*lower*).

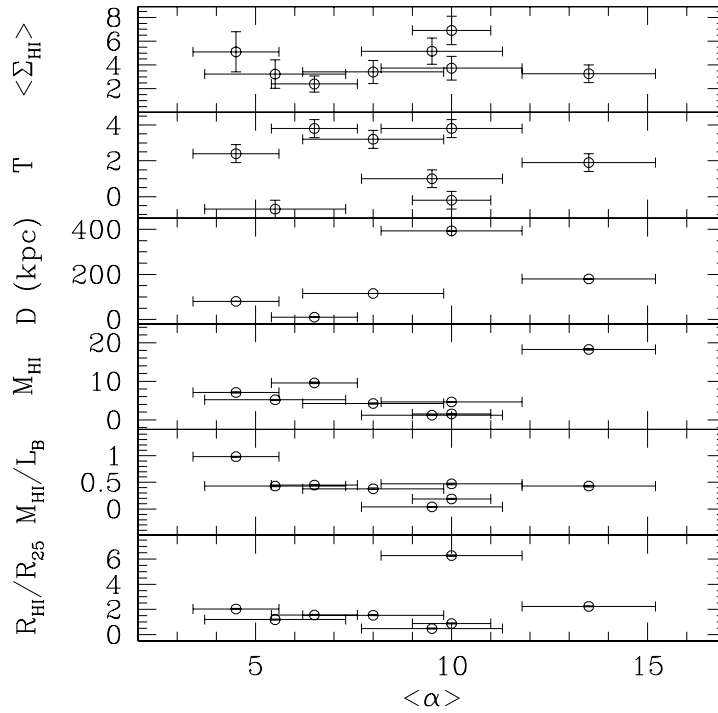


Figure 6.7 Angle of the warped HI distribution, $\langle \alpha \rangle$, versus the global properties of the galaxies.

curve deviations (A_{kin} versus M_{HI}). The gas-rich galaxies show also higher degrees of morphological symmetry in HI, as is observed in the relation A_{ρ} (A_n) versus M_{HI} . Smaller deviations in the mass content between the approaching and the receding side are detected in the galaxies with large HI extents compared with the optical body, even though the trend is not strict. The asymmetries in the mass content and in the distribution of the column density span over all warp characteristics (amplitude and symmetric warp properties). The richness of the gaseous component in galaxies could help in damping the local asymmetries, and this should explain their small kinematic and morphological asymmetries.

The relation observed between A_n and A_{ρ} has been interpreted in two different ways: Firstly, it reflects the closeness of the systemic velocities, derived as mid-point of the HI global profile and the value which minimizes the asymmetries in the p-v diagram. Secondly, small companions and high-velocity gas detected within the antenna beam may contribute to the departure of the HI profiles from the characteristic symmetric two-horned shape which could easily offset the mid-point velocity. Therefore, the closeness of the two velocities estimated using two different approaches should give the information that within the velocity range of the HI profile – above the 3σ emission – no signatures of wings or extra-features are observed. Comparing the relation between the asymmetries in the HI global profiles and the morphological ($A_{\Sigma_{\text{HI}}}$) and kinematic (A_{kin}) deviations, the larger influence of the latter is evident, this confirms the earlier prediction that the shape of profiles is primarily determined by the kinematics within the galaxy and only marginally by the HI distribution (i.e. Richter & Sancisi 1994, Haynes et al. 1998, Schoen-

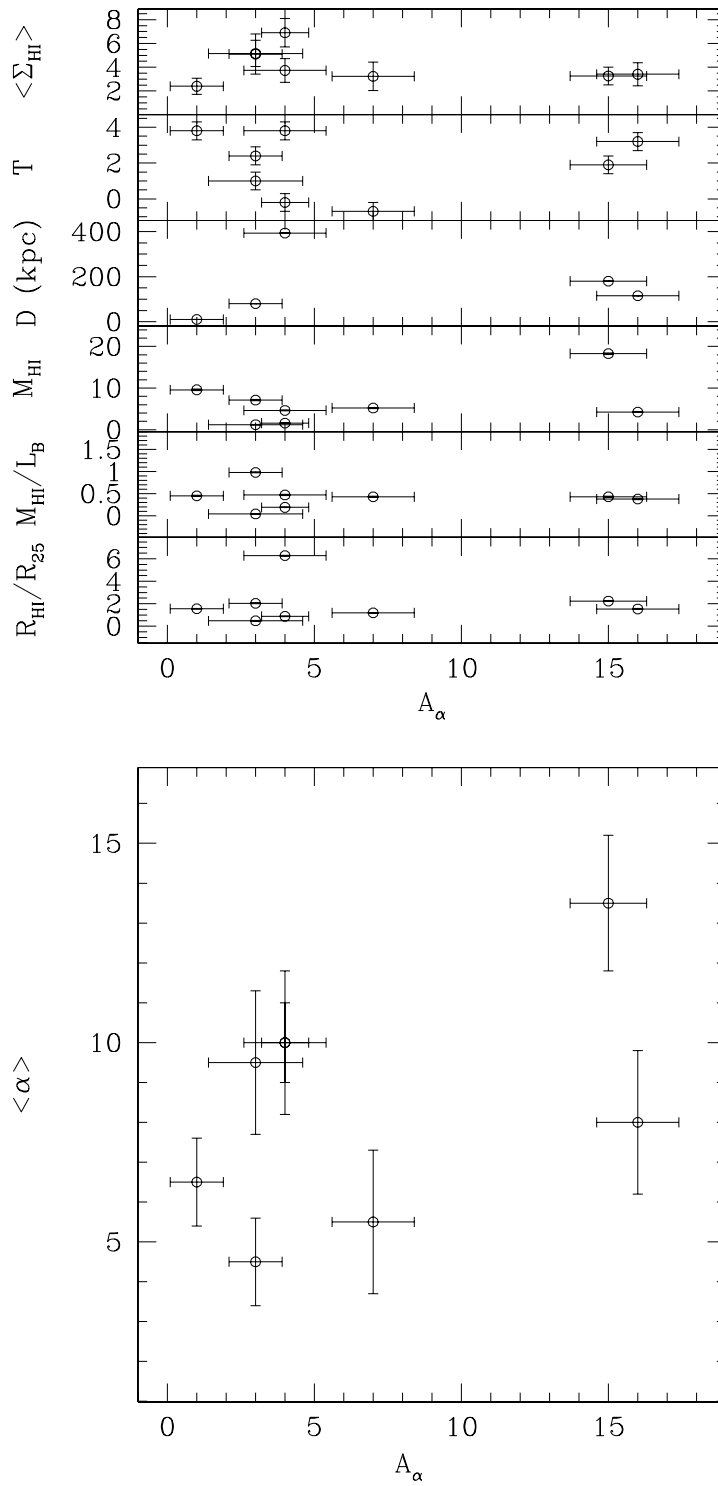


Figure 6.8 Asymmetries of the warped HI distribution, A_α , versus the global properties of the galaxies (*upper*), and the average angle (*lower*).

makers 1999).

The asymmetric warped characteristics are expressed by A_α and $\langle\alpha\rangle$. They appear correlated by showing the trend in which larger warps are likely asymmetric, while smaller amplitudes indicate often a symmetric warp.

An anti-correlation is found between the asymmetric warped characteristics and the kinematic index, A_{kin} . This reflects the tendency of the asymmetric, one-sided, and U-shaped warped disk to have a regular rotation curve, while most of the classical, regular S-shaped warps show often deviations in the kinematics. This independence of the symmetry of the warp from the anomalies in the kinematics suggests that the possible influence from satellites affects only the morphology of a galaxy. Either different mechanisms play a role in the warp formation or different time scales have to be considered. The more asymmetric warps could represent an earlier stage or ongoing interactions which will damp later on. The large fraction of asymmetric warps should represent the large frequency of minor merger events rather than a long-lived, persistent mechanism. The symmetric shape in a warp dominates in the later stage, when the gravitational material or the influenced component have settled down. Otherwise, the origin of symmetric warps can be searched in a lopsided halo distribution (Jog 1999).

The correlation between the asymmetric indicators and the morphological classification of the objects is quite mild. An anti-correlation is observed in the relation A_ρ versus T, and $A_{\Sigma_{HI}}$ versus T.

Apart from the case of UGC 9759 for which a relatively low asymmetric morphology corresponds to a large HI extended distribution, the morphological index $A_{\Sigma_{HI}}$ does not show any correspondence with the quantity R_{HI}/R_{25} .

Finally, lopsidedness is very common both in the kinematics and the morphology of galaxies with thick box/peanut bulges. No correlation between the two indices are established as previously observed in the stellar and gas contents (Kornreich et al. 1998, 2000, 2001; García-Ruiz 2000).

6.3.3 Mechanisms triggering lopsidedness

The influence of the lopsided halo on the disk kinematics predicts a resulting warped distribution and a shape of the rotation curve which rises with different characteristics in one half of the galaxy with respect to the other, as is largely found in the objects of this sample. The large fraction of lopsided galaxies predicted by this lopsided halo model might cause some perplexity. In fact, in the past the galaxies have been kinematically studied as axisymmetric disks by tending to ignore the differences between approaching/receding side and in order to obtain an "averaged-out" rotation curve. However, rotation curves show these lopsided features when they are obtained without forcing the symmetry.

The kinematic center of the HI has been calculated and compared with the center as derived from the stellar distribution in order to estimate the influence of a possibly lopsided halo. Of the 8 galaxies studied in this investigation the kinematic centers of 6 of them (NGC 1055, ESO 383-005, NGC 5719, UGC 10205, IC 4745, and IC 4757) offset by typically 4" from the stellar based determinations. This findings might indicate that galaxies are not in a stationary state of the potential and are influenced by lopsided potential. Two galaxies (UGC 9759, NGC 7183) present a larger offset of approximately 20". In these cases the off-centering is likely due to the strong dust contamination which affects the stellar centering (also in the near-infrared regime) and the overall asymmetric morphology. In the case of NGC 7183, the HI is not homogeneously distributed by peaking on one side which might cause the error of the centering.

In conclusion, the galaxies are clearly warped and the HI is dishomogeneously distributed with a high level of kinematic lopsidedness. These properties are compatible with a scenario of galaxies influenced by a lopsided halo. However, the morphological peculiarities show the typical properties of relicts of past interaction events (e.g. blob of extra emission, non-planar rotation), and they cannot be justified with another mechanism different from minor mergers. But, our study does not reveal any obvious relicts of satellites, and no clear evidence of optical counterparts is found in the surroundings of the HI peculiarities. Neither bridges nor tails which could support an accretion scenario from a companion as origin of the lopsided disks are observed (apart from the spectacular case of NGC 5719). The edge-on orientation could limit our investigation if the traces of the companion were in the plane along the line-of-sight. However, this argumentation is difficult to be maintained for all galaxies. Otherwise the companion is fully accreted by the thick box/peanut bulge galaxy, and it is no longer visible. The only reminders of the past interaction are the peculiarities in the main galaxy.

6.4 Conclusion

The main result of this investigation is the large fraction of stellar and HI kinematic asymmetry measures in a sample of spiral galaxies with thick box/peanut bulges. Morphological and kinematic deviations have been compared with the physical properties of the galaxies. This enables us to measure and quantify the effects of such deviations in the evolution history of the target galaxies.

Deviations from symmetry in the near-infrared regime are concentrated between 0 and 0.3 for spheroidal bulges, while for bulges with box/peanut structure the values for A_{nir} span up to 0.8. Based on this trend of the near-infrared deviations, the conclusion is that the older stellar content is not influenced by the mechanism which triggered the box/peanut bulges.

The following results emerge:

- The sample is strongly dominated by warps, especially asymmetric warps.
- There is no relation between morphological and kinematic asymmetries, neither between these asymmetries and the general properties of a galaxy.
- The mass of the HI content in a galaxy seems to play an important role in damping the asymmetries, both morphologically and kinematically.
- Small offsets between the stellar and kinematic centers have been found, but this can hardly be related to the lopsided halo hypothesis, due to the properties of the peculiar features which resemble merger relicts.

References

- Beale J.S., Davies R.D., 1969, *Nature* 221, 531
- Conselice C.J., 1997, *PASP* 109, 1251
- García-Ruiz I., 2001, Ph.D. thesis, University of Groningen, The Netherlands
- Grogin N.A., Geller M.J., 1999, *AJ* 118, 2561
- Haynes, M.P., van Zee L., Hogg D.E., Roberts M.S., Maddalena R.J., 1998, *AJ* 115 62
- Jog C.J., 1999, *ApJ* 522, 661
- Kornreich D.A., Haynes M.P., Jore K.P., Lovelace R.V.E., 2001, *AJ* 121, 1358
- Kornreich D.A., Haynes M.P., Lovelace R.V.E., van Zee L., 2000, *AJ* 120, 139
- Kornreich, D.A., Haynes M.P., Lovelace R.V.E., 1998, *AJ* 116, 2154
- Lütticke R., Dettmar. R.-J., Pohlen M., 2000, *A&AS* 145, 405L
- Grogin N.A., Geller M.J., 1999, *AJ* 118, 2561
- Rix H.-W., Zaritsky D., 1995, *ApJ* 447, 82
- Richter O.-G., Sancisi R., 1994, *A&A* 290, 9
- Sánchez-Saavedra M. L., Battaner E., Florido E., 1990, *MNRAS* 246, 458
- Schoenmakers R.H.M., 1999, Ph.D. thesis, University of Groningen, The Netherlands
- Schwarzkopf U., Dettmar R.-J. 2001, *A&A* 373,402
- van der Hulst J.M., Terlouw J.P., Begeman K.G., Zwitser W., Roelfsema P R., 1992, 'The Groningen Image Processing SYstem, GIPSY', in: *Astronomical Data Analysis Software and Systems I*, A.S.P. Conference Series, Vol. 25, 1992, D.M. Worrall, C. Biemesderfer & J. Barnes (eds.), p. 131
- Walker I.R., Mihos J.C., Hernquist L., 1996, *ApJ* 460, 121
- Warmels R.H., 1988, *A&AS* 72, 427
- Wevers B.M.H.R., van der Kruit P.C., Allen R.J., 1986, *A&AS* 66, 505
- Zaritsky D., Rix H.-W., 1997, *ApJ* 477, 118

7

A particular case: NGC 1055 and infalling gas from the surrounding intergalactic medium

We present VLA observations of the nearby Sb galaxy NGC 1055 in the 21-cm line of the neutral hydrogen. They reveal an asymmetric distribution of neutral hydrogen being more extended (about 5.5 kpc) in the north-western, approaching side. We also detect the rare signature of an U-shaped warp. Due to the favoured orientation of the tilted disk, this object turns out to be a unique candidate for confirming accretion from external gas for the warping mechanism. We propose a model in order to test whether the entire kinematics of this object could be justified by an accretion event. The scenario in which the neutral gas warp is tracing two different interaction events is discussed. In this hypothesis, the warp in the north-west traces the new accretion event from intergalactic gas, while the S-shaped warp which affects 3/4 of the disk might be the tracer of a past gravitational interaction. A discussion on the origin of the accreted intergalactic gas is presented.

7.1 Introduction

Disks of spiral galaxies present usually deviations from symmetry in the density distribution and in the kinematics. In edge-on galaxies the most striking asymmetry is the deviation from the disk planarity in the outer parts (warp phenomenon).

Several theoretical models for warps in spiral galaxies have been proposed including explanations either through a continuous perturbing agent, or by a mechanism able to stabilize the warp against the differential precession (Binney 1992, and references therein). Discrete normal modes (Sparke & Casertano 1988), misalignment between the disk and the halo (Debattista & Selwood 1999), intergalactic magnetic fields (Battaner, Florido & Sánchez-Saavedra 1990), intergalactic accretion (Steiman-Cameron & Durisen 1984 and others), and tidal interactions with neighboring galaxies (Hunter & Toomre 1969, Schwarz 1985, Jiang & Binney 1999, hereafter JB99) are mechanisms able to create and maintain warps in galaxies.

Different phenomena might be inter-related in forming the warping mechanism. It is very hard to disentangle which of the mechanisms listed above is playing the main role in the formation and the maintenance of the warps. Possibly, none of them accounts for

all the observed warped galaxies, although two facts have to be reported. Firstly, more evidence for infalling gas becomes recently available (López-Corredoira, Betancort-Rijo & Beckman 2002, hereafter LBB02; Block et al. 2002, Sánchez-Saavedra et al. 2003). Secondly, the role of the environment – despite being still controversial – is assuming a growing importance. Optical warps are larger and more frequent – and galaxies more lopsided – in rich than in poor environments (Reshetnikov & Combes 1998), while recent HI studies report a larger fraction of warped objects in poor rather than in dense environments, but with smaller amplitudes and higher symmetries between the two sides of the galaxy (García-Ruiz 2001).

The warping mechanism has been better observed in the HI 21-cm line than at optical wavelengths because HI disks in spiral galaxies are normally more extended than stellar disks reaching distances of about 100 kpc in giant spirals (Bosma 1978). In addition, HI disks of spiral galaxies begin to warp only where the optical surface brightness begins to fall extremely steeply (Sancisi 1976, Bosma 1978, Briggs 1990). Despite these difficulties warped stellar disks exist (Sánchez-Saavedra, Battaner & Florido 1990; Reshetnikov & Combes 1998, Sánchez-Saavedra et al. 2003).

Both optical and HI studies report on a significant percentage of warped stellar disks. Several authors claim that nearly all galaxies possess warps, confirming the earlier prediction made by Bosma (1981). This takes into account the geometrical problem that a warp is not detectable when the line-of-nodes lies close to the line of sight.

Warps have commonly an *integral-sign shape*, bending up on one side of the galaxy and down on the other (e.g. Bosma 1983, Sancisi 1983). Less frequently they are found with an U-shape (*cup-shape*) where the two sides curve into the same direction. The latter are observed in 7% – 29% of all warped cases, depending on the authors. Schwarzkopf & Dettmar (2001) report 20 stellar U-shaped warps of 71 warped galaxies in a sample of 108 edge-on galaxies (2001); García-Ruiz (2001) observed two HI U-shaped warped galaxies in a sample of 20 warped galaxies of a survey of 26 objects. Sánchez-Saavedra et al. (2003) obtain a smaller fraction: 4 stellar U-shaped warped galaxies of 150 warped objects in a complete sample of 276 spiral and lenticular galaxies. The fact that lenticular galaxies were included in the latter survey does not influence the statistics since no warped lenticulars are found.

As a part of a study to investigate the nature of galaxies with thick box/peanut shaped bulges (Lütticke et al. 2000) we have obtained HI synthesis maps to study the large-scale kinematics through the 21-cm line. Here, we discuss the distinctive case of NGC 1055 which presents the signature of the U-shaped warp.

7.2 NGC 1055

NGC 1055 is a nearby edge-on spiral galaxy, of morphological type SBb and located at a distance of 13.22 Mpc ($H_0 = 75 \text{ km s}^{-1} \text{ Mpc}^{-1}$). The assumed distance yields a scale of $3.8 \text{ kpc arcmin}^{-1}$. A systemic velocity of $(991.65 \pm 9.01) \text{ km s}^{-1}$ has been adopted throughout this paper. This value is close to other published velocities for NGC 1055. Shaw (1993) finds $(1016.6 \pm 13.2) \text{ km s}^{-1}$ from optical spectroscopy. A value of $v_{LSR} = 1000 \text{ km s}^{-1}$ was derived from H₂O maser observations by Henkel et al. (1986). A heliocentric systemic velocity of $v_{helio} = 1050 \text{ km s}^{-1}$ was detected with CO observations by Young et al. (1989). Using HI single-dish observations, Arp & Sulentic (1985) found a velocity of $v_{helio} = 1030 \text{ km s}^{-1}$. Giraud (1986) gives $V_{LSR} = 1000 \text{ km s}^{-1}$ from HI measurements, which corresponds to $V_{helio} = 972 \text{ km s}^{-1}$.

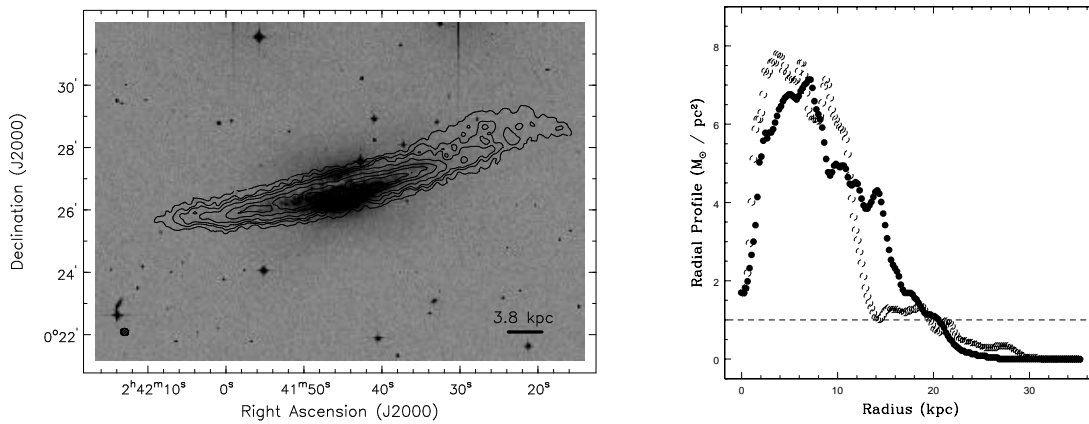


Figure 7.1 (*Left*) The total HI column density distribution of NGC 1055 superimposed on a B-band image (CAHA, 20 minutes). North is up, east to the right. The contour levels are at 2 (4σ), 6, 10 $\times 10^{20}$ atoms cm^{-2} , and from 18 to 88 atoms cm^{-2} in steps of 20×10^{20} atoms cm^{-2} . The spatial resolution of the HI total distribution is $15''.28 \times 13''.71$ (bottom left). (*Right*) Radial HI density profile. The open circles indicate the north-western, approaching side and the filled circles the south-eastern, receding side. The dashed line indicates the radius at $1 M_{\odot} \text{pc}^{-2}$, R_{HI} .

The stellar disk has a position angle of about 105° and a prominent dust lane obscures the stellar light above the major axis (Fig. 1a). NGC 1055 has a bulge with extensive box/peanut isophotes up to 9.5 kpc ($2'.5$) in z -height at an estimated surface brightness of $B = 26^{\text{m}}$ to 26.5^{m} arcsec^{-2} (Shaw 1993). Using absorption-line spectroscopy, Shaw (1993) observed constant circular velocities in z -height up to ≈ 4 kpc ($\approx 1'$), and the overall bulge displays the cylindrical rotation typical of box/peanut shaped bulges. In the innermost region ($10''$ to $30''$, 0.63 kpc to 1.9 kpc), Shaw (1993) derived kinematic profiles which show evidence for strong asymmetries between the two sides of the galaxy with the south-eastern, receding side falling down by $\approx 110 \text{ km s}^{-1}$ below the values to the north-western, approaching side. Shaw (1993) found also that the peak and the systemic velocities fall with increasing z -height from 1023.1 km s^{-1} at $16''$ (1 kpc) to 1001.4 km s^{-1} at $40''$ (2.53 kpc) below the major axis. The nature of this trend is explained either as the influence of the disk component or as an indication of a variation in the rotation of the bulge (Shaw 1993).

NGC 1055 is part of a small group named LGG 73 (Garcia 1993). The nearest member, NGC 1068, is located at the projected distance of $\approx 30'$ (≈ 114 kpc) due south-east.

7.3 Data acquisition and observational results

7.3.1 Observations

NGC 1055 was observed in 21-cm line emission with the Very Large Array¹ (C configuration) in July 1997. We used the 4ABCD spectral line mode with two overlapping spectral

¹The National Radio Astronomy Observatory (NRAO) is a facility of the National Science Foundation operated under cooperative agreement by Associated Universities.

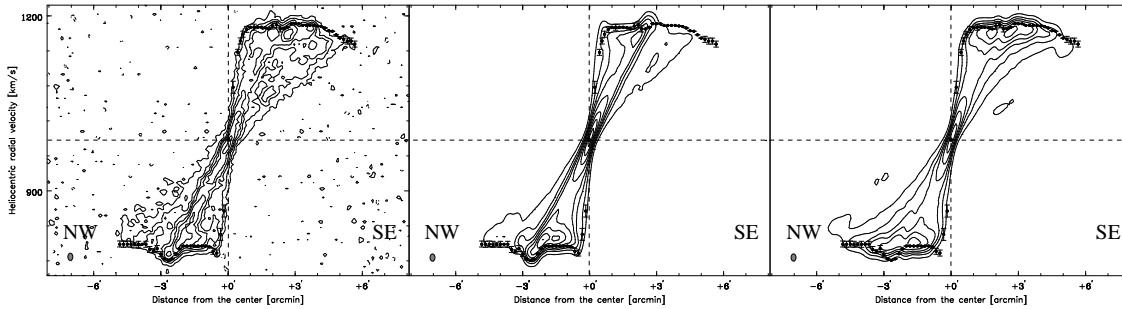


Figure 7.2 Position-velocity diagram taken along the major axis (P.A. = 105°) of the observations (left) and the synthetic data (middle and right) as a result of the tilted-ring method. The middle panel represents the model which best reproduces the characteristics of the approaching side (model A), the left panel displays the model R which is well suited for the receding side. The x -axis indicates arcminutes south-east of the dynamical center. The horizontal line indicates the systemic velocity (991.65 km s^{-1}). The dots represent the unaveraged rotation curve. The contour levels are at -3 , -1.5 (dashed) and from 1.5 ($\approx 1.34 \text{ mJy beam}^{-1}$) to 27σ in steps of 1.5σ . The angular and velocity resolutions are $14'' \times 15.5 \text{ km s}^{-1}$ (ellipse at the bottom left of each panel).

bands of 64 channels each, with an overlap of 5 channels. Hence the total number of channels was 119 with a total velocity coverage of $\approx 613 \text{ km s}^{-1}$ and a channel separation of $\approx 5.15 \text{ km s}^{-1}$. The total integration time was 6 hours, the spatial resolution of the robust-Briggs' weighted cube is $15''.28 \times 13''.71$. The noise in the full resolution cube is 0.91 mJy/beam per channel. The details of the data reductions are reported in Ch. 2.

7.3.2 Morphological and kinematics HI asymmetries

In Fig. 1a the total HI density distribution is displayed superimposed on an optical image (DSS) along with a HI density profile.

The most conspicuous HI column density extends beyond the stellar disk, as commonly observed in spiral galaxies. A value of ≈ 1.5 is found as ratio between the optical (at 25^m ; $R_{25} = 3'.38$) and HI ($R_{\text{HI}} = 5'.2$) radii. The R_{HI} defined as the radius where the density profile falls to $1 \text{ M}_\odot \text{ pc}^{-2}$ is derived from the total HI map. The total inferred HI mass is $4.24 \times 10^9 \text{ M}_\odot$ as computed from the global flux profile.

The spatial distribution of HI shows asymmetries on all scales and has a well-defined hole in the inner $\sim 1 \text{ kpc}$. As it is apparent from Fig. 1a, the HI is more extended on the north-western side. However, asymmetries are seen further in as well. Fig. 1b shows the radial HI density profiles at both sides of the center, derived using the Lucy method as described in Warmels (1988). The HI density distribution is lopsided to the north-western, approaching side in the inner 11 kpc and to the south-east out to $\sim 20 \text{ kpc}$, and again lopsided to the north-west at radii $r > R_{\text{HI}} \approx 20 \text{ kpc}$ (dashed line in Fig. 1b). This outer north-western distribution which is represented by the lowest contour in Fig. 1a, shows an overall unsettled morphology and an U-shaped warp.

The position-velocity (p-v) diagram along the major axis of NGC 1055 is shown in Fig. 7.2 (left panel). The dots show the circular velocities derived with the Warped Modi-

fied Envelope Tracing method (Sect. 5.3.1).

The kinematics of the HI is slightly asymmetric in the receding and approaching sides. The rotation velocity rises quite steeply in both sides of the galaxy reaching the flat part (180 km s^{-1} on average) at about $1'$ (3.8 kpc) from the center. In the north-western, approaching side, a bump towards higher velocities is observed at about $2'5$ (9.5 kpc) from the center. In the south-eastern, receding side, the rotation curve shows quite flat rotation velocities and a final decrease at the outer edge. This trend is not observed in the approaching side where the rotation curve remains flat until the last point, $v(r=5'7) = (177.88 \pm 3.01) \text{ km s}^{-1}$. In Fig. 7.2 the heliocentric systemic velocity of $(991.65 \pm 9.01) \text{ km s}^{-1}$ is shown by a horizontal dashed line. We calculated the systemic velocity by visually inspecting the channel maps and by assuming the velocity which minimizes the asymmetries of the rotation curve.

Fig. 7.3 shows p-v diagrams measured on slices parallel to the major axis (105°) interspaced by $25''$ ($\approx 1.6 \text{ kpc}$). In the northern slices the emission above the plane is traced out to further distances in z -height ($150''$, 9.5 kpc) and from the center ($7'5$, 28.5 kpc, right panels) compared with the southern slices (left panels). This is a direct consequence of the U-shape of the warp; a normal S-shaped warp would have shown emission on the top-left panels of Fig. 7.3.

Relative to the systemic velocity, the channels with equal rotation velocities are displayed in the same panel, as shown in Fig. 7.4. In the latter, the position of the major axis is overlaid on the contour plots in order to evaluate the morphological HI deviations. As observed in the gas distribution above and below the major plane and in the channel maps, the kinematics (Fig. 7.3) and the distribution (Fig. 7.4) of the neutral hydrogen with rotation velocities up to approximately 100 km s^{-1} ($< 2'$) are quite symmetric. Much further, the centroid of the north-western, approaching gas distribution with rotation velocities larger than 100 km s^{-1} is centrally concentrated and peaked at $\approx 2'5$ (9.5 kpc) from the center (in Fig. 7.3 between 92.7 km s^{-1} and 139.1 km s^{-1}). The kinematic counterpart of this feature is the bump at $2'5$ in the p-v diagram (Fig. 7.2). On the contrary, at the same distance from the center on the opposite side the HI morphology is smoothly elongated and the warp appears at the channels around 123.6 km s^{-1} from the systemic velocity. The north-western warp is more pronounced in amplitude and extension and shows the signature only in the last contours at the edge of the emission.

7.4 Modeling

In order to investigate the kinematics of the neutral gas in NGC 1055, we have attempted three-dimensional modeling of the HI data cube using the tilted-ring method (Rogstad et al. 1974).

This method assumes the galaxy to be composed of a set of concentric rings. Each ring is characterized by several parameters which we adopted in the following way: The input values for the HI radial density distribution are computed following the Lucy method, as described in Warmels (1988). The rotation velocities and kinematic axis have been obtained by using the Warped Modified Envelope Tracing method described in Sect. 5.3. A value of 10 km s^{-1} has been assumed for the velocity dispersion of the gas. As described in Sect. 2.3.1, the systemic velocity is derived by visually inspecting the channel maps and the p-v diagram. The center of the HI layer has been fixed by using the internal, symmetric HI distribution. The dynamical center will be the position which lies along the position of the internal major axis (the line at 105° in Fig. 4), and – simultaneously – mini-

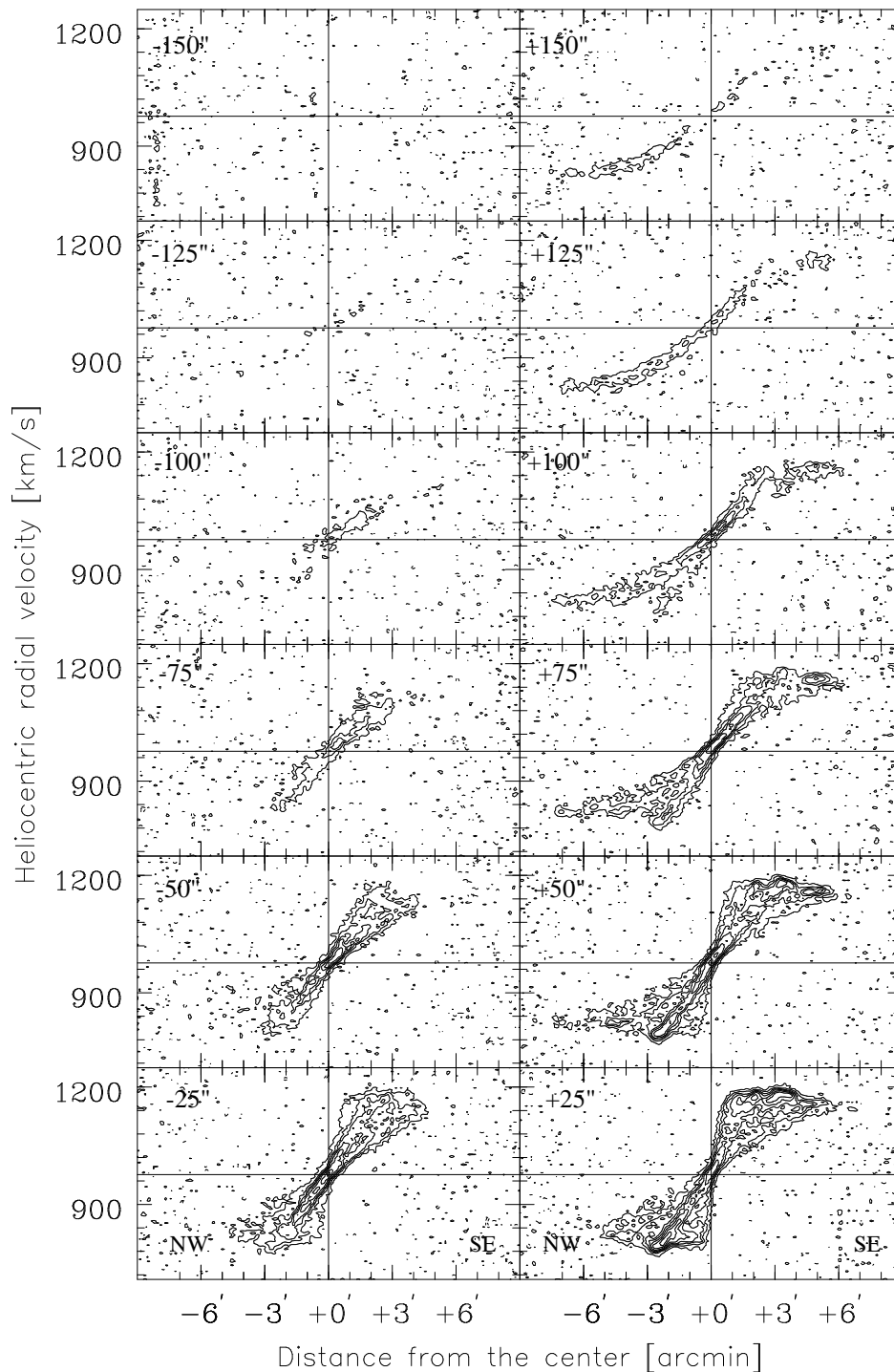


Figure 7.3 Position-velocity diagrams taken parallel to the major axis (P.A. = 105°) above (right) and below (left). They are interspaced by $25''$ as displayed in the upper left ($25'' \approx 1.6$ kpc). The emission above the plane is traced out to $150''$ (9.5 kpc) and reaches much further distances from the center (7.5 , 28.5 kpc) on the western, approaching side. The horizontal line indicates the systemic velocity (991.65 km s^{-1}). The vertical line indicates the dynamical center of the galaxy. The contour levels are at -1.8 (dashed) and from 1.8 ($\approx 2.5\sigma$) to 24 mJy beam^{-1} in steps of 4 mJy beam^{-1} . The angular and velocity resolutions are $14'' \times 15.5 \text{ km s}^{-1}$ (ellipse at the bottom left).

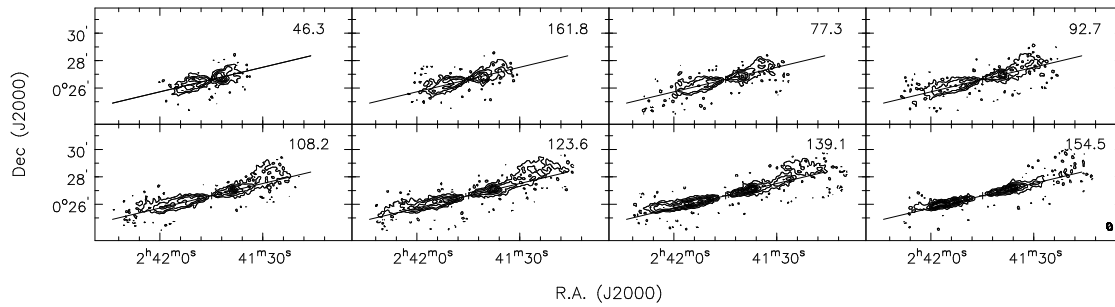


Figure 7.4 The channels which show emission on the receding and approaching side with the same rotation velocities relative to the systemic velocity are shown in one map. Regions without emission are previously blanked. The line at 105° indicates the inner position angle of the galaxy. The rotation velocities relative to the systemic velocity (991.65 km s^{-1}) are displayed in the upper right corner. Contours are $-3, -1.5, 1.5 (2.1\sigma), 3 \text{ mJy beam}^{-1}$ to 28 mJy beam^{-1} in steps of 4 mJy beam^{-1} . The resolutions are $15''.28 \times 13''.71 \times 15.5 \text{ km s}^{-1}$.

mizes the asymmetries of the p-v diagram. The kinematic center offsets a few arcseconds with respect to the tabulated optical coordinates. The initial guess for the inclination is assumed from the optical measurements (65.9° , LEDA).

In order to reproduce the HI disk kinematics, we explored a large range for the input parameters. In particular, the velocities were allowed to vary by $\pm 6 \text{ km s}^{-1}$ from the original findings. The kinematic axis was adjusted by $\pm 2^\circ$, especially in the outer region where the emission is coming from a smaller number of rings. The values for the center, the column density at each radius, and the systemic velocity were kept fixed. As previously observed, the systemic velocity is in good agreement with other published measurements. The initial value for the inclination (65.9°) adopted from optical measurements has been largely increased up to 86° . As a result, either the HI disk is more inclined compared to the optical body or – more likely – the optical inclination has been underestimated.

The goal of this modeling is to describe the general properties of the HI disk (e.g. the extension, the orientation) as well as to reproduce the main peculiar features, like:

- 1) the unsettled, low-level emission in the north-western region and the peculiar orientation (U-shaped warp);
- 2) the bump at 2.5 from the center in the approaching side of the p-v diagram, as well as in the rotation velocities;
- 3) the nearly flattened, receding rotation velocities which gradually decrease outwards.

Despite the exploration of several values for the input parameters, no convergence between the observations and the synthetic data was found. The failure of convergence to a unique solution can be explained because of the peculiar geometry and the lopsided morphology and kinematics.

We find the best agreement between the observations and the synthetic data by adopting different geometrical and physical parameters for the approaching and receding sides, rather than the averaged values. This is justified by the large lopsidedness in the kinematics and density distributions.

To understand the U-shaped warp, we fit tilted-ring models to the approaching and

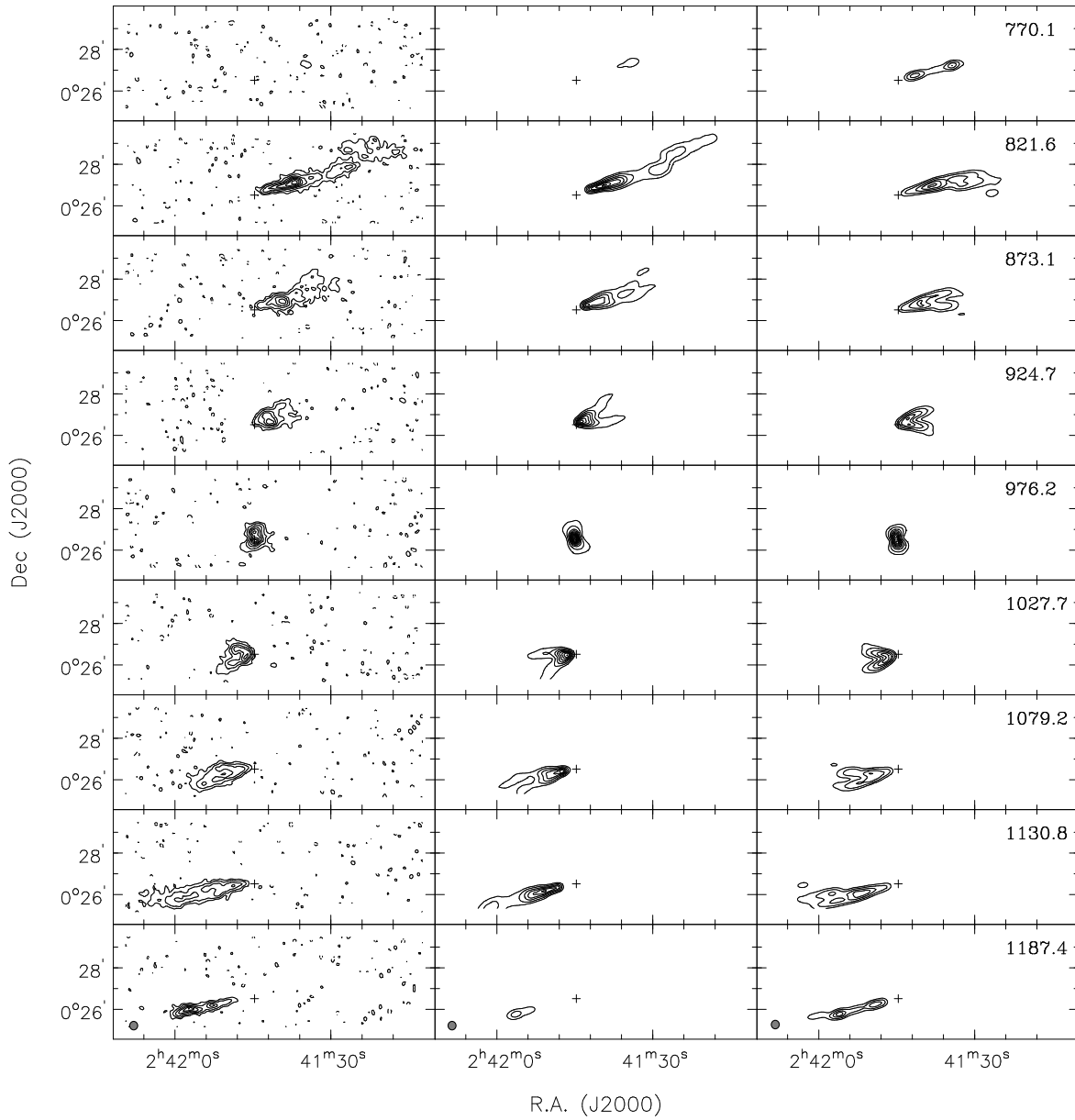


Figure 7.5 Channel maps of the observations separated by 56.6 km s^{-1} (*left*), and the synthetic data for the models A (*middle*), and R (*right*). The rotation velocities relative to the systemic velocity (991.65 km s^{-1}) are given in the panels. The contour levels are at -3 , -1.5 (dashed) and from 1.5 ($\approx 1.34 \text{ mJy beam}^{-1}$) to 27σ in steps of 1.5σ . The angular and velocity resolutions are $14'' \times 15.5 \text{ km s}^{-1}$.

receding sides, separately. We refer to the fit to the receding side as model R and the fit to the approaching side as model A.

The p-v diagrams for the observations, for the models A, and R are shown in Fig. 7.2. Representative channel maps of the observations separated by 56.6 km s^{-1} are displayed in Fig. 7.5 and compared with the two models: A and R.

We find that model R (right panels) provides a good fit to the channels from 924.7 km s^{-1} to 1187.4 km s^{-1} , i.e. it describes the channel maps up to 56 km s^{-1} less than the systemic velocity. At channel 873.1 km s^{-1} , model R matches the down-warp seen at the inner radii, but fails to reproduce the outer, lowest contours which warp up. It entirely misses the upward warp of channel 821.6 km s^{-1} . Conversely, model A accurately describes the upward warp in the approaching channels but fails in the receding channels.

The results of this modeling are:

1) a large part (about 3/4) of the HI disk of NGC1055 is affected by the S-shaped warp, which is especially visible in the south-eastern, receding side. This warp is well settled and can be described by a smooth change of the position angle (P.A.) beyond $\sim R_{25}$ ($200''$) from P.A. = 105° up to 95° to the outer rings. An indication of this warp is also slightly visible in the inner parts of the north-western, approaching side in the total HI map (Fig. 1a). These characteristics are reproduced by model R (Fig. 7.2 and 7.5, right panels).

2) The peculiarities of the north-western, approaching side were reproduced by a position angle which increases rapidly by about $+7^\circ$ beyond $300''$ (19 kpc). With this choice, the bump at 2:5 in the p-v diagram (Fig. 7.2, middle panel), and the extended, tilted low surface density structure at the edge of the north-western disk (Fig. 7.5, velocities around 821.6 km s^{-1}) are well reproduced. The importance of the second result is that, although the north-western structure seems not to be totally settled and somewhat separated from the disk, no discontinuity is observed in the rotation curve. In particular, it shows the expected rotation velocity at that distance but with a rotation axis misaligned by about $+7^\circ$ with respect to the inner disk and by about $+17^\circ$ with the gas at the same distance from the center on the opposite side. It is clear from these diagrams that the two models presented here reproduce the main characteristics of the HI observations.

7.5 Discussion

The main result of this work are the kinematic and morphological lopsided properties observed in the neutral hydrogen disk of NGC 1055. By imposing an unique set of input parameters (i.e. without differentiating between the receding/approaching velocities and the east/western column density distribution and position angle) the three-dimensional modeling does not well describe the observations.

The south-eastern, receding warp is well settled, and affects 3/4 of the disk of the galaxy. The north-western, approaching side seems more unsettled and affects a smaller fraction (1/4) of the disk. We provide an adequate description of the observations with three-dimensional modeling considering the appropriate rotation velocities, HI column densities and position angles for each side of the galaxy individually instead of using averaged values from both sides.

The asymmetric distribution of the HI warp with opposite tilt angle with respect to the inner disk and the described peculiar features may indicate that two distinct phenomena are simultaneously observed in this galaxy.

The proximity of NGC 1068 could have generated a disturbance in NGC 1055 by gravitational interaction. The gravitational influence produced by NGC 1068 acts on the dis-

tribution of NGC 1055 leading to a S-shaped warped disk, as is still observed over a large portion of the HI disk. The optical images are too contaminated by dust to reveal any relevant information in the central stellar disk. However, a hint of the stellar disk's deviation is visible in the south-eastern region which well follows the HI curvature. On the other hand, the overall HI morphology and kinematics of NGC 1068 do not present any strong tidal signature or significant warped distribution which would imply such an interaction. Nevertheless, in NGC 1068 – as commonly found in Seyfert galaxies of which NGC 1068 represents a prototype – HI extends as far as the optical galaxy. HI disks of spiral galaxies begin to commonly warp only at the edges of the stellar disk causing the difficulties in recognizing any deformation. Recent studies on warps (e.g. García-Ruiz 2000) show that all galaxies with HI emission more extended than the optical stellar bodies present warped distributions. In the reverse case – due to the characteristic of HI distribution to turn only at the edges of the HI disk – the relation between HI and optical warps is still not clear. The possible gravitational interaction which could have occurred between NGC 1068 and NGC 1055 is observable only in the latter galaxy due to its HI extent well beyond the optical disk.

The north-western region turned out to be more massive in HI with respect to the opposite side, with masses of $2.35 \times 10^9 M_\odot$ and $1.89 \times 10^9 M_\odot$, respectively. The tidal interaction with the companion galaxy NGC 1068 could have displaced HI complexes in NGC 1055. This mechanism could have created a gas reservoir in the more massive, north-western region which is falling back onto the disk of NGC 1055, as proposed by Sancisi (1983). Both the morphology and the kinematics appear disturbed in this region. The bump at the approaching velocities (at about 2.5 from the center, Fig. 2) could reflect the proposed infalling scenario.

The observed U-shaped warp should be transient, eventually leading to a redistribution of the angular momentum of the outer parts of the disk.

If we consider the effect of differential rotation and take the inner and outer radii of the warp A as $R_i=19$ kpc and $R_o=31$ kpc, we can estimate the age of such a structure as:

$$t_{warp,A} < \frac{\delta\theta}{\omega} = \frac{\delta\theta}{v_{flat}} R_i \times R_o / (R_o - R_i) \quad (7.1)$$

where $\delta\theta$ is the angular part of the galaxy affected by the warp ($\pi/2$), ω is the angular velocity, and v_{flat} is the rotation velocity in the flat part (180 km s^{-1}).

We obtain an age of $< 4 \times 10^8$ yr and an accretion rate of $M_{warp,A}/t_{warp,A} > 0.59 M_\odot \text{ yr}^{-1}$. The mass included in the warp model A was computed by summing up the column densities of the warped rings, starting from 19 kpc. The revolution time in the region of the warp is about 10^9 yr and this would be roughly the lifetime of the S-shaped warp. Based on these computations the U-shaped warp is a younger structure compared to the S-shaped warp.

As recently proposed, the reorientation of the galactic disk might be produced as a redistribution of angular momentum to compensate the differential precession due to a torque (LBB02). The torque possibly generated by tidal interaction with the companion galaxy could have strong influence in generating U-shaped warps. Actually, in the survey of García-Ruiz (2001) the two U-shaped warped galaxies are strongly interacting with nearby companions.

The galaxy studied here can reflect a case where such a phenomenon is observed at an intermediate stage. The infalling material from the gas reservoir with different angular momentum is starting to settle down and to influence the kinematics of the pre-existing

S-shaped warp. If this is the case, the development of U-shaped and asymmetric S-shaped warps observed in other galaxies should be generated by the same mechanism of the net angular momentum reorientation like the one observed in NGC 1055.

On the other hand, a small gas-rich dwarf in an advanced stage of disruption could also explain the scenario (e.g. JB99, LBB02). Despite the fact that we cannot reject this hypothesis, no clear sign of an optical counterpart or excess of luminosity is found in the north-western region. Apart from the innermost asymmetries in the optical rotation curve (Shaw 1993) no indication of an accretion event has been found.

Therefore, we propose a recent ($< 4 \times 10^8$ yr) infall of intergalactic material onto a pre-existing S-shaped warped disk as the most likely explanation of the U-shaped warp observed on the large-scale in the HI disk. This may be at an intermediate stage of the formation, or the re-settling, of a warp in the outer part of a galactic disk due to infalling material. This material has different angular momentum and was displaced by gravitational interaction with the nearby galaxy, NGC 1068, which has created a gas reservoir in the massive, north-western region.

7.6 Conclusion

The present observations show a lopsided NGC 1055 in morphology and kinematics. A peculiar warped geometry anticipates the failure of convergence to an unique solution when modeling the galaxy with a three-dimensional circular rotating tilted-ring method. Best agreement between the observations and the synthetic data is found by adopting different geometrical and physical parameters for the approaching and receding sides.

Two events separated in time could have occurred in the history of NGC 1055, the first of which has reshaped the largest part of the HI morphology and kinematics of the neutral gaseous component into an S-shape by gravitational interaction with the nearby NGC 1068. Later on, an U-shaped warp has formed as result of infalling of the HI-reservoir onto the S-shaped disk.

A. Appendix

The formula 7.1 is a simple estimate of the persistence of a deformation in a certain location of a galaxy. Due to differential rotation, the inner orbits have a larger angular velocity with respect to the external ones. Assuming that a deformation in a distribution influences an angle $\delta\theta$ of a galaxy, the deformation itself will subtend this angle for a time scale $t_{warp} < \frac{\delta\theta}{\omega}$, where ω is the angular velocity of the inner system in an external reference. $\delta\theta$ is expressed in radians. For a time t larger than t_{warp} the structure will not anymore subtend the angle $\delta\theta$, and the angular velocity is $\omega_{in} - \omega_{out}$ in an external reference. As the velocity is flat in this region $v_{in} = v_{out} = v_{flat}$, we obtain the formula 7.1.

References

- Arp H., Sulentic J., 1985, ApJ 291, 88
- Battaner E., Florido E., Sánchez-Saavedra M. L., 1990, A&A 236, 1
- Binney J., 1992, ARA&A 30, 51
- Block D. L., Bournaud F., Combes F., Puerari I., Buta R., 2002, A&A 394, 35
- Bosma A., 1978, Ph.D. thesis, Groningen
- Bosma A., 1983, IAU 100, 11 in Internal kinematics and dynamics of galaxies; Proceedings of the Symposium, Besancon, France
- Bottema R., 1995, A&A 295, 605
- Briggs F. H., 1990, ApJ 352, 15
- Burke B. F., 1957, AJ 62, 90
- Debattista V. P., Sellwood J. A., 1999, ApJ 513, 107
- Garcia A. M., 1993, Lyon Groups of Galaxies
- García-Ruiz I., 2001, Ph.D. thesis, Groningen
- García-Ruiz I., Sancisi R., Kuijken K., 2002, A&A, 394, 769, GSK02
- Giraud E., 1986, ApJ 309, 512
- Henkel C., Wouterloot J., Bally J., 1986, A&A 155, 193
- Hunter C., Toomre A., 1969, ApJ 155, 747
- Jiang I.-G., Binney J., MNRAS 303, L7; JB99
- Kamphuis J., 1993, Ph.D. thesis, Univ. Groningen
- Kerr F. J., 1957, AJ 62, 93
- López-Corredoira M., Betancort-Rijo J., and Beckman J. E., 2002, A&A 386, 169; LBB02
- Lütticke R., Dettmar R.-J., Pohlen M., 2000, A&AS 145, 405L
- Newton K., Emerson D. T., 1977, MNRAS 181, 573

- Reshetnikov V., Combes F., 1998, *A&A* 337, 9
- Rogstad D. H., Lockhart I. A., Wright M. C. H. 1974, *ApJ* 193, 309
- Sánchez-Saavedra M. L., Battaner E., Florido E., 1990, *MNRAS* 246, 458
- Sancisi R., 1983, *IAUS* 100, 55 in *Internal kinematics and dynamics of galaxies; Proceedings of the Symposium, Besancon, France*
- Sancisi R., 1976, *A&A* 53, 159
- Shaw M., 1993, *A&A* 280, 33
- Sofue Y., Rubin V., 2001, *ARA&A* 39, 137
- Sparke L. S. & Casertano S., 1988, *MNRAS* 234, 873
- Steiman-Cameron T. Y., Durisen R. H., 1984, *ApJ* 276, 101
- Schwarz U. J., 1985, *A&A* 142, 273
- Schwarzkopf U., R.-J. Dettmar, 2001, *A&A* 373, 402
- van der Kruit P. C., 1979, *A&AS* 38, 15
- Warmels R. H., 1988, *A&AS* 72, 427
- Young J., Xie S., Kenney J., Rice W., 1989, *ApJS* 70, 699

8

Summary and Future Research

8.1 H I observational results

We have presented HI data of a sample of spiral galaxies with thick and prominent box/peanut bulge galaxies to investigate the distribution and the kinematics of the neutral hydrogen. The important finding is the large fraction of irregularities in the distribution of the HI and strong deviations from the disk planarity: All the target galaxies are warped. Relicts of past interactions and signatures of on-going mergers are detected in the majority of the target galaxies.

8.2 Optical and near-infrared analysis

Peculiarities in the light distribution and dust lanes even on several planes are often observed.

Using the plateau of the light in the radial profiles, one strong bar and other three possibly weak bars are found among the fourteen galaxies observed in the near-infrared. In total, less than 30% of the target objects are barred galaxies. Peculiarities in the light distribution are interpreted as possible relics of recent accretion events. The rate of bars in galaxies indicates the hybrid scenario (as introduced in Ch. 2) as likely formation mechanism for thick box/peanut bulges: Interactions excite the development of a bar in a disk as a response to the perturbation of a companion, the light distribution reshapes into a boxy/peanut structure due to buckling.

From a vertical fit to the light distribution using the Sérsic functional form turns out that bulge parameters do not correlate with the morphological type in the target galaxies. Bulges are well described with the bulge parameter $n = 2$. Vertical surface brightnesses in box/peanut bulges are structurally different from those of the more spheroidal bulges: Fainter effective surface brightnesses and larger effective radii are indeed detected in thick box/peanut bulges with respect to the classical box/peanut and spheroidal bulges.

8.3 Stellar and gaseous kinematics in the central regions

For a subsample of four galaxies, optical long-slit spectroscopy along the major axis was performed in order to investigate the kinematics of the stellar and gaseous components. The distribution of both stellar and gaseous components are quite settled. In two cases

the kinematics of the approaching and receding sides present some asymmetries. Rotation velocities rise with a different slope and are slightly differently extended.

In one case, a counter-rotating stellar system with the gaseous component is detected with a signature of a possibly second stellar population rotating with the gas. Stellar and gaseous components with opposite angular momentum with respect to the host galaxy are thought to be the final result of a second event that occurred in the history of the host galaxy.

8.4 Rotation curves in edge-on spirals

The rotation curves of the observed galaxies have been derived with a method which accounts for the changes in the kinematic axis of warped galaxies. In the case of HI, which extends far beyond the optical body where self-gravity is weaker and warping more pronounced, the changes in the kinematic axis represents a severe effect to be considered in the procedure when extracting rotation curves, especially in the small angular size, and moderately resolved galaxies. In order to test the final HI rotation curve, model data cubes are built for three of the galaxies in the sample. With known input rotation velocity – derived with the above-mentioned method – and HI orientation and distribution from the observations, the synthesized data match the observations very well.

8.5 Asymmetries in the stellar and gaseous components

The older stellar content is influenced by the mechanism which triggered the box/peanut bulges, but no differences are detected between classical box/peanut bulges and thicker structures.

A large number of asymmetric HI warps with a large variety of shapes (S, U-, and L-shape) are found in the thick box/peanut bulge galaxies.

As previously reported, there is no relation between morphological and kinematic asymmetries nor between these asymmetries and the general properties of a galaxy. As a consequence of two or more un-correlated encounters of different orientations, the lopsidedness in different radial regions could have different strength (Jog 1997). The result is a different gas asymmetry in the outer regions (HI component) which might not be correlated with that in the stellar component in the innermost regions as argued by Jog (1997).

The mass of the HI content in a galaxy seems to play an important role in damping the asymmetries, both morphologically and kinematically. Small offsets between the photometric and kinematic centers have also been detected.

8.6 Future work

As a result of this project, we found that most spiral galaxies show a fairly significant rotational asymmetry. In fact, large-scale asymmetries of rotation curves were observed at almost all wavelengths when accurately analyzed. Usually, the global asymmetry of rotation curves is not widely recognized because the observational data are generally averaged out to present an “enforced” axisymmetric rotation curve. Moreover, precious information is lost due to the technique to minimize the differences between the two halves of the velocities in order to better constrain the center and the systemic velocity. Inaccuracies in centering and small minor-axis displacements produce systematic errors in the shape and interpretation of the rotation curves (Beauvais & Bothun 2001, ApJS 136, 41).

Any non-circular and/or anomalous motions lying along the slit axis are included and interpreted as rotations. Moreover, the line-of-nodes often shows a twist or warp which leads to an underestimation of the derived rotation velocities (present work).

From several studies it has become clear that 3-D measurements of galaxies contain valuable information, and the difficulties mentioned above are reduced using 3-D techniques. Whereas radio astronomy has dealt with 3-D data for many decades already and extracted full kinematic information without strong assumption on the orientation, optical astronomy still proceeded with the traditional 2-D spectrography.

Only recently, a trend towards 3-D spectroscopy is observed also at optical wavelengths. Along with the advent of 8 to 10-m class telescopes new investigations on galaxy evolution at redshifts larger than 1 are being performed, but also studies on the physics of many processes which underlie galaxy evolution are expected to be investigated in the local Universe. Of particular interest is the investigation of the possibly interrelated phenomena: lopsidedness – warps – accretion events. The role of the environmental effects with regard to the internal secular processes should be quantified as a function of the redshift. Mechanisms which trigger asymmetries in different environments could be analyzed in a systematic way.

Up to now, most of the 3-D kinematic studies are concerned with individual peculiar objects or small and non-homogeneous samples, apart from the following ones: Sauron, P.I.s: de Zeeuw, Bacon, and Davies; Gassendi H Alpha survey of SPirals (GHASP), P.I.s: Amran, Marcellin, Bouleix, & Garrido; Westerbork observations of neutral Hydrogen in Irregular and SPiral galaxies (WHISP), P.I.: van Albada. Using the capability of this new instrumentation other surveys will soon yield insights into many problems of the galaxy structure and dynamics in the local Universe.

Acknowledgments

In the time I worked on my Ph. D. project I had the pleasure to meet many wonderful people at my host institutes, during my travels and observations. I want to thank all those people from which I have received support and encouragement. The completion of this thesis would be impossible without their help.

I want to thank my supervisor, Prof. Ralf-Jürgen Dettmar, who has always motivated me despite the distance. This project would have never been possible without his enthusiasm. My gratitude to Prof. Uli Klein who offered me the opportunity to come to Germany and to join his institute. A special acknowledgment goes to Dr. Marc Balcells for his invaluable remarks on my projects and for questioning my un-realistic time-scales.

I greatly enjoyed every single experience during the Ph. D. time, it has been one of the most influential parts in my life. I consider myself fortunate for having had the opportunity of broadening my horizon – not only geographically. I would like to thank Germany as a country, where I spent three years of my life. I appreciated the tranquility and the respect of the rules, which is well known not to be the dominant quality of an Italian. Despite the fact that I risked several times my life in Italy after this injection of respects, now those strange white lines painted on the asphalt have a sense for me.

I am very grateful to the staff at the *Radioastronomisches Institut* in Bonn and at the *Instituto de Astrofísica de Canarias* for saving me from innumerable computer problems.

I would like to warmly thank Ms. Christine Stein-Schmitz and Ms. Nieves Villoslada for helping me struggling through the (unfortunately still too rigid) European bureaucracy and for arranging many things for me.

I would like to dedicate this work to my family and close friends, who always supported me and never complained with my long periods of absence, also at times of necessity. This is perhaps one of the hardest aspects of my life to be accepted.

This work is based on observations taken using several telescopes. In particular, I appreciated the support of the staff at the following sites:

The European Southern Observatory: NTT, 3.6-m telescope, and 1.5-m Danish telescope (La Silla, Chile). I am deeply indebted to the favored allocations of telescope time made by the ESO committee for this project.

The Centro Astronómico Hispano Alemán (Calar Alto, Spain): the 1.23-m telescope, and 2.2-m telescope.

The National Radio Astronomy Observatory (Socorro, NM, USA): the Very Large Telescope.

The Paul Wild Observatory (Narrabri, AU): the Australia Telescope Compact Array.

This research was supported by the *Deutsche Forschungsgemeinschaft* in the framework of the *Graduiertenkolleg* on “The Magellanic System, Galaxy Interaction, and the Evolution of Dwarf Galaxies” (GRK 118), and by a Marie Curie Fellowship of the European Community program “EARASTARGAL”.

This research has made use of the LEDA database (P.I. Prugniel), and the NASA/IPAC Extragalactic Database (NED) which is operated by the Jet Propulsion Laboratory, California Institute of Technology, under contract with the National Aeronautics and Space Administration, and NASA’s Astrophysical Data System Abstract Service (ADS).

Curriculum Vitae

Name: Daniela Vergani
Date and Place of Birth: 9 June 1972, Milan (Italy)
Citizenship: Italian

Education

January 2003 – June 2003 Marie Curie Visiting Fellowship for postgraduate students training site "EARASTARGAL" at the IAC in Tenerife, Spain

September 2002 – December 2002 Research Assistant position at the *Astronomische Institute der Universität Bonn*

September 1999 – August 2002 Ph.D. fellowship at the *Astronomische Institute der Universität Bonn* in the framework of the graduate school "The Magellanic Clouds and Other Dwarf Galaxies" by the German Science Foundation (Deutsche Forschungsgemeinschaft).

June 1999 – August 1999 Summer Research Program at the Netherlands Foundation for Research in Astronomy in Dwingeloo

January 1998 – October 1998 Master Thesis at the C.N.R. Istituto di Radioastronomia, Bologna. Title: *HI Emission in Dust-Lane Elliptical Galaxies* (in Italian). Supervisor: Prof. C. Giovannini Fanti, Advisors: Dr. R. Morganti, Dr. T. A. Oosterloo

October 1991 – December 1997 Study of Astronomy at the University of Bologna.

September 1986 – June 1991 High school, General certificate of education at *Istituto Tecnico Sperimentale* (Specialization: Economics), Milan.

Daniela Vergani